PLUME CHARACTERISTICS OF A MULTIPLE ION SOURCE THRUSTER

Thesis by

C. Michael Tierney

In Partial Fulfillment of the Requirements

for the Degree of

Aeronautical Engineer

California Institute of Technology

Pasadena, California

1995

(Submitted May 30, 1995)

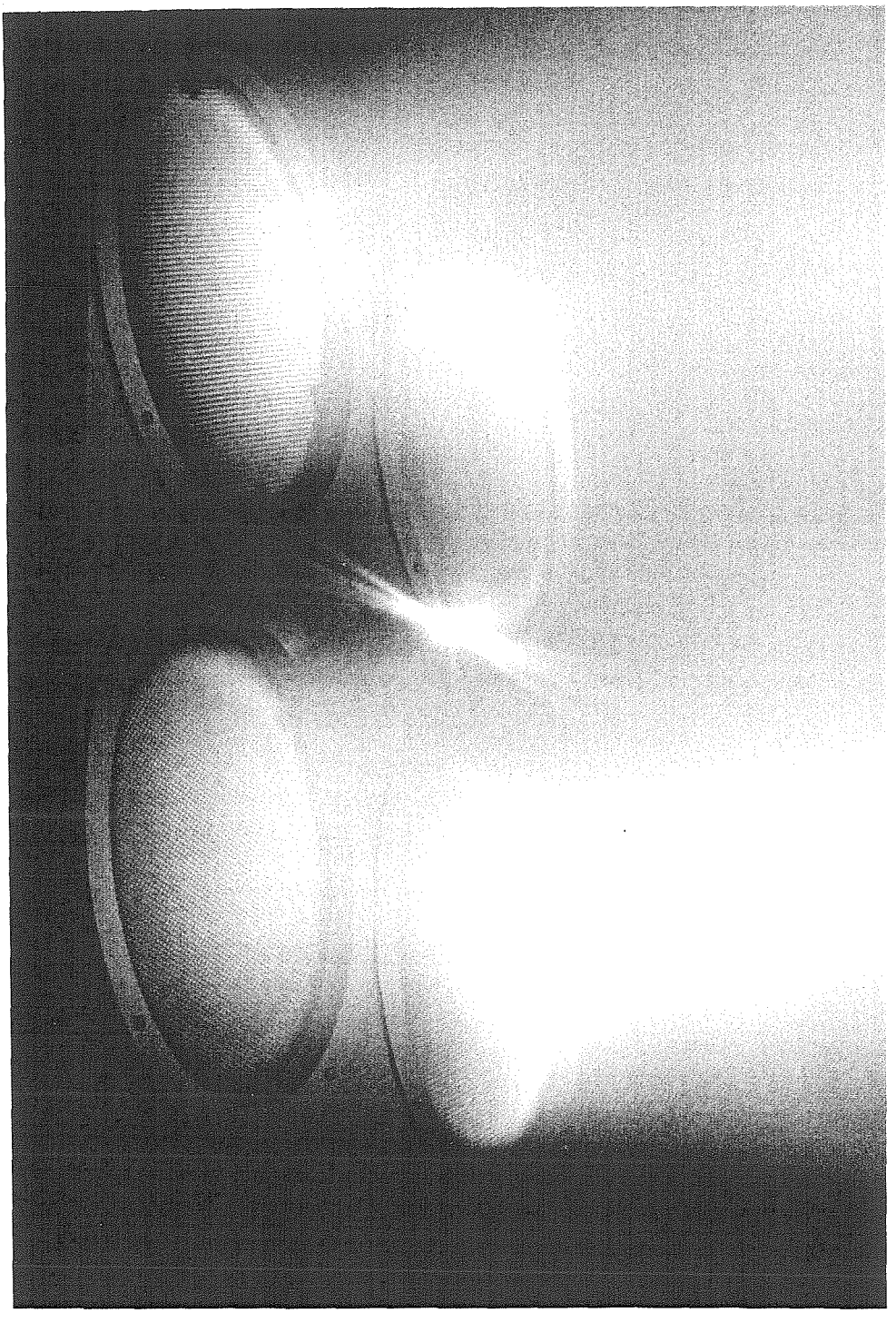

The work described in this report was funded by the California Institute of Technology, Jet Propulsion Laboratory under contract to NASA and a fellowship from TRW Inc., Space and Electronics Group.

First and foremost I would like to thank John Brophy for the opportunity of working with him and all of the folks at JPL. I very much appreciate all the time, effort and support given to me over the last two years in making this a tremendous learning and growing experience. I would also like to thank my advisor, Fred Culick, for all of his support and giving me the freedom to pursue my studies and research at JPL.

The assistance given to me at TRW was invaluable and I would like to expressly thank Carol Schamp and Bob Webb for their belief in me and support of my studies at Caltech. Many others at TRW were also very helpful by allowing me the time necessary to concentrate on my academic endeavors and giving me the pep talks when I needed them. Some of these people include, Frank Cartier, Steve Toner, Rich Rosenthal, Bob Cote, Kaz Mizuba, Ed Simmons, and Steve Sheffield.

In my research, I cannot express enough, my many thanks to the staff at JPL for all the guidance and tutoring they gave me. The talents and capabilities of these people often amaze me. Specifically I would like to thank doctors Juergen, John and Dave; almost doctors Jay, Keith, Stephanie, John; and Chuck, Al, Bill, and Bob. I wish them the best of luck in the future and hope all of their hopes and dreams are fulfilled. I would also like to express my thanks to the late Lou Pless, who was of great help in trouble shooting problems that arose throughout the design and construction of the probe positioning and data acquisition systems.

My sanity during this experience can be directly attributed to Kev, Nic, Steve, John, Lisa, Perry, Linda, Stacy, Dave, Sean, Kev O, Chris, John, Scott, Jake, Buddy, and Manny. Thank you very much for giving me the opportunities to blow off steam when I needed them.

Finally, I would like to thank Mom, without her support and belief in me, and the courage to deal with me and all the other adversities in life, none of this could have been possible. Thank you!

Abstract

This report describes ion plume characteristics of a multiple ion source thruster that are important to propulsion subsystem, spacecraft system, and mission design engineers with respect to incorporation of the segmented ion thruster (SIT) within a space mission. These characteristics will address issues related to operational performance, lifetime, thruster interaction with a host spacecraft, multiple ion beam interaction, and repeatability of construction and operation. Information contained within this report can be helpful in evaluating subsystem / mission performance, and resolve possible thruster / spacecraft integration issues.

Characteristics of the exhausted ion beam(s) were evaluated through two sets of experiments. The first involved measuring the two-dimensional ion current density distribution at several downstream locations from the thruster with concurrent operation of up to three ion sources. Assessments were made of plume symmetry, plume development as a function of downstream position, interactions between multiple ion beams, and beam divergence angles were calculated for individually operated ion sources. Ion beam asymmetries about the ion source centerline were observed. Construction of multiple ion source current density profiles through superposition of data obtained from operation of individual ions sources was attempted. Charge exchange effects appear to have impacted the analyses and some discrepancies between 'real' and 'constructed' results were observed. Beam divergence angles for R = 0.893 cases ranged from 10° to 18° and from 16° to 22° for R = 0.643 cases.

The second set of experiments involved collection of ion charge state data with the use of an ExB mass spectrometer placed downstream of the thruster. Charge state data was collected along the ion source centerline for 3 fixed propellant flow rates and varible beam currents. Data was also collected for a fixed flow rate and beam current at positions located along the horizontal and vertical axes passing throught the ion source centerline. Correction factors for thrust and propellant utilization based upon doubly charged ion production, as well as propellant backflow into the discharge chamber were determined. Asymmetries in the radial profiles, as well as inconsistencies between the profiles of singly and doubly charged ions and charge state ratio, were observed.

Table of Contents

List of Figures

List of Tables

Nomenclature

α	Beam divergence angle (°) (see fig. 2.5-1)
A_a	Actual collector area of a Faraday probe (m^2) (see fig. 5.1-3).
A_e	Effective collector area of a Faraday probe (m^2) (see fig. 5.1-3).
A_g	Grid area (m^2).
A_p	Area of the Faraday probe data acquisition plane (m^2).
β	Beam ion correction factor.
$\bar{B}$	Magnetic field strength (tesla).
C_{scc}	Charge carried by one standard cubic centimeter of xenon assuming atoms are ionized and only singly charged ions are present.
R_C	Charge state current ratio.
R_n	Charge state number ratio.
$\bar{d}$	Distance between ExB probe deflector plates (m) (see figure 3.3-4).
e	Electric charge = 1.602×10^{-19} Coul
$\bar{E}$	Electric field strength (V/m).
ε_{int}	Uncertainty in total measured beam current (%).
$\varepsilon_{operation}$	Uncertainty in total measured beam current due to operation of the thruster (%).
$\varepsilon_{acquisition}$	Uncertainty in total measured beam current due to data acquisition uncertainty (%).
$\varepsilon_{calculation}$	Uncertainty in total measured beam current due to numerical integration scheme (%).
ε_{StdDev}	Portion of $\varepsilon_{acquisition}$ associated with standard deviation of currents measured by the Faraday probes (%).
$\varepsilon_{hardware}$	Portion of $\varepsilon_{acquisition}$ associated with uncertainties introduced by data acquisition hardware (%).
ε_{probes}	Portion of $\varepsilon_{acquisition}$ associated with Faraday probe actual area (%).
ε_{calc}	Uncertainty in the theoretical total beam current that should be measured donwstream of the thruster (%).
$\varepsilon_{divergence}$	Uncertainty in the calculated beam divergence angle (%).
f_t	Total thrust correction factor.
f_d	Beam divergence thrust correction factor.
f_c	Charge State thrust correction factor.
F	Beam flatness parameter.
$\bar{F}_B$	Force on ion due to magnetic field (N).
$\bar{F}_E$	Force on ion due to electric field (N).

F_t	Total mass flow rate of propellant from the thruster, including all active discharge chambers and the neutralizer (sccm, mA_{eq}, mg/s).
g	Gravity constant = 9.8 m/s^2.
h	Width of strips used in Simpson's Rule application (m).
I_α	Current passing within beam divergence angle-α (A).
I_{sp}	Specific impulse (s).
I_B	Total beam current metered by thruster control electronics (A).
I_S	Current measured at the screen grid (A).
I_A	Current measured at the accelerator grid (A).
I_i	Current measured by a single Faraday probe located downstream of the thruster (A).
I^+	Beam current due to singly charged ions (A).
I^{++}	Beam current due to doubly charged ions (A).
I^{+++}	Beam current due to triply charged ions (A).
I_c	Current collected by the ExB probe (A).
I_{bias}	Bias subtracted from Faraday probe data (A).
I_{actual}	Actual current collected by Faraday probe after accounting for bias and secondary electron emission (A).
I_Z	Total beam current measured downstream of the thruster (A).
I_{xy}	Current measured by a Faraday probe at a distance of X and Y from the pre-defined origin (A).
I_y	Integrated beam current of all J_X values = I_Z (A).
J_α	Current denstiy passing within beam divergence angle-α (Am^2).
J_{avg}	Average current density across a plane of Faraday probe data (A/m^2).
J_{max}	Max current density measured by a single Faraday probe (A/m^2).
J_i	Current density measured at a single Faraday probe location (A/m^2).
J_{xy}	Current density measured by a Faraday probe at a distance of X and Y from the pre-defined origin (A/m^2).
J_x	Integrated current along 1 column of Faraday probe measurements (A/m).
J_z	Beam current density measured downstream of the thruster (A/m^2).
K_C	Klausing conductance factor.
k	Boltzman's constant = 1.3807×10^{-23} J/K.
m_i	Mass of a xenon atom = 2.1808×10^{-25} kg.
$\dot{m}$	Mass flow rate (sccm, mA_{eq}, mg/s).
$\dot{m}_f$	Total mass flow rate of propellant into vacuum facility (sccm, mA_{eq}, mg/s).

$\dot{m}_t$	Mass flow rate of xenon into a discharge chamber through propellant feed system (sccm, mA_{eq}, mg/s).
$\dot{m}_{ion}$	Mass flow rate of ions from a discharge chamber (sccm, mA_{eq}, mg/s).
$\dot{m}_n$	Neutralizer mass flow rate (sccm, mA_{eq}, mg/s).
$\dot{M}_T$	Total mass flow rate of xenon into a discharge chamber, including propellant through the cathode, main feed line, and propellant ingestion (sccm, mA_{eq}, mg/s).
$\dot{m}_I$	Mass ingestion flow rate of xenon into a discharge chamber (sccm, mA_{eq}, mg/s).
M_{xe}	Molecular mass of xenon (133.33 g/mol).
η_p	Propellant utilization efficiency - uncorrected.
η_{pc1}	Propellant utilization efficiency - corrected for doubly charged ions.
η_{pc2}	Propellant utilization efficiency - corrected for both mass ingestion and doubly charged ions.
η_{pc3}	Propellant utilization efficiency - corrected for mass ingestion.
n	Number of mols of xenon.
n_b	Number density of background propellant atoms (#/m^3).
N	Number of measurements made by Faraday probes in order to determine average measured current.
P	Vacuum facility background pressure (N/m^2).
P_s	Standard Pressure = 1.01325 x 10^5 N/m^2.
P.S.	Pumping speed of vacuum facility on xenon (L/s).
q^+	Charge on a singly charged ion (Coul) = e.
q^{++}	Charge on a doubly charged ion (Coul) = 2e.
Q	Ratio of measured beam current to metered beam current.
R_α	Radius of a circle through which 95% of the downstream measured beam current passes (m) (see figure 2.5-1).
R_t	Radius of the thruster (ion source) (m) (see fig. 2.5-1).
R_i	Radius of a Faraday Probe (m).
R	Ratio of net to total accelerating voltage.
R	Gas Constant = 8.3145 J/mol K.
R_R	Resistance of resistors (Ohms).
R_{plane}	Radius associated with the data acquisition plane (m).
R_{max}	Maximum radius allowed with size of data plane (m).
S_I	Width of upstream ExB probe collimator slit (m) (see fig. 3.3-3).

S_2	Width of downstream ExB probe collimator slit (m)(see fig. 3.3-3).
S_3	Width of ExB probe collector slit (m)(see fig. 3.3-3).
$\sigma_{x,y}$	Standard deviation of Faraday probe measurement at (x,y) (A).
$\gamma_{x,y}$	Standard deviation density of Faraday probe measurement at (x,y) (A/m^2).
λ_x	Standard deviation linear density of a column of Faraday probe measurements at (X) (A/m).
σ_B	Total standard deviation of a plane of Faraday probe measurements (A).
SEEC	Secondary electron emission coefficient.
T_{calc}	Measured thrust using telemeter performance parameters (N).
T_{act}	Actual thrust produced by the thruster (N).
T_S	Standard temperature (273 K).
T	Temperature of the tank wall or background xenon gas (K).
θ_i	Impinging ion angle of incidence (°) (see fig. 5.1-3).
V_B	Ion beam potential (V).
V_S	Screen grid potential (V).
V_D	Decelerator grid potential (V).
V_{cn}	Neutralizer coupling voltage (V).
V_d	Bias applied to ExB probe deflector plates (V).
V	Volume of propellant (m^3).
$\bar{V}_i$	Velocity of an accelerated ion (m/s).
$\bar{V}_a$	Velocity of a propellant atom within vacuum facility due to thermal motion (m/s).
V_R	Voltage drop across data acquisition resistor (V).
V_{Dis}	Discharge chamber voltage (V).
Φ_a	Open area fraction of accelerator grid.
W	Bias width of the ExB collected current peaks (V).
X_f	Offset between downstream ExB collimator slit and collector slit (m) (see fig. 3.3-4).
X_c	Offset between upstream and downstream ExB collimator slits (m) (see fig. 3.3-4).
X	tan (α).
X	North - South axis or distance along X axis from origin (m) (see fig. 3.1-1).
Y	Up - Down axis or distance along Y axis from origin (m) (see fig. 3.1-1).
Z	East - West axis or distance along Z axis from origin (m) (see fig. 3.1-1).
z	Number of charges on a particle.

Z_f Distance between downstream ExB collimator slit and collector slit (m) (see fig. 3.3-4).

Z_c Distance between upstream and downstream ExB collimator slits (m) (see fig. 3.3-4).

Chapter 1 Introduction

The primary objective of this effort was to assist in the development of the segmented ion thruster (SIT) [31], a concept conceived by Dr. J.R. Brophy at the California Institute of Technology, Jet Propulsion Laboratory (JPL). The information contained in this report describes the results found through two types of experiments to characterize the SIT exhaust plume: Faraday probe current density and $\bar{E}x\bar{B}$ mass spectrometer ion charge state. These results will be used by propulsion subsystem, spacecraft system and mission design engineers in order to assess the benefits, risks, and costs associated with incorporating the SIT with a given spacecraft and mission. In addition, these results will be used by the SIT designers in order to assess issues regarding thruster performance, lifetime, interaction with the spacecraft, interaction between multiple ion beams, and repeatability of construction and operation.

Ion propulsion has been under development for over 30 years and been proposed for application as auxiliary propulsion for orbit raising and station keeping of earth orbiting satellites [1] and as primary propulsion for deep space and planetary exploration platforms [2,3,4,5]. It has also been proposed for use in the operation of large space systems that could have an extensive set of earth orbiting and planetary missions [6]. The segmented ion thruster (SIT) in particular has also been proposed for application to several solar system exploration missions [7, 8]. Shown in figures 1.0-1 and 1.0-2, the segmented ion thruster consists of four separate ion sources, each with its own 3-grid ion optics.

1.1 Segmented Ion Thruster

The segmented ion thruster is an electron-bombardment ion thruster which contains four separate ion sources with a single common neutralizer and has been under development at JPL since 1993. It utilizes 3-grid SAND (see section 2.4) ion optics and operates with xenon propellant. The concept for a segmented ion thruster was first proposed in 1991 [31]. This early concept was for a high power (10^5 to 10^6 watts), high thrust ion propulsion system with an I_{sp} of close to 10,000 s. Many of the advantages identified for this high power concept could also be

derived from a lower power version, such as in the current design used throughout this investigation.

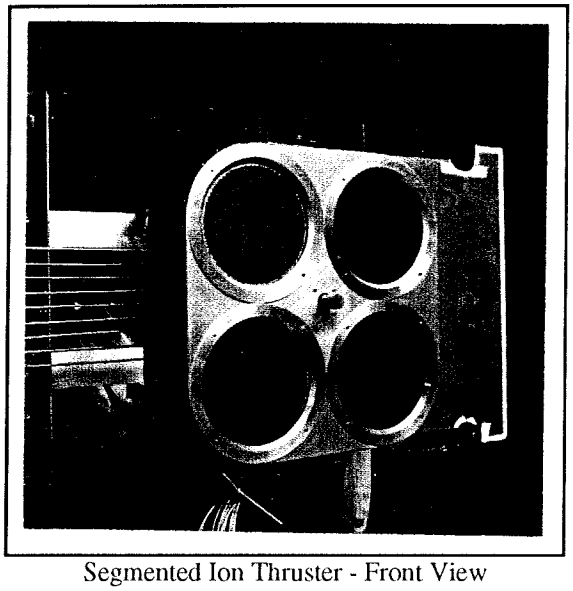

Segmented Ion Thruster - Front View
Figure 1.0-1

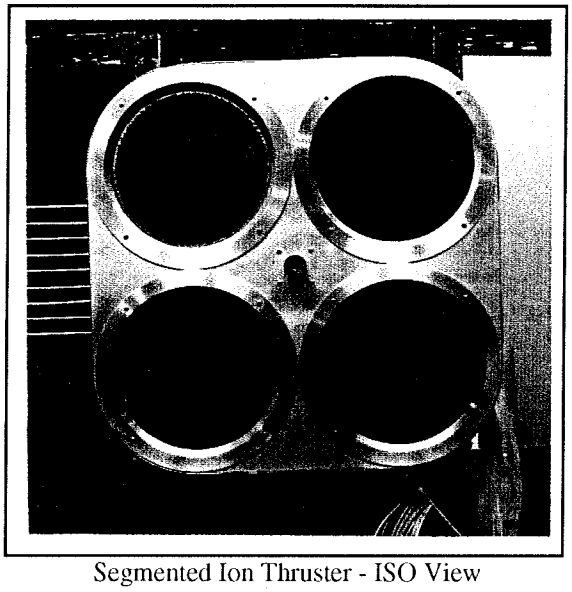

Segmented Ion Thruster - ISO View
Figure 1.0-2

Space charge effects limit the amount of thrust that can be produced from an ion engine. In order to increase thrust, the ion source diameter must be increased. However, as the diameter of the accelerator system increases, difficulties arise in maintaining the gap between the grids, and results in a maximum attainable span-to-gap ratio associated with ion thruster accelerator systems. Span-to-gap is the ratio of the diameter of the accelerator system to the gap between the grids. Limitations in the fabrication and assembly of the grids as well as thermal effects which alter grid gap during operation restrict this maximum. The segmented concept for an ion thruster is to divide the accelerator area of a large aperture thruster into several smaller ion sources with a total accelerator area comparable to the original large aperture thruster. Division of a larger area thruster in to several smaller thrusters reduces the span-to-gap limitations and offers a new throttling capability as well. Although the segmented ion thruster built at JPL consists of four 15-cm diameter ion sources, many other concepts were also identified [31]. The appropriate configuration would be dependent upon mission requirements and available spacecraft power.

Some of these potential configurations are shown in figures 1.1-2 and 1.1-3 with the current segmented design shown in figure 1.1-1.

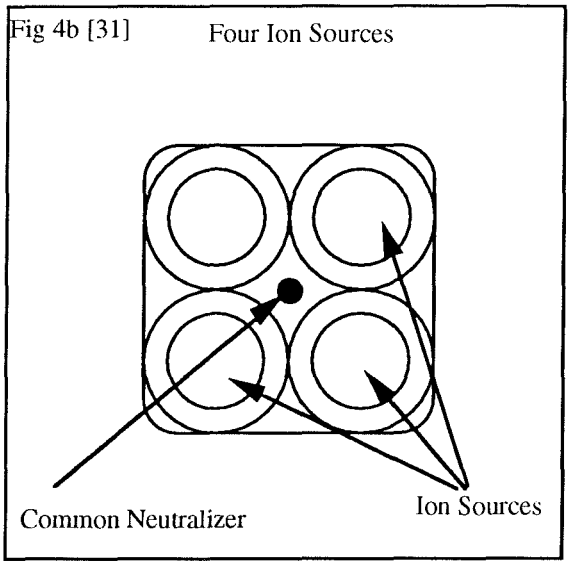

JPL Developed Segmented Ion Thruster Configuration
Figure 1.1-1

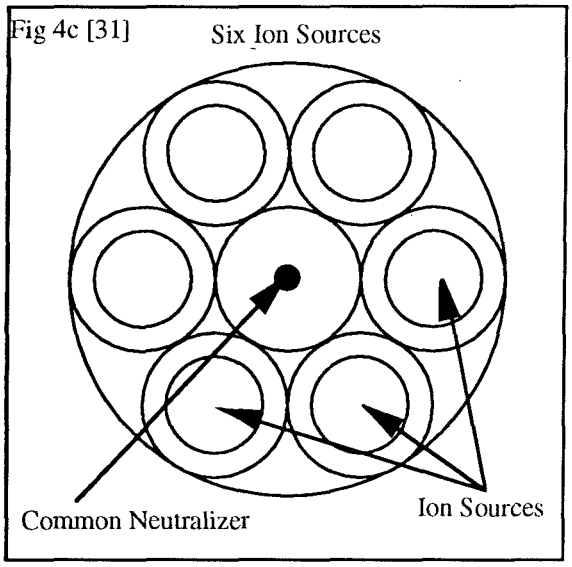

Alternative Segmented Ion Thruster Configuration #1
Figure 1.1-2

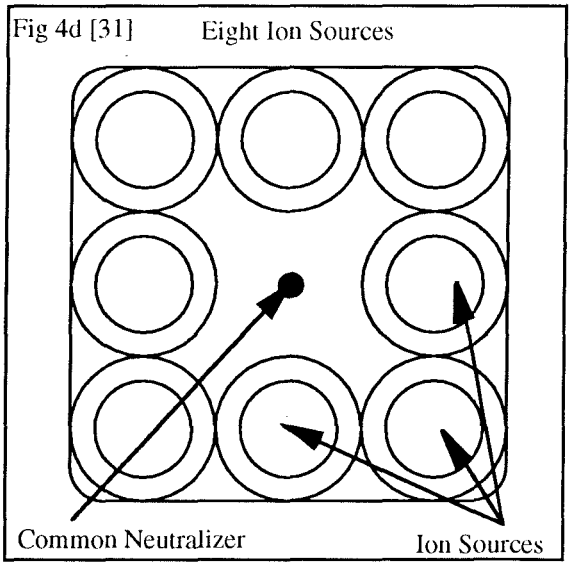

Alternative Segmented Ion Thruster Configuration #2
Figure 1.1-3

The SIT possesses a total power input throttling capability of about 8 to 1 which is attained through a combination of techniques. Gross throttling is accomplished by operation of only the

required number of ion sources and deactivating those segments not needed. This provides a 4 to 1 throttling capability. Adjustment of the power processing electronics with a fixed propellant flow rate allows for finer throttling over a range of about 2 to 1. However, the primary advantage of the SIT configuration over conventional designs is lifetime. This is created by deactivating unnecessary ion sources, and reactivating them when needed. The deactivated ion sources are not subject to wear and will allow a longer mission duration. According to Brophy [8], this could reduce the necessary lifetime of ion source components by as much as a factor of two for typical small body rendezvous missions. Another significant benefit of the segmented design is that, together with the use of SAND ion accelerator systems, the cost associated with full design lifetime endurance testing of an ion thruster could be substantially reduced.

Brophy [31] also points out other potential benefits derived through the use of a segmented configuration. Some of these include: reduced pumping speeds of the vacuum system, increased system fault tolerance from inherent redundancies in the design, and reduced span-to-gap limitations (as discussed above). Although there exist clear advantages of the segmented configuration, these advantages must be weighed against increased complexity of the propulsion subsystem and potential impacts to integration of the subsystem with a spacecraft.

1.2 Motivation for Investigation

Thrust (T) and propellant utilization efficiency (η_p) are the two performance parameters addressed in this report. The production of multiply charged ions within the discharge chamber of an ion thruster degrades the ideal performance of the thruster (i.e. both parameters decrease). In this investigation the charge state of the accelerated ions was measured along the centerline of a single segment in order to assess the degradation of performance with respect to the ion source beam current (I_B). This was accomplished by placing an $\bar{E}x\bar{B}$ mass spectrometer downstream of the operating segment and measuring the collected current as a function of voltage applied to the deflector plates.

Lifetime of an ion thruster is primarily limited by erosion of the accelerator system grids due to sputtering of grid material from impingement of accelerated ions and backstreaming charge exchange ions. The three ion beam characteristics evaluated in this investigation that address lifetime were beam circularity, beam flatness, and multiply charged ion production as a function of radial position with respect to the ion source centerline. Maximum grid lifetime is achieved with circular, flat beams with production of only singly charged ions. A non-circular or non-flat beam profile will produce uneven erosion of the grid material and therefore accelerate the erosion rate in some regions compared to that caused by circular, flat beams. These characteristics were assessed through the use of Faraday probe current density data collected at several downstream locations from the thruster. The radial distribution of multiply charged ion production also affects the distribution of grid erosion and was determined through use of the $\bar{E}x\bar{B}$ which traveled across the ion source centerline parallel to the X and Y axes.

Divergence of the extracted ion beams can be described by the beam divergence angle (α) and help identify "keep out" regions for solar arrays and other spacecraft appendages in order to prevent direct ion impingement on spacecraft surfaces. This angle is defined as the half cone angle measured from the edge of the active ion source, which contains 95% of the measurable beam current. Due to charge exchange effects, the measurable beam current tends to decrease as a function of distance from the thruster (Z). The beam divergence angle (α) was calculated for each plane of Faraday probe current density data collected during the individual operation of each ion source.

The primary design feature of the segmented ion thruster which makes it different from other ion thrusters is the four ion source configuration. Although many proposed ion propulsion systems for deep space exploration are to utilize multiple thruster configurations [1,2,3,4,5,64], little information is available regarding multiple beam interaction [65]. In order to study the operation of multiple ion sources, this investigation will compare the beam current density

profiles generated from multiple ion source operation to the equivalent profiles created mathematically through superposition of the data obtained from operation of single sources.

There are several aspects of the segmented ion thruster design which are considered experimental, such as multiple ion source operation, use of carbon-carbon grids, and use of SAND ion optics. It is of interest to those at JPL who designed the thruster to understand the repeatability of system construction and operation in order to minimize future flight hardware inconsistencies. In this investigation two methods will be used to assess this repeatability. The first is to compare the ion current density contour plots from each segment. Differences in shape will be noted and possible explanations will be discussed. Differences in beam divergence angles calculated for each segment at the different thruster operating conditions will also be noted and discussed.

1.3 Report Overview and Road map

This investigation is divided into two sets of experiments. The first involves collection of Faraday probe current density data at up to five downstream locations from the thruster for several different thruster operational configurations. The second experiment involved collection of ion beam charge state data with the use of an $\bar{E}x\bar{B}$ mass spectrometer probe placed at a single downstream location.

Chapter 2 of this report describes additional background information regarding ion thruster development and performance. The experimental setup and procedures / methodology followed for this effort are given in chapters 3 and 4 respectively. Chapters 5 and 6 explain the data reduction processes and analyses performed with the collected data and chapter 7 discusses the results obtained from the analyses. In each of these chapters the work involving Faraday probe and $\bar{E}x\bar{B}$ probe data collection are divided into subsections. Chapter 8 gives a short summary of the results and conclusions as well as some recommendations for future investigations. Appendix A contains the data table used in the data analyses and appendix B displays a collection of all

macurrent density contour plots with 2.54 cm spacing between the Faraday probe locations. Appendix C contains the current density contour plots generated for comparisons between Faraday probe data collected with 2.54 cm spaced data and 1.27 cm spaced data.

Chapter 2 Background

2.1 Benefits of Ion Propulsion

Advantages of ion propulsion are derived from its high specific impulse (I_{sp}) compared to that of conventional chemical propulsion. For propulsion intensive missions, such as deep space exploration, the advantages of increased specific impulse generally outweigh disadvantages and result in two potentially significant total mission benefits. The first possible benefit could be through direct addition of mission performance capability, such as increasing payload and subsystem design margin / reliability or by increasing the design lifetime of the spacecraft through addition of propellant or redundancy of hardware. Addition to the payload mass could allow for increased design margin of the original payload(s), involve the addition of new payloads, or increase the onboard data processing capability to reduce data downlink requirements. Shorter total trip times are also possible with the constant operation of ion propulsion systems, which could reduce space vehicle lifetime and reliability requirements. Reduction of total system mass with incorporation of ion propulsion and possible downsizing of the launch vehicle could be a potential cost benefit. Launch vehicle and launch services costs have always been significant drivers of mission lifecycle cost. If total system mass were sufficiently decreased by using ion propulsion, a less expensive launch vehicle could be employed and the savings could be realized in a lower total mission cost or be applied to increase mission utility. Although this increase in I_{sp} could result in off loading of propellant for a given mission, an increase in total system mass may still be required for the incorporation of power processing electronics or more capable solar arrays.

2.2 Ion Propulsion Evolution

Benefits of electrical propulsion were realized as early as 1906 by Dr. Robert H. Goddard [9], but it was not until 1954 when the first detailed analysis of electric propulsion was presented by Dr. Ernst Stuhlinger and another 6 years passed before Dr. Harold R. Kaufman operated the first electron bombardment ion thruster [10].

The basic theoretical concept of ion propulsion is quite simple. It involves the ionization of a gas and acceleration of this ionized gas through an electric field to create thrust. The expelled plasma is then quasi-neutralized through the introduction of electrons from an emitting cathode located outside of the accelerating system. Although the basic concept behind ion propulsion is simple, implementation and the associated plasma physics are far from trivial. Kaufman [10] and Jahn [11] both provide descriptions of the important theoretical and design considerations in the development and operation of ion thrusters.

The Space Electric Rocket Test (SERT I and SERT II) programs [1,12,13] first demonstrated ion propulsion in space. The SERT I platform, flown on July 20, 1964, was a 50 minute sounding rocket flight test that confirmed in-space neutralization of the exhausted plasma beam. This was demonstrated by the fact that incorrect neutralization would have decreased the thrust of the ion engine from the levels expected. The thrust measured showed that this was not the case. On February 3, 1970 the SERT II spacecraft was launched. The mission was to demonstrate long duration ion engine operation with the equipment and operational environment that would be similar to a typical mission. SERT II also showed that the thrust calculated from the operating parameters of the thruster agreed well with the values measured by accelerometers onboard the spacecraft.

Most recently ion propulsion was to be operationally used on the National Space Development Agency (NASDA) of Japan Experimental Test Satellite-VI (ETS-VI), launched in the summer of 1994. The Ion Engine System (IES), which included a four 20 mN xenon thrusters, each with 3-grid ion optics, was to be used for north-south station keeping of ETS-VI [14, 15, 16]. Unfortunately, the upper stage of the launch vehicle did not perform properly and placed ETS-VI in a highly elliptical, instead of a geosynchronous orbit. Even though the primary mission was significantly degraded, all four ion engines were operated at their full thrust levels and valuable operational data should be obtainable.

NASA is currently pursuing a program called NSTAR - NASA Solar Electric Propulsion Technology Application Readiness, which will operate, on orbit, a 30-cm diameter lightweight xenon ion thruster[43]. The NSTAR mission is to validate ion propulsion technology for primary propulsion applications. This thruster is currently the baseline for most deep space mission analyses.

The concept of ion propulsion is nothing new with the first space based demonstration of ion propulsion occurring in 1964, but very few spacecraft with ion propulsion systems will have flown by the mid 1990's [17]. These will all have been only flight experiments with the exception of the ETS-VI flight which would have been the first operational use of ion propulsion. It is surprising that ion propulsion has not been more extensively used with such a dramatic increase in specific impulse over conventional chemical propulsion. According to Brophy [8], a significant cause for this situation is the conservatism of program managers who are unwilling to assume technical and schedule risks and the associated costs of being the first user of ion propulsion. Brophy continues to point out that no flight program will use ion propulsion without successful design-lifetime endurance testing. Endurance testing is thus one of the keys to demonstrating the utility of ion propulsion systems.

Terrestrial based applications of electron bombardment ion sources, which are similar in design to those used for space propulsion, are being developed and used for materials processing. Sputter cleaning and coating, ion plating and implantation are just some of the possible applications of broad beam ion sources. Wilbur and Buchholtz [18] have identified some of the key design requirements which are similar for both terrestrial and space based applications and they include the desires for (1) high current density; (2) uniform beam profile; and (3) a wide ion beam. In a research program at Colorado State University, Fort Collins, Wilbur and Buchholtz [18] have demonstrated that considerable improvements in tribological surfaces have been achieved through use of ion materials processing. Some of these improvements exhibited include: (1) rolling-contact-fatigue lifetime of a bearing steel induced by diamond like

hydrocarbon coating; (2) the resistance to galling of an austenitic stainless steel induced by nitrogen ion implantation and (3) the lifetime of a lubricant in contact with a bearing steel induced by titanium ion implantation. Due to the similarity in performance and design requirements between the two types of ion thruster applications, there has recently been a renewed push for transfer of this technology to the commercial world.

2.3 Propellant

The ion thruster tested by Kaufman in 1960 used mercury as the propellant. Similarly, the SERT I and SERT II thrusters also used mercury. Although mercury was the propellant of choice early in the development of ion thrusters, cesium was also extensively tested in the 1960s. Use of these propellants, according to Owens [19], was attractive because of their large atomic mass, large propellant density, and ease of flow control by vaporization. Owens also noted that the choice to use mercury and cesium was probably made based on propulsion subsystem issues rather than potential spacecraft integration problems. In light of some of these spacecraft integration difficulties, Owens [19] proposed that argon, krypton, and xenon may be suitable alternatives. Some of the reasons given by both Owens [19] and Rawlin [20] as to potential advantages from using noble gases included: they are chemically and metalurgically inert which means noncontaminating and nonreactive to other space system elements; they are nontoxic and nonreactive with the biosphere which should minimize ion and neutral atom environmental contamination; they have lower charge exchange cross-sections than either cesium or mercury; simple electrical isolation is possible thus allowing central propellant storage; no thermal conditioning is required; they allow for simple propellant storage without the requirement for bellows, bladders or low gravity propellant management; no neutralizer or discharge chamber propellant vaporizers are required and they allow for the possibility of faster thrust response and potentially instantaneous startup.

Xenon has mostly replaced mercury in recent years as the propellant for both developmental and operational systems. This came about due to a combination of large atomic mass, high

compressibility [19] and the performance with xenon being similar in propellant utilization and discharge loss to that of mercury [10]. Although xenon does have many favorable attributes in comparison to mercury, there are drawbacks as well. Rawlin [20] noted that with decreased atomic mass the discharge performance of inert gas propellants decreased as well. In addition, the erosion rate of the screen grid was several times higher with inert gas propellants as compared to the rate for mercury [21], although operation at lower discharge voltages is expected to eliminate this effect.

Another push in the arena of ion thruster propellants has been towards the use of heavy molecules. Byers et al. [22] and Milder [23] experimented with some potential candidate molecules but found that excessive fragmentation occurred which significantly degraded system performance. In a recent proposal by Leifer [24], the use of carbon-60 molecules has been identified and efforts to develop such a heavy molecule propellant ion thruster system are being pursued.

2.4 Ion Optics Design

The primary life-limiting mechanism of modern electron bombardment ion thrusters is the erosion of the accelerator system grids due to sputtering of grid material from either the impact of charge-exchange ions backstreaming from the exhausted plasma or from the accelerated ions created in the discharge chamber. Whether the mechanism is structural deterioration of the grids due to excessive erosion or flaking of the grid material creating an irrecoverable short between the grids, system failure results.

There exist two operational methods for reducing the sputter erosion rates of the inner most grid of the ion accelerator system identified by Garner et al. [21]. The first is to operate the engine at a lower discharge voltage which would reduce the energy of the impinging ions. Operating the engine at a lower propellant utilization efficiency to reduce the multiply charged ion production is the other. Although these methods will reduce erosion of the grids, performance of the thruster will also be degraded. Because degraded thruster performance is not desirable,

efforts lately have been directed towards the design and development of ion optics that possess improved erosion-resistance characteristics. Presently, three areas of interest are being explored to help reduce this erosion: 1) grid material, 2) use of three grid optics and 3) grid coatings.

In order to help explain these areas of development it would be best to first describe standard ion thruster configurations currently in use. Molybdenum has long been the material of choice for ion engine grids because of its low coefficient of thermal expansion (CTE), relatively good sputter erosion resistance, good high temperature strength, and its ability to be mechanically dished. The grids are dished in order to compensate for differential thermal expansion. The NASA 30-cm thruster currently is baselined to use ion optics that consist of a two closely spaced, dished, molybdenum grids.

Flat graphite grids were proposed in 1963 as a possible solution to the problem of grid thermal distortion because of graphite's lower CTE compared to molybdenum [25]. It has also long been recognized that carbon has a lower sputter rate than molybdenum and empirical data offers the possibility that erosion may be one-seventh that of conventional molybdenum [26]. However, graphite grids are not considered suitable for spacecraft thrusters because of their high flexibility (low strength) and fragility. Even though these grids are not applicable to space missions, graphite grids are commonly used in ground based applications.

Recent evaluations of carbon-carbon fiber matrix composite grids has offered some promising results due to their higher strength and rigidity relative to graphite and low sputter yield relative to molybdenum. Demonstration and development of these carbon-carbon grids is currently being carried out at both Boeing Defense & Space Group [26, 27] and at JPL [28, 29]. Meserole and Hedges [26] have found carbon-carbon accelerator grid erosion to be approximately an order of magnitude lower than molybdenum accelerator grid at a grid voltage of -300 volts. Garner and Brophy [28], however, showed that a carbon-carbon screen grid, which was subjected to bombardment by ions with energies of only ~28 V, eroded at a rate of only 25% below that of molybdenum under similar conditions.

Application of anti-sputtering coatings to ion thruster components, primarily ion optics grids, are also being studied in hopes of decreasing erosion. Efforts are currently underway at the NASA Lewis Research Center (LeRC) and also within NASDA to develop and evaluate some of these coatings. Ceramic coatings were applied to several parts of the engines used in the ion engine system developed by the Mitsubishi Electric Corporation for the ETS-VI spacecraft. These coatings were applied to the baffle, cathode polepiece, downstream polepiece, accelerator grid and screen grid [14].

The third recent development in ion optics design is that of the SAND (Screen, Accelerator, Negative Decelerator) grid configuration. Shown in figure 2.4-1, this concept developed by Brophy et al. [30] was designed primarily to accommodate the higher background pressures of vacuum chambers compared to that of free space. As previously mentioned, conventional ion accelerator systems consist of two grids, accelerator and screen. Addition of a negatively biased decelerator grid downstream of the accelerator grid is the feature which makes the SAND ion optics different.

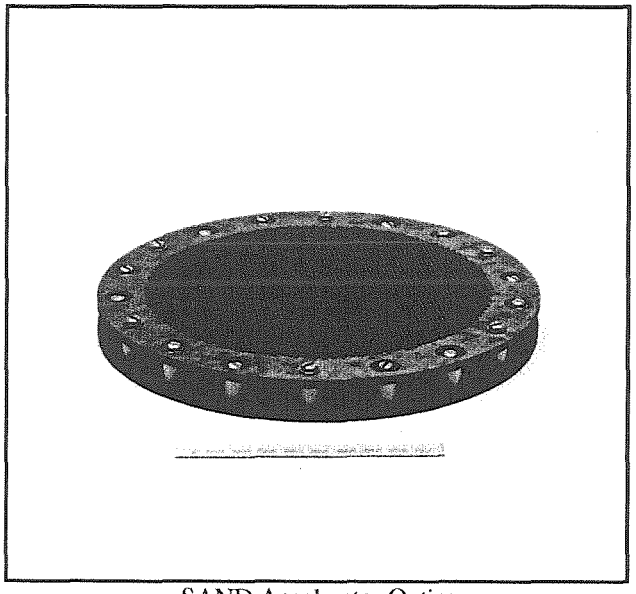

SAND Accelerator Optics
Figure 2.4-1

Charge exchange ions are known to be a leading cause of grid erosion and existence of background pressures within testing facilities cause an increase in the production rate of these ions. Charge exchange ions are created when an ion that is accelerated and expelled by the grid optics collides with a slow moving neutral atom. This results in the exchange of an electron between the fast ion and slow neutral thus created a fast neutral and slow ion. Due to their low momentum and positive charge, these slow ions are attracted to negative potentials and therefore backstream and strike the negatively biased accelerator grid of a conventional two grid system. This is one of the principle causes for grid erosion and a major life limiting phenomena for the engine.

In the SAND optics, the decelerator grid is biased 50 to 100 volts negative of the neutralizer cathode potential to act as a shield for the accelerator grid. This shielding is to protect the accelerator grid from impingement of the charge-exchange ions. Because the decelerator grid is more 'visible' to the charge-exchange ions, the majority of these ions hit the decelerator grid instead of the accelerator grid, thus reducing the erosion rate of the accelerator grid. The negative voltage on the decelerator grid also allows a reduction in the magnitude of the negative voltage on the accelerator. Not only is the backstreaming charge-exchange current reduced, the energy of the impinging ions is also lower, therefore, resulting in less sputtering of the grid material.

According to Brophy et al. [30], the use of the SAND optics resulted in a reduction factor of greater than 100 in accelerator grid erosion when compared to that of standard two grid ion optics under similar tests performed at high vacuum chamber pressures. Even though this reduction by itself is important, the more significant result from use of SAND optics is in the increase of testing facility effective pumping speed. In other words, the amount of erosion experienced by the SAND optics would also be experienced by a conventional two grid system if the testing facility pressure were significantly lower than that found during the SAND tests. In tests conducted at JPL [30], the effective pumping speed of the vacuum chamber was increased by

over an order of magnitude relative to that required for endurance testing of ion thrusters that use the conventional two grid design.

2.5 Thruster Performance

Ideal performance of individual ion sources within the segmented ion thruster can be determined from the currents and voltages measured at the thruster control console. The data acquisition computer in this console calculates values for thrust (T), specific impulse (I_{sp}), beam current (I_B), beam voltage (V_B), and propellant utilization efficiency (η_p). However, these ideal performance parameters must be corrected for real ion source operational characteristics. The following are the equations used to determine the real performance of an ion thruster, which includes the ideal performance relations and the associated correction factors:

Eq. 2.5-1 $$T_{actual} = f_t I_B \sqrt{\frac{2V_B m_i}{e}}$$

Eq. 2.5-2 $$I_{sp} = f_t \eta_{pc2} \frac{1}{g} \sqrt{\frac{2V_B e}{m_i}}$$

Eq. 2.5-3 $$I_B = I_S - I_A$$

Eq. 2.5-4 $$V_B = V_S - |V_N|$$

Eq. 2.5-5 $$\eta_{pc1} = \beta \frac{\dot{m}_{ion}}{\dot{m}_t}$$

Eq. 2.5-6 $$f_t = f_d f_c$$

In this investigation the charge state thrust correction factor (f_c) and beam ion correction factor (β) were determined for several thruster operational configurations. The correction factor for beam divergence (f_d) was beyond the scope of this investigation but will be discussed later in this section. The charge state thrust correction factor (f_c) is the ratio of the actual thrust produced with both singly and doubly charged ions to the thrust calculated from the metered beam current and is used to adjust the calculated thrust for the existence of doubly charged ions within the extracted beams. Production of doubly charged ions is also one of the primary life limiting

mechanisms for ion engines. Multiply charged ions created in the discharge chamber are usually doubly charged, however, it has been shown that creation of triply charged ions is possible [37] with a sufficiently high discharge voltage (V_{DIS}). The following derivation, partially reproduced from Vahrenkamp [36], assumes production of only singly and doubly charged ions:

Eq. 2.5-7 $$I_B = I^+ + I^{++}$$

The thrust calculated from this current is

Eq. 2.5-8 $$T_{calc} = I_B\sqrt{\frac{2m_iV_B}{q^+}} = I^+\sqrt{\frac{2m_iV_B}{q^+}} + I^{++}\sqrt{\frac{2m_iV_B}{q^+}}$$

The actual thrust, however, is

Eq. 2.5-9 $$T_{act} = I^+\sqrt{\frac{2m_iV_B}{q^+}} + I^{++}\sqrt{\frac{2m_iV_B}{q^{++}}}$$

Where $q^+ = e$ and $q^{++} = 2e$, therefore

Eq. 2.5-10 $$T_{calc} = I^+\sqrt{\frac{2m_iV_B}{e}} + I^{++}\sqrt{\frac{2m_iV_B}{e}}$$

Eq. 2.5-11 $$T_{act} = I^+\sqrt{\frac{2m_iV_B}{e}} + I^{++}\sqrt{\frac{m_iV_B}{e}}$$

Eq. 2.5-12 $$f_c = \frac{T_{act}}{T_{calc}} = \frac{I^+ + \frac{1}{\sqrt{2}}I^{++}}{I^+ + I^{++}}$$

The discharge voltage used in this investigation was generally around 28 V. Sovey [37] found that triply charged ions were only 1-2% of the singly charged ions at a discharge voltage of approximately 46 V. Therefore triply charged ion are neglected in this study.

The beam ion correction factor (β) is used to scale the metered values of propellant utilization efficiency (η_p) to compensate for the existence of doubly charged ions. Propellant utilization efficiency is the ratio of rate of ion mass extraction over the total mass flow rate of propellant into the discharge chamber. It can also be represented as the ratio of the beam current (I_B) expressed in mA over the total mass flow rate of propellant ($\dot{m}_t$) into the discharge chamber in units of milliamp equivalent (mA_{eq}), which is obtained by assigning a charge of e to each

propellant atom. A detailed derivation for conversion between mass flow rate units of standard cubic centimeters per minute (sccm), milligrams per second (mg/s) and milliamps equivalent (mA_{eq}) is given in section 5.3.1. The beam ion correction factor is the ratio of the actual propellant utilization efficiency (η_{pcl}) over the propellant utilization efficiency calculated with the metered beam current (η_p). The following is a derivation of the beam ion correction factor (β):

Eq. 2.5-13 $$\eta_p = \frac{\dot{m}_{ion}}{\dot{m}_t}$$

Eq. 2.5-14 $$\dot{m}_{ion} = \frac{I_B m_i}{q}$$

Eq. 2.5-15 $$\eta_p = \frac{I_B m_i}{\dot{m}_t q^+} = I^+ \frac{m_i}{\dot{m}_t q^+} + I^{++} \frac{m_i}{\dot{m}_t q^+}$$

Eq. 2.5-16 $$\eta_{pcl} = \frac{I^+ m_i}{\dot{m}_t q^+} + \frac{I^{++} m_i}{\dot{m}_t q^{++}}$$

Since $q^+ = e$ and $q^{++} = 2e$, then the beam ion correction factor (β) is

Eq. 2.5-17 $$\beta = \frac{\eta_{pcl}}{\eta_p} = \frac{I^+ + \frac{1}{2} I^{++}}{I^+ + I^{++}}$$

and therefore the corrected propellant utilization efficiency is

Eq. 2.5-18 $$\eta_{pcl} = \beta \eta_p .$$

The beam divergence thrust correction factor (f_d), which was not addressed here, compensates for the fact that ions leaving the accelerator system do not exit with a trajectory that is exactly parallel to the centerline of the discharge chamber. The calculations discussed above assume for determination of system thrust that ions travel in a highly collimated fashion that is parallel to, and undeflected from, the centerline axis. The beam divergence thrust correction factor is the ratio of the actual axial thrust produced to the theoretical thrust produced if the beam were perfectly collimated. Aston [33]; Aston, Kaufman, and Wilbur [34]; Aston and Kaufman

[35], and Vahrenkamp [36] have tests to address this phenomenon. The equation used to the beam divergence factor (f_d) is given in equation 2.5-19.

Eq. 2.5-19
$$f_d = \frac{\sum_{i=1}^{X} I_i R_i \cos\theta_i}{\sum_{i=1}^{X} I_i R_i}$$

The beam divergence thrust correction factor (f_d) can be determined through the use of a highly accurate Faraday probe that has the capability to align the normal vector of the collector surface with the direction of the impinging ions. Knowing the collected current (I_i), radial position of the probe (R_i), and the angle between the ion trajectory and discharge chamber centerline (θ), equation 2.5-19 can be applied to determine f_d. The charge state thrust (f_c) and beam ion correction (β) factors can be calculated by measuring the ratio of doubly to singly charged ions with the use of an $\bar{E}x\bar{B}$ mass spectrometer and applying the results to equations 2.5-12 and 2.5-17.

There exists an alternative method for determining the charge state thrust correction factor. As pointed out by Sovey and Rawlin [17], it is possible, through the use of a highly accurate and precise thrust stand, to measure the total thrust correction factor (f_t). Faraday probes can then be used to accurately measure f_d. Once these values are determined, f_c and β can be computed using equations 2.5-6, 2.5-12, and 2.5-14.

2.6 Spacecraft Interaction

Issues regarding interaction of the ion beams with spacecraft surfaces have been significantly reduced with the transition to inert gas propellants from mercury and cesium. Inert gas propellants are nonreactive and will not bond with other spacecraft elements. The exhausted mercury and cesium ions could potentially bond with spacecraft surfaces and degrade optical, solar cell, or thermal radiator performance.

Xenon, which was the propellant used in this investigation, had the potential for sputtering spacecraft surfaces due to the high ion velocities if the extracted ions were to directly strike the spacecraft. Impingement of charge exchange ions is also a concern, but substantially less than direct ion impingement. Beam divergence angles and the potential requirement of thrust vector steering must be assessed in the design of spacecraft geometry and operation so as to avoid direct ion impingement. This investigation will determine the ion beam divergence angles (α) for several operating conditions of the thruster with the use of Faraday probe data.

Eq. 2.6-1 $$\alpha = \arctan\left[\frac{R_\alpha - R_t}{Z}\right]$$

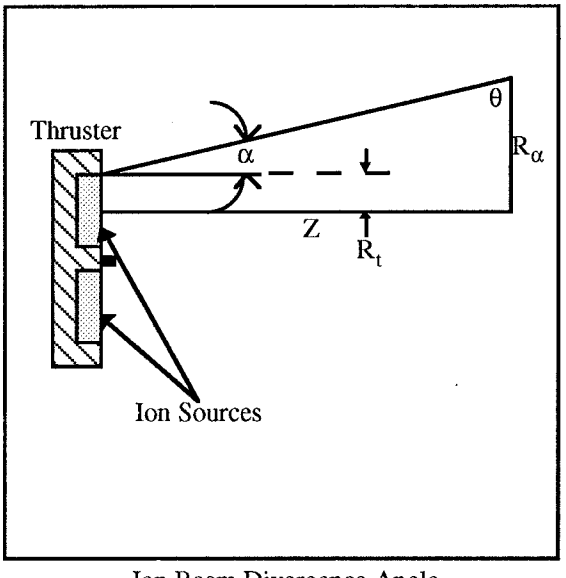

Ion Beam Divergence Angle
Figure 2.6-1

2.7 Lifetime

Assessing the lifetime of the segmented ion thruster was beyond the scope of this investigation. However, it is possible to describe some of the plume characteristics which are closely associated with the operational lifetime of an ion thruster. In addition, the hours logged of thruster operation in this investigation will be of use in future lifetime studies.

Two ion beam characteristics that are known to be contributors to grid erosion are beam flatness and the production of multiply charged ions. Ideally the ion beams would be flat, a flatter

beam means a more uniform current density which results in greater uniformity of accelerator system grid erosion. If the ion beams are not flat, then there will be regions of the grids that will erode at an accelerated rate. Beam flatness is a discharge chamber phenomena that affects accelerator system lifetime and is described by the beam flatness parameter (F). F is defined as the ratio of the average beam current density to the peak current density and describes the uniformity of the extracted ion beam as given in equation 2.7-1. It is desirable for the beam to be flat in both ground based material processing and space based thruster applications.

Eq. 2.7-1 $$F = \frac{J_{avg}}{J_{max}}$$

Although beam flatness at the thruster exit plane will not be specifically addressed in this study, information regarding ion beam shape will be obtained, which will give an indication of beam flatness.

The existence of multiply charged ions within the beams is one of the primary life limiting mechanisms for ion engines. The higher energy of doubly charged ions increases the erosion rate of the screen grid due to direct ion impingement. The ratio of doubly to singly charged ions will be measured for segment A at several different thruster operating conditions.

Chapter 3 Apparatus

3.1 Test Facilities

All work conducted for this report was performed at the California Institute of Technology, Jet Propulsion Laboratory (JPL), Pasadena, CA. The facilities and equipment described in this section are located in Building 149 at JPL.

3.1.1 Vacuum Chamber

'Big Green', the vacuum chamber used for testing of the segmented ion thruster, was of stainless steel construction measuring 5.0 m in length with a 2.4 m inner diameter. The segmented ion thruster was mounted to a removable header located at the west end of the tank. Located within the interior of the chamber, towards the east end, were two sets of graphite baffles used to minimize back sputtering of material during the operation of plasma thrusters. A graphoil [55] covered, stainless steel, liquid nitrogen (LN_2), cryoliner resided within the tank. The cryoliner was not used in this investigation since LN_2 will not pump xenon. The graphoil covering was in place to reduce back sputtering.

The tank header was fastened to the end of the tank with the use of vise clamps and became sealed to the tank only when pumping was initiated. Because of this method for sealing the tank, position of the header with respect to the tank, and therefore position of the segmented ion thruster with respect to the tank, may have been slightly different for each time the system was closed. The total displacement of the thruster between closures is estimated to be no more than ±3 mm.

Data lines and probe positioning system control wiring were fed into the tank through a flange that was located on the bottom of the tank, close to the west end. Connections on both sides of the flange were made through the use of 26 pin pygmy connectors. High voltage lines for the $\bar{E}x\bar{B}$ mass spectrometer were fed into the tank via high voltage (DC) connectors located on the same flange as the data and control lines. The data lines, which consisted of twisted shield pairs, were placed on the opposite side of the flange from the $\bar{E}x\bar{B}$ bias line feed throughs in order to minimize signal noise.

Windows were located on both the north and south sides of the tank close to the header as well as at the east end and on the top towards the east end of the tank. These windows were used for monitoring thruster and probe positioning system operation.

3.1.2 Facility Frame of Reference

The frame of reference for this investigation pertained to the design and operation of the probe positioning system for which the origin was fixed within the vacuum chamber. This reference system, depicted in figure 3.1-1, used rectangular coordinates in which the Z axis of the traverse runs parallel to the East-West centerline of the tank. The X axis of the traverse corresponded to the North-South direction across the tank, or horizontal direction with respect to the laboratory floor. The Y axis ran parallel to the 'up-down' direction of the vacuum chamber.

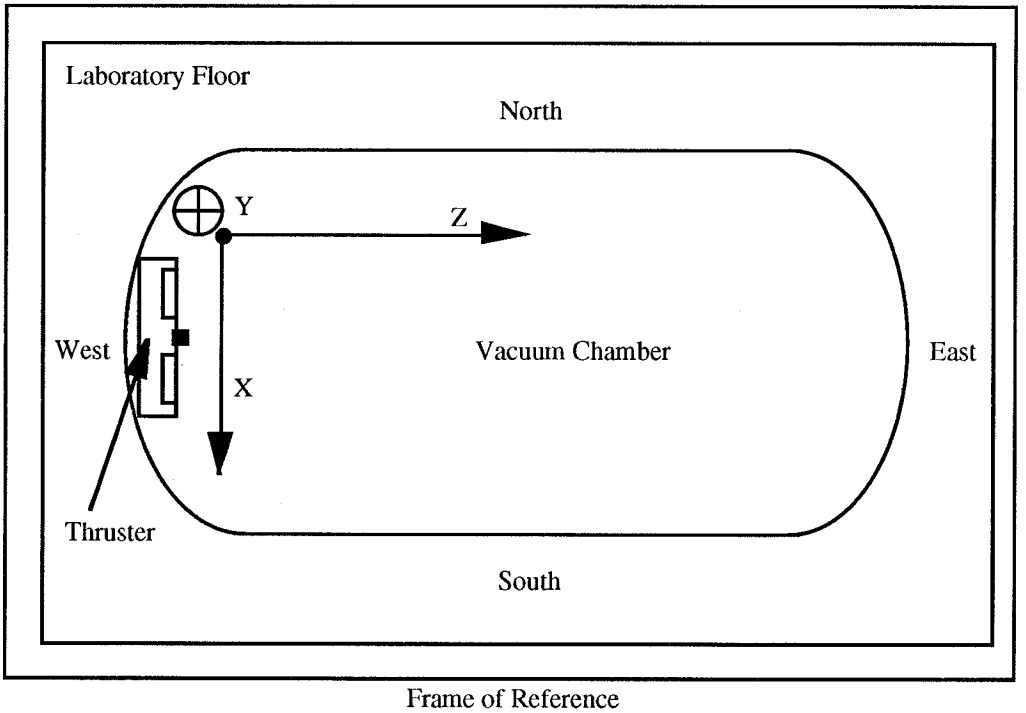

Frame of Reference
Figure 3.1-1

3.1.3 Vacuum Pumps

Three oil diffusion pumps were connected to vacuum chamber with a total pumping speed on xenon of ~16,000 Liters/sec. The use of SAND ion optics with the SIT effectively increased the pumping speed to over 160,000 Liters/sec [41] from the stand point of accelerator grid erosion.

3.2 Segmented Ion Thruster

The segmented ion thruster, which consists of four 15-cm diameter ion sources, was designed to be equivalent to the NASA 30-cm diameter lightweight thruster [42, 43]. Both configurations have a total active accelerator area of approximately 700 cm^2. Figures 1.0-1 and 1.0-2 show the segmented ion thruster (SIT) alone and figures 3.2-1 and 3.2-2 show both the SIT and the standard NASA 30-cm thruster side by side.

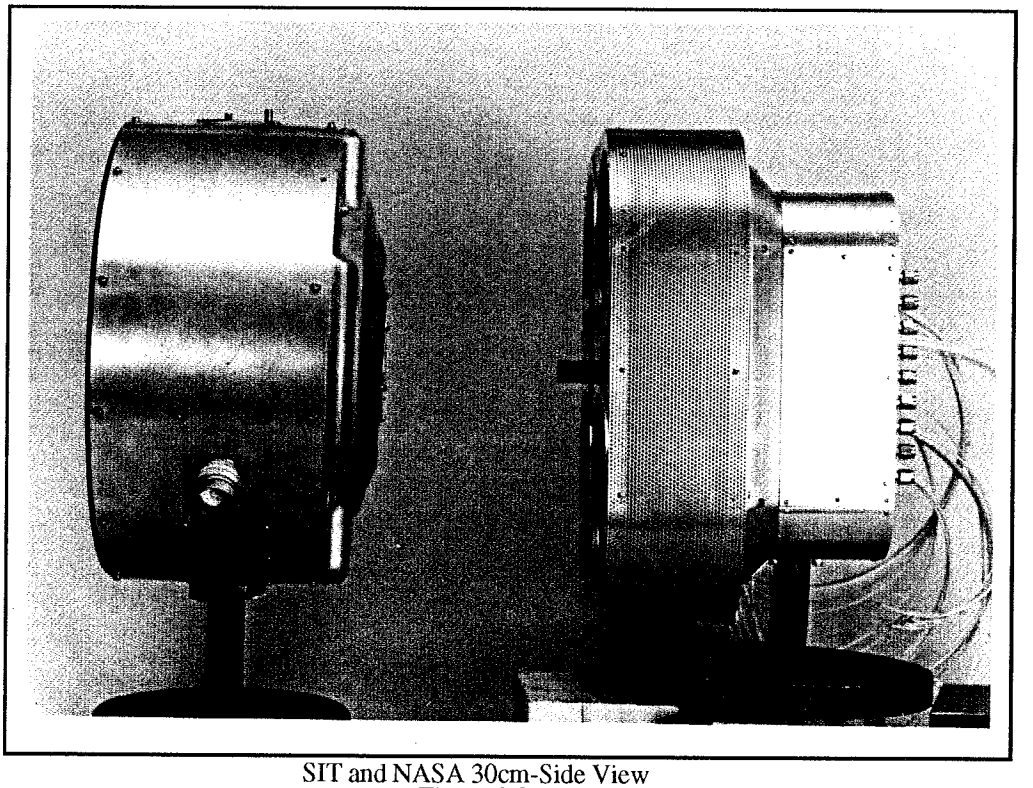

SIT and NASA 30cm-Side View
Figure 3.2-1

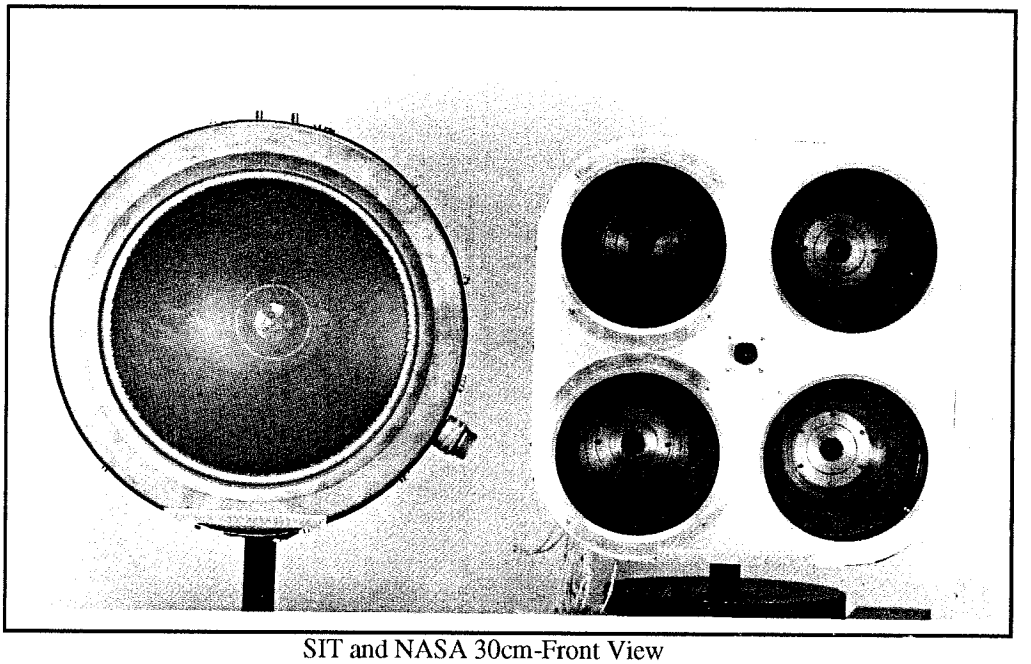

SIT and NASA 30cm-Front View
Figure 3.2-2

3.2.1 Ion Source Design

Each 15-cm diameter ion source [7, 44] is a modified and scaled down version of the NASA 30-cm diameter ring-cusp thruster [42, 43]. The discharge chamber body of each 15-cm ion source was made from 1.6 mm thick T6061 aluminum fabricated through a spinning process. Four of these discharge chambers were integrated to a structural base plate which was at ground potential to make up the segmented configuration.

The ring-cusp magnetic circuit of the discharge chamber consisted of two rings of samarium-cobalt magnets. One ring was located near the accelerator system and the other ring near the discharge cathode. Segments A and C had magnetic polarity reversed from that of segments B and D to reduce the far field magnetic flux density.

3.2.2 Propellant and Flow Control

Xenon gas was delivered to the discharge cathode and discharge chamber propellant main feed of each ion source, and the neutralizer cathode through a low-pressure feed system. Independent control of the main feed lines was made possible through the use of micrometer

valves located outside of the vacuum facility. Control of all cathode flow rates was accomplished through the use of micrometer valves located inside the vacuum chamber. This was done to guarantee that air, which would poison the cathodes, could not leak into the feed system. The propellant flow system schematic is shown in figure 3.2-3.

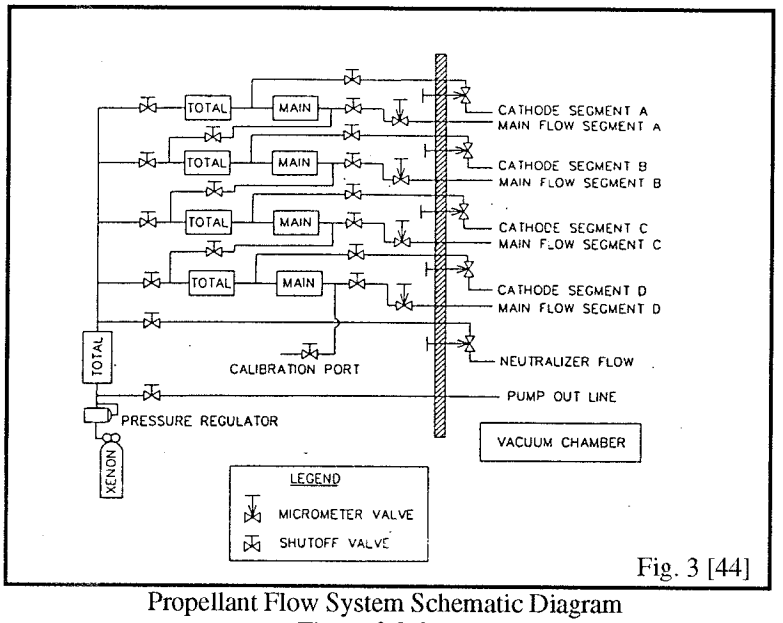

Propellant Flow System Schematic Diagram
Figure 3.2-3

3.2.3 Accelerator System

Each ion source was initially equipped with SAND ion optics. Segments A, B, and C had grids made of carbon-carbon and segment D originally had grids fabricated of G540 grade graphite. Segment D was later equipped with a 2-grid carbon-carbon system due to excessive thruster recycling of the graphite grids. Excessive recycling of segment D persisted with the 2-grid system and required deactivation throughout the investigation. Fabrication and processing of the carbon-carbon SAND optics were described by Mueller et al. [45]. Table 3.2-1 gives a short description of the ion optics used with segments A, B, and C.

Construction of the carbon-carbon grids was itself experimental [45]. Drilling of the accelerator and decelerator grid holes was accomplished by standard mechanical machining and posed no difficulty. This was enabled by the relatively large thickness and low open area fraction

Segmented Thruster Accelerator System Design

Component	Grid Set A	Grid Set B	Grid Set C
Grid Material	Carbon-Carbon	Carbon-Carbon	Carbon-Carbon
Grid Shape	Flat	Flat	Flat
Grid Diameter (cm)	19.4	19.4	19.4
Beam Diameter (cm)	15.0	15.0	15.0
Hole Quantity	4268	4268	4268
Hole Spacing (cm)	2.21	2.21	2.21
Screen Grid			
Thickness (mm)	0.52 (+0.01/-0.04)	0.44(+0.02/-0.08)	0.56(+0.00/-0.00)
Hole Diameter. (mm)	1.86(+0.06/-0.06)	1.84(+0.05/-0.03)	1.93(+0.01/-0.003)
Open Area Fraction	0.64	0.63	0.69
Mass (gram)	14.1	12.3	16.4
Manufacturing Technique	EDM*	EDM*	EDM*
Accelerator Grid			
Thickness (mm)	0.94(+0.00/-0.00)	0.93(+0.01/-0.02)	0.94(+0.00/-0.00)
Hole Diameter (mm)	1.18(+0.00/-0.00)	1.18(+0.00/-0.00)	1.18(+0.00/-0.00)
Open Area Fraction	0.26	0.26	0.25
Mass (gram)	42.5	41.6	42.9
Manufacturing Technique	Mechanical Drilling	Mechanical Drilling	Mechanical Drilling
Decelerator Grid			
Thickness (mm)	0.94(+0.02/-0.004)	0.94(+0.00/-0.00)	0.94(+0.00/-0.00)
Hole Diameter (mm)	1.7(+0.03/-0.03)	1.78 nominal	1.72(+/-0.004)
Open Area Fraction	0.54	0.59 nominal	0.55
Mass (gram)	31.6	32.0	31.3
Manufacturing Technique	Mechanical Drilling	Mechanical Drilling	Mechanical Drilling
Screen-Accel Grid Gap(mm)	0.635	0.635	0.635
Accel-Decel Grid Gap(mm)	0.254	0.380	0.254
Mount Ring			
Material	G540 Graphite	G540 Graphite	G540 Graphite
Mass (gram)	67.7	67.9	67.9
Manufacturing Technique	Mechanical	Mechanical	Mechanical
Spacers	Steatite	Steatite	Steatite

*Electric Discharge Machining

Table 3.2-1

of the grids. Fabrication of the screen grids was not so simple and straightforward due to the desired high open area fraction and thinness of material. Initially mechanical drilling was attempted for the screen grids. However, in the first attempt, delamination of the grid material occurred and significant breakage in the webbing resulted which rendered the grid unusable. Electric discharge machining (EDM) was used for fabrication of the remaining screen grids. Slight webbing breakage still occurred on segments B and C and required some minor patching along the edges of the grids.

3.2.4 Neutralizer and Discharge Chamber Cathodes

The segmented ion thruster design contained a total of five cathodes, one within each discharge chamber for emission of ionizing electrons, and one exterior to the discharge chambers for neutralization of accelerated ions. Figure 3.2-4 shows the hollow cathode design used for all five cathodes. This design was similar, with some modifications, to that tested by Brophy and Garner [46].

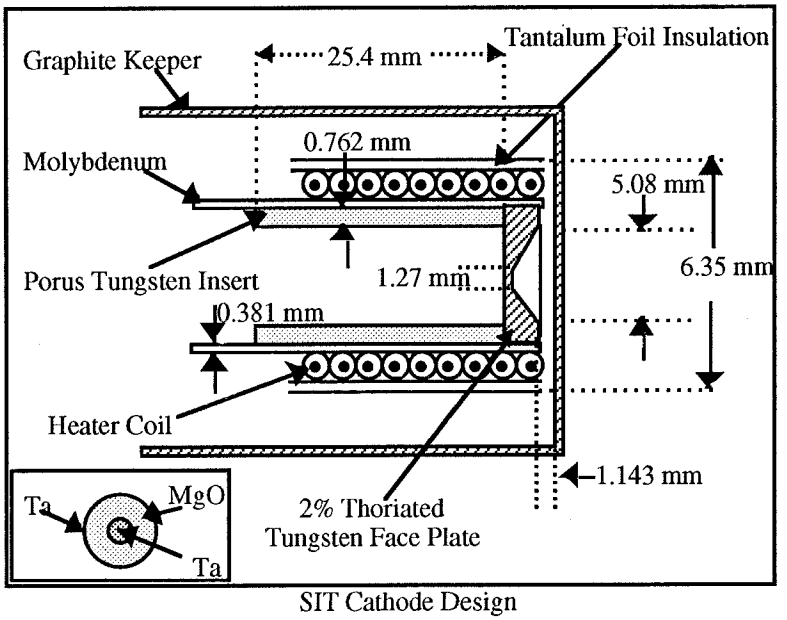

SIT Cathode Design
Figure 3.2-4

3.2.5 Electrical Integration and Control

The segmented ion thruster was operated from a single power processing unit as shown in figure 3.2-5. A single set of power supplies was used for biasing the accelerator system grids, while each discharge has its own dedicated power supply. This power processing concept could be expanded to accommodate additional segments by including another discharge power supply for each added segment.

Occasionally a low voltage, high current short developed between the grids and effectively disabled the accelerator system. In order to remove this arc and restore the system to operation, a recycle routine was included in the hardware that controlled the SIT power supplies. When one of these shorts was detected, the control system deactivated the high voltage applied to the grids, scaled back the discharge currents from all operating segments, reestablished the high voltage and then brought back the discharge currents to operational levels. This process required approximately two seconds. This recycle process occasionally had to be conducted multiple times in order to reestablish thruster operation.

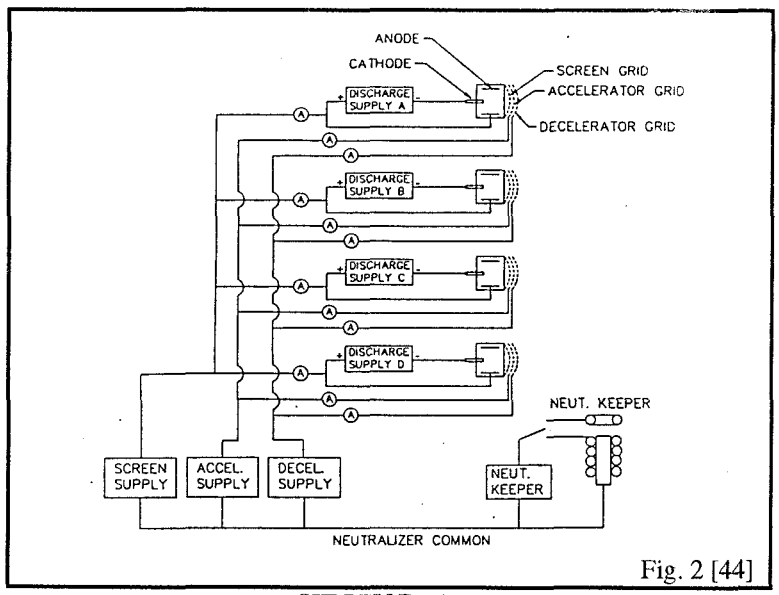

SIT PPU Design
Figure 3.2-5

3.3 Plasma Probes

3.3.1 Faraday Probes

The Faraday probe is one of the most basic forms of charged particle detectors and is well described by Osher [38]. A Faraday probe is simply a button that collects the current from impinging charged particles and a typical Faraday probe design, which is the type used in this investigation, is shown in figure 3.3-1. Passing the collected current through a resistor of known impedance and measuring the voltage drop across that resistor allows calculation of the current. Dividing this current by the effective area of the probe results in the current density of the ion beam at the location of the probe. Translation of the probe in a plane normal to the centerline axis of the thruster discharge chamber produces a current density map of the ion beam given the appropriate probe effective area for each location.

Modifications were made to the button in order to minimize potential errors associated charged particle measurement. Secondary electron emission from the collector surface of the Faraday probe results in measurement of ion current which is larger than the actual current collected by the probe. Secondary electron emission occurs when an ion striking the collector surface imparts sufficient energy to the collector material that an electron is 'knocked off'. This results in the data acquisition electronics indicating the impingement of two ions, not one. A collector material with a low secondary electron emission coefficient for the ion of interest was used to help minimize this effect. The secondary electron emission coefficient is dependent upon both the collector material and the type of ion striking the collector.

Not only does emission of these secondary electrons have to be minimized, impingement of plasma electrons on the Faraday probe collector surface must also be minimized, or avoided, if possible. A simple mechanism for accomplishing this is to bias the collector surface sufficiently negative so as to repel these plasma electrons (for ion collection). Although repulsion of electrons is necessary, one must be careful to not bias the probe to such an extent that beam ions,

that would not normally strike the probe, are deflected from their nominal trajectories and hit the collector.

A total of 24 Faraday probes were utilized for current density mapping of the extracted ion beams. Each probe consisted of a collector; cup; insulated collector support; cup bias lead; and a collector current wire. Figure 3.3-1 depicts the design used here. This design also had been utilized in several other research programs at JPL for investigating plume characteristics of other advanced electric propulsion concepts [66, 67]. Each collector was 2.286 ± 0.010 cm in diameter giving a total area of 4.104 ± .036 cm^2. The cup had an outer diameter of 2.54 cm and an inner diameter of 2.41 cm. Each cup had a length of approximately 2.54 cm.

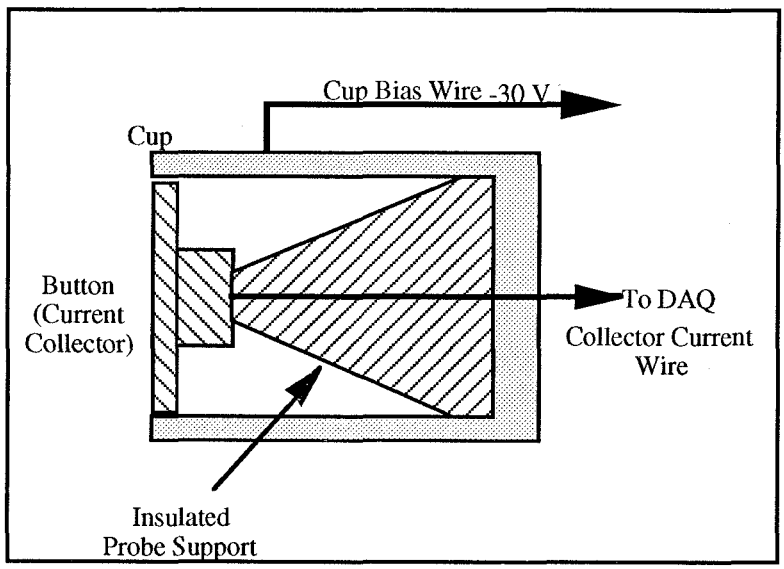

Faraday Probe Schematic Diagram
Figure 3.3-1

The collector, made from aluminum, was plasma spray coated with a layer of tungsten that had a thickness of approximately 0.10 cm. The low secondary electron emission coefficient (SEEC) of tungsten with impinging xenon ions made it a good choice for this investigation. The secondary electron emission coefficient for a 1 keV singly charged xenon ion striking tungsten is 0.005 [38]. This assumes normal incidence on a glassy surface. However, the plasma spray coating of the collector did not leave a glassy finish and the motion of the probes did not allow for normal incidence at all probe locations. Even with these departures from the assumptions, and

the energy of the ions were not 1 keV, this value gave a reasonable prediction for the SEEC expected in this study.

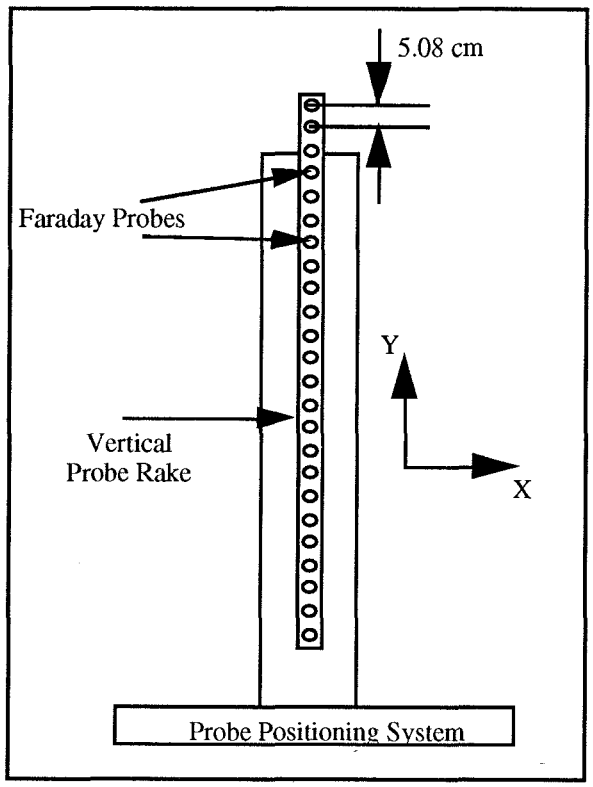

Faraday Probe Rake
Figure 3.3-2

The 24 Faraday probes were mounted vertically to a rake structure shown in figure 3.3-2. Individual probes were mounted on 5.08 cm centers. Initially the probe rake, which was mounted horizontally, consisted of only nine probes and was used for preliminary data acquisition. During this preliminary data acquisition [52], the 9 probe design was found to be too slow to be practical. The larger 24 probe configuration allowed the traverse to cover a larger acquisition area than the 9 probe configuration for a given amount of time. Even though the 24 probe configuration was significantly faster than the 9 probe configuration, it was still found to be too slow for some tests.

3.3.2 **ExB** Mass Spectrometer

An $\bar{E}x\bar{B}$ mass spectrometer, also known as an $\bar{E}x\bar{B}$ probe, is essentially a charged particle velocity filter. The most basic type of $\bar{E}x\bar{B}$ probe is one with a fixed magnetic field ($\bar{B}$) that is

normal to the nominal ion velocity vector ($\bar{V}$) and a controllable electric field ($\bar{E}$) normal to both $\bar{B}$ and $\bar{V}$. The $\bar{E}$ and $\bar{B}$ fields are oriented in such a way that the force on a charged particle due to the $\bar{E}$ field is in the opposite direction as the force due to the $\bar{B}$ field. An example of an $\bar{E}x\bar{B}$ mass spectrometer is shown in figure 3.3-3.

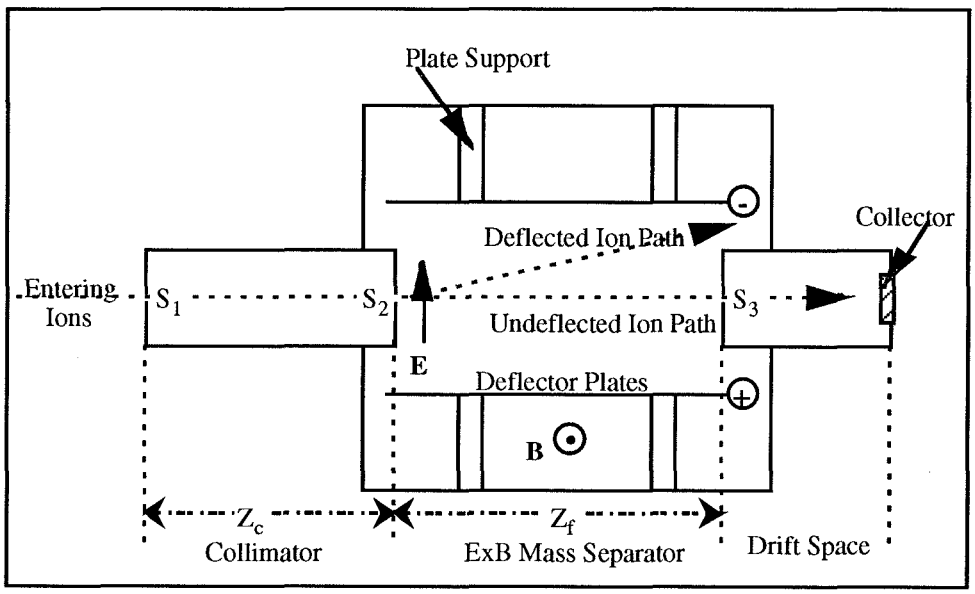

ExB Probe Diagram
Figure 3.3-3

This type probe has been used in numerous investigations of ion beams including those by Vahrenkamp [36], and Byers [39].

An $\bar{E}x\bar{B}$ probe of this type operates in the following fashion. Ions enter the collimator through a slit or hole in the front of the collimator with a velocity $\bar{V}$. This collimator serves to filter out ions that do not travel along the axis of the collimator. The slit creates an ion beamlet inside of the probe. Those ions that travel along the probe axis enter the $\bar{E}x\bar{B}$ mass separator section. Here they experience the force effects of the $\bar{E}$ and $\bar{B}$ fields. Ion velocity is the only variable upon which the strength of the $\bar{B}$ field force is dependent (the ions are assumed homogenous throughout and q and $\bar{B}$ are given and fixed).

Eq. 3.3-1 $$\bar{F}_B = q\bar{V} \times \bar{B}$$

The potential difference between the deflector plates (V_d) is the only variable upon which the strength of the $\vec{E}$ field is dependent assuming that q and $\vec{d}$ are fixed and given.

Eq. 3.3-2 $$\vec{F}_E = q\vec{E} = q\frac{V_d}{\vec{d}}$$

When the force on the charged particle due to the $\vec{E}$ field is equal to that due to the $\vec{B}$ field, the ion is allowed to pass undeflected through the $\vec{E}x\vec{B}$ mass separator section, into the drift space section, and strike the collector. This occurs when:

Eq. 3.3-3 $$q\vec{E} = q\vec{V}x\vec{B}$$

Eq. 3.3-4 $$\vec{V} = \frac{|\vec{E}|}{|\vec{B}|} = \frac{V_d}{|\vec{d}||\vec{B}|}$$

In practice, the $\vec{E}x\vec{B}$ mass spectrometer would be placed in an ion beam with the axis of the collimator parallel to the centerline of the ion beam. The potential difference between the bias plates is then ramped. When

Eq. 3.3-5 $$V_d = |\vec{V}||\vec{d}||\vec{B}|$$

the forces will be equal and the collector will receive an ion current. Otherwise, the collector will register zero current. Using an energy balance, the velocity of the ions extracted from the accelerator system will be,

Eq. 3.3-6 $$qV_B = \frac{1}{2}m_i\vec{V}^2$$

Eq. 3.3-7 $$|\vec{V}| = \sqrt{\frac{2qV_B}{m_i}} = \sqrt{\frac{2zeV_B}{m_i}}$$

and therefore the bias between the defector plates required to register a current is

Eq. 3.3-8 $$V_d = \sqrt{\frac{2zeV_B}{m_i}}|\vec{d}||\vec{B}|$$

For $\bar{E}x\bar{B}$ mass spectrometers of this type, $|\bar{d}|$ and $|\bar{B}|$ are given. V_B and m_i are given for the specific operating conditions of the ion thruster and e is the electron charge. The degree of ionization (z) is equal to 1 for singly charged ions and 2 for doubly charged ions. The current read by the collector is I^+ for z = 1 and I^{++} for z = 2.

If the construction of the $\bar{E}x\bar{B}$ probe was inexact in alignment of the slits, or the combination of collimator length and slits width were not sufficient to filter out all off axis ions (which was the case for this investigation), the voltage differential of the deflector plates which would allow ions to strike the collector would shift from the theoretical values given in equation 3.3-8. Corrections to this equation were derived by Anderson [40] at JPL and results are given in equation 3.3-9.

Eq. 3.3-9
$$V_d = \sqrt{\frac{2zeV_B}{m_i}}|\bar{d}||\bar{B}| + \frac{4|\bar{d}|V_B}{Z_f}\left[\frac{X_c}{Z_c} - \frac{X_f}{Z_f}\right]$$

Z_C and Z_f refer to the length of the collimator and the axial distance between the collimator and collector slits, respectively. X_C and X_f refer to the lateral distance by which the upstream and downstream collimator slits are misaligned and the lateral distance by which the downstream collimator slit and the collector slit are misaligned. Figure 3.3-4 depicts the layout of the probe and identifies the misalignments. Note that the dimensions shown in figure 3.3-4 are exaggerated to better show angles.

Figure 3.3-5 shows a typical profile obtained with the $\bar{E}x\bar{B}$ probe used in this investigation. The Y axis represents the ion current collected by the probe (I_C) and the X axis represents the total bias between the deflector plates of the probe (V_d). Visible in the profile are two peaks, one at approximately 132 V and the other at 202 V. The first peak, at 132 V, is due to singly charged ions and the second peak, at 202 V, represents the doubly charged ion current measured by the probe.

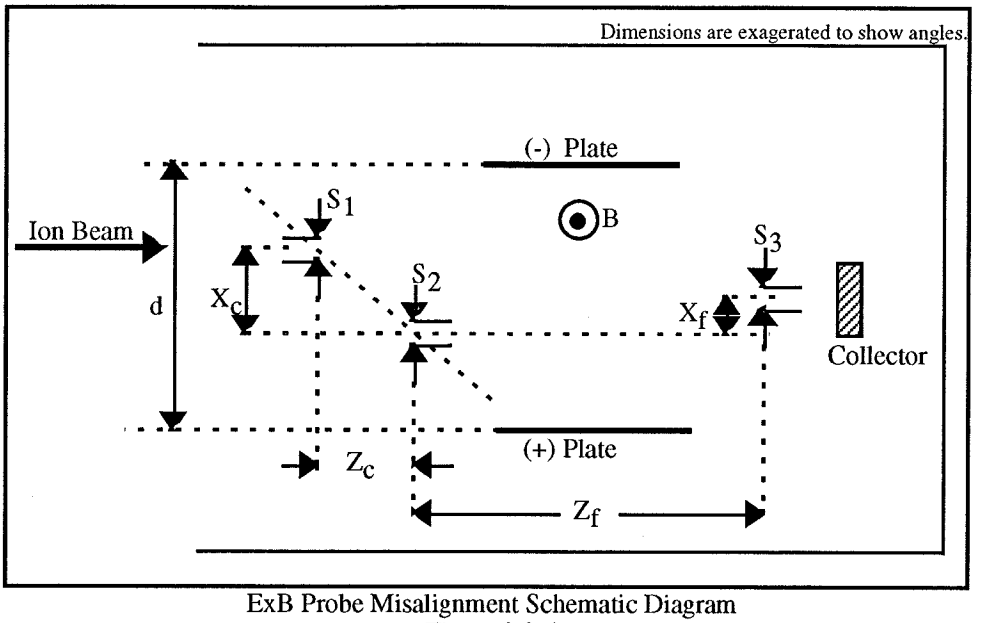

ExB Probe Misalignment Schematic Diagram
Figure 3.3-4

A noticeable characteristic of the peaks shown in figure 3.3-5 is that they have a finite width. If the ion beam was monoenergetic, perfectly collimated, the slits were perfectly aligned and sufficiently thin, the profile shown in the figure would consist of a pair of spikes, not curves. Since these ideal conditions do not exist, the peaks have a finite width. A calculation for the width of the peaks was derived by Anderson [40] with the result relationship given in equation 3.3-10.

Eq. 3.3-10
$$W = \left(\frac{2|\bar{d}|}{Z_f}\right) V_B \left[\left(\frac{S_1 + S_2}{Z_c}\right) + \left(\frac{S_2 + S_3}{Z_f}\right)\right]$$

S_1, S_2, and S_3 refer to the widths of the upstream collimator slit, downstream collimator slit, and the collector slit respectively.

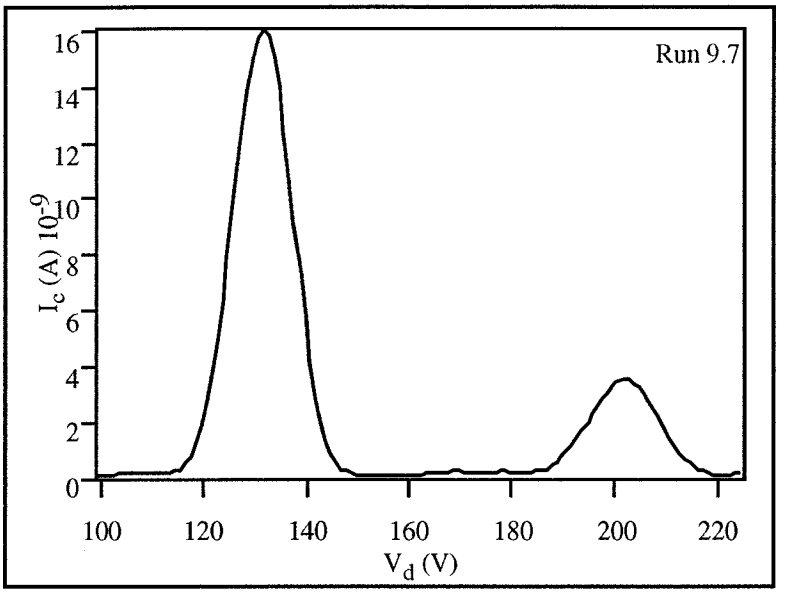

ExB Probe Current Profile
Figure 3.3-5

The $\vec{E}x\vec{B}$ mass spectrometer used in this study, shown in figure 3.3-6, was modeled after a design conceived by Fitzgerald of the California Polytechnic University, Pomona who is on staff at JPL. Testing and analysis of this design has been conducted by Anderson of JPL for other ion thruster investigations [47].

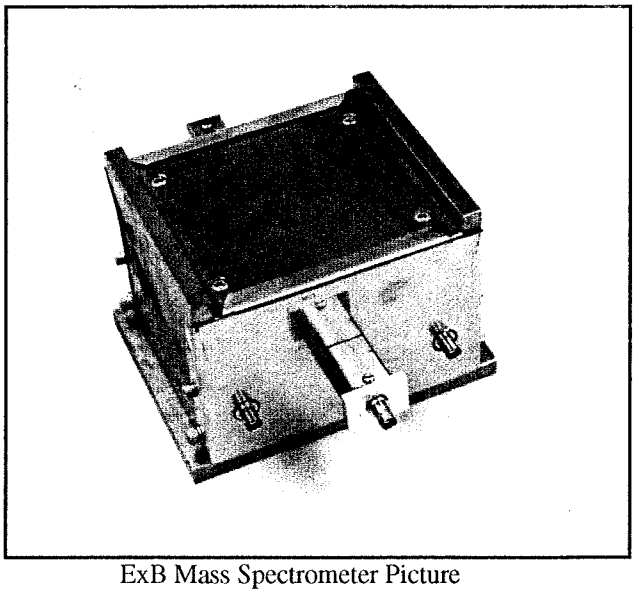

ExB Mass Spectrometer Picture
Figure 3.3-6

The primary difference between the original design and the design used for this investigation was that, in the present design, the collimators were welded to the probe face plates. In the original configuration the collimators were bolted to the face plates which allowed for slight movement. The deflector plate bias lines, as well as the current collector data line, were connected to the $\bar{E}x\bar{B}$ probe via BNC connectors located on the downstream side of the probe. The current collector used in the $\bar{E}x\bar{B}$ probe was similar to the current collectors of the Faraday probes as discussed above except in size. The aluminum button of the $\bar{E}x\bar{B}$ collector was also plasma spray coated with tungsten in order to reduce the secondary electron emission.

3.4 Probe Positioning System

One of the primary efforts required in performing the plume diagnostic tests in this investigation was to design and construct a computer controlled probe positioning system that had a minimum total travel of at least one meter in the X, Y, and Z directions. It was also important that this system could be used for other investigations conducted in the vacuum chamber. The traverse mechanism constructed to meet these requirements is pictured in figures 3.4-1 and 3.4-2. The motion capability of the final design allowed travel of 1.07 m, 1.17 m, and 1.85 m respectively for the X, Y and Z axes.

The probe positioning system was primarily of stainless steel and aluminum construction. Attention during the design phase was paid to minimizing the quantity of steel in order to avoid any potential magnetic interference problems. As shown in the figures above, the system consists of 3 pairs of 1.905 cm dia. stainless steel slide rails, 1 pair running along each of the 3 axes. Two recirculating ball bearing pillow blocks are mounted to each slide rail to allow for ease of motion. Mounted upon the pillow blocks are aluminum structural platforms which support the loads from each of the subsequent system components. For example, the pillow blocks that travel along the Z axis support a 1.27 cm thick aluminum plate to which the X axis slide rails are mounted. A smaller aluminum plate is attached to the X axis pillow blocks, and the Y

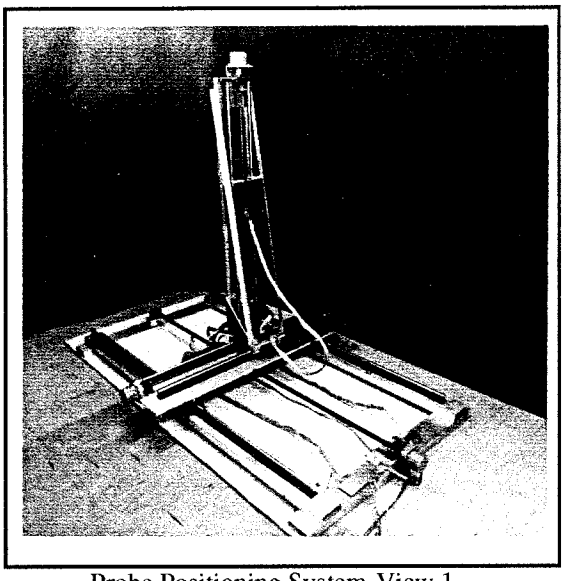

Probe Positioning System-View 1
Figure 3.4-1

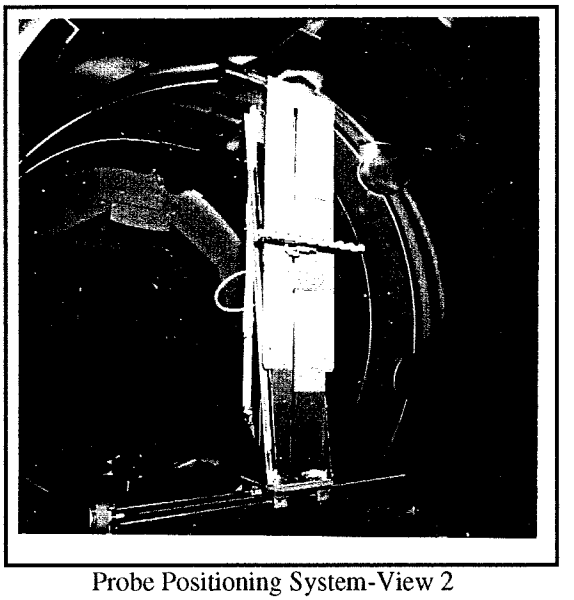

Probe Positioning System-View 2
Figure 3.4-2

axis slide rails are connected to this plate. A final support plate is connected to the Y axis pillow blocks, and the data acquisition probes are connected there.

Motion of the system is enabled through the use of rolled ball screws that run between each pair of slide rails. A nut with recirculating ball bearings is connected to each of the support plates. The rolled ball screws pass through the nuts and are fastened at each end with the use of bearing end journals. Turning of each screw causes the probe positioning system to move. Actuation of the nut-screw assembly is facilitated through use of computer controlled stepper motors connected to one end of each screw. Rigid aluminum couplings are used to connect the ends of the screws to the stepper motor drive shafts. Flexibility in the motor-screw assembly was needed to compensate for slight misalignments. This is enabled by use of aluminum motor mounts that bend as the screw turns. Safety wire and Loctite [61] were used to assure no slippage between the motor shafts and screws. The X and Y axis ball screws translate the system 2.54 cm for every 5 turns of the screw. Four turns of the Z axis screw move the traverse 2.54 cm.

Control of the stepper motors is enabled with the use of a Macintosh Centris 650 computer [62], National Instruments DIO-32F digital interface card and LabView Software; and Superior

Electric 230-T stepper motor drive electronics. The LabView software was programmed to command the DIO card to produce TTL pulses, one pulse per step of the motor. The stepper motor drive electronics read these TTL pulses and generate the appropriate voltages and currents to step the motor. The DIO card, in combination with the stepper motor drive electronics, are also capable of controlling motor direction (clockwise or counterclockwise) and step size (1° per step or 2° per step).

With the ability of the stepper motors to move in 1° increments, and with the screw design specifications, the X and Y axes could ideally be moved in 13.97 μm increments and the Z axis in 17.53 μm increments. There was some lag in the screws and the flexibility of the motor mounts added some error to this ideal movement as well. It is estimated that motion of the system could be controlled to within 25.4 μm per step and this resolution was more than adequate for this investigation.

Danger of over turning the ball screws and running the traverse carriages beyond the ends of the slide rails is a potential failure mechanism. Electrical limit switches are used to disconnect the power supply from the stepper motors if an overdrive of any one of the ball screws, in either direction, is detected. These limits switches are positioned at each end of all three axes. If one of the screws were to be over-driven, the limit switch will close and send current through a relay which will then open the stepper motor power supply circuit. A manual override is also included so that if a screw is overdriven it will be possible to reset the system by moving the traverse off of the limit switch without the need to open the vacuum chamber.

The $\bar{\mathbf{E}}\mathbf{x}\bar{\mathbf{B}}$ probe was sufficiently massive that the Y axis ball screw would auto-rotate when the stepper motor windings were not energized. The probe would then fall until it came to rest against the bottom of the traverse. However, the probe assembly would easily break through the Y axis bottom limit switch that was located above the bottom of the traverse. It was therefore necessary to construct a mechanism that would allow the probe to rest against a motion stopper when the windings were not energized. This mechanism would have to be flexible enough so that

if the Y axis stepper motor were over-driven, the probe carriage would engage the Y axis bottom limit switch and not damage the system. However, for initialization of the Y axis, it was also necessary that this mechanism ensure that the probe come to rest at the same place every time. The mechanism devised for this task was a spring placed at the bottom of the Y axis such that the weight of the probe would cause the spring to partially compress. If the stepper motors were to have been over-driven, the spring would compress further until the Y axis limit switch was engaged.

3.5 Data Acquisition System

The same LabView software and Macintosh personal computer as was utilized for the probe positioning system control was used to control the data acquisition system. In addition to acquisition of the data, the LabView software also performed some calculations and analyses with the acquired data, and then organized and archived the data. Three types of data were collected during this investigation: Faraday probe current, $\bar{\mathbf{E}}\mathbf{x}\bar{\mathbf{B}}$ probe current, and stepper motor temperature measurements. The thruster control console collected operating data and saved it to disk, as well as printed hard copies. There were a few instances when the data was not archived properly and educated guesses were made to fill in the missing data. Values given in the tables of appendix A that are in bold print represent data that was calculated with the fill in data.

3.5.1 Faraday Probe Data Acquisition Equipment

The electronic equipment used for collection of Faraday probe data consisted of: a Macintosh Centris 650 with 8 MB RAM; National Instruments analog interface card MIO-16XL, National Instruments data multiplexer AMUX-64T; two National Instruments 5D backplanes; 24 ±50 mV to ±5V National Instruments 5D voltage conversion modules; and the probe rake consisting of 24 Faraday probes. Figure 3.5-1 displays the connectivity and interfaces of this equipment.

The data electronics wiring diagram for a single Faraday probe is displayed in figure 3.5-2. As shown in the figure, current collected by the Faraday probe passes through a resistor and the

voltage drop across that resistor is read by the data acquisition electronics. The currents measured by each probe can be determined by applying Ohm's law with the known resistance and measured voltage drop.

In order to accurately determine the currents measured by the probes it was necessary to accurately measure the resistance of each resistor. Resistances were determined by connecting each resistor to a precision 1 mA current supply and measuring the voltage drop using a high quality, Fluke 45 multimeter. Ohm's Law was used to calculate the resistance from the current and voltage values obtained. Carbon composite, ±5%, 1/2 watt resistors were chosen for this experiment. A different impedance resistor set was needed for each nominal beam current and net-to-total accelerating voltage ratio (R) tested in order to utilize the entire range of the voltage

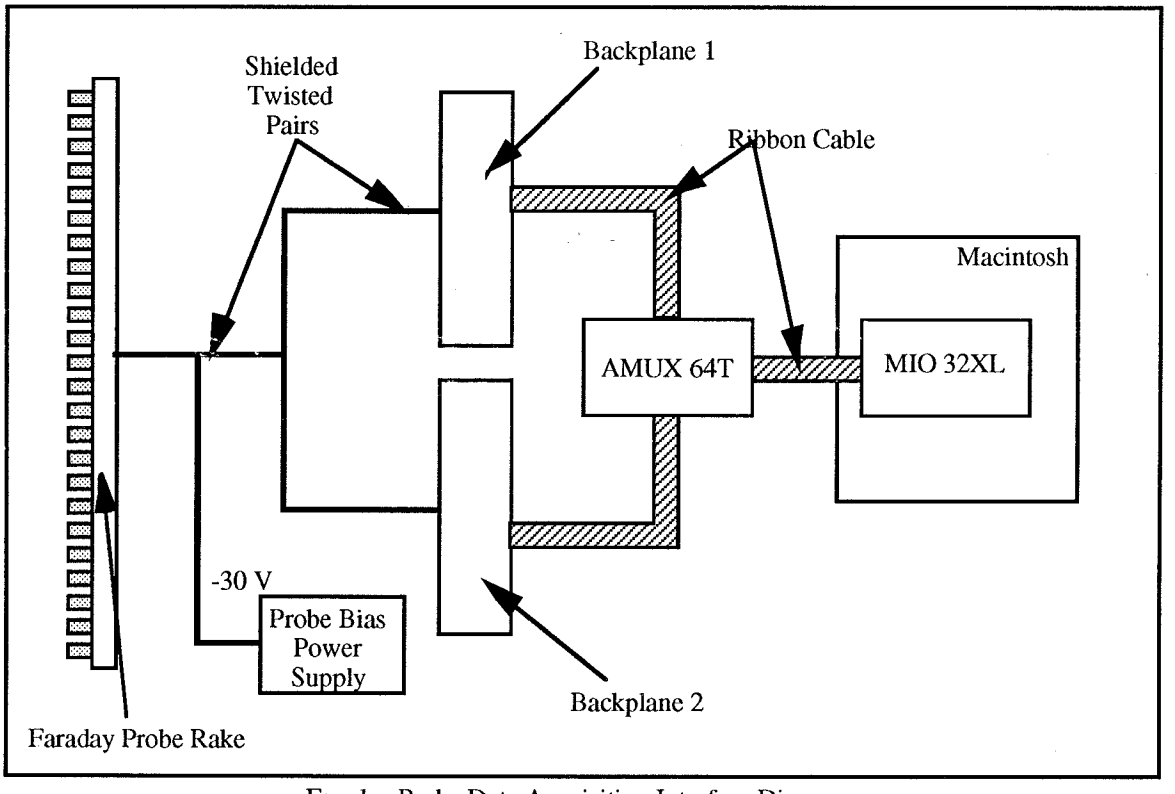

Faraday Probe Data Acquisition Interface Diagram
Figure 3.5-1

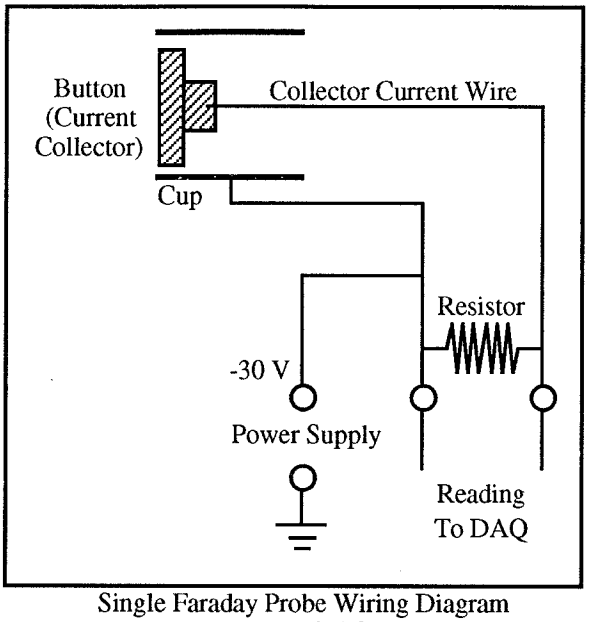

Single Faraday Probe Wiring Diagram
Figure 3.5-2

conversion modules. Table A-1 of appendix A lists all of the resistors used for each channel and resistor set.

During data acquisition, current collected by the Faraday probes passed through the resistors. The voltage drop across each resistor was converted from the specified ± 50 mV range to the ± 5 V range by the voltage conversion modules. Next, through the use of a multiplexer, the voltage produced by each conversion module was read into the computer via the MIO card.

A trial run under ambient laboratory conditions was attempted once the data acquisition system was completely assembled. A value of zero was expected from each channel. As it turned out, values read by the computer were not zero, but varied between 0.003 and 0.022 mA. In discussions with personnel within the advanced propulsion group at JPL, it was learned that this phenomenon was not uncommon. Inspection of the data files revealed that these offset values were stable and subtracting an offset value from the sampled data would produce the correct current readings. Several offset measurements were taken for each probe and averaged in order to determine the appropriate values. The offset values applied for each probe are given in

table 3.5-1. Data acquisition was again attempted in the ambient laboratory conditions. This time the values read were 0.000 ± 0.002 mA.

The next test consisted of attaching the precision 1 mA current source to each of the probes, one at a time. Values read by the computer, with inclusion of the offsets were 1.000 ± 0.002 mA for each of the probes. The error for the 1 mA test and for trial run with offset included were roughly the same. This implies, at least for the purpose of this investigation, that the offset error does not scale significantly with current collected by the probe and the offsets calculated will be assumed appropriate for operation with probe collected ion currents of up to 10 mA.

Faraday Probe Channel Offsets

Probe #	Offset (mA)	Probe #	Offset (mA)
0	0.009	12	0.013
1	0.003	13	0.013
2	0.006	14	0.018
3	0.011	15	0.015
4	0.012	16	0.013
5	0.009	17	0.016
6	0.014	18	0.020
7	0.016	19	0.019
8	0.014	20	0.022
9	0.014	21	0.019
10	0.012	22	0.022
11	0.013	23	0.020

Table 3.5-1

Both the Faraday probe cup and collector were biased -30V relative to ground in order to repel free electrons. Figure 3.5-3 shows the current collected by a single probe in the ion beam as a function of the voltage potential applied to the cup and collector. As can be seen, the curve asymptotically reaches a maximum before -20V. Since the collector current does not increase

significantly beyond this asymptotic value, it is believed that -30V does not deflect ion trajectories and collect an artificially high current.

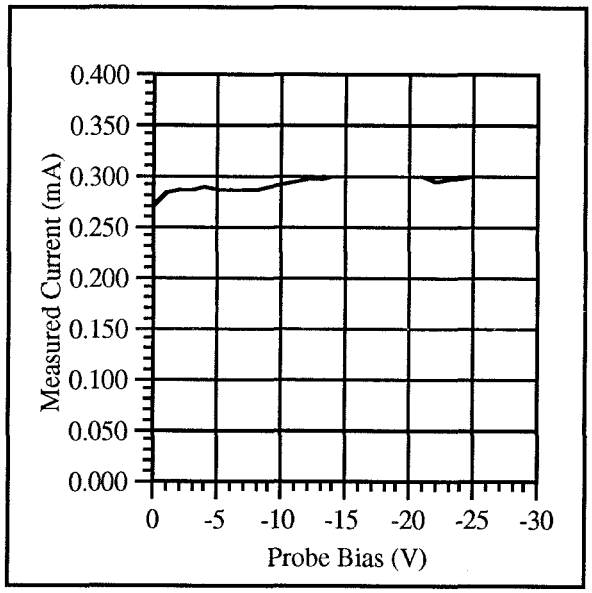

Collector Current vs. Applied Potential
Figure 3.5-3

3.5.2 **ExB** Mass Spectrometer Data Acquisition Equipment

Equipment used for $\bar{\mathbf{E}}\mathbf{x}\bar{\mathbf{B}}$ probe measurements consisted of: the same Macintosh Centris 650 personal computer; a National Instruments General Purpose Interface Bus (GPIB) interface card, a Hewlet Packard 6005, 0-500V, programmable power supply; and a Keithly Model 617 Electrometer. Both the power supply and the electrometer were GPIB compatible. The interface diagram for this investigation is shown in figure 3.5-4.

Current collected by the $\bar{\mathbf{E}}\mathbf{x}\bar{\mathbf{B}}$ probe was measured by the Keithly electrometer and the value was transmitted in a digital format to the GPIB card resident within the Macintosh computer. The GPIB card then translated the current value to the computer. This current value was then registered on the real time display of collected current (I_c) vs. deflector plate bias (V_d) and saved to disk. At the completion of this measurement phase, the computer sent a digital command via the GPIB interface to the HP power supply to step the output voltage by one volt.

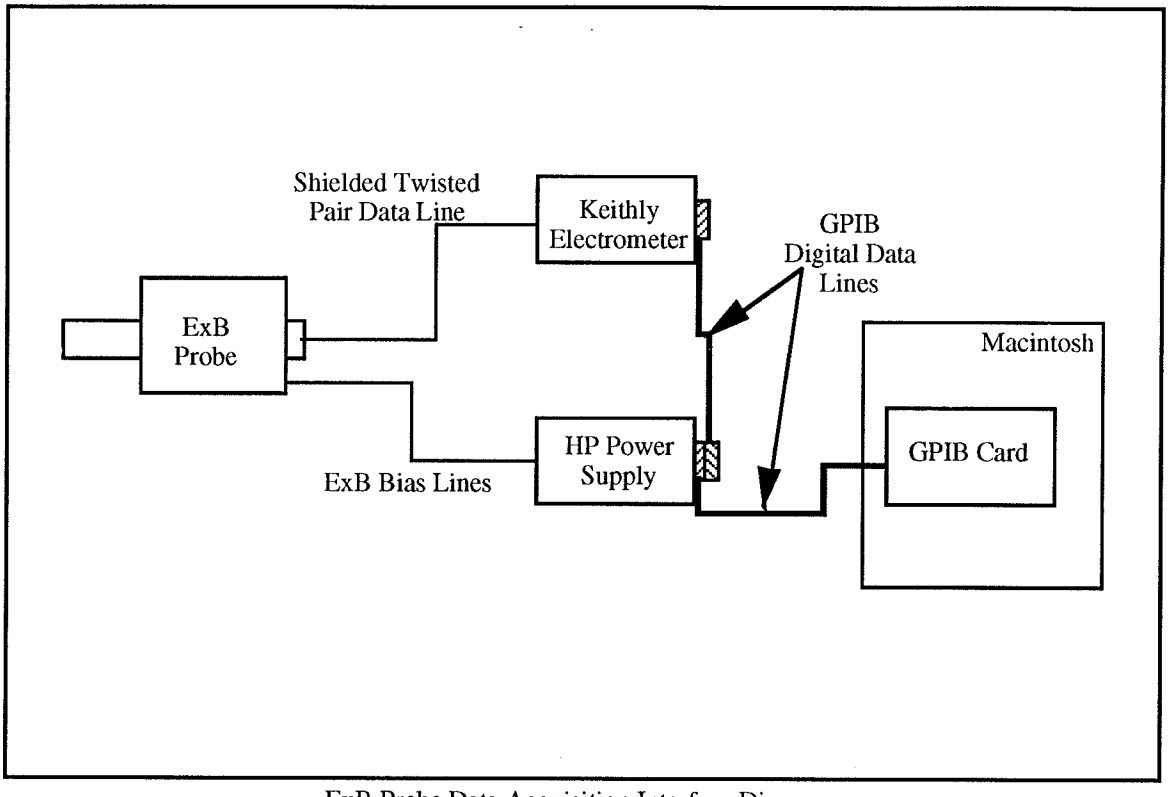

ExB Probe Data Acquisition Interface Diagram
Figure 3.5-4

This measurement / voltage step cycle was repeated until the desired total voltage range had been covered.

Digital interfacing between the Macintosh computer and both the power supply and electrometer was done to minimize noise with a signal that was expected to be on the order of tens of picoamps. Initial attempts to operate the system with analog interfaces between a pico-ammeter and the computer through the use of a backplane and MIO card, as used for the Faraday probe measurements, resulted in signals with unacceptably high noise levels. The digital interface, with the GPIB capable equipment, reduced the signal noise to an acceptable level. Although the noise level was substantially lower with the use of GPIB, the amount of time required to ramp through the voltage range applied to the deflector plates was greatly increased.

Prior to closing the vacuum chamber, trial runs were performed to ensure the power supply would correctly step through the appropriate voltage ranges. A voltmeter was connected to the

power supply to verify calibration. Calibration of the electrometer was conducted prior to use in this investigation. No testing was conducted outside the vacuum chamber beyond performing continuity checks of the circuit regarding the $\bar{\mathbf{E}}\mathbf{x}\bar{\mathbf{B}}$ probe collector signal. It was decided that if the current measurement circuit was not functioning properly during data acquisition, it would be obvious and could be corrected outside the chamber as necessary.

Chapter 4 Experimental Procedures

4.1 Beam Current Density Mapping

Mapping of the extracted ion beam current density was necessary to address issues of thruster performance, spacecraft interaction, lifetime, interaction of multiple ion beams, and repeatability of ion source construction and operation. These current density maps were used to make current density contour plots for both single and multiple ion source operation and to calculate beam divergence angles for individual ion sources. Current density maps were developed for a total of four different thruster operating conditions at up to five different downstream locations. The following describes the methodology and techniques employed to produce these maps as well as operation of the thruster, probe positioning and data acquisition systems.

4.1.1 Segmented Ion Thruster Operation

Parameters that were varied to achieve the four different thruster operational settings included discharge current (I_D) for each ion source, ion optics grid potentials (V_S, V_A, V_D), and propellant flow rates ($\dot{m}_t$, $\dot{m}_n$). Discharge currents and flow rates were controlled so that three different nominal beam currents were utilized in the study. Voltage potentials applied to the grids allowed for operation at two different net-to-total accelerating voltages ratios (R ratio). Equation 4.1-1 defines the R ratio.

$$\text{Eq. 4.1-1} \qquad R = \frac{V_S}{V_S + |V_A|}$$

The nominal beam currents extracted from individually operated ion sources were 312 mA, 430 mA, and 500 mA. Beam currents produced by each ion source for a given propellant flow rate ($\dot{m}_t$), were controlled by adjusting the discharge current (I_D) of that source. For cases in which multiple ion sources were active, the nominal beam currents extracted from each ion source were equal. The beam current produced by the entire thruster was therefore the nominal beam current of a single ion source multiplied by the number of operating ion sources. For example, in the case where segments A and B were operational and the nominal beam current for

each ion source was 430 mA, the total beam current produced by the thruster was 860mA. The column labeled 'I_B' in table A-2 gives the total thruster nominal beam current for each run.

Beam current values for each ion source were individually monitored during testing and tended to drift slightly. In order to keep operational beam current values consistent throughout testing, the discharge currents was adjusted when the actual beam current varied by more than ±1% from the nominal value.

The R ratio is strongly correlated with focusing of the ion beam and therefore impacts divergence of the ion beam. A high R ratio results in a highly collimated beam while a low R ratio produces a more divergent beam. Two different R ratios are evaluated in this investigation and are given for each run in the column labeled 'R Ratio' of table A-2. The first R ratio of 0.893 was attained with a screen grid voltage (V_S) of 1250 V, accelerator grid voltage (V_A) of -150 V, and decelerator grid voltage (V_D) of -100 V. A screen grid voltage (V_S) of 900 V, accelerator gird voltage (V_A) of -500 V, and decelerator grid voltage (V_D) of -200 V produced an R ratio of 0.643 for the second. The screen grid, accelerator grid and decelerator grid potentials are also given in table A-2 for each data collection run. The columns that contain this data are labeled 'V_S', 'V_A', and 'V_D' respectively.

Propellant flow rates for this investigation were dependent upon the desired nominal beam current. In order to operate the thruster at a high efficiency it was necessary to provide an appropriate amount of propellant such that the system had a high propellant utilization efficiency with low production of multiply charged ions. It was not possible to analyze the propellant utilization efficiency vs. multiply charged ion ratio prior to data collection with Faraday probes because the Faraday probe work was conducted first. The nominal, unadjusted, propellant utilization efficiency (η_p) was chosen to be 90% based on past experience. During testing, however, the propellant flow rate was not continually adjusted and generally tended to drift to lower mass flow rates over time. Since the beam current from each ion source was kept constant throughout each set of tests, and the propellant flow rate tended to decrease, the propellant

utilization efficiency tended to increase. The uncorrected propellant utilization efficiency, which can be found in the 'η_p' column of table A-2, ranged from 0.680 to 1.067.

Operation of the neutralizer was not strictly controlled during Faraday probe data acquisition. The only controllable function associated with neutralizer operation was the status of the keeper power supply (LVK). The condition of low voltage keeper, either "On" or "Off", was not recorded for each data collection run, however, the actual value for the neutralizer coupling voltage was recorded by the thruster control computer. The values for coupling voltage (V_{cn}) and neutralizer mass flow rate ($\dot{m}_n$). for each Faraday probe data acquisition run, are given in table A-2 of appendix A.

A total of seven combinations of operational ion sources were investigated for each of the operational settings. Table A-2 of appendix A gives a complete description of thruster operational conditions for all successful data acquisition runs. All combinations of segments A, B, and C were operated for each of the thruster operational settings. These included the individual operation of segments A, B, and C as well as the simultaneous operation of segments AB, AC, BC, and ABC. Segment D was not functioning properly during this investigation and no data was obtained regarding its operation. The combination of active ion sources for each run is given in the column labeled 'Seg' in table A-2 of appendix A.

Unsuccessful data acquisition runs were ignored here and not used for data analysis. Causes for unsuccessful runs includes excessive recycling of the thruster, unexpected shut-down of either the thruster or the probe positioning system, and improper operation of either the thruster or probe positioning system. Thruster operational data was saved both in electronic and printed formats. Occasionally, after review of the acquired data, it was determined that the data quality was poor due to some unknown causes and re-acquisition was required.

4.1.2 Probe Positioning System Operation

Entire planes of Faraday probe data were collected for each thruster operational setting and configuration of active segments. For the cases in which the nominal beam current was 430 mA

and R = 0.893, data was collected at 5 downstream locations, each separated by 0.152 m. A total of 3 planes of data were collected for each of the other thruster settings and configurations with 0.305 m spacings between the planes. The first plane of data in all cases was located approximately 0.356 m downstream from the thruster decel grid. Location of the data plane with respect to the decelerator grid plane for each run is given in the column labeled 'z' of table A-2.

Time to complete a scan became a significant driver in deciding how to operate the probe positioning system. It was desirable to keep the primary traverse structure out of the ion beam as much as possible because of the physical size of the probe positioning system. This desire for speed to pass through the beam quickly had to be balanced with the need for high quality data. Spacing between data points, the size of the data collection area, number of passes across the beam of the probe positioning system, and the method for measuring probe location all factored in to this trade off.

Initially the spacing between probe measurements was 2.54 cm in the X and Y directions. This was chosen because the diameter of the probe was just slightly less than 2.54 cm and it seemed this would be a logical value with which to begin. Preliminary tests of the probe positioning and data acquisition systems were conducted using a 5.08 cm spacing. Significant differences between the 2.54 cm and 5.08 cm spacings were noted. Spacing of less than 2.54 was contemplated, however, due to the design of the traverse motion this was deemed too slow to be operationally feasible. Even so, in order to assess the adequacy of 2.54 cm spaced data, several planes of current density data were collected with 1.27 cm spacings for individually operated segments A and B at a metered 430 mA beam current and an R ratio of 0.893.

Results from the two data types agree relatively well and it can be generally accepted that the larger spacing between data points is adequate for this investigation. The following paragraphs discuss in more detail the results generated from comparison of the 2.54 cm and 1.27 cm spaced data. Data was collected at downstream axial positions of z = 0.356, 0.508, and 0.660 m. Figures 4.1-1 and 4.1-2 display an example comparisons between 2.54 cm and 1.27 cm spaced data.

Figures C-1 through C-6 of appendix C display all 2.54 cm and 1.27 cm spaced data for comparison.

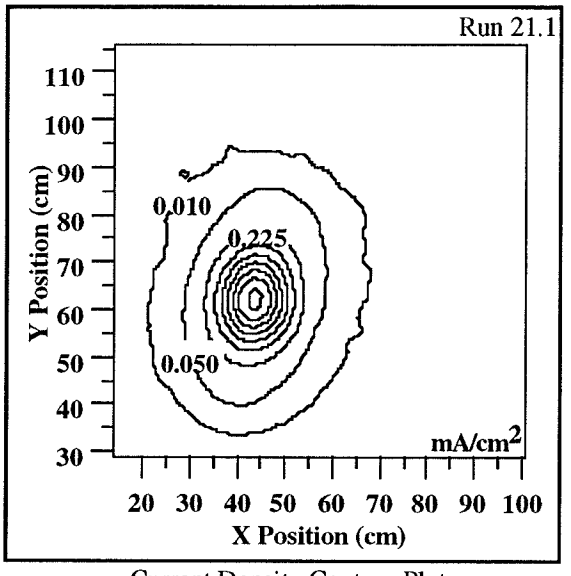

Current Density Contour Plot
2.54 cm Spaced Data
Figure 4.1-1

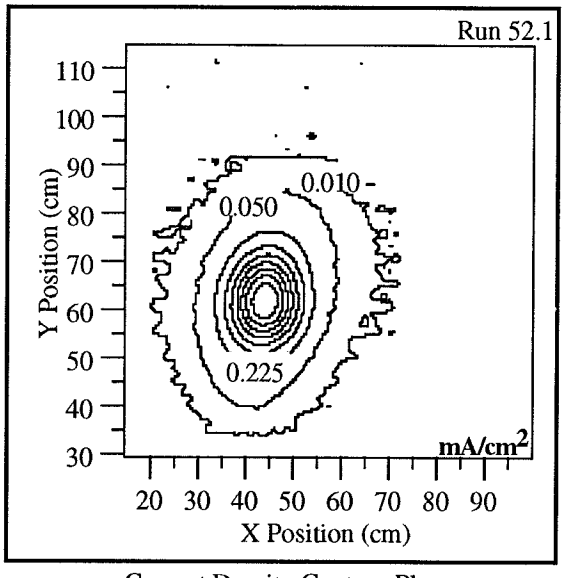

Current Density Contour Plot
1.27 cm Spaced Data
Figure 4.1-2

Comparison of the individual contours within the two figures reveals some slight differences. There are the same number of contours displayed in each of the figures, however, the 1.27 cm peak contours are generally larger in size than the 2.54 cm peak contours. This characteristic is consistent throughout all of the 1.27 cm spaced data cases.

The most likely cause for the differences in contour size at the higher current density values was that of the biases subtracted from the raw data to account for background plasma / system noise as discussed in section 5.1.3. A slight variation in the bias could account for the differences in contour size. Other possible causes relate to consistency of thruster operation, such as drifting of beam current, grid biases, discharge current and voltage, and propellant flow rate. Although these possibilities exist, there is no evidence to conclude they are the primary cause.

Results of current density integrations performed with both 2.54 cm and 1.27 cm spaced data are given in table 4.1-1. According to the column labeled "Delta", the variation of 1.27 cm results never exceeded 2.2% as compared to 2.54 cm results. This fell well within the margin for error as

displayed in the dI_B column. The values found in this column represent the uncertainty associated with each integrated beam current given in the column labeled I_B (mA).

1.27 cm vs. 2.54 cm Spaced Data Beam Current Comparison

Run	Data Spacing	Segment	z (m)	I_B (mA)	dI_B/I_B	Delta
21.0	2.54 cm	A	0.356	430	3.81%	-0.46%
52.0	1.27 cm	A	0.356	428	6.26%	
21.1	2.54 cm	A	0.508	412	3.59%	+0.97%
52.1	1.27 cm	A	0.508	416	5.62%	
21.2	2.54 cm	A	0.660	398	3.56%	-1.26%
52.2	1.27 cm	A	0.660	393	5.09%	
22.4	2.54 cm	B	0.356	431	3.51%	+0.70%
50.1	1.27 cm	B	0.356	434	6.78%	
22.0	2.54 cm	B	0.508	417	3.65%	+2.16%
50.2	1.27 cm	B	0.508	426	6.80%	
22.1	2.54 cm	B	0.660	403	3.53%	-0.50%
51.0	1.27 cm	B	0.660	401	6.55%	

Table 4.1-1

Comparison of the ion beam divergence angles calculated with 1.27 cm spaced data and 2.54 cm (converted to 0.635 cm spaced data for analysis) spaced data revealed some differences. The divergence angles computed for segment B were fairly consistent between the 1.27 cm and 2.54 cm data and the differences found were less than the summed total of the errors associated with calculation of the angles. Although the uncertainty of the beam divergence calculations are greater than the difference between the beam divergence angle calculated with 2.54 cm and 1.27 cm data for segment B, this was not the case for segment A. At locations of 0.508 m and 0.660 m downstream from segment A, the discrepancy was larger than the total uncertainty. Beam divergence angles and associated uncertainty are given in table 4.1-2 for both data spacing types.

1.27 cm vs. 2.54 cm Spaced Data Beam Divergence Comparison

Run	Data Spacing	Segment	z (m)	α(deg)	dα(deg)	Delta (deg)
21.0	2.54 cm	A	0.356	15.126	0.488	0.958
52.0	1.27 cm	A	0.356	14.168	0.782	
21.1	2.54 cm	A	0.508	14.242	0.387	2.157
52.1	1.27 cm	A	0.508	12.085	0.558	
21.2	2.54 cm	A	0.660	14.580	0.356	3.363
52.2	1.27 cm	A	0.660	11.217	0.438	
22.4	2.54 cm	B	0.356	11.030	0.393	0.888
50.1	1.27 cm	B	0.356	10.142	0.734	
22.0	2.54 cm	B	0.508	11.635	0.354	0.926
50.2	1.27 cm	B	0.508	10.709	0.637	
22.1	2.54 cm	B	0.660	10.959	0.300	-0.515
51.0	1.27 cm	B	0.660	11.474	0.570	

Table 4.1-2

Beam divergence angles calculated with 1.27 cm spaced data were all less than those determined with 2.54 cm data for segment A. This trend was also found for the Z = 0.356 m and Z = 0.508 m cases of segment B. The Z = 0.660 m case was the only one where the 1.27 cm segment B data generated an angle that was larger. These differences could be an identification of the data spacing having an impact on the calculated beam divergence values.

The data sampling area was controlled through operator inputs to the LabView software, instructing the system what motion limits to use. For planes of data collected close to the thruster it was possible to keep the total data sampling area small. As distance of the data plane from the thruster increased, it became necessary to expand the total data sampling area since the extracted ion beams also expanded with distance from the thruster. Initial data acquisition areas were determined by assuming a 15° beam divergence, knowing which ion sources were operational, and the distance between the thruster and data plane. There were some instances where the data sampling areas were chosen incorrectly with regions of important data being excluded from sampling. Shown below is a comparison between the resulting current density contour plots

where the data sampling area of figure 4.1-3 was chosen correctly and that for figure 4.1-4 was not. Runs in which the data sampling areas were grossly incorrect were discarded and run again.

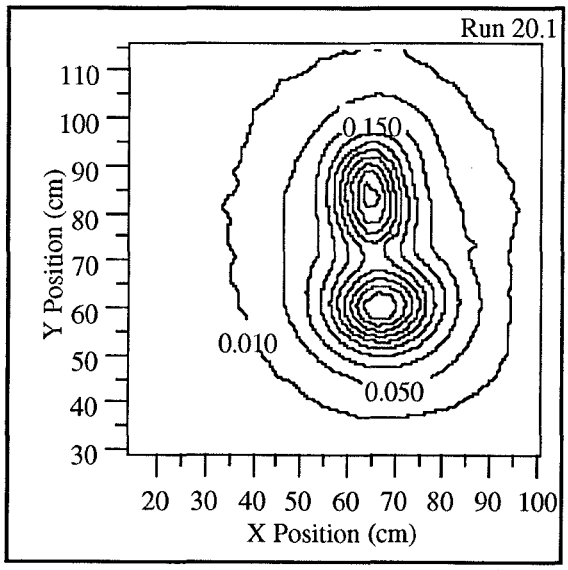

Appropriately Selected Data Sampling Area
Figure 4.1-3

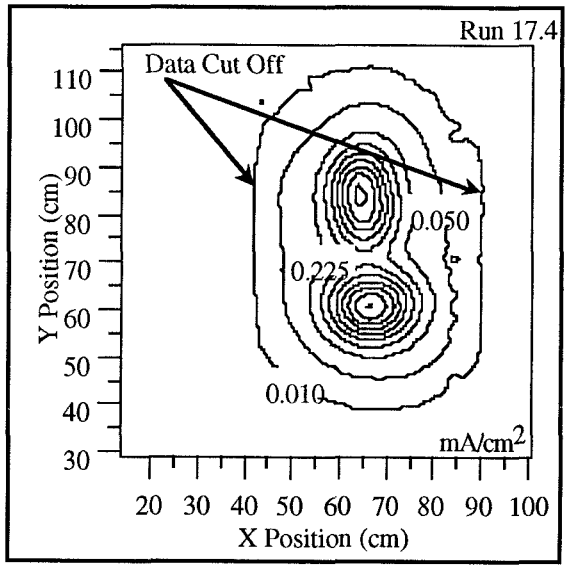

Inappropriately Selected Data Sampling Area
Figure 4.1-4

This problem was also noted in an earlier study [52] and the truncation of the data collection area was much more pronounced. This led to significant errors in some of the integrated beam current calculations. The truncations noted in this study are not expected to cause significant errors in future analyses, however, due to some of the data collection areas being thin along the X axis, there may be difficulties in determining the beam divergence angles. Calculation of the beam divergence angle requires the data collection area to have roughly equal dimensions in the X and Y directions.

Each axis of the probe positioning system was initialized prior to each data collection run by placing the probe carriage at the origin. This origin was defined as a position within the limit switch boundaries where the traverse was located 0.635 cm from the Z-West, X-North, and Y-down limit switch triggering positions. This positioning was accomplished by backing each axis traverse carriage, one at a time, into the limit switches. This would disconnect the power supply from the stepper motors. Then, with the use of the limit switch manual override, each axis was moved 0.635 cm away from the triggering position. The Y axis initialization was performed last

because if either the X or Z axis were done after the Y axis, the Y axis carriage could fall due to the force of gravity while the stepper motor power supply was disconnected. Repeatability of this process was estimated to be within 0.1 cm for initialization of each axis.

It was necessary to devise a method for traverse motion that would move the probe rake in such a manner to collect data with both 2.54 cm and 1.27 cm spacing between measurements in spite of the 5.08 cm probe spacing on the rake. A motion scheme to compensate for high thruster recycle rate also had to be developed. Motion of the probe positioning system was designed so that the probe rake would pass through the ion beam and then retrace its previous steps and recollect data. If a recycle were to occur, at least one good set of data would be collected at each given probe position since it was rare that a recycle would occur with probes at the repeated positions. However, in order to reduce the total data collection time and minimize the amount of time the traverse spent in the primary portion of the ion beam(s), the motion did not retrace probe positions that were at the very high or very low Y positions. This was done because the data collected at these positions was not expected to contain significant current levels. There were operational settings in which the thruster would run with minimal recycling. In these cases the traverse was operated such that the probes would not retrace their previous steps. There were instances, however, in which recycles did occur and the runs were repeated in their entirety.

4.1.3 Faraday Probe Data Acquisition System Operation

The raw data required to accomplish the task of developing ion beam current density maps included: probe identification number showing which probe acquired the data; location of each probe with respect to the predefined origin; the voltage drop measured across each probe resistor; a time and date stamp for each set of data; and the temperature of each stepper motor. Along with these measured parameters it was also necessary to input to the computer the appropriate resistor values. Once voltages from each probe were acquired, the resistances could then be used to determine the ion current collected. Each probe was sampled 100 times at each location for each pass of the probe rake. This allowed the computer to calculate the mean and standard deviation

of the current collected by each probe. The standard deviation was used to estimate the uncertainty associated with each probe measurement.

Several different resistor values were needed throughout the investigation due to large variations in the expected current collected by the Faraday probes for each downstream position, operating condition of the thruster, and combination of active ion sources. The resistor set used for a given data acquisition run was chosen so that the maximum voltage drop across the resistors was on the order of 45 mV. Voltage conversion module saturation occurred at 50 mV. Table A-1, in appendix A, gives the impedance values for each resistor set and table A-2, column 'R Set', identifies which resistor set was used for each run.

Recording the probe identification number and time and date stamp for each set of data was done in case of data analysis problems that may have arisen. The time and date stamp allowed for coordination with the archived thruster operational data, which also carried a time and date stamp. Knowing which probe was used to collect a particular set of data allowed for performance comparison between probes and thus help identify faulty probes.

The Macintosh computer, through the use of LabView software, sampled the voltage drop across each probe resistor beginning with probe 0 and ending with probe 23. The 100 samples from each probe channel were placed in a 1x100 array. Mean and standard deviation statistics were calculated from each of these 24 arrays. In order to compensate for the offset discussed in section 3.5.1 it was necessary to subtract this value from the statistical mean voltage value prior to calculating the respective current. The standard deviation values were converted from units of voltage to units of current and did not require offset adjustment.

Positions of the individual probes were determined by assigning probe 0 to the location (0,0,0) when the traverse mechanism was positioned at the origin. From there, the computer calculated the positions of the remaining probes knowing that the probe centers were separated by 5.08 cm and all probes were mounted in a vertical fashion. The location of the traverse was

known throughout the data acquisition by counting the incremental TTL pulses, and therefore the resulting steps taken by the traverse. It was then possible to calculate the location of each probe.

The temperature of the stepper motors was saved so that in case of motor failure during the investigation it would be possible to determine if lack of convective cooling was the cause. The most probable failure mechanism of the probe positioning system was melting of the solder connections within the stepper motors.

4.2 Charge State Ratio Determination Experimental Procedure

Determining the ratio of doubly to singly charged ions in the extracted ion beam was accomplished by placing an $\bar{E}x\bar{B}$ mass spectrometer downstream of the thruster and executing two separate sets of tests. The first experiment called for placing the $\bar{E}x\bar{B}$ probe along the centerline of an active ion source and collecting data at various thruster operational settings to establish the relationship between propellant utilization efficiency and the ratio of doubly to singly charged ions. The second involved holding the thruster operational settings fixed and collecting $\bar{E}x\bar{B}$ probe data along both the horizontal and vertical axes that pass through the centerline of an active ion source. The following describes the methodology followed to determine these ratios and profiles. When nominal beam current is referred to within the charge state portion of this investigation, it refers to the beam current that would be extracted from an ion source at an uncorrected propellant utilization efficiency (η_p) of 0.90 for a given propellant flow rate.

4.2.1 Segmented Ion Thruster Operation

For both the centerline charge state and radial charge state profile investigations, the ion optics were operated identically as for the R = 0.893 current density study. The voltage potentials applied to the grids were: V_S = 1250 V, V_D = -100 V, and V_A = -150 V. Grid potential values did have a slight tendency to drift during testing and required occasional adjustment. Manual adjustment of the thruster console controls assured that the actual biases to the grids were never

more than ±1 V different from these nominal values. All thruster operational data was stored on disk and hard copies were printed as well.

The first part of the charge state investigation examined the effects of changes in ion source propellant utilization efficiency on the centerline ratio of doubly to singly charged ions. The propellant utilization efficiency was dependent on thruster parameters such as propellant flow rate and discharge current. A total of five different operating conditions were evaluated and are described below and in table 4.2-1.

Charge State Thruster Operation

Operating Condition	Data Set	Nominal I_B (mA)	Nominal $\dot{m}_t$ (sccm)	Neutralizer LVK
1	5	430	6.66	Off
2	6	312	4.83	On
3	9	312	4.83	Off
4	7	470	7.27	On
5	8	470	7.27	Off

Table 4.2-1

Discharge chamber total propellant flow rates used for the centerline charge state investigation were set so that the amp equivalent flow rates were 111% of the nominal beam currents. This resulted in uncorrected propellant utilization efficiencies (η_p) of 0.90. The nominal beam currents used for centerline charge state determination were 312 mA, 430 mA, and 470 mA and these corresponded to total propellant flow rates of 347 mA_{eq}, 478 mA_{eq}, and 522 mA_{eq} which are respectively equal to 4.83 sccm, 6.66 sccm, and 7.27 sccm.

Once the flow rate was set at one of the values given above, the discharge current was stepped through a range such that the propellant utilization efficiency displayed by the thruster control console ranged from approximately 0.50 to over 1.00 where possible. During the period in which the $\bar{E}x\bar{B}$ probe deflector plate bias was ramped, the discharge current was monitored and adjusted via the thruster control console so that the value did not drift more than 1% from the

value recorded for the run. The values of discharge current and uncorrected propellant utilization efficiency for each run are given in tables A-3 and A-4 of appendix A. Tables A-3 also shows the neutralizer coupling voltage (V_{cn}) and neutralizer xenon mass flow rate ($\dot{m}_n$) values for all centerline $\vec{E}x\vec{B}$ probe data acquisition runs.

A profile of the charge state number ratio (R_n) as a function of radial position along the vertical and horizontal axes made up the second part of the investigation. This was done for a single operational setting of the thruster. The nominal beam current was 430 mA with a total propellant flow rate of 478 mA_{eq} (6.66 sccm) to produce an uncorrected propellant utilization efficiency of 0.90. LVK was set to 'Off' for all charge state radial profile data acquisition runs. Table A-4 gives a description of the operating condition for the operational system parameters for radial charge state mapping.

4.2.2 ExB Mass Spectrometer Operation

The $\vec{E}x\vec{B}$ mass spectrometer was aligned such that the centerline of the ion sources were parallel with the collimator of the probe and that the slits of the collimator and current collector were aligned with the Y axis. Operation of the $\vec{E}x\vec{B}$ probe involved stepping of the deflector plate bias voltage (V_d) through such a range that ion current signals (I_c)were registered for both singly (I^+) and doubly (I^{++}) charged ions. Stepping of the power supply voltage was enabled by a logic loop within the control software that would step the voltage up one volt for each step in the loop. Referring to section 3.3.2, in order to register a signal from the current collector it was necessary for the force ($\vec{F}_B$) on the moving ions by the fixed magnetic field ($\vec{B}$)to be equal and opposite to the force ($\vec{F}_E$) created by the variable electric field ($\vec{E}$). The electric field strength was dependent upon the bias applied to the probe deflector plates (V_d). Using ideal assumptions for performance of the probe, the equations found in section 3.3.2 can be utilized to calculate the deflector plate biases (V_d).that would allow the current to be collected (I_c) for singly (I^+) and doubly (I^{++}) charged ions. Once the deflector plate potential range for both single and double charged ions was calculated, the range would then be ramped by the computer controlled power

supply and collected current values would be obtained. As discussed in section 2.5, the existence of triply charged ions was assumed negligible. Effects of probe aperture misalignments and motion of the probe across the ion beam required modifications to the voltage stepping range.

4.2.3 Probe Positioning System Operation

Prior to the beginning of each use of the probe positioning system for data acquisition, the system was initialized so the starting position was always (0,0,0). Initialization of both the X and Z axes was performed in the same manner as for the Faraday probe positioning system initialization as previously described. In preliminary trials the starting position of the probe along the Y axis did not vary more that about 0.1 cm.

Distance along the Y axis between the origin and the centerline of the segment A was measured to be approximately 60.96 cm by using the top edge of the X axis support plate for a reference. The vertical distance between this same reference and the centerline of the $\bar{E}x\bar{B}$ probe collimator at the Y axis initialization position was measured to be 43.82 cm. Thus the probe had to be raised 17.14 cm in order to align the centerlines of the thruster and the collimator. From the X = 0 position, the horizontal distance between the thruster and probe collimator centerlines was measured to be 45.72 cm. These distances were verified visually. The best estimated error for these probe travel distances would be approximately $\pm$0.635 cm.

For the centerline charge state measurements the probe positioning system began at (0,0,0) and then positioned the $\bar{E}x\bar{B}$ probe at (45.72 cm, 17.14 cm, 30.48 cm). Once at this location the probe was not moved until conclusion of testing for that session. At the conclusion of a testing session the traverse mechanism was moved back to (0,0,0). In order to prevent gravitational force from moving the probe during testing the stepper motors were energized at all times.

The same steps just described were also followed for the charge state radial profile measurements. The $\bar{E}x\bar{B}$ probe initially moved from (0,0,0) to (45.72 cm, 17.14 cm, 30.48 cm) and this position was then declared the 'new' origin. All subsequent motion of the probe was measured with respect to this new origin. The probe was then moved in the horizontal direction,

stopping every 0.635 cm to acquire data. The limits of this travel were defined as the positions at which no singly or doubly charged ion current signals could be detected. Typically this was just outside the active grid area. This same procedure was conducted for the probe traveling from the 'new' origin in the vertical direction.

4.2.4 **ExB** Probe Data Acquisition System Operation

In the centerline investigation two items of data were collected. These consisted of the measured current collected (I_c) by the $\vec{E}x\vec{B}$ probe and the total bias applied to the deflector plates (V_d) by the computer controlled power supply. An additional piece of data pertaining to the position of the $\vec{E}x\vec{B}$ probe was required in order to develop the charge state radial profiles for the operating segment.

The same Macintosh computer that was used to control the $\vec{E}x\vec{B}$ probe deflector plate power supply was also used to control the Keithly electrometer which was used to measure the collected current. Each time the bias was stepped the electrometer sampled the resulting current collected by the probe. Only one sample of the collector current was possible due to the slowness of the digital GPIB system and therefore no statistical information was obtained regarding the performance of the system.

Chapter 5 Data Reduction

Manipulation of data from both the Faraday and $\bar{E}x\bar{B}$ probes, as well as thruster operational data was performed in order to more easily extract useful information needed to address the key issues related to plume characterization of the segmented ion thruster. Manipulations of this data is described in the following sections and typical results are identified. Results particular to this investigation are presented in chapter 6.

5.1 Faraday Probe Data Reduction and Adjustment

Several manipulations to the Faraday probe data were required in order to transform the data into such a form that it could easily be interpreted and presented. These manipulations included: thruster recycle data removal, matrix formation of data, beam current bias removal, secondary electron emission adjustment, metric conversion of data, conversion of probe collector current data to current density data, construction of superimposed multiple ion source operation data and interpolation of data to create data sets with 0.635 cm spacing between probe centers.

5.1.1 Thruster Recycle Event Data Removal

The first step in manipulating the Faraday probe data involved the removal of data collected during thruster recycle events. During a recycle the high voltages applied to the ion accelerator system of each operating segment were effectively deactivated, resulting in zero beam current. The occurrence of thruster recycle events during data acquisition are evident in the data as shown in the comparisons of figures 5.1-1 and 5.1-2. Figure 5.1-1 displays the current density contour plot of a run which contains data obtained during a thruster recycle and figure 5.1-2 shows the same data set with the recycle affected data removed.

The probe positioning and data acquisition systems were nominally operated such that multiple data sets were acquired from each probe location. This allowed for the removal of recycle affected data while still having data for the probe locations from where data was removed. Removal of recycle data required visual inspection of collected current contour plots. If recycle effects were evident within a contour plot, then a manual process was executed that involved

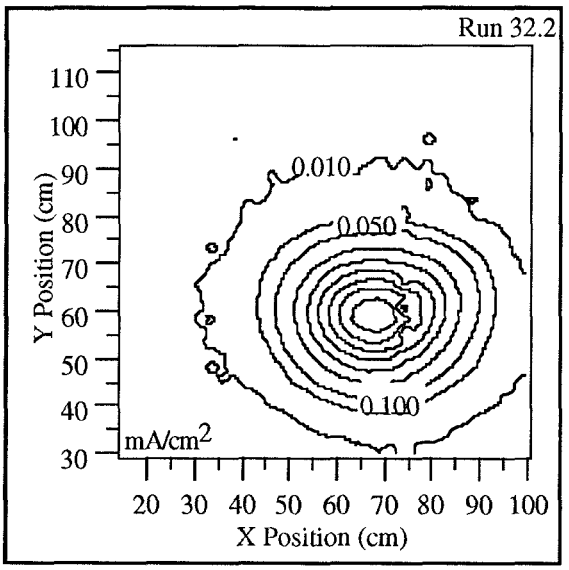

Current Density Plot with Recycle Data
Figure 5.1-1

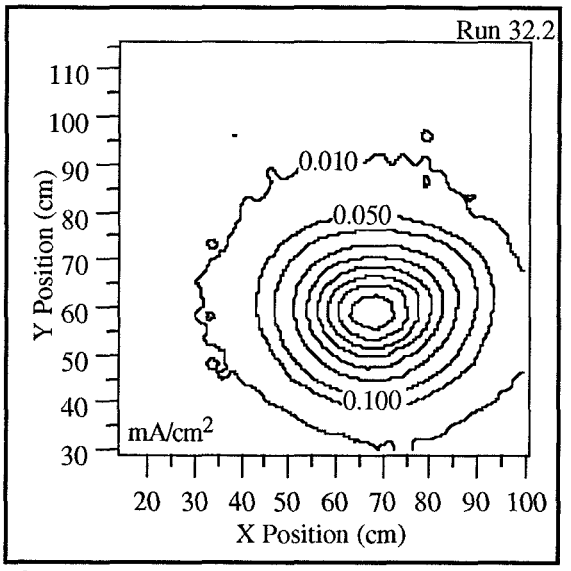

Current Density Plot After Recycle Data Removal
Figure 5.1-2

identifying the probe positioning system location during the recycle event and deleting that data from the stored data files. The contour plot was then regenerated with the new data set and inspected to verify that the correct data was removed. Recycle affected data was removed from a total of 25 of 104 Faraday probe data collection runs and are listed in table 5.1-1. The first row in the table displays the nominal beam current and R ratio for the runs during which thruster recycles occurred.

Current density contour plots generated with "after recycle event removal" data are similar in shape to current density contour plots that did not require the adjustment. The integrated values of total beam current for runs in which recycle data was removed did not show any irregular deviation from the calculated values as compared to the data runs that did not require recycle event data removal. This shows the procedures used for removal of recycle affected data were adequate in meeting the objectives for data quality.

Faraday Probe Data Acquisition Runs With Thruster Recycles

430 mA - R = 0.893	312 mA - R = 0.893	500 mA - R = 0.893	430 mA - R = 0.643
16.1	24.2	32.2	41.0
16.2	25.1	32.4	41.1
18.2	25.2	33.0	41.2
18.4		33.3	43.1
19.1		33.4	44.1
		35.2	
		37.1	
		38.2	
		48.0	
		48.1	
		48.3	
		49.0	

Table 5.1-1

5.1.2 Matrix Formation of Data

Most of the analyses performed and graphical representations generated with the Faraday probe data required the data in a matrix form with the X and Y probe coordinates as the indices of the matrix. Due to the large quantity of data obtained for each run and the number of runs performed, an automated procedure for conversion of the column formatted data was implemented. In addition, problems arising from removal of recycle affected data and multiple data values for a single probe location had to be reduced to a single data value for each position within the matrix. This was accomplished through the use of a commercial software package called Spyglass Transform 3.01 [58]. Although only one run could be transformed to matrix format at a time, this was much more time efficient than programming a specific application in order to achieve the desired results. A spyglass interpolation function was used to fill in positions where data affected by recycles was removed. An exponential interpolation function was used and preliminary tests showed that no significant deviations from the original data occured. Trial

runs were performed to assess the performance of this interpolation scheme and a range value of 5 was chosen. In order to accommodate instances where more than one data value existed for a single probe position, Spyglass was used to simply average the available values. This procedure for creating matrix files was applied to both probe collected current and standard deviation data.

5.1.3 Beam Current Bias Removal

During performance of the Faraday probe data acquisition it was noticed that when the probes were as far out of the beam as possible (such as behind the thruster) a positive ion current value was registered by the system. Unfortunately, at the time this was overlooked and not studied further. Later however, during initial analyses of the Faraday probe current data it was noticed that the integrated total beam currents were higher than the values expected. These two facts would suggest that some type of bias was being introduced to the system.

Two possible causes for the existence of this bias were identified. The first was that the background pressure within the test facility was partially made up of xenon charge exchange ions. With the Faraday probes being biased at -30 V, ions from this background plasma can be collected and registered as a current. The other alternative was the possibility of thruster operation introducing noise to the data acquisition system through the probe wiring. Significant effort was made during the design and assembly of the probe positioning and data acquisition systems to guard against this but the possibility could not be discounted. The bias values seemed to increase with increasing beam current, thus giving more credibility to the system noise effect. However, the bias values also tended to increase with greater xenon mass flow rates, such as for the operation of multiple ion sources, and the increased propellant flow rate associated with higher beam currents. The increased propellant flow rates, which cause greater vacuum chamber pressure and greater charge exchange, lends credibility to the background ion effect.

To determine the bias value for each thruster operational configuration, the average of the column of matrix data located at a position as far from the active ion sources in a horizontal direction as possible was calculated. The average of this column of data, as opposed to a row of

data, was chosen because the column method would use data from all probes, not just a single probe. The bias calculation was only done using the plane of data at the closest downstream position to the thruster for each thruster operational configuration. This was done in order to filter out those ions simply traveling at high divergence angles that would be collected if the data plane were located further downstream. Occasions arose when the data for the different downstream locations could not be collected on the same day for a given thruster configuration. Bias values calculated for the first day of data collection may not have been appropriate for data collected on the other days due to slight differences in thruster, vacuum chamber and data acquisition system operation. This resulted in the need to calculate more than one bias value for a single thruster operational configuration. No bias adjustment was necessary for the standard deviation data.

The biases used were generally no more than 1% of the maximum current collected for each of the data acquisition planes. Table A-2 of appendix A gives the bias values used for each data collection run. One favorable verification of this procedure was the calculation of integrated total beam currents that agreed well with theory for cases in which R = 0.893.

5.1.4 Secondary Electron Emission Adjustment

After the biases described in section 5.1.3 were subtracted from the probe current values, the secondary electron emission coefficient (SEEC) was applied to the result as shown in equation 5.1-1.

$$\text{Eq. 5.1-1} \qquad I_{actual} = (1 - SEEC) \times (I_i - I_{bias})$$

where SEEC = 0.005. This adjustment was applied to every Faraday probe current value found in the data matrix.

5.1.5 Metric Conversion of Data

Probe locations in the data files were specified in inches since motion of the ball screws were specified by the manufacturer in English units. For presentation, all the position values were converted from inches to centimeters.

5.1.6 Conversion to Current Density Data

Current density distribution of the ion beam is an important characteristic of the ion beams extracted from the thruster. The Faraday probes placed downstream of the thruster measured the total ion flux passing through the effective area of the collector. Current density was calculated by dividing the measured current by the effective area of the probe collector. This effective area, was dependent upon the angle at which the ions were traveling as shown in figure 5.1-3 and can be determined from

Eq. 5.1-2 $$A_e = A_a \cos\theta,$$

where the current density is

Eq. 5.1-3 $$J_i = \frac{I_i}{A_e}.$$

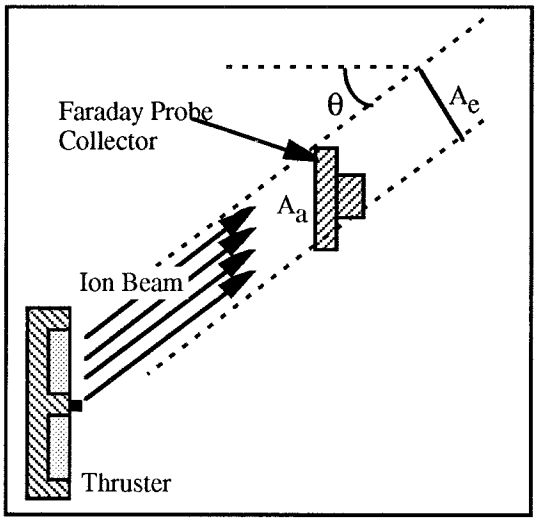

Faraday Probe Effective Area
Figure 5.1-3

Determination of this effective area is not necessarily a straightforward process. The difficulty lies in determining the appropriate angle to use in equation 5.1-2. If only a single ion source was operating, the angle, θ, depicted in figure 2.6-1 could be assumed appropriate. This would only be an assumption because it would have to be assumed that the ion trajectories, within one discharge chamber radius of the centerline, travel in a direction parallel to the centerline while those ions outside this radius travel in the direction specified by the beam divergence angle (α). In the cases where multiple ion sources were operated it became difficult to distinguish the appropriate angle (α) to use because of the uncertainty in which source generated the collected ions.

An effective area of 4.104 cm^2 was assumed for each probe at all radial and downstream locations. Beam divergence analyses determined the divergence angles ranged from approximately 10° to a maximum of 20° (see Chapter 7). Even with use of the maximum divergence angle, the effective area of the probe was about 94% of the probe's total planar area. This meant that out in the fringes of the ion beam the error in calculating the current density would have had a maximum of about 6%. Impacts to the current density contour plots were expected to be minimal because the currents collected by the probes at these radial positions were substantially lower than the currents collected toward the center of the beam. However, those radial positions covered a much greater area, and in order to compensate an assumed uncertainty of 2% was included in subsequent calculations. This procedure was used for both single and multiple ion source operation and facilitated direct comparison of the plume current density contour plots from the operation of multiple ion sources to those from the mathematical synthesis of multiple ion source operation as described in the next section.

5.1.7 Construction of Multiple Ion Source Current Density Data

Mathematical superposition of data obtained from individual ion source operation was computed in order to construct data sets that would have been obtained from the simultaneous

operation of multiple ion sources. This was done for all possible combinations of ion sources, each of the four operating conditions and at all downstream data acquisition locations. The single source current density data used was that which resulted after correction for recycle event affected data, bias subtraction, secondary electron emission, conversion to metric units and conversion to current density.

Each of the single source data matrices were adjusted in size so that they all had the same dimensions and origin. This allowed for simple matrix addition. The regions of the larger data matrix that did not contain real data were given the value of 0 mA/cm^2. This was assumed acceptable since those regions filled with zero values were located far out in the fringes of the beam where the current density was small and ideally should be approximately 0 mA/cm^2.

Once each single ion source matrix was developed, a constructed matrix was calculated by simply adding the data of the appropriate single source matrices together. For example, the synthesized operation of segments A and B at an R ratio of 0.893 and a thruster nominal beam current of 860 mA was generated by adding the current density matrix of segment A at R = 0.893, I_B = 430 mA to the current density matrix of segment B at R = 0.893, I_B = 430 mA. Figure 5.1-4 graphically depicts this process using current density contour plots, which are described in section 6.1.1.

5.1.8 Creation of Data with 0.635 cm Spacing

The scheme devised to determine the beam divergence angle for individually operating ion sources would produce better results with smaller spacing between data points. The data collected with the Faraday probes was fixed with 2.54 cm spacings between probe locations except for a few cases where the spacings were 1.27 cm. Creation of data with a smaller spacing between these data points would be beneficial so long as an interpolation method could be found that would retain the fidelity of the original data. Since Spyglass Transform seemed to work well to fill in for data removed due to recycles, it was suggested that Spyglass may also perform well for this application. As for the earlier insertion of data, the exponential interpolation method with

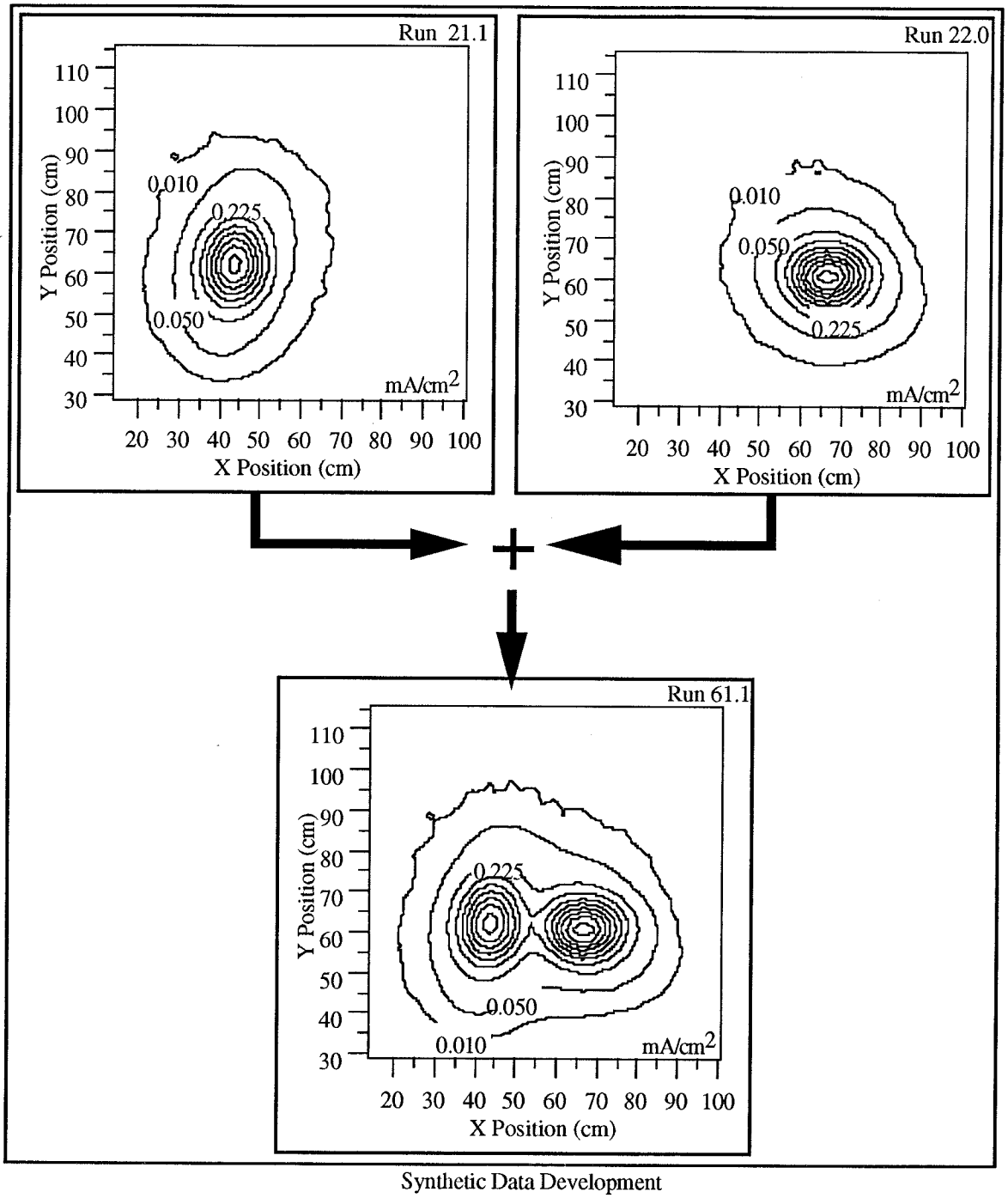

Synthetic Data Development
Figure 5.1-4

a range of 5 was selected. The desire for minimum spacing between data points had to be balanced with other criteria such as, keeping the data file small due to limited disk space and RAM storage of the computer, and retaining the fidelity of the data. After a few trial runs and comparisons, spacings of 0.635 cm were found to provide the best balance.

5.2 ExB Probe Data Manipulation and Alteration

Two types of modifications of the raw $\bar{E}x\bar{B}$ charge state data were required before the data could be used for the analyses explained in section 6.2. The raw data format was of the form shown in figure 5.2-1, where the Y axis of the plot corresponds to the current collected (I_c) by the $\bar{E}x\bar{B}$ probe and measured by the Keithly Electrometer. The X axis displays the total deflector plate bias (V_d) generated by the HP power supply. As can be seen in this figure, the flat portion of the data line lies below the zero value of the collected ion current. This implies that the system was reading a negative current. In order to correct this, a bias was added to the data so that the flat portion of the profile would lie at zero amps. Figures 5.2-1 is an $\bar{E}x\bar{B}$ collected current raw data profile without bias adjustment and figure 5.2-2 shows the same profile after the bias had been added.

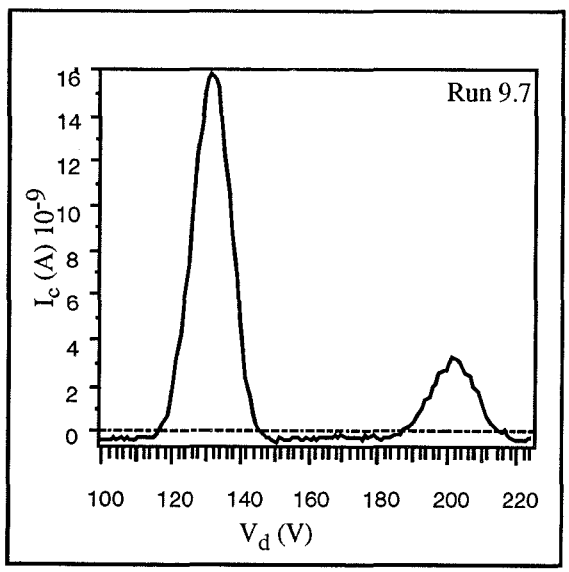

Sample ExB Charge State Raw Data Profile
Figure 5.2-1

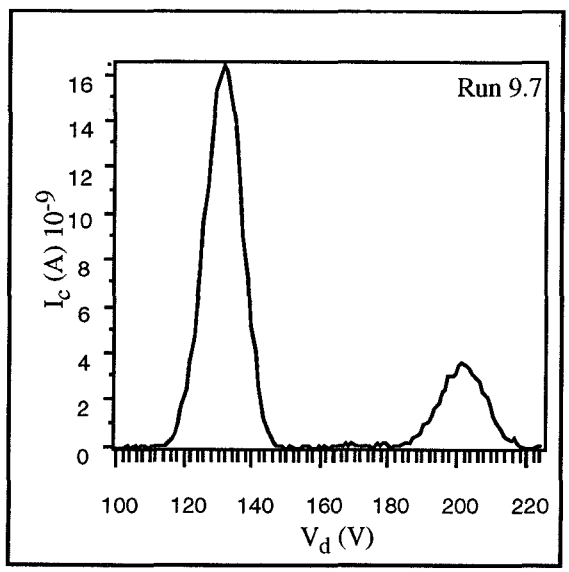

Sample ExB Charge State Data with Bias Removed
Figure 5.2-2

Two possible causes for this negative current have been identified. The first was that electrons emitted from the neutralizer were capable of contacting the probe collector due to their high mobility. This registering of an electron current would result in a negative value since the system registered a positive current with ion collection. A second possible source involved the possibility that the probe data lines, both inside and outside of the vacuum chamber, were not sufficiently shielded and a bias due to system noise was the cause of the negative value. It is believed at this time that either cause was likely since the Faraday probe studies also suggested both were possible. In addition, during the current density studies the Faraday probes were biased 30 volts negative of ground potential in order to repel free electrons. Due to integration difficulties with the electrometer and the $\bar{E}x\bar{B}$ probe, addition of the negative bias to the collector was omitted.

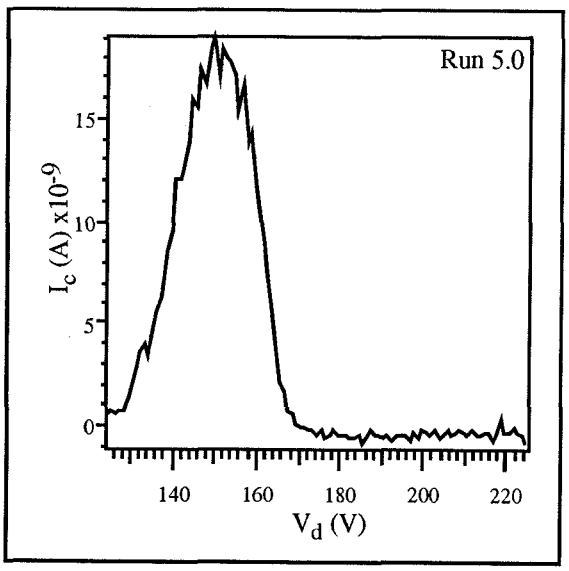

Sample ExB Charge State Data Profile
Before Data Smoothing
Figure 5.2-3

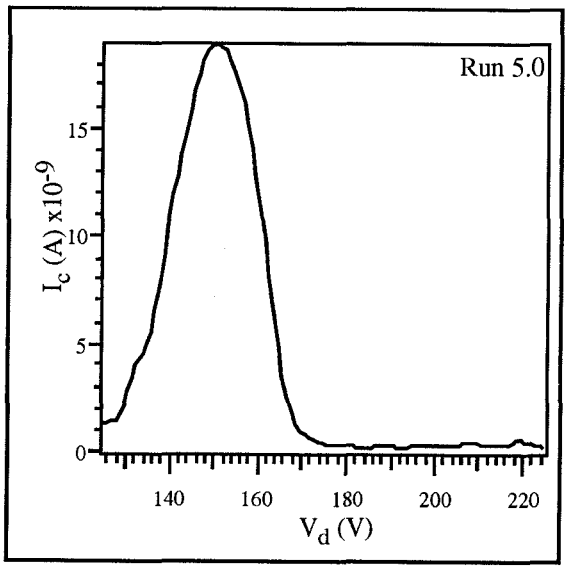

Sample ExB Charge State Data Profile
After Data Smoothing
Figure 5.2-4

The second modification required was to smooth the singly and doubly charged ion current peaks. With ragged curves it was difficult to determine the peak current values. Using Igor Pro [56], another commercial data analysis software package, a smoothing function was applied to the

data. A total of three smoothing passes were applied to each data set. Figures 5.2-3 and 5.2-4 demonstrate the before and after effects of the applying data smoothing algorithm.

5.3 Thruster Operational Data Conversion

Two modifications to the propellant flow rates were required for the charge state investigation. All propellant flow rates recorded by the thruster control console had units of sccm. It was useful to convert the propellant flow rates to units of mA_{eq} and mg/s for various aspects of the investigation. The second modification accounted for backflow of neutral xenon atoms into the discharge chambers due to background pressure within the vacuum facility.

5.3.1 Conversion of Propellant Flow Rate Units

Data regarding the mass flow rate of xenon through the discharge chambers as well as through ionization and neutralization cathodes, was saved in units of standard cubic centimeters per minute (sccm). Conversion of the data from sccm to units of mA_{eq} was required in order to determine the propellant utilization efficiency (η_p). In addition, it was necessary to calculate and convert the xenon gas backflow rate from mg/s to both sccm and mA_{eq}. The following gives the derivation for conversion between propellant flow rates with units of sccm, mg/s, and mA_{eq}:

Eq. 5.3-1 $$PV = nRT$$

Eq. 5.3-2 $$V = \frac{1}{P} nRT$$

At standard temperature (273 K) and pressure (1.01325×10^5 N/m^2) one mol of xenon has a volume of:

Eq. 5.3-3 $$V = \frac{1}{1.01325 \times 10^5 \ \frac{N}{m^2}} \times 1 \text{ mol} \times 8.3145 \ \frac{J}{molK} \times 273 \text{ K}$$

Eq. 5.3-4 $$V = 0.02240176 \ \frac{Jm^2}{N} = 0.02240176 \ m^3 = 22401.76 \ cm^3$$

Since there are 6.022×10^{23} atoms per mol and assuming every atom is singly ionized, then the total charge carried by one standard cubic centimeter of xenon is:

$$\text{Eq. 5.3-5} \qquad Cscc = 6.022 \times 10^{23} \text{ atoms} \times \frac{1}{22401.76 \text{ scc}} \times 1.602 \times 10^{-19} \frac{\text{coul}}{\text{atom}}$$

$$\text{Eq. 5.3-6} \qquad Cscc = 4.30646 \frac{\text{coul}}{\text{scc}}$$

Therefore, the amp equivalent flow rate for 1 sccm is:

$$\text{Eq 5.3-7} \qquad \dot{m}(A_{eq}) = 1 \frac{\text{scc}}{\text{min}} \times 4.30646 \frac{\text{coul}}{\text{scc}} \times \frac{1}{60} \frac{\text{min}}{\text{sec}}$$

$$\text{Eq. 5.3-8} \qquad \frac{\dot{m}(A_{eq})}{\dot{m}(\text{sccm})} = 0.071775$$

Since one mol of xenon has a mass of 131.33 g

$$\text{Eq. 5.3-9} \qquad \dot{m}(\text{mg/s}) = 1 \frac{\text{scc}}{\text{min}} \times \frac{131.33 \text{ g}}{22401.76 \text{ scc}} \times \frac{1000 \text{ mg}}{1 \text{ g}} \times \frac{1 \text{ min}}{60 \text{ sec}}$$

Therefore, the flow rate expressed in mg/s of one sccm is:

$$\text{Eq. 5.3-10} \qquad \frac{\dot{m}(\text{mg/s})}{\dot{m}(\text{sccm})} = 0.097708$$

and the conversion between flow rates expressed in amps equivalent and mg/s is:

$$\text{Eq. 5.3-11} \qquad \frac{\dot{m}(A_{eq})}{\dot{m}(\text{mg/s})} = \frac{\frac{\dot{m}(A_{eq})}{\dot{m}(\text{sccm})}}{\frac{\dot{m}(\text{mg/s})}{\dot{m}(\text{sccm})}} = \frac{0.071775}{0.097708} = 0.73459$$

5.3.2 Discharge Chamber Xenon Backflow Rate

Initial calculations of propellant utilization efficiency (η_p) produced values greater than 1.0, which is physically impossible. This was even true for some cases that corrected (η_{pc1}) for the presence of doubly charged ions within the beam. The most likely cause for the error was associated with the propellant flow rate specified by the thruster control electronics. The propellant flow rate must account for ingestion of xenon gas by the discharge chamber due to finite facility background pressure. This is a common correction as described by Sovey [37], and

is caused by free molecular flow of xenon gas from the test chamber into the ion engine through the holes in the accelerator system. Kinetic gas theory predicts that the flow rate into the discharge chamber would be:

$$\text{Eq. 5.3-12} \qquad \dot{m}_I = \frac{1}{4} n_b \overline{V}_a A_g \Phi_a m_i$$

where for each ion source A_g = 0.01767 m^2, Φ = 0.26, and m_i = 2.1808 x 10^{-25} kg. No correction for the Klausing conductance factor (K_C) [17] is included since this is a fine correction and the tank pressure is not known well enough to warrant this additional correction.

$$\text{Eq. 5.3-13} \qquad n_b = \frac{P}{kT}$$

$$\text{Eq. 5.3-14} \qquad \overline{V}_a = \sqrt{\frac{8kT}{\pi M_{xe}}}$$

and M_{xe} = 133.33 g/mol. Therefore the total mass flow rate into the discharge chamber is the measured value plus the mass flow rate associated with gas ingestion from the vacuum facility.

Chapter 6 Data Analyses

6.1 Faraday Probe Data Analyses

This section describes the analyses performed with collected Faraday probe data. Objectives of these analyses included characterization of extracted ion beams regarding downstream spatial development, consistency of the collected data with calculated values that account for charge exchange effects, comparison of superimposed single ion source operation data with data collected from actual multiple ion source operation, and ion beam divergence for the thruster at different operational conditions.

6.1.1 Current Density Contour Plots

The simplest graphical presentation of the Faraday probe data that could provide meaningful insight into the shape of the extracted ion beams was through two-dimensional current density contour plots. Using Spyglass Transform again, these contour plots could be made easily and quickly. Contour plots were constructed for each data run including those constructed with single ion source data to simulate multiple ion source operation. Figures 6.1-1 through 6.1-7 show examples of the beam shape for each segment and all combinations of multiply operating segments. These figures correspond to operation of segments A, B, C, AB, BC, AC, and ABC respectively. The data for these example plots was collected with a metered beam current of 430 mA from each ion source with an R ratio of 0.893 at a distance of 0.660 m from the thruster. A complete collection of all current density contour plots can be found in appendix B, organized by thruster operational configuration (i.e. I_B, R ratio, number of operating segments) and downstream location of the data acquisition plane.

The vertical axis of the contour plots represents the Y axis coordinates of the probe positioning system. Likewise, the horizontal axis represents the X axis coordinates. All dimensions are in units of centimeters. The contours depict lines of constant current density with units of mA/cm^2. Some of the contours are labeled. The step size between contours is equal to the magnitude of the maximum contour that is labeled. For example, in figure 6.1.2, the greatest labeled contour represents a current density of 0.150 mA/cm^2. The first contour within the 0.150

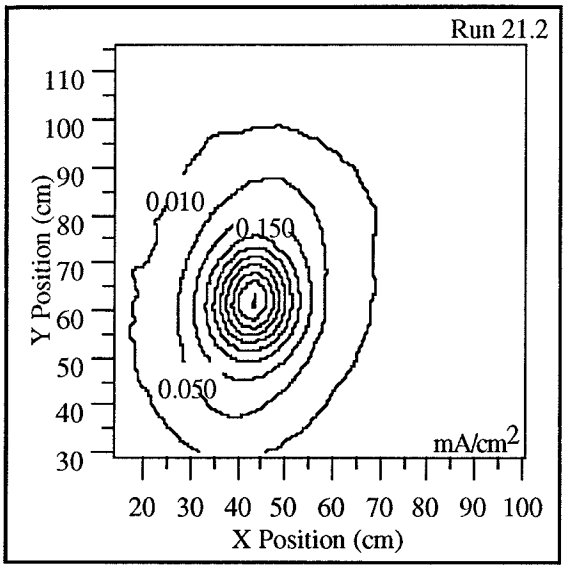

Example Current Density Contour Plot - Seg A
Figure 6.1-1

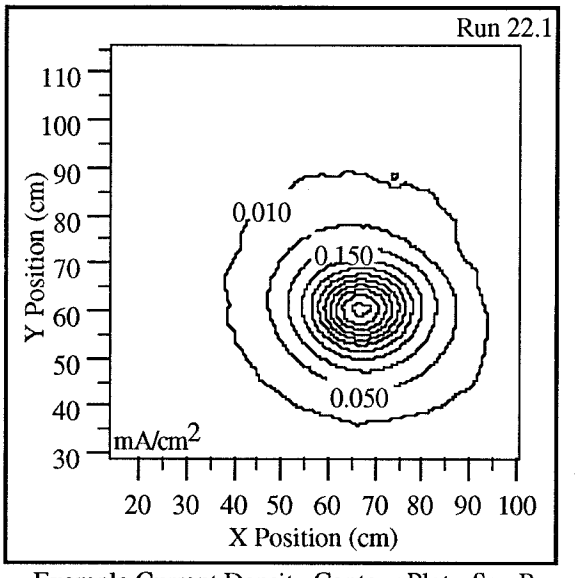

Example Current Density Contour Plot - Seg B
Figure 7.1-2

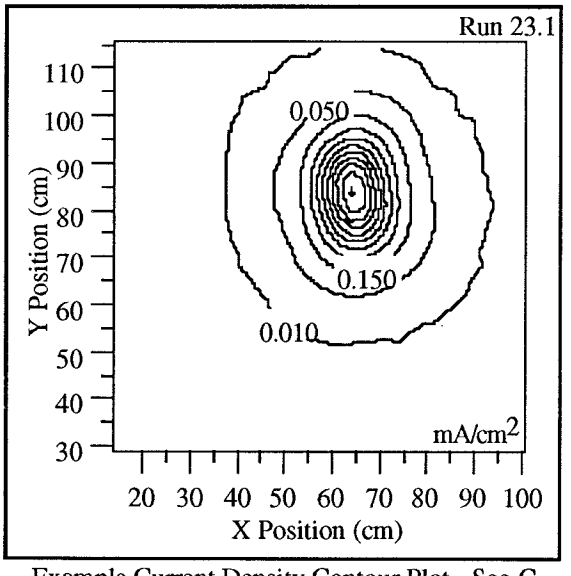

Example Current Density Contour Plot - Seg C
Figure 6.1-3

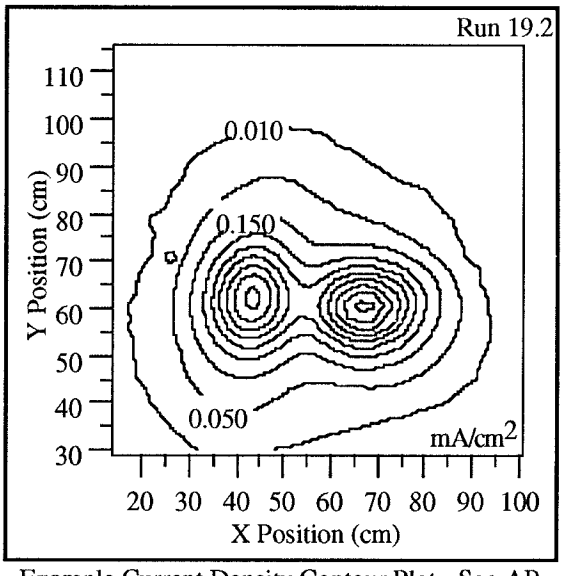

Example Current Density Contour Plot - Seg AB
Figure 6.1-4

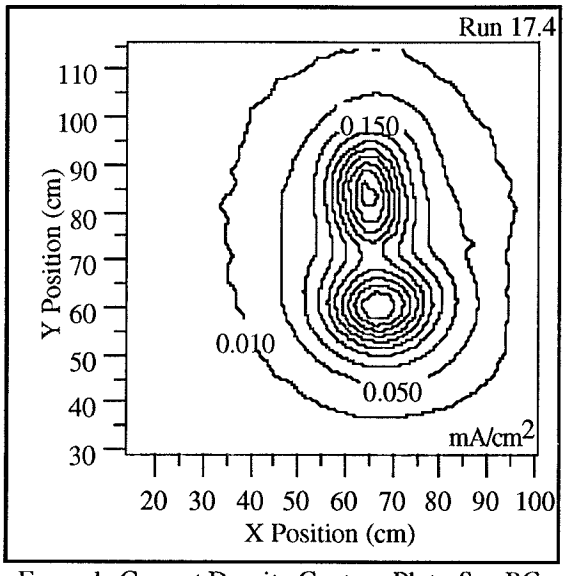

Example Current Density Contour Plot - Seg BC
Figure 6.1-5

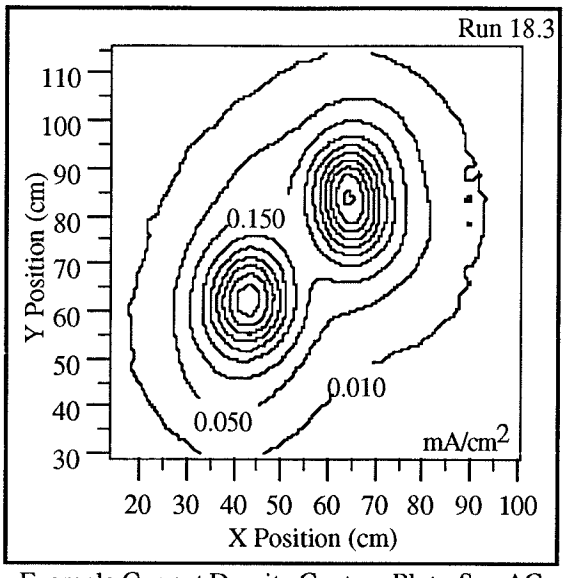

Example Current Density Contour Plot - Seg AC
Figure 6.1-6

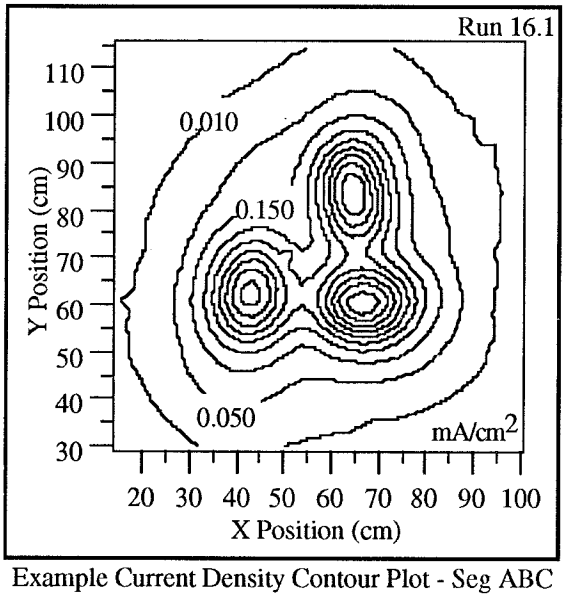

Example Current Density Contour Plot - Seg ABC
Figure 6.1-7

mA/cm^2 contour represents a current density of two times 0.150, or 0.300 mA/cm^2. The next contour represents 0.450 mA/cm^2 and so on.

The lowest current density represented in each of the plots corresponds to the outer most contour and is labeled 0.010 mA/cm^2. This value was chosen because it was the smallest value that would consistently, throughout most all downstream probe locations and thruster operating

conditions, produce an identifiable contour that would encompass the thruster centerline. Values smaller than this would often produce multiple contours that did not surround the center of the thruster.

6.1.2 Total Collected Beam Current Determination

Using Faraday probe data, the total extracted beam current was calculated through a numerical integration scheme involving a two-dimensional application of Simpson's Rule. This was done for all operating conditions of the thruster.

It was expected that the total integrated beam current values would be less than the metered beam current values due to facility background pressures and the resultant creation of charge exchange plasma. This charge exchange plasma effectively reduced the total measurable beam current at downstream locations. The calculated total beam current for each operating condition of the thruster was compared to the measured (integrated) value. This calculated vs. measured total beam current comparison was performed with both real data sets as well as the superimposed data sets.

The data used for beam profile integration was that which had been adjusted for removal of thruster recycle affected data, subtraction of background plasma bias and secondary electron emission, formatting of the data in a matrix fashion and conversion to current density. The two-dimensional Simpson's 1/3 rule integration scheme was applied in order to determine the total beam current. Application of Simpson's 1/3 rule was straightforward and relatively simple due to the equal spacing between all probe measurements within the matrix. The first step in this scheme involved the integration of each column of data within the matrix. The second step was to integrate all of the resulting column integrations. The numerical relations used for this integration were as follows:

$$\text{Eq. 6.1-1} \qquad I_B = \iint \frac{I_{x,y}}{A_a} dxdy = \iint J_{x,y} dxdy$$

Eq. 6.1-2 $$\Psi_x = \frac{h}{3}\sum(J_{x,1} + 2J_{x,2} + 4J_{x,3} + 2J_{x,4} \ldots + 2J_{x,n-3} + 4J_{x,n-2} + 2J_{x,n-1} + J_{x,n})$$

Eq. 6.1-3 $$I_B = \frac{h}{3}\sum(\Psi_1 + 2\Psi_2 + 4\Psi_3 + 2\Psi_4 \ldots + 2\Psi_{m-3} + 4\Psi_{m-2} + 2\Psi_{m-1} + \Psi_m)$$

where the number of data rows and columns are referred to as m and n respectively.

Reduction of total measurable beam current, due to creation of charge exchange ions, as a function of distance from the ion sources is described by equation 6.1-4.. System operating parameters that affected the calculated beam current include: metered beam current (I_B); facility background pressure (P); extracted ion velocity ($\vec{V}$); and axial distance between the ion extraction plane and measurement plane (Z). The expected downstream measurable beam current is given by the following equations:

Eq. 6.1-4 $$\frac{I_z}{I_B} = e^{(-n_b \sigma_{ce} Z)}$$

Eq. 6.1-5 $$n_b = \frac{P}{kT}$$

The charge exchange cross sections, σ_{ce}, used for these calculations are given by Smirnov and Chibisov [49] and reproduced in figure 6.1-8. The charge exchange cross section is given as a function of ion velocity. Using the energy balance described in section 3.3.2, ion velocity was calculated as a function of beam voltage, ion charge and propellant atomic mass.

Eq. 6.1-6 $$qV_B = \frac{1}{2} m_i \vec{V}^2$$

Eq. 6.1-7 $$\left|\vec{V}\right| = \sqrt{\frac{2qV_B}{m_i}} = \sqrt{\frac{2zeV_B}{m_i}}$$

Eq. 6.1-8 $$V_B = V_S - \left|V_N\right|$$

For an R ratio of 0.893, V_S = 1250 V and a singly charged ion, the calculated ion velocity is 4.20 x 10^6 cm/s, and according to figure 6.1-8, the resulting charge exchange cross section ranged from about 39 x 10^{-16} cm^2 to approximately 58 x 10^{-16} cm^2. Likewise, for the R ratio of 0.643,

V_S = 900 V the singly charged ion velocity is 3.64 x 10^6 cm/s with a charge exchange cross section of between 40 x 10^{-16} and 60 x 10^{-16} cm^2. Due to this large range of possible charge exchange cross section values, uncertainty arose regarding where in this range the appropriate values lie for this experiment. Randolf et al. [50] performed analyses similar to this in relation to

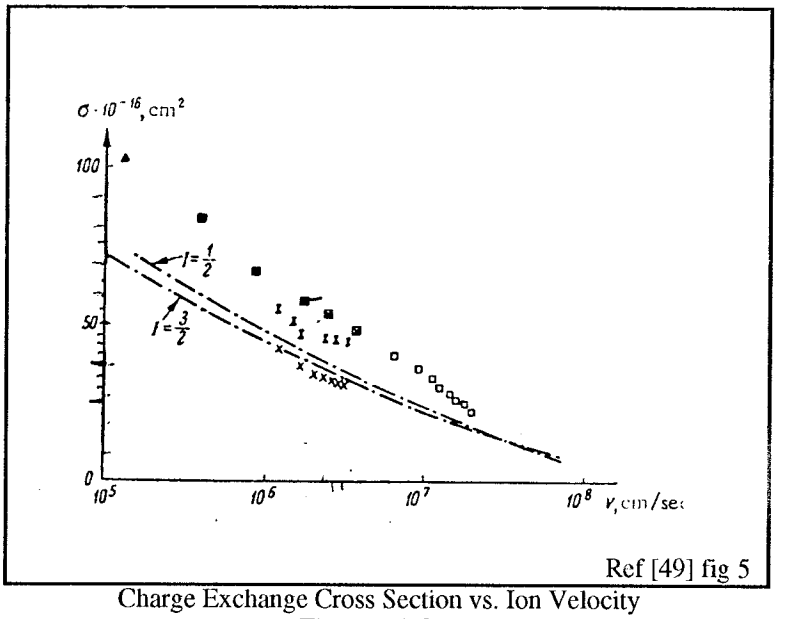

Ref [49] fig 5

Charge Exchange Cross Section vs. Ion Velocity
Figure 6.1-8

the charge exchange cross section of xenon ions and background xenon atoms. In their investigation the values toward the lower portion of the identified range were deemed appropriate for ion velocities similar in magnitude to those presented here. Because of uncertainty as to the appropriate values for this investigation, values toward the lower portion of the spread were chosen with uncertainties sufficiently large to cover most of the range. Charge exchange cross section values of 42x10^{-16} cm^2 were chosen for both the singly and doubly charged ions.

The number density, as shown in equation 6.1-5, is dependent upon the facility pressure (P), Boltzman's constant (k = 1.3807x10^{-23} J/K), and the facility temperature (T). Facility temperature was not measured during testing and will be assumed a constant 300K with an assumed maximum error of ±5 K. Facility pressure was also not measured during testing and will be estimated using a relationship between the pumping speed of the vacuum facility and the total

xenon flow rate into the facility through the thruster. This relationship was used by C. Garner [41] in order to characterize the facility for testing of several Russian Stationary Plasma Thrusters. In Garner's work, given flow rates and facility pressures read via an ionization gauge were used to calculate the effective pumping speed of the diffusion pumps. The relationship used by Garner is given in equation 6.1-9.

$$\text{Eq. 6.1-9} \qquad P = \frac{0.01267\dot{m}_f}{P.S.} + 7\times10^{-7}$$

According to the calculations performed by Garner, the pumping speed of the facility on xenon was approximately 16,000 L/s. In equation 6.1-9 the facility pressure (P) is specified in torr and will be converted to metric units for presentation. The total mass flow rate ($\dot{m}_f$) of xenon into the facility is specified in standard cubic centimeters per minute (sccm). The total thruster mass flow rates for all data acquisition runs are given in tables A-2, A-3, A-4 and A-5 of appendix A. In order to simulate the facility background pressures that would have been expected for the superimposed single ion source operation, the individual segment mass flow rates were averaged for the respective synthetic data sets with inclusion of the neutralizer mass flow rate as well as the discharge chamber flow rates. For example, the mass flow rate for segment A of run 21.0 (6.76 sccm) and that for segment B of run 22.4 (6.45 sccm) were averaged to determine the mass flow rate for segments A and B of synthetic run 60.1 (6.61 sccm). The respective neutralizer flow rates were 8.05 sccm and 8.00 sccm to produce a total superimposed flow rate of 14.63 sccm. Averaging of the propellant flow rate values was more appropriate than adding all of the flow rates together because each individual ion source experienced charge exchange effects generated by the operation of only a single ion source, not multiple. The propellant flow rate values for the synthetic data runs are given in table A-5.

6.1.3 Beam Divergence Determination

Initially in determination of the beam divergence angle (α), the 2-D Simpson's Rule integration routine was used to find the total integrated beam current for each single source run.

The next step was to determine the maximum possible radius for a given plane of Faraday probe data. This maximum radius was based on the physical area covered by the data plane and the assumed location of the ion source centerline intersection with the data plane. Since most of the data planes were rectangular with the longer dimension along the Y axis, the maximum radius was dependent upon the X dimension of the data plane. In order to determine the beam current that passed through this maximum radius circle, the radial distance from the centerline of each data point within the matrix was calculated to determine whether the point fell inside or outside of the circle. For those points outside of the circle, the data value was set to zero and those located within the circle were left alone. The beam current passing through the maximum circle was calculated using the same integration method as before, except now with some of the data points set to zero. If this maximum circle value was less than the 95% value of the total integrated current found in the first step, then the process was halted and an error declared. This error did occur for some cases, especially for those data planes located far downstream from the thruster. If the beam current that passed through the maximum radius was greater than the 95% total beam current, then the process continued. This processing then involved an iterative procedure of adjusting the radius of the circle, calculating the new value of beam current passing through, and readjusting the radius until the current passing through the circle was 95 $\pm$ 0.5% of the total measured current. This iterative process was automated through use of a numerical secant method applied with the assistance of Goodfellow of JPL [59]. The radius was then used, with the appropriate distance of the data plane from the thruster exit plane, to determine the divergence angle using a cosine relationship as shown in figure 2.6-1.

Choice of the centerline intersection position required review of the collected Faraday probe data. The location was chosen to be the matrix position in the adjusted data file which corresponded to the maximum current density value. These positions were found through visual inspection of the data and are given in table A-7. As seen in the table, the center positions seem to drift slightly and could have been a potential source of error.

6.1.4 Beam Flatness Parameter Determination

The beam flatness parameter (F) is defined as the ratio of average beam current density to the peak current density.

$$\text{Eq. 6.1-10} \qquad F = \frac{J_{avg}}{J_{max}}$$

This parameter was calculated for all single ion source operation cases using data obtained from the Faraday probes. The value for J_{max} was identified during the process of determining the intersection point of the centerline with the data acquisition plane. J_{avg} was calculated using equation 6.1-12, where I_α is the 95% current passing through the circle associated with the beam divergence angle with a radius of R_α. Calculated values for F are given in table A-8 of appendix A.

$$\text{Eq. 6.1-11} \qquad J_{avg} = \frac{I_\alpha}{\frac{1}{2}\pi R_\alpha^2}$$

6.2 Ion Beam Charge State Data Reduction and Analysis

This section describes the data reduction and analyses performed with the data obtained from the $\bar{E}x\bar{B}$ probe. The primary objective of these analyses was to develop a characterization of the ion beam charge state for the thruster at different operating conditions and probe radial locations.

6.2.1 ExB Raw Data Presentation

The first step in analyzing the charge state data was plotting the raw collected current data (I_C) obtained from the $\bar{E}x\bar{B}$ probe against the total bias of the probe deflector plates (V_d). This was accomplished through the use of the commercial plotting package, IGOR Pro 2.01. A sample of these plots is shown in figure 6.2-1. There were instances when a thruster recycle occurred while the data was being acquired. The important portion of the data is the region of the single and doubly charged ion current peaks. If the recycle occurred at places other than the peak locations, the data could still be used and these recycle events were ignored.

6.2.2 Centerline Charge State Data Profiles

The charge state current ratio was determined by dividing the doubly charged ion current (I^{++}) peak (right) values by the singly charged ion current (I^{+}) peak (left) values given in plots similar to figure 6.2-1. Equation 6.2-1 gives the mathematical expression for this calculation. Equation 6.2-2 gives the expression for the charge state number ratio (R_n), which is the charge state current ratio (R_c) divided by 2. The division by two is in order to account for a doubly charged ion registering twice the current as a singly charged ion when collected by the data acquisition system.

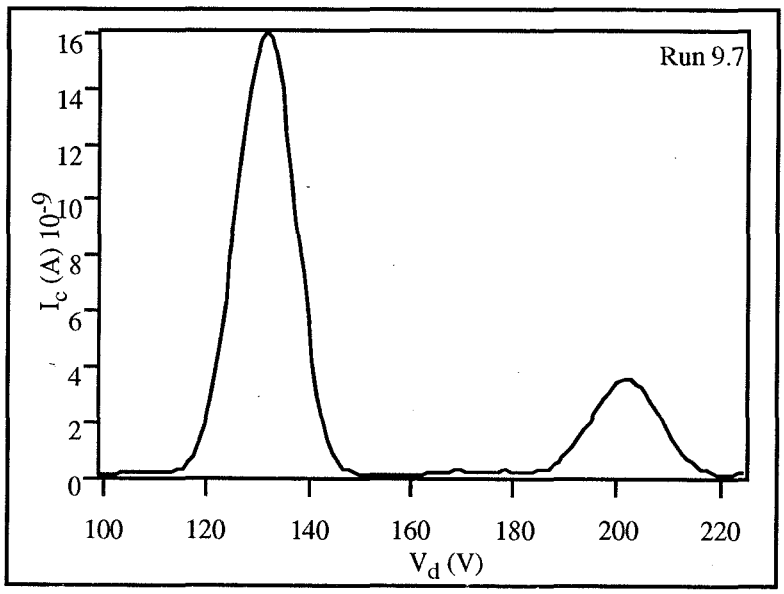

Sample ExB Charge State Data Profile
Figure 6.2-1

Eq. 6.2-1 $$R_c = \frac{I^{++}}{I^{+}}$$

Eq. 6.2-2 $$R_n = \frac{R_c}{2}$$

There were instances when a value for the peak of the doubly charged ion current could not be distinguished from the zero current signal. In these cases the doubly charged ion currents were declared to be zero.

The relations between the charge state number ratio (R_n) and the uncorrected propellant utilization efficiency (η_p) were plotted for each of the thruster operating conditions. An example of this is shown in figure 6.2-2.

The data used to generate figure 6.2-2 was not corrected for multiply charged ions or discharge chamber ingestion of xenon gas due to background facility pressures. Note that the value for η_p is greater than 1 and the error bars do not extend back over the unity line. Figure 6.2-3 used the same data set except this time it was corrected for multiply charged ions and background propellant ingestion. Note here that values for η_{pc2} are less than 1. The procedures for determining values for the error bars will be presented in section 6.3. The resulting values from these calculations are given in table A-9 of appendix A.

6.2.3 Radial Charge State Data Profiles

The same procedures to determine charge state current (R_c) and number (R_n) ratios described above were performed for each of the radial profile runs. Current peaks associated with the singly and doubly charged ions were recorded for each radial position and the charge state current ratios and charge state number ratios were calculated. These values are given in table A-10 of appendix A.

6.2.4 Ion Beam Charge State Thrust Correction Factors

The ion beam charge state thrust correction factor, calculated with equation 2.5-12, was determined for each operational run specified in table A-9 of appendix A.

Eq. 2.5-12
$$f_c = \frac{T_{act}}{T_{calc}} = \frac{1 + \frac{1}{\sqrt{2}} \frac{I^{++}}{I^{+}}}{1 + \frac{I^{++}}{I^{+}}}$$

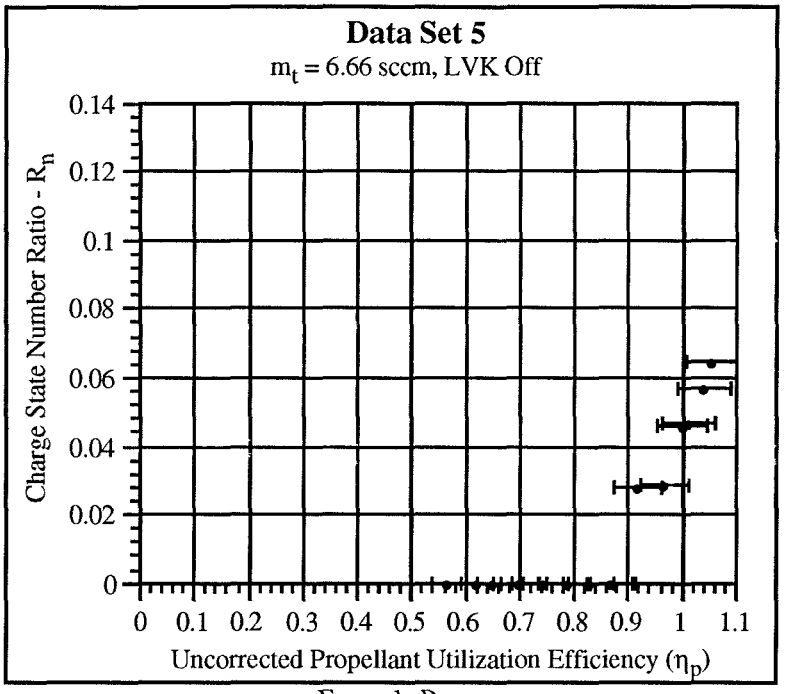

Example R_n vs.η_p
Figure 6.2-2

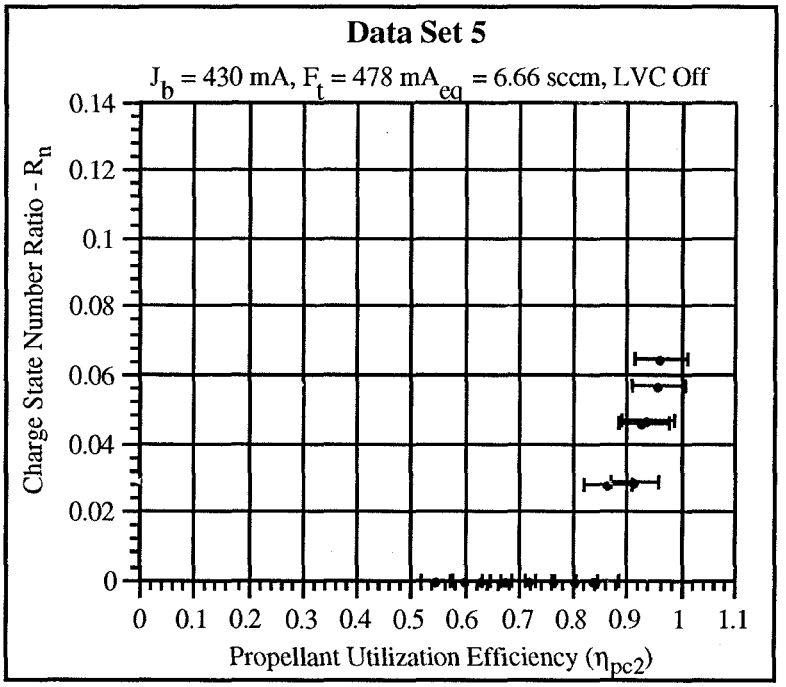

Example R_n vs. η_{pc2}
Figure 6.2-3

6.3 Faraday Probe Error Analyses and Propagation

Throughout this investigation several analyses of the collected data were performed. Some of these analyses were qualitative in nature, such as comparison of ion beam shapes from each ion source, while others were quantitative. These quantitative analyses use values that have some associated uncertainty. In order to understand the effects of the uncertainties an error propagation analysis was performed and is discussed below.

6.3.1 Integrated Beam Current Error Analysis and Propagation

Several sources of uncertainty to the integrated total beam current calculations were identified during this investigation. Some of these uncertainties were associated with operation of the thruster, some with the performance of the data acquisition system, and some that were associated with the procedures and calculation methods used. The total uncertainty associated with the measured beam current was calculated by adding the portions discussed below in quadrature as shown in the following equations:

Eq. 6.3-1
$$\varepsilon_{int} = \left(\frac{dI_z}{I_z}\right)_{int} = \sqrt{\varepsilon^2_{operation} + \varepsilon^2_{acquisition} + \varepsilon^2_{calculation}}$$

During operation of the segmented ion thruster, the metered beam currents values tended to drift slightly for the various data acquisition runs. In order to minimize this drifting, the operator continually monitored, and when necessary, manually adjusted the beam current for each ion source through control of the discharge chamber current. This was done so that the value never drifted by more than ±1% of the desired beam current. The uncertainty associated with thruster operation is expressed in the form:

Eq. 6.3-2
$$\varepsilon_{operation} = \left(\frac{dI_z}{I_z}\right)_{operation} \leq 1\%$$

Total uncertainty related to data acquisition was determined by adding in quadrature the portions associated with standard deviation, hardware voltage to current conversion and the area of the probes as shown in equation 6.3-3.

Eq. 6.3-3 $$\varepsilon_{\text{aquisition}} = \left(\frac{dI_z}{I_z}\right)_{\text{aquisition}} = \sqrt{\varepsilon_{\text{StdDev}}^2 + \varepsilon_{\text{hardware}}^2 + \varepsilon_{\text{probes}}^2}$$

Each time data was acquired from one of the Faraday probes a total of 100 samples were taken. The 100 samples were averaged and the standard deviation calculated by the data acquisition computer. Using the 2-D Simpson's Rule again, the standard deviation data collected was integrated to determine an intermediate value of the error associated with the total beam current as shown in the equations below.

Eq. 6.3-4 $$\sigma_B = \iint \frac{\sigma_{x,y}}{A_e} dxdy = \iint \gamma_{x,y} dxdy$$

Eq. 6.3-5 $$\lambda_x = \frac{h}{3}(\gamma_{x,1} + 2\gamma_{x,2} + 4\gamma_{x,3} + 2\gamma_{x,4} \ldots + 2\gamma_{x,n-3} + 4\gamma_{x,n-2} + 2\gamma_{x,n-1} + \gamma_{x,n})$$

Eq. 6.3-6 $$\sigma_B = \frac{h}{3}(\lambda_1 + 2\lambda_2 + 4\lambda_3 + 2\lambda_4 \ldots + 2\lambda_{m-3} + 4\lambda_{m-2} + 2\lambda_{m-1} + \lambda_m)$$

The uncertainty associated with the mean current value was the standard deviation of the mean, which is the standard deviation shown above, divided by the square root of the total number of data samples taken for each probe location.

Eq. 6.3-7 $$\varepsilon_{\text{StdDev}} = \left(\frac{dI_z}{I_z}\right)_{\text{StdDev}} = \frac{\sigma_B}{\sqrt{N}}$$

An additional uncertainty was introduced to the measurements from the data acquisition hardware, which includes the voltage conversion modules, backplanes, MIO interface card and associated resistors. Preliminary testing of the data acquisition system with a precision 1.000 mA current source revealed that the current values measured were within ±0.002 mA of the true value. Assuming that 1 mA is the average current collected by each of the Faraday probes during

data acquisition, the error associated with each measurement would be approximately ±0.20%. Another approach to evaluating the uncertainty associated with each measurement was to apply a partial differential analysis to Ohm's Law as given below:

Eq. 6.3-8 $$I_z = \frac{V_R}{R_R}$$

Eq. 6.3-9 $$dI_z = \left[\left(\frac{\partial I_z}{\partial V_R} dV_R\right)^2 + \left(\frac{\partial I_z}{\partial R_R} dR_R\right)^2\right]^{\frac{1}{2}}$$

Eq. 6.3-10 $$(dI_z)^2 = \left(\frac{1}{R_R} dV_R\right)^2 + \left(\frac{-V_R}{R_R^2} dR_R\right)^2$$

Eq. 6.3-11 $$\frac{(dI_z)^2}{(I_z)^2} = \left(\frac{dV_R}{V_R}\right)^2 + \left(\frac{dR_R}{R_R}\right)^2$$

Eq. 6.3-12 $$\varepsilon_{hardware} = \left(\frac{dI_z}{I_z}\right)_{hardware} = \left[\left(\frac{dV_R}{V_R}\right)^2 + \left(\frac{dR_R}{R_R}\right)^2\right]^{\frac{1}{2}}$$

$\frac{dV_R}{V_R}$ refers to the measurement uncertainty of the voltage drop across the resistor. The source of this uncertainty lies with the National Instrument voltage conversion modules, backplane, and analog interface card. Another source of error is associated with the discrepancy between the true impedance of the resistors and the values used by the data acquisition computer. The error is incorporated through the $\frac{dR_R}{R_R}$ term in equation 6.3-11. Estimated values for the $\frac{dV_R}{V_R}$ and $\frac{dR_R}{R_R}$ terms are 0.10% and 0.20% respectively.

Faraday probe area also introduced uncertainty to the determination of the voltage and resulting current signals. This uncertainty was calculated by applying a partial differential analysis to equation 6.3-13 . The nominal diameter of the Faraday probe current collectors were 2.286 ± 0.025 cm. Assuming $A_e = A_a$,

Eq. 6.3-13 $$I_z = J_z A_a$$

Eq. 6.3-14 $$(dI_z)^2 = \left(\frac{\partial I_z}{\partial J_z} dJ_z\right)^2 + \left(\frac{\partial I_z}{\partial A_a} dA_a\right)^2$$

Eq. 6.3-15 $$(dI_z)^2 = (A_a dJ_z)^2 + (J_z dA_a)^2$$

Eq. 6.3-16 $$\frac{dI_z}{I_z} = \left[\left(\frac{dJ_z}{J_z}\right)^2 + \left(\frac{dA_a}{A_a}\right)^2\right]^{\frac{1}{2}}$$

It is assumed that,

Eq. 6.3-17 $$\frac{dJ_z}{J_z} = 0$$

and it was assumed that due to differences between actual and effective probe area and uncertainty of 2% would be included.

Eq. 6.3-18 $$\varepsilon_{probe} = \frac{dI_z}{I_z} = \frac{dA_a}{A_a} \approx 2\%$$

Simpson's 1/3 Rule is only an estimate of the true integrated value of a given curve and is related to the size of the interval between integration points. According to theorem 5.36 of Swokowski [51], "If M is a positive real number such that $\left|f^{(4)}(x)\right| \le M$ for all x in [a,b], then the error involved in using Simpson's Rule is not greater than $M(b-a)^5/180n^4$." It is assumed that the current density distribution can be approximated with a normal probability density curve $f(x) = We^{\frac{-x^2}{2}}$ where W is some arbitrary constant. The fourth derivative of this function is $f^{(4)}(x) = x^4 We^{\frac{-x^2}{2}}$ and with the maximum value of x is about 30. This results in a value for M of 1 being sufficient. Assuming the values of a, b, and n to be 60, 0, and 60 respectively, the resulting error in the Simpson's Rule integration is on the order of 0.333. Since the integrated beam currents were calculated using a double application of Simpson's Rule the errors for each integration would be added in quadrature and result in a total error of approximately 0.471 mA. The resulting uncertainty is then this error divided by the nominal thruster operating beam current

which is significantly less than 1%. Because the order of this uncertainty is substantially less than the other contributing factors, this uncertainty is neglected in all future calculations.

6.3.2 Calculated Beam Current Error Analysis and Propagation

The calculated values for measured beam current at axial locations downstream of the thruster were dependent on metered beam current (I_B), charge exchange cross section (σ_{ce}), particle number density (n_b), and downstream location (z). Each of these parameters had an associated uncertainty. The following partial differential analysis, applied to equation 6.3-19, shows the methodology used to determine the total uncertainty in the theoretical beam current.

Eq. 6.3-19 $$Q = \frac{I_z}{I_B} = e^{(-\sigma_{ce} n_b z)}$$

Eq. 6.3-20 $$(dQ)^2 = \left(\frac{\partial Q}{\partial \sigma_{ce}} d\sigma_{ce}\right)^2 + \left(\frac{\partial Q}{\partial z} dz\right)^2 + \left(\frac{\partial Q}{\partial n_b} dn_b\right)^2$$

Eq. 6.3-21 $$(dQ)^2 = \left[(n_b z Q d\sigma_{ce})^2 + (\sigma_{ce} z Q dn_b)^2 + (\sigma_{ce} n_b Q dz)^2\right]$$

Eq. 6.3-22 $$(dQ)^2 = Q^2\left[(n_b z d\sigma_{ce})^2 + (\sigma_{ce} z dn_b)^2 + (\sigma_{ce} n_b dz)^2\right]$$

Eq. 6.3-23 $$(dQ)^2 = (\sigma_{ce} n_b z)^2 Q^2\left[\left(\frac{d\sigma_{ce}}{\sigma_{ce}}\right)^2 + \left(\frac{dn_b}{n_b}\right)^2 + \left(\frac{dz}{z}\right)^2\right]$$

Eq. 6.3-24 $$\frac{dQ}{Q} = \sigma_{ce} n_b z\left[\left(\frac{d\sigma_{ce}}{\sigma_{ce}}\right)^2 + \left(\frac{dn_b}{n_b}\right)^2 + \left(\frac{dz}{z}\right)^2\right]^{\frac{1}{2}}$$

Eq. 6.3-25 $$n_b = \frac{P}{kT} = P(kT)^{-1}$$

Eq. 6.3-26 $$(dn_b)^2 = \left(\frac{\partial n_b}{\partial P} dP\right)^2 + \left(\frac{\partial n_b}{\partial k} dk\right)^2 + \left(\frac{\partial n_b}{\partial T} dT\right)^2$$

but dk = 0, therefore,

Eq. 6.3-27 $$(dn_b)^2 = \left(\frac{1}{kT} dP\right)^2 + \left(\frac{-P}{kT^2} dT\right)^2$$

Eq. 6.3-28 $$(dn_b)^2 = (n_b)^2\left[\left(\frac{\frac{1}{kT}dP}{\frac{P}{kT}}\right)^2 + \left(\frac{\frac{P}{kT^2}dT}{\frac{P}{kT}}\right)^2\right]$$

Eq. 6.3-29 $$\left(\frac{dn_b}{n_b}\right) = \left[\left(\frac{dP}{P}\right)^2 + \left(\frac{dT}{T}\right)^2\right]^{\frac{1}{2}}$$

$\frac{dP}{P}$ is assumed to be ±50%, $\frac{dT}{T} \leq 1.7\%$, dz = 0.635 cm, and $\frac{d\sigma_{ce}}{\sigma_{ce}} = \pm 50\%$

Eq. 6.3-30 $$Q = \frac{I_z}{I_B}$$

Eq. 6.3-31 $$(dI_z)^2 = \left(\frac{\partial I_z}{\partial Q}dQ\right)^2 + \left(\frac{\partial I_z}{\partial I_B}dI_B\right)^2$$

Eq. 6.3-32 $$\varepsilon_{calc} = \left(\frac{dI_z}{I_z}\right)_{calc} = \left[\left(\frac{dQ}{Q}\right)^2 + \left(\frac{dI_B}{I_B}\right)^2\right]^{\frac{1}{2}}$$

6.3.3 Beam Divergence Error Analysis and Propagation

The uncertainty associated with ion beam divergence angle was evaluated using a partial differential analysis applied to equation 6.3-33 (see also figure 2.6-1).

Eq. 6.3-33 $$\alpha = \arctan\left(\frac{R_\alpha - R_t}{z}\right) = \arctan(X)$$

Eq. 6.3-34 $$(d\alpha)^2 = \left(\frac{\partial\alpha}{\partial R_\alpha}dR_\alpha\right)^2 + \left(\frac{\partial\alpha}{\partial R_t}dR_t\right)^2 + \left(\frac{\partial\alpha}{\partial z}dz\right)^2$$

Eq. 6.3-35 $$(d\alpha)^2 = \left(\frac{\partial\alpha}{\partial X}\frac{\partial X}{\partial R_\alpha}dR_\alpha\right)^2 + \left(\frac{\partial\alpha}{\partial X}\frac{\partial X}{\partial R_t}dR_t\right)^2 + \left(\frac{\partial\alpha}{\partial X}\frac{\partial X}{\partial z}dz\right)^2$$

Eq. 6.3-36 $$\frac{d\alpha}{dX} = \frac{1}{1+X^2}$$

and $dR_t = 0$,

Eq. 6.3-37 $$(d\alpha)^2 = \left(\frac{1}{1+X^2}\frac{1}{z}dR_\alpha\right)^2 + \left(\frac{1}{1+X^2}\left(-\frac{R_\alpha - R_t}{z^2}\right)dz\right)^2$$

Eq. 6.3-38 $$(d\alpha)^2 = \left(\frac{X^2}{1+X^2}\right)\left[\left(\frac{dR_\alpha}{R_\alpha - R_t}\right)^2 + \left(\frac{dz}{z}\right)^2\right]$$

Eq. 6.3-39 $$d\alpha = \left\{\left(\frac{X^2}{1+X^2}\right)\left[\left(\frac{dR_\alpha}{R_\alpha - R_t}\right)^2 + \left(\frac{dz}{z}\right)^2\right]\right\}^{\frac{1}{2}}$$

In order to determine the uncertainty associated with the ion beam divergence angle ($d\alpha$) an intermediate step was required, finding the errors associated with the radius of the 95% ion current circle and the downstream probe location. The error associated with the radius of the circle that contains 95% of the measured beam current was evaluated using a partial differential analysis as shown below.

Eq. 6.3-40 $$I_z = \int_{A_p} J_z dA$$

Eq. 6.3-41 $$I_z = J_z A_p$$

Eq. 6.3-42 $$I_z = J_z \frac{1}{2}\pi R_p^2$$

Eq. 6.3-43 $$I_\alpha = J_\alpha \frac{1}{2}\pi R_\alpha^2$$

Eq. 6.3-44 $$R_\alpha = \left(\frac{2I_\alpha}{\pi J_\alpha}\right)^{\frac{1}{2}} = \sqrt{\frac{2}{\pi}}\left(\frac{I_\alpha}{J_\alpha}\right)^{\frac{1}{2}}$$

J_α is assumed constant over the area of the 95% circle, which implies the assumption of a flat beam profile.

Eq. 6.3-45 $$(dR_\alpha)^2 = \left(\frac{\partial R_\alpha}{\partial I_\alpha} dI_\alpha\right)^2 + \left(\frac{\partial R_\alpha}{\partial J_\alpha} dJ_\alpha\right)^2$$

and since dJ_z is assumed zero,

Eq. 6.3-46 $$\frac{\partial R_\alpha}{\partial I_\alpha} = \frac{1}{2J_\alpha}\sqrt{\frac{2}{\pi}}\left(\frac{I_\alpha}{J_\alpha}\right)^{-\frac{1}{2}}$$

Eq. 6.3-47 $$\frac{\partial R_\alpha}{\partial I_\alpha} = \frac{1}{\sqrt{2\pi J_\alpha I_\alpha}}$$

Eq. 6.3-48 $$dR_\alpha = \left(\frac{1}{\sqrt{2\pi J_\alpha I_\alpha}} dI_\alpha \right)$$

Eq. 6.3-49 $$\frac{dR_\alpha}{R_\alpha - R_t} = \frac{1}{(R_\alpha - R_t)\sqrt{2\pi J_\alpha I_\alpha}} dI_\alpha$$

The error associated with the downstream location of the Faraday probes was previously evaluated in section 6.3.1.

Therefore,

Eq. 6.3-39 $$d\alpha = \left\{ \left(\frac{X^2}{1+X^2} \right) \left[\left(\frac{dR_\alpha}{R_\alpha - R_t} \right)^2 + \left(\frac{dz}{z} \right)^2 \right] \right\}^{\frac{1}{2}}$$

The resulting uncertainty in the calculated beam divergence angle is:

Eq. 6.3-50 $$\varepsilon_{\text{divergence}} = \frac{d\alpha}{\alpha} = \frac{\left\{ \left(\frac{X^2}{1+X^2} \right) \left[\left(\frac{dR_\alpha}{R_\alpha - R_t} \right)^2 + \left(\frac{dz}{z} \right)^2 \right] \right\}^{\frac{1}{2}}}{\arctan\left(\frac{R_\alpha - R_t}{z} \right)}$$

6.3.4 Beam Flatness Error Analysis

The uncertainty associated with beam flatness parameter was evaluated using a partial differential analysis applied to equation 6.3-51. Values for these calculations are given in table A-8 of appendix A.

Eq. 6.3-51 $$F = \frac{J_{avg}}{J_{max}}$$

Eq. 6.3-52 $$F = \frac{I_\alpha}{\pi R_\alpha^2 J_{max}}$$

Eq. 6.3-53 $$(dF)^2 = \left(\frac{\partial F}{\partial I_\alpha} dI_\alpha\right)^2 + \left(\frac{\partial F}{\partial R_\alpha} dR_\alpha\right)^2 + \left(\frac{\partial F}{\partial J_{max}} dJ_{max}\right)^2$$

Eq. 6.3-54 $$(dF)^2 = \left(\frac{1}{\pi R_\alpha^2 J_{max}} dI_\alpha\right)^2 \left(\frac{-2I_\alpha}{\pi R_\alpha^3 J_{max}} dR_\alpha\right)^2 + \left(\frac{-I_\alpha}{\pi R_\alpha^2 J_{max}^2} dJ_{max}\right)^2$$

Eq. 6.3-55 $$(dF)^2 = \left(F\frac{dI_\alpha}{I_\alpha}\right)^2 + \left(-2F\frac{dR_\alpha}{R_\alpha}\right)^2 + \left(-F\frac{dJ_{max}}{J_{max}}\right)^2$$

Eq. 6.3-56 $$\frac{dF}{F} = \left[\left(\frac{dI_\alpha}{I_\alpha}\right)^2 + 4\left(\frac{dR_\alpha}{R_\alpha}\right)^2 + \left(\frac{dJ_{max}}{J_{max}}\right)^2\right]^{\frac{1}{2}}$$

where, Eq. 6.3-57 $$\left(\frac{dI_\alpha}{I_\alpha}\right) = \left(\frac{dI_z}{I_z}\right)_{int}$$

and $\frac{dJ_{max}}{J_{max}}$ is assumed to be 3%.

6.4 ExB Mass Spectrometer Probe Error Analyses

The two primary parameters used to describe the discharge chamber centerline charge state characteristics consisted of charge state current ratio (R_c) and propellant utilization efficiency (η_p). Likewise, the important parameters for both the charge state radial profile investigations were probe position (x, y) along the X and Y axes and charge state number ratio (R_n).

Two mechanisms were identified that may introduce uncertainty into the measured charge state current ratios. The first was due to smoothing of the raw $\bar{E}x\bar{B}$ probe collected current vs. deflector plate potential profile with the use of IGOR Pro. The second shifting of the I_c vs. V_d in order to account for a bias that was causing the curve to fall below zero amps. A rough estimate of the total uncertainty in I^{++}/I^{+} is ±1%.

The absolute position of the $\bar{E}x\bar{B}$ probe with respect to the segment A discharge chamber centerline had an uncertainty of about 0.635 cm in both the X and Y directions. Motion of the probe, about the centerline, was known to at least ±25.4 μm should not have contributed any uncertainty to the data.

Propellant utilization efficiency is a parameter that calculated with the beam current produced by an ion source, the total propellant flow rate into the discharge chamber and the ratio of doubly to singly charged ions extracted in the beam. The total propellant flow rate must account for flow through the discharge cathode, main propellant flow into the discharge chamber for ionization, and backflow of propellant atoms from the vacuum facility due to background pressures. Equation 6.4-1 gives the relationship between these three parameters used to calculate the corrected propellant utilization efficiency.

Eq. 6.4-1 $$\eta_{pc2} = \frac{I_B}{\dot{m}_t + \dot{m}_i} \frac{1 + \frac{1}{2}\frac{I^{++}}{I^+}}{1 + \frac{I^{++}}{I^+}} = \eta_{pc3}\beta$$

The uncertainty associated with the calculation of corrected propellant utilization efficiency was evaluated through a partial differentiation analysis performed on equation 6.4-1.

Eq. 6.4-2 $$\eta_{pc2} = \frac{I_B}{\dot{m}_t + \dot{m}_t} \frac{1 + \frac{1}{2}\frac{I^{++}}{I^+}}{1 + \frac{I^{++}}{I^+}} = \frac{I_B}{\dot{M}_T}\beta = \eta_{pc3}\beta$$

Eq. 6.4-3 $$\left(d\eta_{pc2}\right)^2 = \left(\frac{\partial \eta_{pc2}}{\partial \eta_{pc3}} d\eta_{pc3}\right)^2 + \left(\frac{\partial \eta_{pc2}}{\partial \beta} d\beta\right)^2$$

Eq. 6.4-4 $$\left(d\eta_{pc2}\right)^2 = \left(\beta d\eta_{pc3}\right)^2 + \left(\eta_{pc3} d\beta\right)^2$$

Eq. 6.4-5 $$\frac{d\eta_{pc2}}{\eta_{pc2}} = \left[\left(\frac{d\eta_{pc3}}{\eta_{pc3}}\right)^2 + \left(\frac{d\beta}{\beta}\right)^2\right]^{\frac{1}{2}}$$

Eq. 6.4-6 $$\eta_{pc3} = \frac{I_B}{\dot{M}_T}$$

Eq. 6.4-7 $$\left(d\eta_{pc3}\right)^2 = \left(\frac{\partial \eta_{pc3}}{\partial I_B} dI_B\right)^2 + \left(\frac{\partial \eta_{pc3}}{\partial \dot{M}_T} d\dot{M}_T\right)^2$$

Eq. 6.4-8 $$\left(d\eta_{pc3}\right)^2 = \left(\frac{1}{\dot{M}_T} dI_B\right)^2 + \left(-\frac{I_B}{\dot{M}_T^2} d\dot{M}_T\right)^2$$

Eq. 6.4-9 $$\frac{d\eta_{pc3}}{\eta_{pc3}} = \left[\left(\frac{dI_B}{I_B}\right)^2 + \left(\frac{d\dot{M}_T}{\dot{M}_T}\right)^2\right]^{\frac{1}{2}}$$

and since instantaneously $\frac{dI_B}{I_B} = 0$

Eq. 6.4-10 $$\frac{d\eta_{pc3}}{\eta_{pc3}} = \frac{d\dot{M}_T}{\dot{M}_T}$$

Eq. 6.4-11 $$\dot{M}_T = \dot{m}_t + \dot{m}_i$$

Eq. 6.4-12 $$\left(d\dot{M}_T\right)^2 = \left(\frac{\partial \dot{M}_T}{\partial \dot{m}_t} d\dot{m}_t\right)^2 + \left(\frac{\partial \dot{M}_T}{\partial \dot{m}_i} d\dot{m}_i\right)^2$$

Eq. 6.4-13 $$d\dot{M}_T = \sqrt{\left(d\dot{m}_t\right)^2 + \left(d\dot{m}_i\right)^2}$$

using equation 4.3-12 for the discharge chamber xenon ingestion rate,

Eq. 5.3-12 $$\dot{m}_i = \frac{1}{4} n_b \overline{V}_a A_g \Phi_a M_{xe}$$

Eq. 6.4-14 $$\left(d\dot{m}_i\right)^2 = \left(\frac{\partial \dot{m}_i}{\partial n_b} dn_b\right)^2 + \left(\frac{\partial \dot{m}_i}{\partial \overline{V}_a} d\overline{V}_a\right)^2 + \left(\frac{\partial \dot{m}_i}{\partial A_g} dA_g\right)^2 + \left(\frac{\partial \dot{m}_i}{\partial \Phi_a} d\Phi_a\right)^2 + \left(\frac{\partial \dot{m}_i}{\partial M_{xe}} dM_{xe}\right)^2$$

assuming $dA_g = d\Phi_a = dM_{xe} = 0$

Eq. 6.4-15 $$\left(d\dot{m}_i\right)^2 = \left(\frac{1}{4} \overline{V}_a A_g \Phi_a M_{xe} dn_b\right)^2 + \left(\frac{1}{4} n_b A_g \Phi_a M_{xe} d\overline{V}_a\right)^2$$

Eq. 6.4-16 $$\frac{d\dot{m}_i}{\dot{m}_i} = \left[\left(\frac{dn_b}{n_b}\right)^2 + \left(\frac{d\overline{V}_a}{\overline{V}_a}\right)^2\right]^{\frac{1}{2}}$$

according to section 6.3.2

Eq. 6.3-29 $$\left(\frac{dn_b}{n_b}\right) = \left[\left(\frac{dP}{P}\right)^2 + \left(\frac{dT}{T}\right)^2\right]^{\frac{1}{2}} \approx 0.500$$

and accordingly,

Eq. 5.3-14 $$\overline{V}_a = \sqrt{\frac{8kT}{\pi M_{xe}}}$$

Eq. 6.4-17 $$\left(d\overline{V}_a\right)^2=\left(\frac{\partial\overline{V}_a}{\partial k}dk\right)^2+\left(\frac{\partial\overline{V}_a}{\partial T}dT\right)^2+\left(\frac{\partial\overline{V}_a}{\partial M_{xe}}dM_{xe}\right)^2$$

since $dk=dM_{xe}=0$

Eq. 6.4-18 $$d\overline{V}_a=\frac{\partial\overline{V}_a}{\partial T}dT=\frac{1}{2}\left[\frac{8kT}{\pi M_{xe}}\right]^{-\frac{1}{2}}\left[\frac{8k}{\pi M_{xe}}\right]dT$$

Eq. 6.4-19 $$d\overline{V}_a=\frac{1}{2}\frac{\overline{V}_a}{T}dT$$

Eq. 6.4-20 $$\frac{d\overline{V}_a}{\overline{V}_a}=\frac{1}{2}\frac{dT}{T}$$

Eq. 6.4-21 $$\frac{d\dot{m}_i}{\dot{m}_i}=\left[\left(\frac{dP}{P}\right)^2+\left(\frac{1}{2}\frac{dT}{T}\right)^2\right]^{\frac{1}{2}}$$

Eq. 6.4-22 $$d\dot{m}_i=\dot{m}_i\left[\left(\frac{dP}{P}\right)^2+\left(\frac{1}{2}\frac{dT}{T}\right)^2\right]^{\frac{1}{2}}$$

$\frac{dP}{P}\approx 0.50$ and $\frac{dT}{T}\approx 0.017$

Eq. 6.4-23 $$d\dot{m}_i=0.500\dot{m}_i$$

and $d\dot{m}_t$ is estimated to be $0.05\dot{m}_t$, therefore

Eq. 6.4-24 $$d\dot{M}_T=\sqrt{\left(d\dot{m}_t\right)^2+\left(d\dot{m}_i\right)^2}=\sqrt{\left(0.05\dot{m}_t\right)^2+\left(0.500\dot{m}_i\right)^2}$$

Eq. 6.4-25 $$\frac{d\eta_{pc3}}{\eta_{pc3}}=\frac{d\dot{M}_T}{\dot{M}_T}=\frac{\sqrt{\left(0.05\dot{m}_t\right)^2+\left(0.50\dot{m}_i\right)^2}}{\dot{m}_t+\dot{m}_i}$$

Eq. 6.4-26 $$\beta=\frac{1+\frac{1}{2}\frac{I^{++}}{I^{+}}}{1+\frac{I^{++}}{I^{+}}}=\frac{1+.5R_c}{1+R_c}=\left(1+.5R_c\right)\left(1+R_c\right)^{-1}$$

Eq. 6.4-27 $$d\beta=\frac{\partial\beta}{\partial R_c}dR_c=\left[\frac{1}{2\left(1+R_c\right)}-\frac{\left(1+.5R_c\right)}{\left(1+R_c\right)^2}\right]dR_c$$

Eq. 6.4-28 $$\frac{d\beta}{\beta} = \frac{1}{2}\frac{dR_c}{1+1.5R_c+R_c^2}$$

and since it is assumed that $dR_c \approx 0.01R_c$

Eq. 6.4-29 $$\frac{d\beta}{\beta} = \frac{1}{2}\frac{0.01R_c}{1+1.5R_c+R_c^2}$$

recalling equation 6.4-5

Eq. 6.4-5 $$\frac{d\eta_{pc2}}{\eta_{pc2}} = \left[\left(\frac{d\eta_{pc3}}{\eta_{pc3}}\right)^2 + \left(\frac{d\beta}{\beta}\right)^2\right]^{\frac{1}{2}}$$

and the resulting corrected propellant utilization efficiency (n_{pc2}) uncertainty is:

Eq. 6.4-30 $$\frac{d\eta_{pc2}}{\eta_{pc2}} = \left\{\left[\frac{\sqrt{(0.05\dot{m}_t)^2+(0.50\dot{m}_i)^2}}{\dot{m}_t+\dot{m}_i}\right]^2 + \left[\frac{1}{2}\frac{0.01R_c}{1+1.5R_c+R_c^2}\right]^2\right\}^{\frac{1}{2}}$$

Chapter 7 Results and Discussion

7.1 Ion Beam Current Density Results

7.1.1 Single Source Ion Beam Symmetry Evaluation

Figure 7.1-1, 7.1-2, and 7.1-3 depict typical current density contour plots for the ion beams extracted from segments A, B, and C respectively. The plots were generated from data collected 0.66 m from the thruster a metered beam current (I_B) of 430 mA and R = 0.893. One of the first noticeable characteristics of these contours is they are not round, but elliptical, or oval in shape. Similar investigations into the characteristics of other ion thruster plumes generally present results of circular beams, such as in the work done by Fearn et al. [53] and Groh et al. [54]. In addition, the degree to which each segment produces non-circular beams is different as well as the orientation of the beam profiles. Orientation of the ion beam profiles can be described by using the vertical axis (Y) through the center of an ion beam with the 12 o'clock position being zero rotation, measuring positive rotation in a clockwise direction from that position.

As shown in figures 7.1-1 through 7.1-3, the ion beam extracted from segment A appears to be the most asymmetric in comparison to those from segments B and C. The segment A "semi-major axis" is canted about +15°. Segment B seems to produce the least asymmetric beam and the "semi-major axis" lies at approximately 90°. With an orientation of close to 0°, the beam extracted from segment C appears closer to segments A with respect to the degree of asymmetry.

The most likely cause for non-circular beam profiles involves misalignment between the grid holes of the accelerator system. Alignment of these holes affects the trajectories of the accelerated ions. If all holes of adjacent grids are not radially consistent in alignment, the ions will exit in such a manner that the resulting current density profile will not be symmetric. Variable spacing between the grids, position errors in drilling of the holes, inexact assembly of the grids, and variations in thermal expansion of the grids are all potential factors in hole misalignment. Variations in spacing between the grids could be caused by differences in spacer thickness or by non-flatness of the grids.

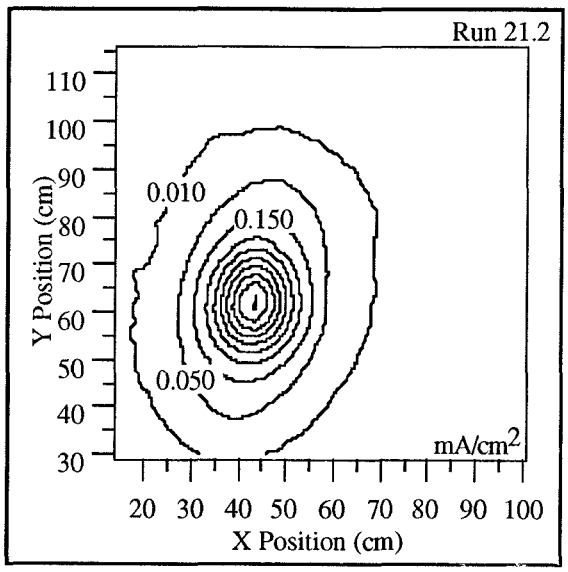

Example Current Density Contour Plot - Seg A
Figure 7.1-1

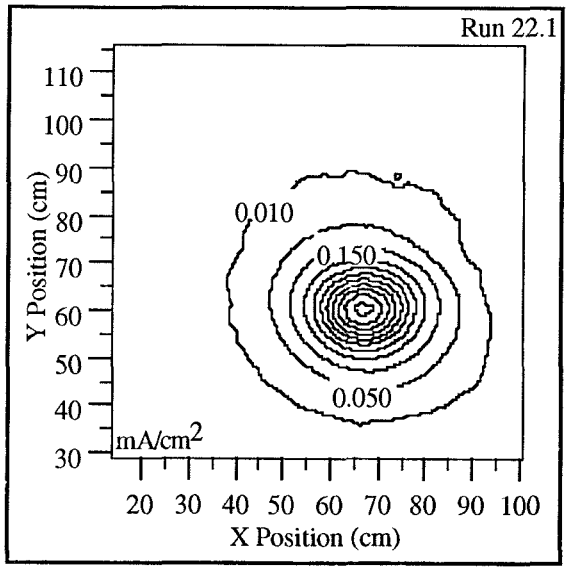

Example Current Density Contour Plot - Seg B
Figure 7.1-2

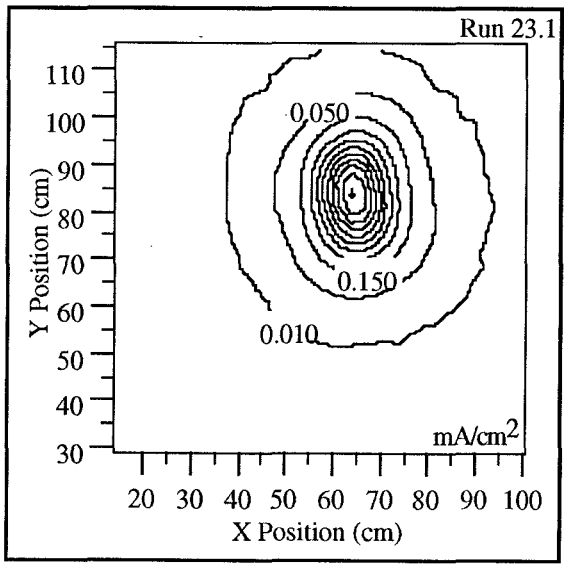

Example Current Density Contour Plot - Seg C
Figure 7.1-3

Shapes of the current density contours developed for this study are similar in shape to those generated in earlier work [52], however, the beam profile orientations are different. Figures 7.1-4 through 7.1-6 show the contour plots developed in the previous work and correspond to segments A, B, and C operating at a metered beam current (I_B) of 425 mA, R ratio of 0.897 and screen voltage (V_S) of 1300 V.

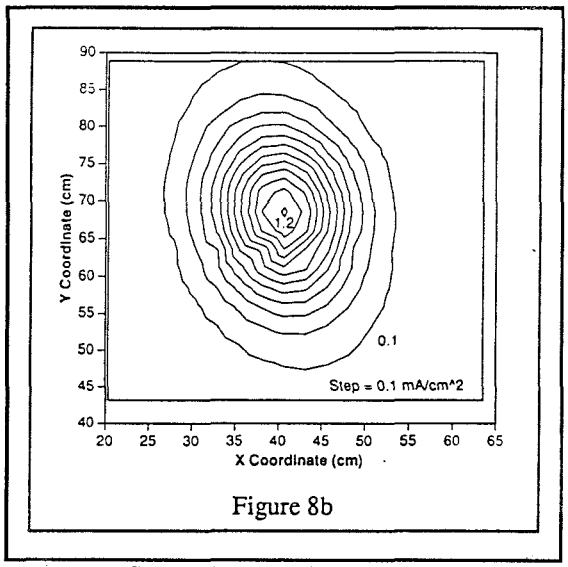

Figure 8b

Current Density Contour Plot-
Inital Testing Segment A
Figure 7.1-4

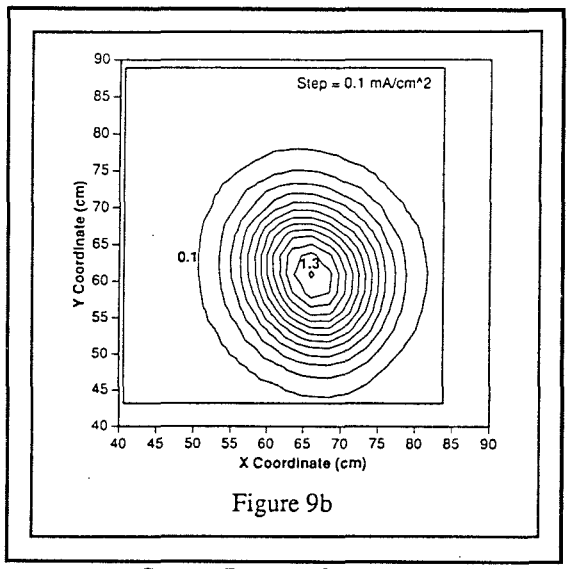

Figure 9b

Current Density Contour Plot-
Initial Testing Segment B
Figure 7.1-5

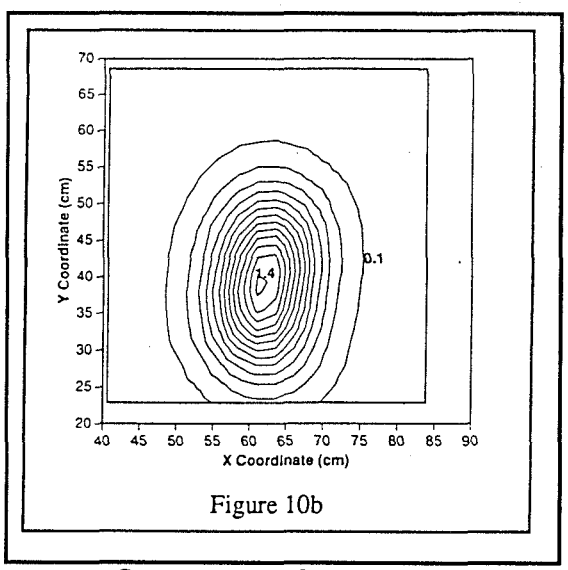

Figure 10b

Current Density Contour Plot-
Initial Testing Segment C
Figure 7.1-6

Orientation of the ion beam profile corresponding to segment A produced in the earlier study can be seen in figure 7.1-4. The "semi-major axis" is oriented at approximately -15° with respect to the vertical axis. The "semi-major axes" pertaining to segments B and C are oriented at about -25° and +5° respectively and are shown in figures 7.1-5 and 7.1-6. These angles are substantially different than those observed in this investigation.

There exist some important differences between the previous investigation and this one. First, the Faraday probe rakes were different in size and orientation. The earlier work involved the use of a probe rake with nine Faraday probes mounted in a horizontal fashion. Also, during the time between the two studies, the probe positioning system was removed from the vacuum chamber, modified with reliability improvements, re-installed, and aligned with the tank walls. Had the alignment of the probes in the first study been significantly different from the alignment of the later study, similarity in beam shapes would not be expected. This implies that probe alignments within both studies were at least consistent and the probe rake alignment was such that the probe centerlines were close to parallel with the tank centerline. It also implies that probe misalignment was not a significant factor in producing asymmetric beam profiles.

During the time between the two studies all grid sets were removed, re-gapped and replaced. Spacing of the grids was intended to be consistent between the two studies and thickness measurements were made of all spacers prior to initial assembly and reassembly. There were some slight variations in spacer thickness due to inherent uncertainties created in the process of fabricating the spacers and may have created slight differences in grid spacing between each study. In addition, grid hole alignment may have shifted slightly during reassembly.

The individual grids were not mixed between grid sets and the grid sets were mounted to the same discharge chamber in both studies. Orientation of the mounting ring to the discharge chamber may not have been consistent before and after adjustment, however, orientation of the accelerator grid, decelerator grid, and screen grid with respect to each other were consistent. This, implies the ion beam orientation differences between studies were most likely the result of the grid-to-grid hole alignment differences between the two studies.

Differences in beam shape were noted in this investigation between different metered beam current levels. These differences were observed primarily in comparisons of the current density contour plots generated for 312 mA and 500 mA cases. Variations were also noted in the current density contour plots of 430 mA when compared to both the 312 mA and 500 mA cases, although

they were slight. Symmetry differences between segment A profiles at 312 mA and 500 mA are pictured in figures 7.1-7 through 7.1-10. The most likely cause for these observed differences is differential thermal expansion between the 312 mA and 500 mA cases.

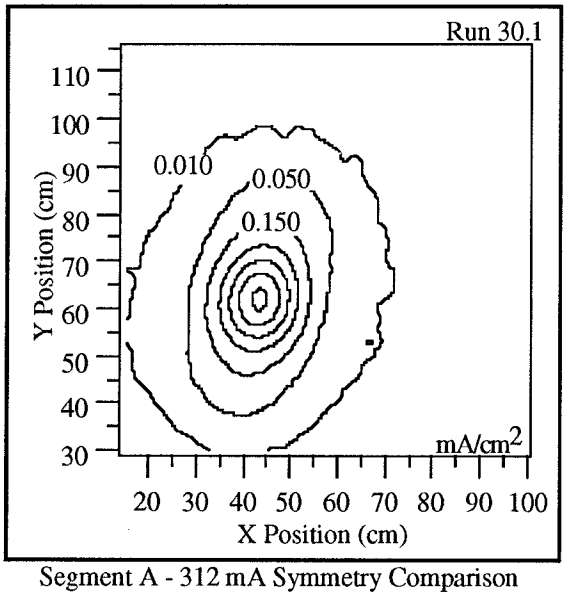

Segment A - 312 mA Symmetry Comparison
Figure 7.1-7

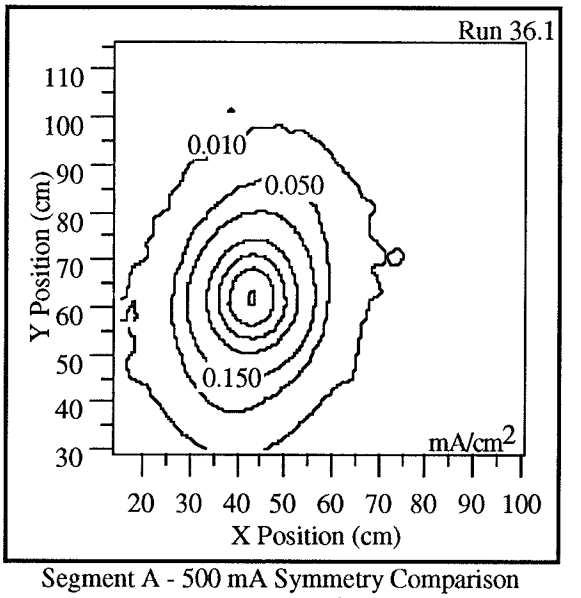

Segment A - 500 mA Symmetry Comparison
Figure 7.1-8

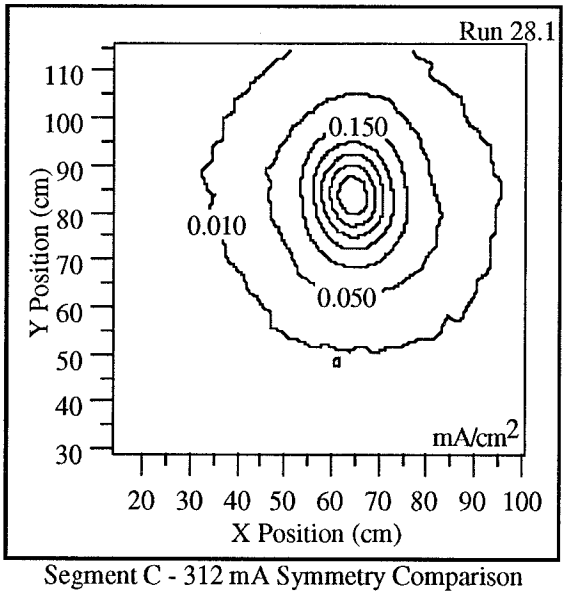

Segment C - 312 mA Symmetry Comparison
Figure 7.1-9

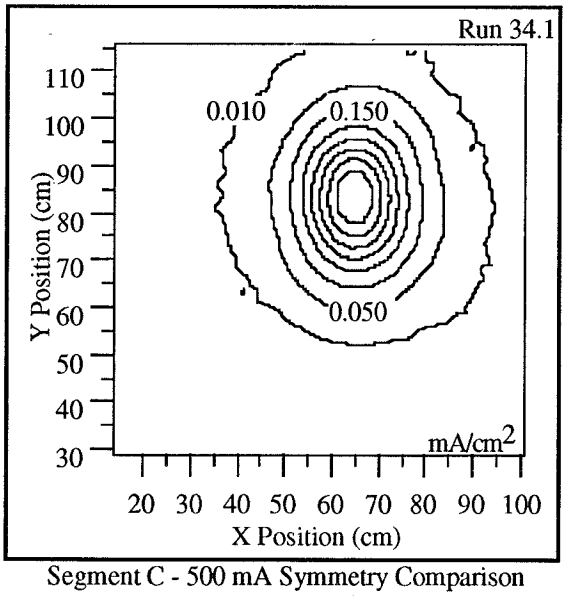

Segment C - 500 mA Symmetry Comparison
Figure 7.1-10

7.1.2 Ion Beam Current Density Contour Plot Spatial Development

Figures 7.1-11 to 7.1-13 display example current density contour plots at three different downstream locations. The data used to create figure 7.1-11 was acquired at a distance of 0.356 m from the ion exit plane of the thruster with data for figures 7.1-12 and 7.1-13 collected at 0.660 m and 0.965 m respectively. Each ion source had a metered beam current (I_B) of 430 mA and an R ratio of 0.893 with a screen voltage (V_S) of 1250 V.

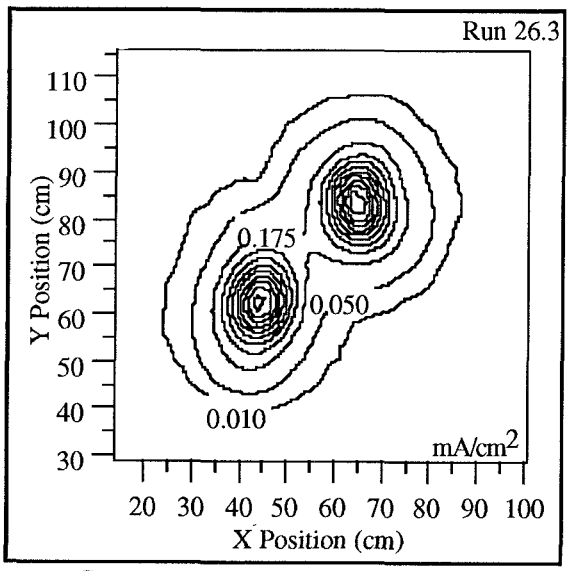

Current Density Contour Plot - 0.356 m
Figure 7.1-11

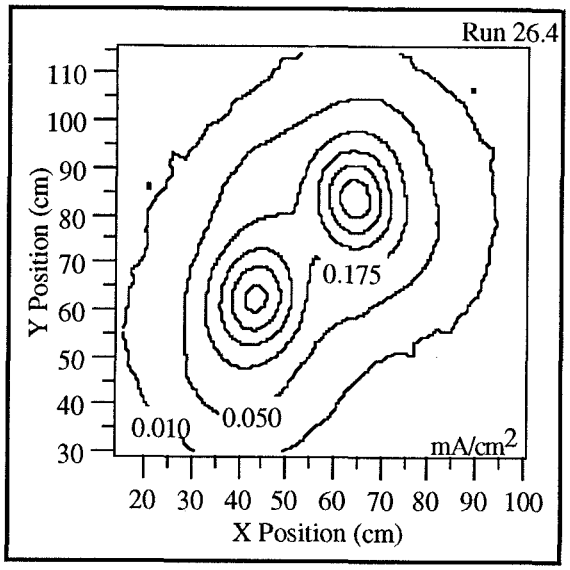

Current Density Contour Plot - 0.660 m
Figure 7.1-12

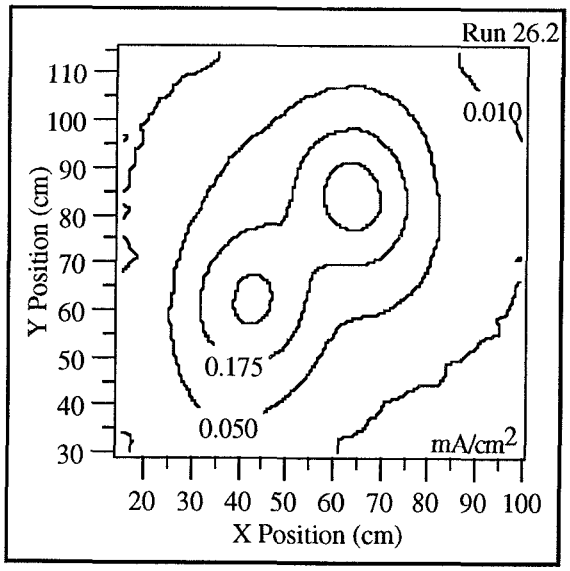

Current Density Contour Plot - 0.965 m
Figure 7.1-13

As distance from the thruster increases, the beam tends to spread and the peak current density decreases. The 0.050 and 0.175 mA/cm2 contours do not appear to increase in size and seem to retain the initial shape. The 0.010 mA/cm2 contour however, does cover a greater area with distance from the thruster. This beam development is primarily due to divergence of the individual ion beamlets extracted from each hole of the accelerator system.

7.1.3 Real and Superimposed Current Density Contour Plots.

The general shape, orientation, and location of the superimposed current density contour plots agree well in comparison to the current density plots generated with data acquired from the actual operation of multiple ion sources. Figures 7.1-14 through 7.1-21 depict four sample comparisons. A complete display of synthetic and real contour plots is found in appendix B. Although the general shapes are similar, the current density contour plots display possible evidence of interaction between the ion beams.

Additional current density contour lines appear in most of the superimposed data (synthetic) plots. This difference is evident in comparison of figures 7.1-18 and 7.1-19 where it can be seen there exists one additional contour line in the plot of superimposed data than of real data. The extra contour line signifies a greater peak current density value for the constructed data plots.

Background plasma / system noise biases subtracted from the raw Faraday probe current measurement data are a likely contributor for the addition of contours. As previously explained, the method for determining the biases was inconsistent. The effect of inaccurate bias choice would cause the current density contour plot to shift in magnitude. If the peak of the real data contour were close to a contour step, differences in biases applied to individual ion source data sets may cause an additional contour to be displayed in the superimposed data plots. Although addition of contours may occur due to bias choice, it is believed that the chosen biases were appropriate because of the agreement between total measured beam currents and those expected after accounting for charge exchange effects as will be discussed in section 7.1.4.

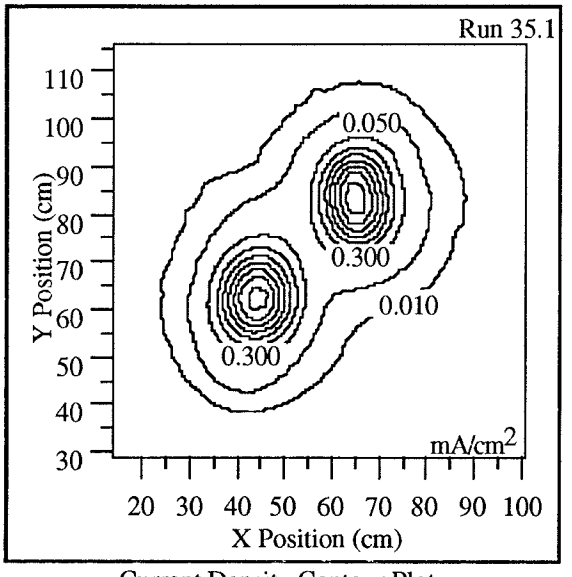

Current Density Contour Plot
Real Data-Z = 0.356 m
Figure 7.1-14

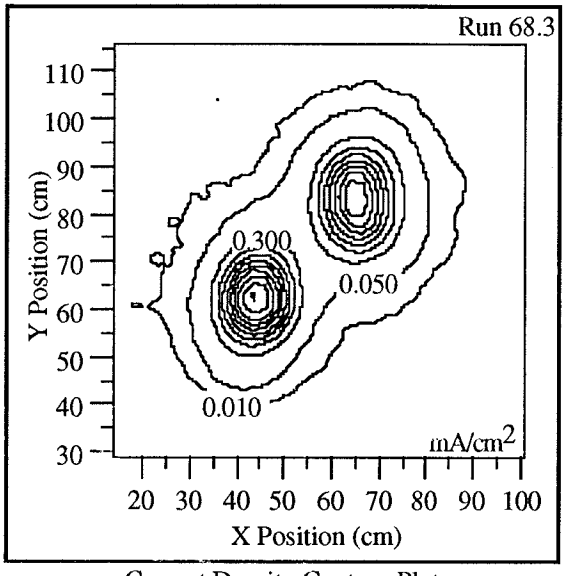

Current Density Contour Plot
Syn Data-Z = 0.356 m
Figure 7.1-15

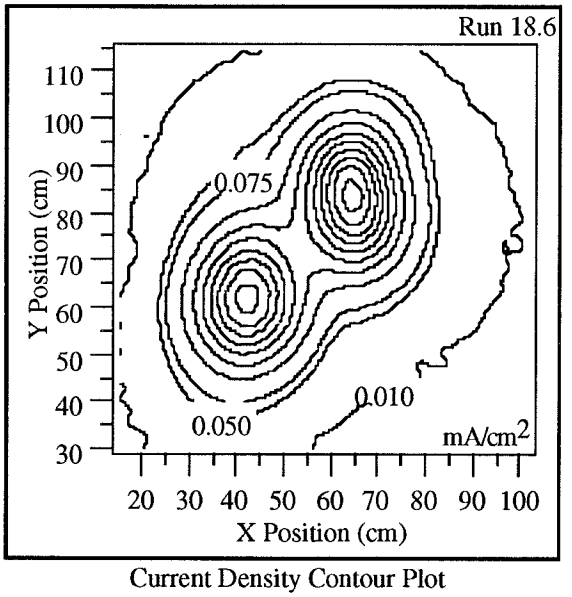

Current Density Contour Plot
Real Data - Z = 0.965 m
Figure 7.1-16

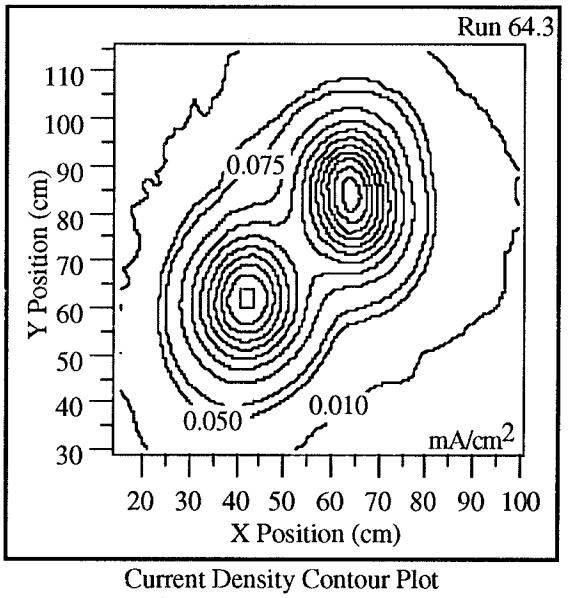

Current Density Contour Plot
Syn Data - Z = 0.965 m
Figure 7.1-17

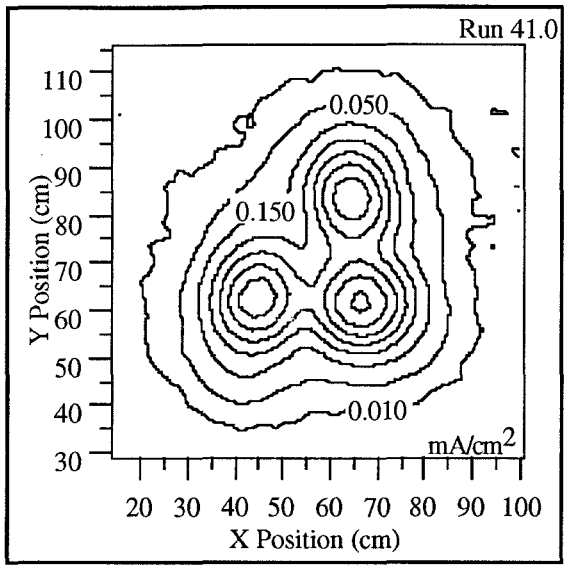

Current Density Contour Plot-Real Data-Seg ABC
Figure 7.1-18

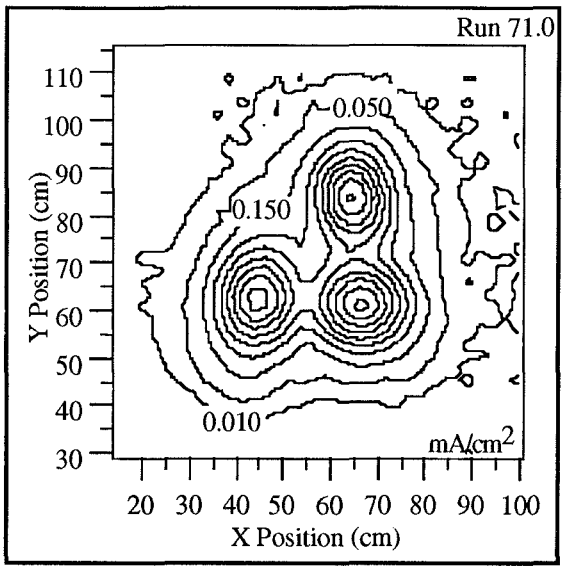

Current Density Contour Plot-Syn Data-Seg ABC
Figure 7.1-19

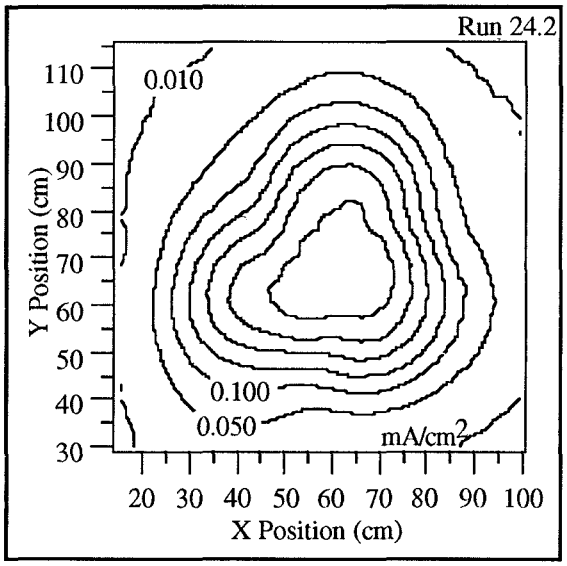

Current Density Contour Plot
Real Data - Z = 0.965 m
Figure 7.1-20

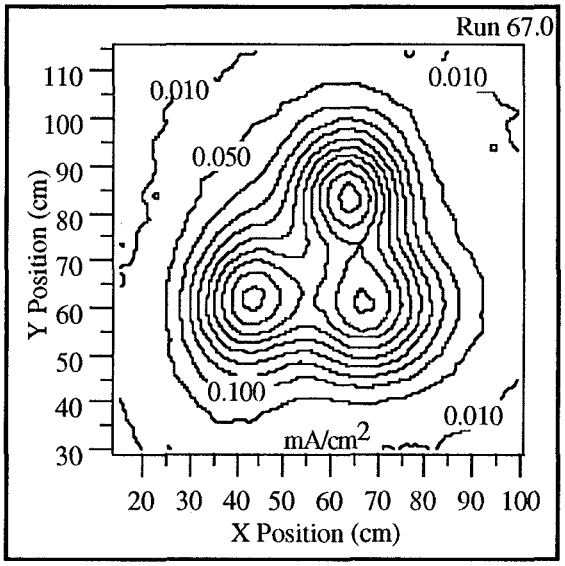

Current Density Contour Plot
Syn Data - Z = 0.965 m
Figure 7.1-21

In cases where Faraday probe data was collected at positions close to the thruster there is little discrepancy between real and synthetic contour plots (figures 7.1-14 and 7.1-15). However, as distance from the thruster increases, the differences become more pronounced. These differences may indicate interaction between the ion beams, however, this interaction may be due to facility effects. The differences between figures 7.1-20 and 7.1-21 are much more pronounced than those between figures 7.1-16 and 7.1-17. The only difference in the operating conditions between run 18.6 (figure 7.1-16) and run 24.2 (figure 7.1-20) is the number of active ion sources, 3 for run 24.2 and 2 for run 18.6. Addition of an active ion source in run 24.2 would have increased the facility pressure compared to that found in run 18.6 due to the higher propellant flow rate, and therefore increased the charge exchange effects to the ion beams. These increased charge exchange effects could potentially have been the cause for the observed differences.

7.1.4 Ion Beam Current Profile Integration

A compilation of all integrated (measured) and calculated (accounting for charge exchange effects) beam current values and their associated uncertainties are given in table A-6 of appendix A. Included in this table is information regarding thruster operation and downstream location of the data acquisition plane. The beam currents and associated uncertainties were calculated using the equations given in chapter 5. In the column labeled 'CHECK' of table A-6 are the words "OKAY" and "NO". The word "OKAY" refers to the condition of a data acquisition run in which the errors associated with the computed beam currents can account for the discrepancy between the calculated and the integrated values. "NO" refers to the condition in which the discrepancy could not be accounted.

The column labeled 'TYPE' in table A-6 contains the words "MAT", "RFND", and "SYN". "MAT" refers to data files which contain only adjusted matrix data as described in section 5.1. "RFND" refers to data files, also discussed in section 5.1, where interpolation of the data has been done so that spacing between data points was 0.635 cm. "SYN" refers to the data files created for

comparison of superimposed multiple ion source operation to the actual operation of the multiple ion sources.

7.1.4.1 Comparison of Measured and Calculated Beam Current

Differences between the integrated (measured) beam currents using adjusted matrix data (MAT) and the theoretically calculated beam currents are given in the column labeled 'Error' of table A-6. Most of the discrepancies were less than 10% for cases in which R = 0.893. The range was as high as 20% and as low as 2%. However, for cases in which R = 0.643, the discrepancies were rarely less than 15%, with some as high as 28%. In a total of 66 out of the 83 cases that used "MAT" data and R = 0.893, the uncertainties associated with the theoretical and integrated beam currents could account for the discrepancies between the values. This agreement between the calculated and measured values does not hold well for cases where R = 0.643. Shown in table A-6 column 'CHECK' are the "OKAY" / "NO" conditions for R = 0.643 cases. Only 1 of the 21 cases listed there could account for the differences. This level of disagreement between the measured and calculated values was unexpected and attempts were made to better understand this.

The first step made in order to reconcile the differences of the R = 0.643 runs was to repeat the data adjustment and integration steps to be sure procedures were followed correctly. In addition numerical values used in calculating the theoretical beam current, such as: number density (n_b), charge exchange cross section (σ_{ce}), and distance from the thruster (z) were checked. Testing of the 2-D integration coding with analytical data sets ruled out software errors. The discrepancy between theory and experiment persisted.

Attention was then focused on the assumptions used to account for charge exchange effects. One of the assumptions used in the theory was that of a highly collimated beam. With a lower R ratio for these cases, the ion beam tended to be wider than for a higher R ratio. This dependence of beam divergence angle on R ratio will be discussed further in section 7.1-5. The charge exchange calculations used the axial distance between the probes and the thruster exit plane,

which were fixed at 0.356, 0.506, 0.660, 0.813 or 0.965 m. It would have been more appropriate to use the distance between the center of the thruster at the ion exit plane and each individual probe, as opposed to the normal distance to the data acquisition plane. This would have accounted for the physical distance the ions traveled. Although using this off axis distance would have been more accurate, it would have been difficult to determine where on the exit plane of the multiple ion sources would be the appropriate spot from which to measure.

7.1.4.2 Integrated Beam Currents with Synthetic Data

Similar to the "MAT" data, most of the differences between the theoretical and integrated beam currents using "SYN" data for R = 0.893 could be accounted for by including the associated uncertainties. Although integrated beam current values of superimposed "SYN" data agreed well with calculated data for an R ratio of 0.893, this conformity still did not hold for cases of R = 0.643.

Comparison of the "MAT" and "SYN" data results showed that the integrated beam currents using "SYN" data were generally greater than those using "MAT" data. The differences were normally less than 8% with a few exceptions as shown in the column labeled 'Delta' of table A-10 found in appendix A. Differences in 40 of the 56 cases could be accounted for by evaluating the uncertainties associated with both integrated values. There seemed to be some dependence of these differences on the number of active ion sources. The discrepancies tended to be higher for cases in which three ion sources were operating. This could have been related to either the interaction of ion beams or there may have been a facility effect that was dependent upon the xenon mass flow rate and pumping speed. There did not appear to be any dependence of this on R ratio, ion source beam current, or distance from the thruster.

7.1.5 Ion Beam Divergence

Beam divergence angles (α) tended to vary between segments and were dependent upon, metered beam current (I_B)and the R ratio. Although the divergence angle varied with downstream position, no trend was identified. Results from the calculations described in section 6.1.3 are found in table A-8 of appendix A.

Figures 7.1-22 through 7.1-24 display the beam divergence angles for each segment at the different operating conditions. Segment B tended to produce the most collimated beam among the three segments. Segments A and C traded positions for having the most divergent plumes as metered beam current and R varied. The available beam divergence angles were averaged along with their associated uncertainties in order for a quantitative comparison of the results between the different thruster operating conditions and are presented in table 7.1-1.

Average Beam Divergence Angle Results

Segment	I_B (mA)	R	α (deg)	$d\alpha$ (deg)
A	430	0.893	14.7	0.4
B	430	0.893	11.0	0.3
C	430	0.893	13.6	0.4
A	312	0.893	14.2	0.5
B	312	0.893	12.1*	0.4*
C	312	0.893	16.4	1.2
A	500	0.893	13.5	0.3
B	500	0.893	12.2	0.3
C	500	0.893	13.0	0.3
A	430	0.643	19.7	0.9
B	430	0.643	17.2	0.9
C	430	0.643	22.2	1.2
*Run 31.0 was not included in these calculations.				

Table 7.1-1

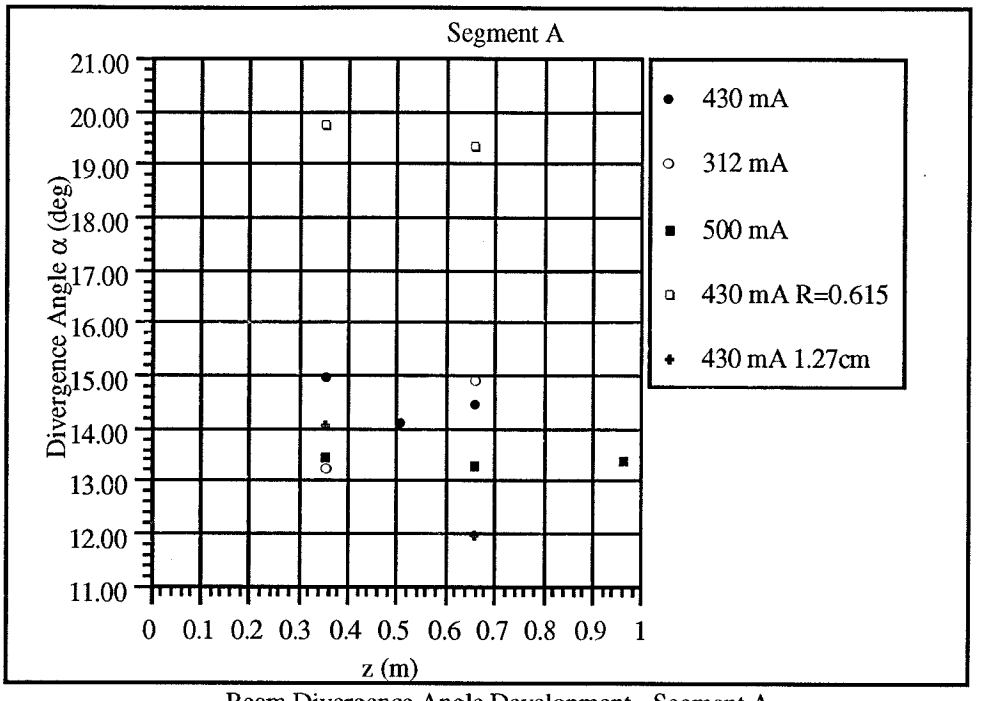

Beam Divergence Angle Development - Segment A
Figure 7.1-22

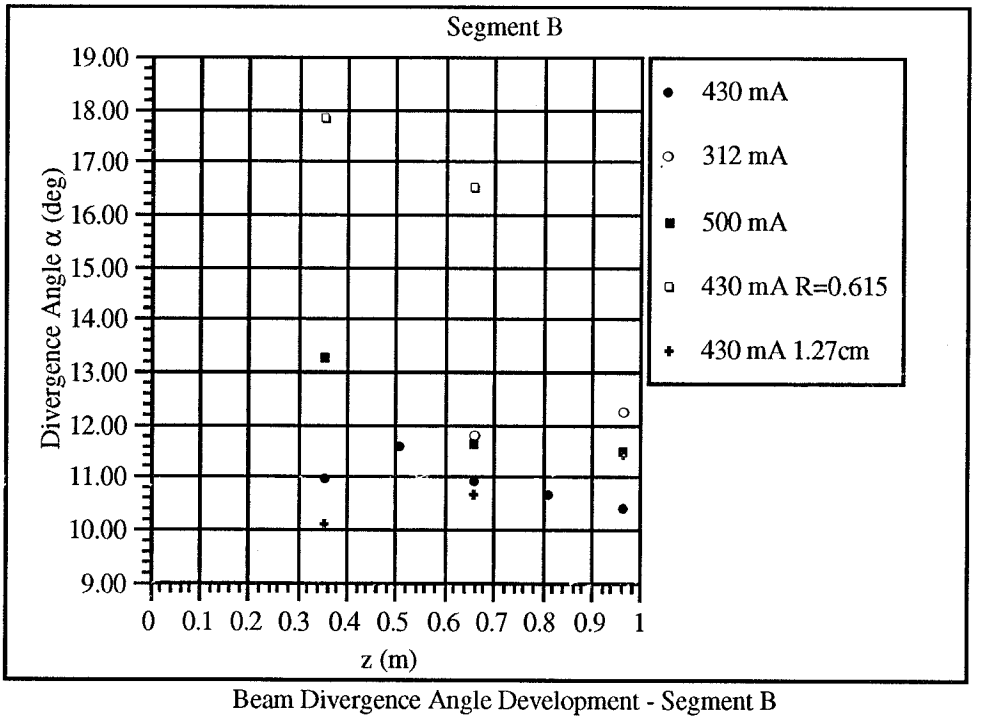

Beam Divergence Angle Development - Segment B
Figure 7.1-23

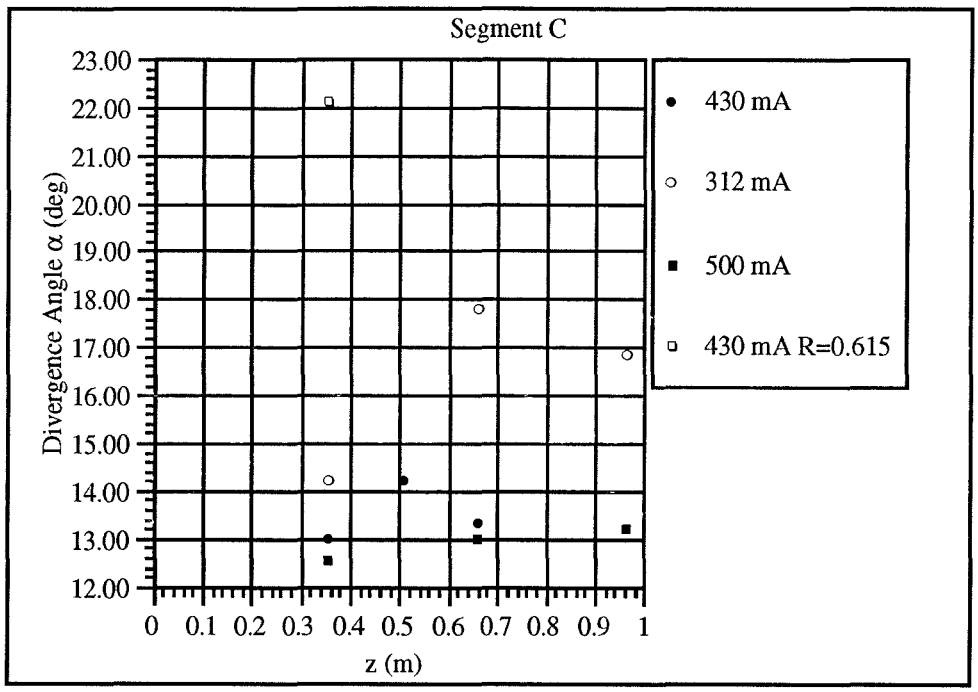

Beam Divergence Angle Development - Segment C
Figure 7.1-24

The most dramatic shift in beam divergence angle (α) occurs when the R ratio changes from 0.893 to 0.643. The width of the ion beams emanating from each of the segments increase 34, 56, and 63 percent for segments A, B, and C when compared to the beams produced with the thruster operating at 430 mA with R = 0.893. This increase in beam divergence has been identified as a possible cause for R = 0.643 integrated beam current values to be on the order of 20% lower than the beam current values expected after accounting for charge exchange effects. A large change in α is also visible between segment C at 312 mA and 430 mA or 500 mA.

As identified at the bottom of table 7.1-1, run 31.0 was not included in these calculations. This was due to the unexplainably large value of $\alpha = 37.4°$. Data and procedures were checked twice in hopes to identify the cause. The same result persisted throughout all attempts. Figure B-59 of appendix B displays the current density contour plot for run 31.0, and as can be seen, no significant features distinguish this contour plot from other plots. In comparison with the contour plot it becomes obvious that this beam divergence angle is not possible. For this reason, the value of 37.4° was not used in any calculations and will not be included in any further discussions.

7.1.6 Beam Flatness Downstream Development

Figures 7.1-25 through 7.1-27 display the calculated beam flatness parameters (F) for each segment and operating condition as a function of distance from the thruster (z). There does not appear to be any consistency with the dependence of beam flatness on beam current (I_B) or R ratio in comparison between the segments. In some cases, F tends to decrease as a function of Z, such as for segment A at 430 mA, and in some cases F tends to increase, such as for segment B at 430 mA (for Z > 0.508 m). The calculated values for F are given in table A-8 of appendix A. Also in this table are the calculated values for the uncertainty in F. The error bars were not shown in these figures because they would have overlapped and made reading of the figures difficult.

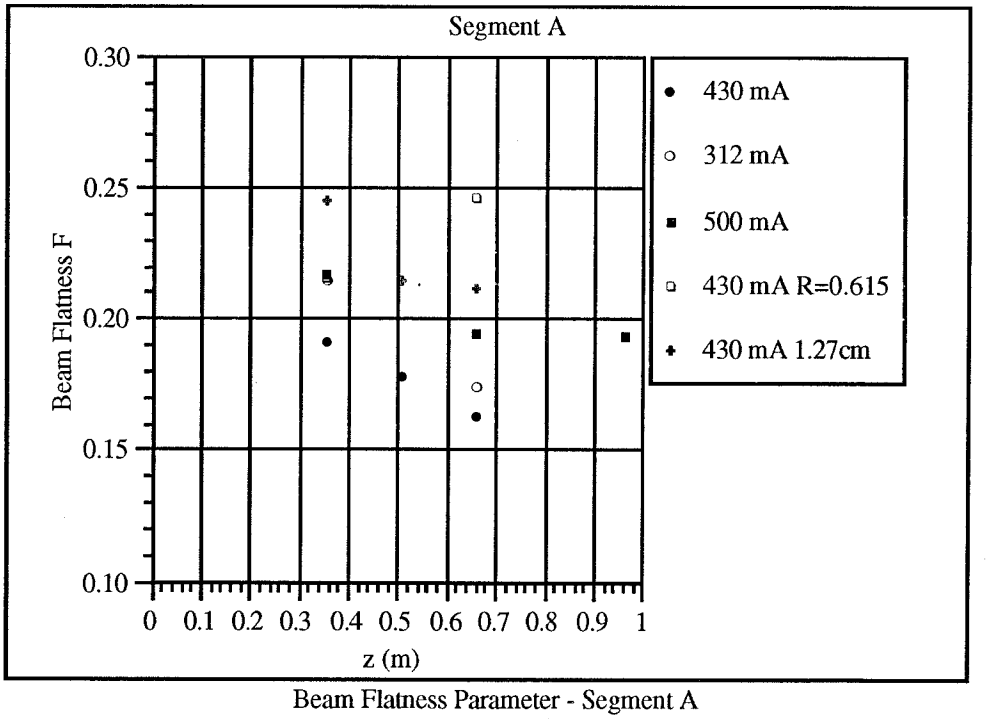

Beam Flatness Parameter - Segment A
Figure 7.1-25

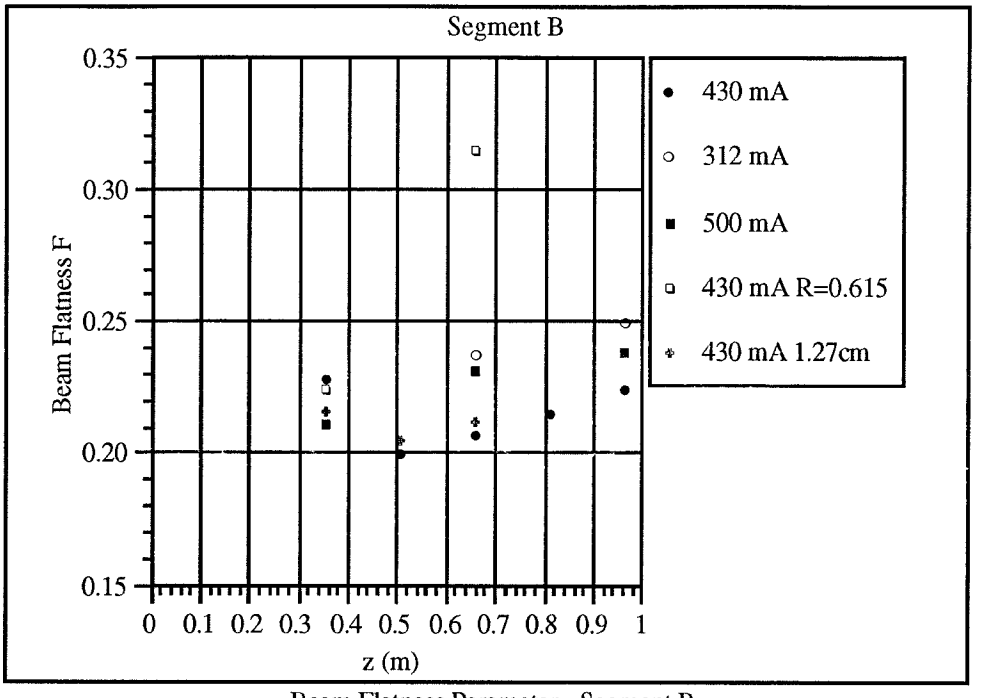

Beam Flatness Parameter - Segment B
Figure 7.1-26

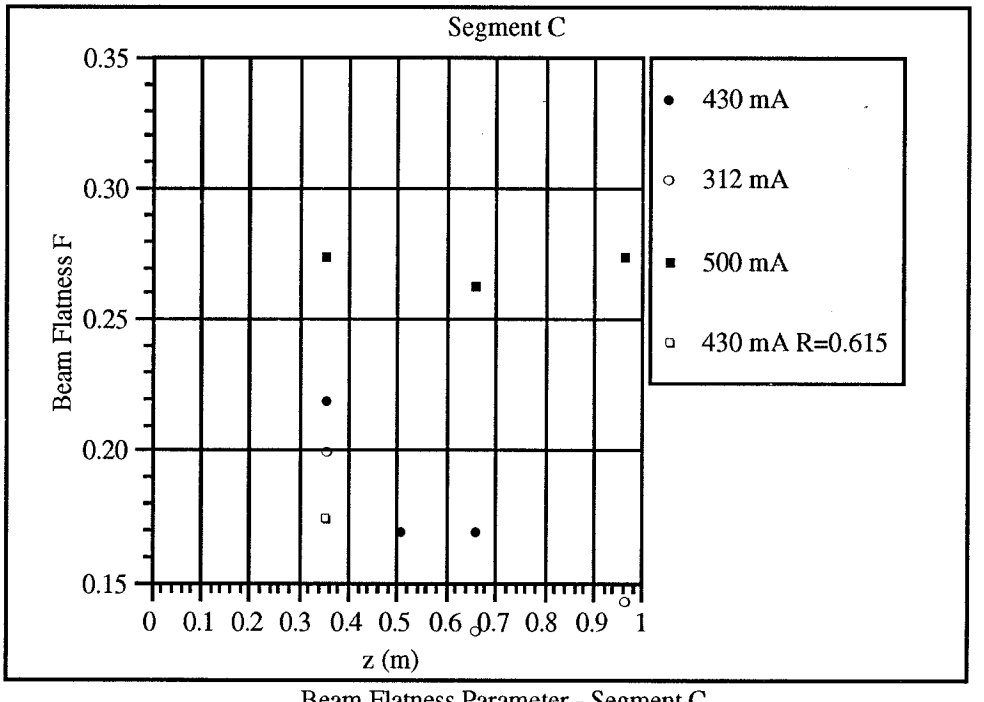

Beam Flatness Parameter - Segment C
Figure 7.1-27

7.2 Ion Beam Charge State

7.2.1 Ion Source Centerline Data Plots

Ion beam centerline charge state was evaluated for a total of five different thruster operating conditions. These conditions correspond to nominal beam currents of 312 mA, 430 mA, and 470 mA. The 312 mA and 470 mA cases were evaluated with neutralizer low voltage keeper in both the "On" and "Off" modes, however, the 430 mA case was only studied with low voltage keeper off. Nominal beam current refers to the metered beam current at which the uncorrected propellant utilization efficiency (η_p) is 0.90.

Data generated from these measurements are presented in charge state number ratio (R_n) vs. corrected propellant utilization efficiency (η_{pc2}) plots such as the one given below in figure 7.2-1. The propellant utilization presented here was corrected for doubly charged ions and xenon mass ingestion due to the ambient facility pressure. Error bars, based on the error analysis of section 6.3, are included in the plots to show uncertainties in the calculation of η_{pc2}. No data is available regarding the uncertainty related to R_n. The data used to develop the centerline R_n vs. η_{pc2} plots discussed in this section can be found in table A-11 of appendix A.

Figure 7.2-1 displays the centerline charge state number ratio (R_n) vs. corrected propellant utilization efficiency (η_{pc2}) for runs with a nominal beam current of 430 mA and the neutralizer low voltage keeper deactivated. As shown in the figure, no doubly charged ion current could be discerned from the collected current profiles for η_{pc2} less than approximately 0.84 ± 0.04. The maximum η_{pc2} of 0.96 ± 0.04 was reached with a discharge voltage and 30.2 V and beam current of 501 mA.

The R_n vs. η_{pc2} curves for cases with nominal beam currents of 312 mA, as displayed in figures 7.2-2 and 7.2-3, show evidence of doubly charged ion production at corrected propellant utilization efficiencies of as low as 0.50. The maximum η_{pc2} of 1.05 ± 0.05 was reached with a discharge voltage and 49.1 V and beam current of 425 mA.

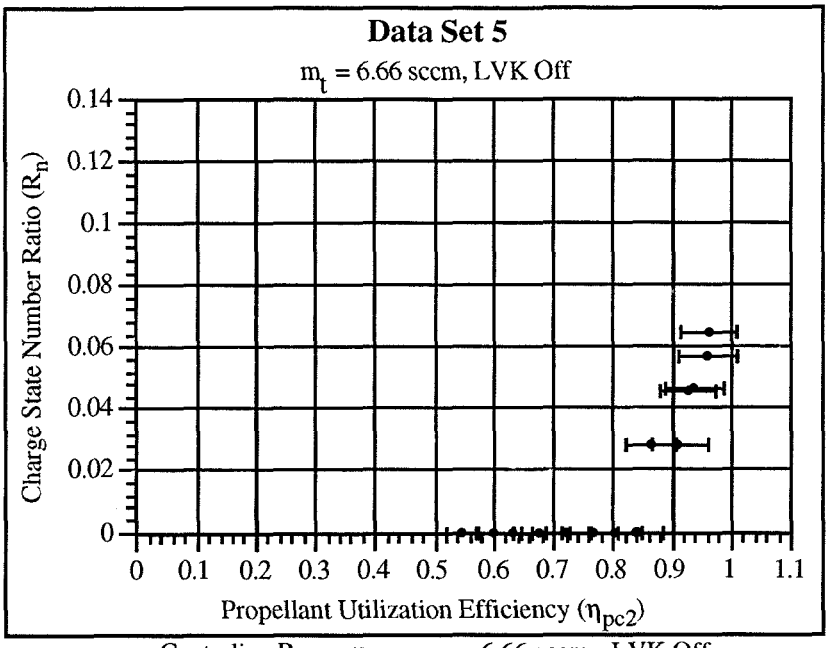

Centerline R_n vs. η_{pc2} - m_t = 6.66 sccm - LVK Off

Figure 7.2-1

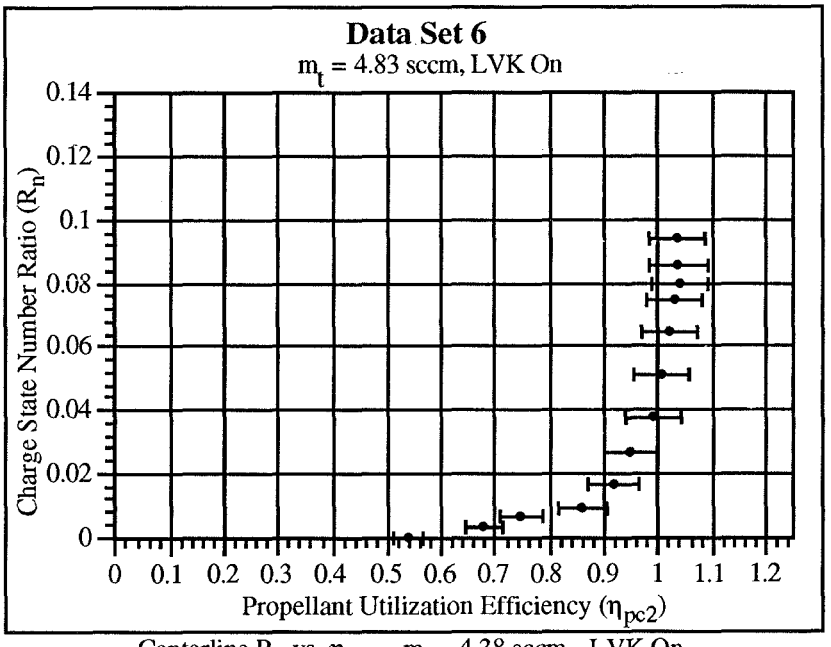

Centerline R_n vs. η_{pc2} - m_t = 4.38 sccm - LVK On

Figure 7.2-2

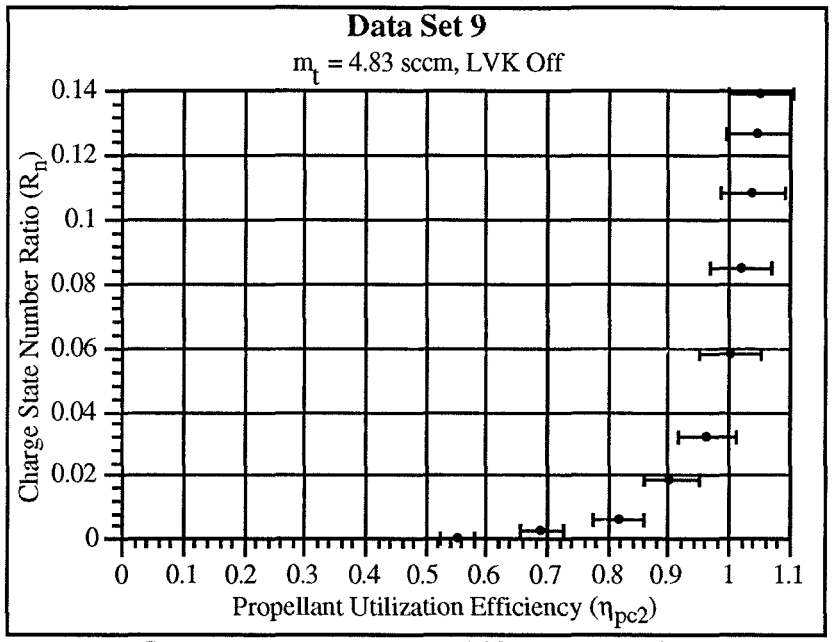

Centerline R_n vs. η_{pc2} - m_t = 4.38 sccm - LVK Off
Figure 7.2-3

A significant aspect of these curves is that the corrected propellant utilization efficiency is greater than 1 for beam currents greater than about 370 mA. Since it is physically impossible, attempts were made to explain this regarding uncertainty in measuring doubly charged ion production and discharge chamber propellant ingestion. For the data points in which η_{pc2} is greater than 1, the associated error bars extend over the $\eta_{pc2} = 1$ line for all but one case, which means that only one data point is truly suspect. This data point of $\eta_{pc2} = 1.05$, shown in figure 7.2-3, corresponds to thruster operating conditions of $I_B = 425$ mA, $\dot{m}_t = 4.85$ sccm, and $V_{DIS} = 49.1$V.

Initially in this investigation it was assumed that production of triply charged ions could be neglected. According to Sovey [37], production of triply charged ions did not begin until the discharge voltage reached approximately 42 V. The reason it was assumed that triply charged ion production would be negligible was because reaching discharge voltages of over 40 V was not anticipated. Sovey found that at discharge voltages of 46 V the triply charged ion production rate was 2% of the singly charged ions. If triply charged ion were produced at these higher discharge

voltages in this investigation, then the propellant utilization efficiency corrected for doubly and triply charged ions as well as propellant ingestion, using equation 7.2-1, would be 1.041 ± 0.046. Note here that the uncertainty would allow the error bars to extend over the $\eta_{pc2} = 1$ line and account for the greater than 1 value.

Eq. 7.2-1
$$\beta = \frac{1 + \frac{1}{2}\frac{I^{++}}{I^{+}} + \frac{1}{3}\frac{I^{+++}}{I^{+}}}{1 + \frac{I^{++}}{I^{+}} + \frac{I^{+++}}{I^{+}}}$$

Figures 7.2-4 and 7.2-5 show the R_n vs. η_{pc2} curves for a nominal beam current of 470 mA and both neutralizer low voltage keeper on and off. As can be seen in the figures, R_n becomes non-zero at η_{pc2} values of above 0.45 and increases at a rate similar to that of the 312 mA and 430 mA cases. The maximum η_{pc2} attained for these runs was about 0.90 at a beam current of 500 mA. Excessive thruster recycling occurred as the beam current reached a beam current of 500 mA and it was decided not to proceed beyond this point.

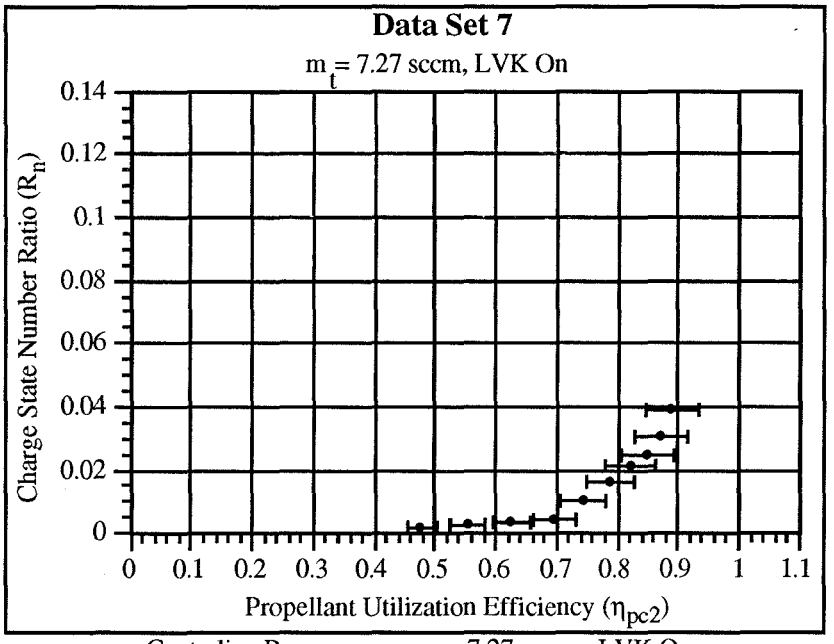

Centerline R_n vs. η_{pc2} - m_t = 7.27 sccm - LVK On

Figure 7.2-4

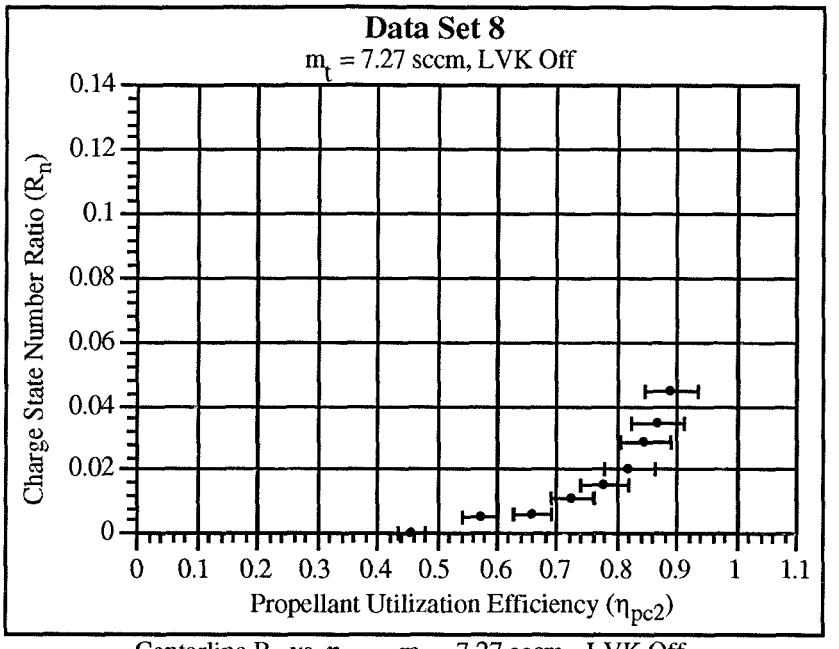

Centerline R_n vs. η_{pc2} - m_t = 7.27 sccm - LVK Off
Figure 7.2-5

7.2.2 Ion Beam Charge State Thrust Correction Factor

Figures 7.2-6 through 7.2-10 display the ion beam charge state thrust correction factors (f_c) as a function of beam current for given propellant flow rates. These profiles were created by applying equation 2.5-14 to the same data sets as were used to generate the centerline R_n vs. η_{pc2} plots discussed above. The data found in these figures can be used for correction of the calculated thrust produced by each 15 cm ion source.

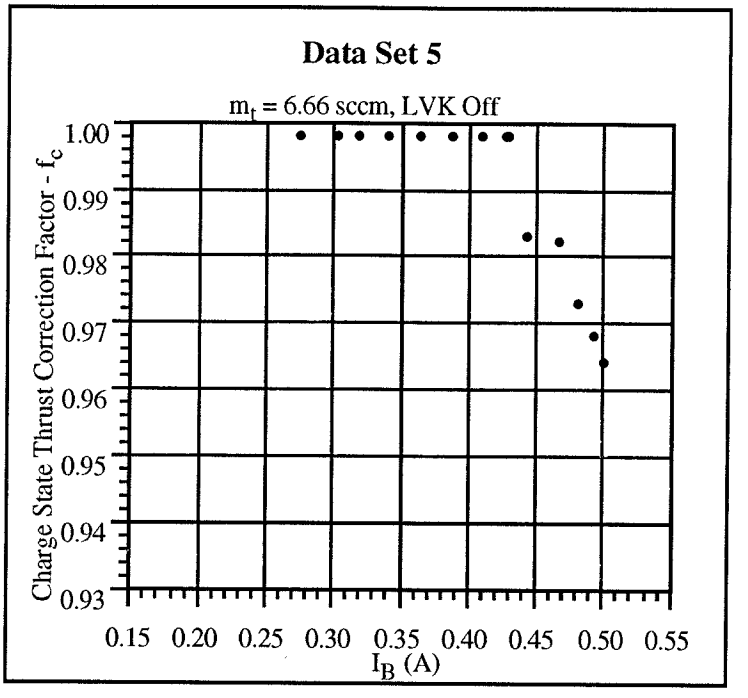

Centerline f_c vs. I_B - 6.66 sccm - LVK Off
Figure 7.2-6

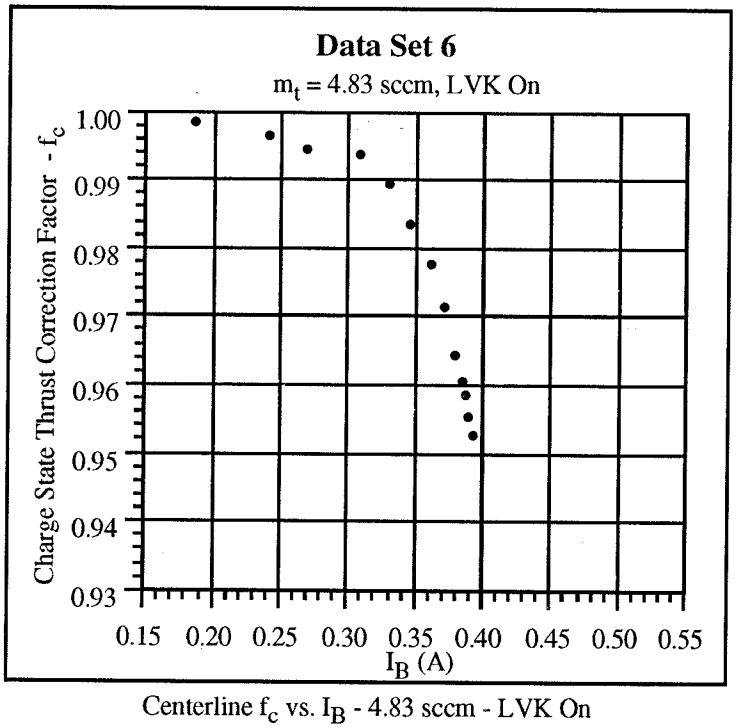

Centerline f_c vs. I_B - 4.83 sccm - LVK On
Figure 7.2-7

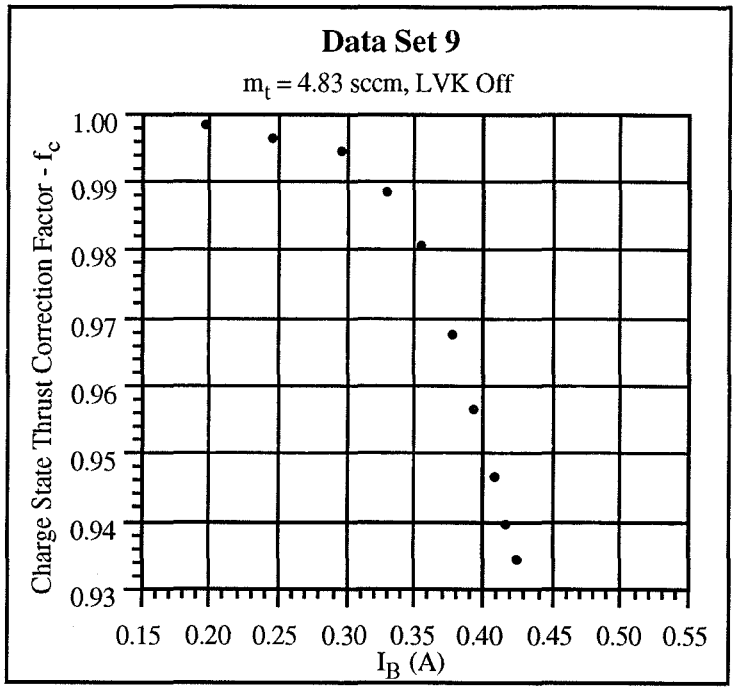

Centerline f_c vs. I_B - 4.38 sccm - LVK Off
Figure 7.2-8

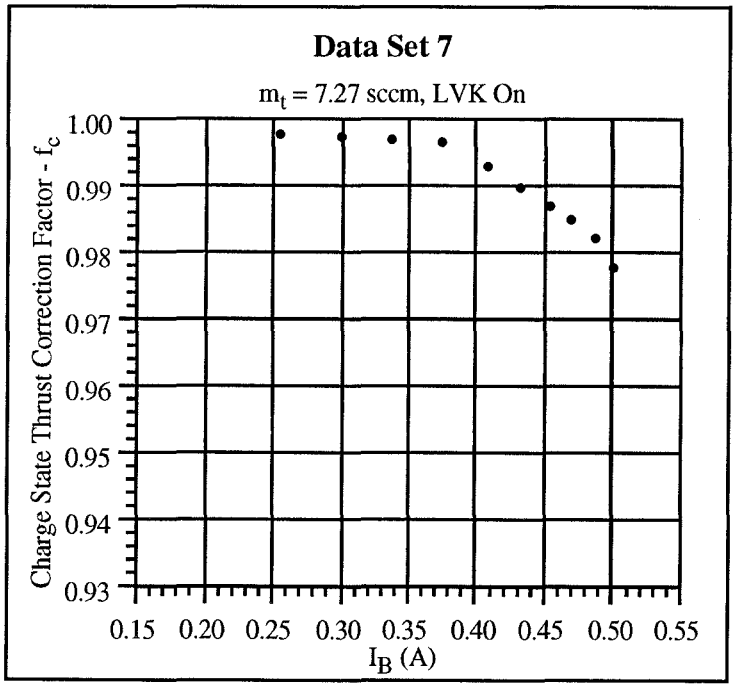

Centerline f_c vs. I_B - 7.27 sccm - LVK On
Figure 7.2-9

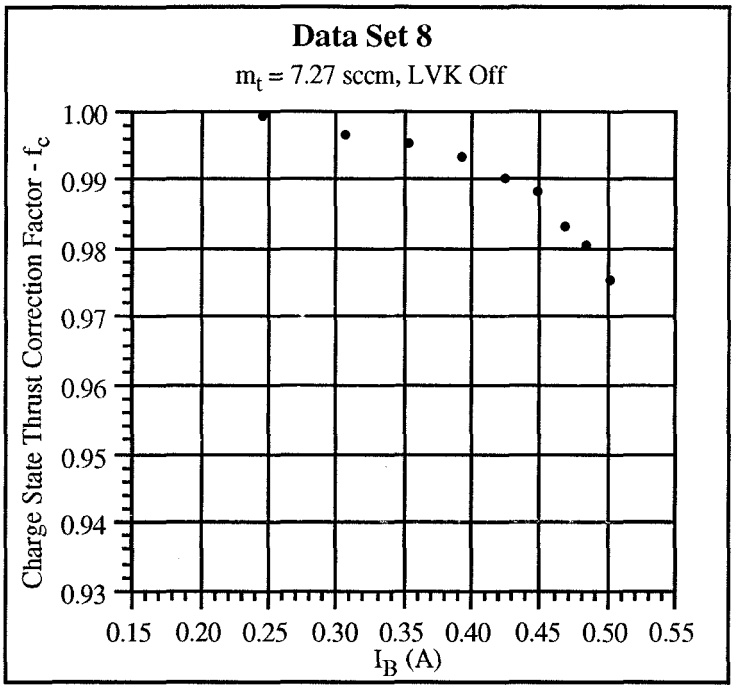

Centerline f_c vs. I_B - 7.27 sccm - LVK Off
Figure 7.2-10

7.2.3 Ion Source Radial Ion Charge Ratio Plots

Figures 7.2-11, 7.2-12, 7.2-14, and 7.2-16 display the collected current radial profiles for singly (I^+) and doubly (I^{++}) charged ions generated by segment A. These profiles were created with measurements from an $\bar{E}x\bar{B}$ mass spectrometer probe, which was located 0.61 m downstream of the thruster. Figures 7.2-13 and 7.2-17 show the resulting charge state number ratio (R_n) radial profiles. Some unexpected characteristics of the radial profiles resulted, however, and there was insufficient data to assess repeatability of the results.

7.2.3.1 Charge State Radial Profile Along X Axis

In reference to figure 7.2-11, it can be seen that the I^+ radial profile is not symmetric about the X = 0 axis and is not smooth with a gaussian or parabolic distribution as might have been expected. Associated with this asymmetry, it can also be observed that zero current was registered at about X = -9 cm and X = +11 cm. Although the profile is not symmetric, a peak in the profile of close to 3.9×10^{-8} amps was found at the X = 0 position. Another interesting characteristic of the profile is the existence of a sudden drop in collected current at approximately X = -2.5 cm.

The shape of this horizontal singly charged ion current profile does not agree well with the Faraday probe current density contour plots generated for segment A. The current density contour plot seems to be fairly symmetric along the X axis through the thruster centerline, unlike the profile in figure 7.2-11. In addition, the current density contour plot does not show any large deviation that would be related to the current drop shown in singly charged ion current profile.

Two potential causes for the asymmetry have been identified. The first deals with the non-circular shape of the ion beams as discussed in section 7.1.1. Since the beam current is not spread evenly about the Y axis, there is the possibility that the X axis profile measured by the $\bar{E}x\bar{B}$ probe would not be evenly distributed either. However, even though the beam shapes were non-circular, the current gradients present within the current density contour plots do not appear to be as pronounced as the charge state profile would require to produce such an unsmooth curve.

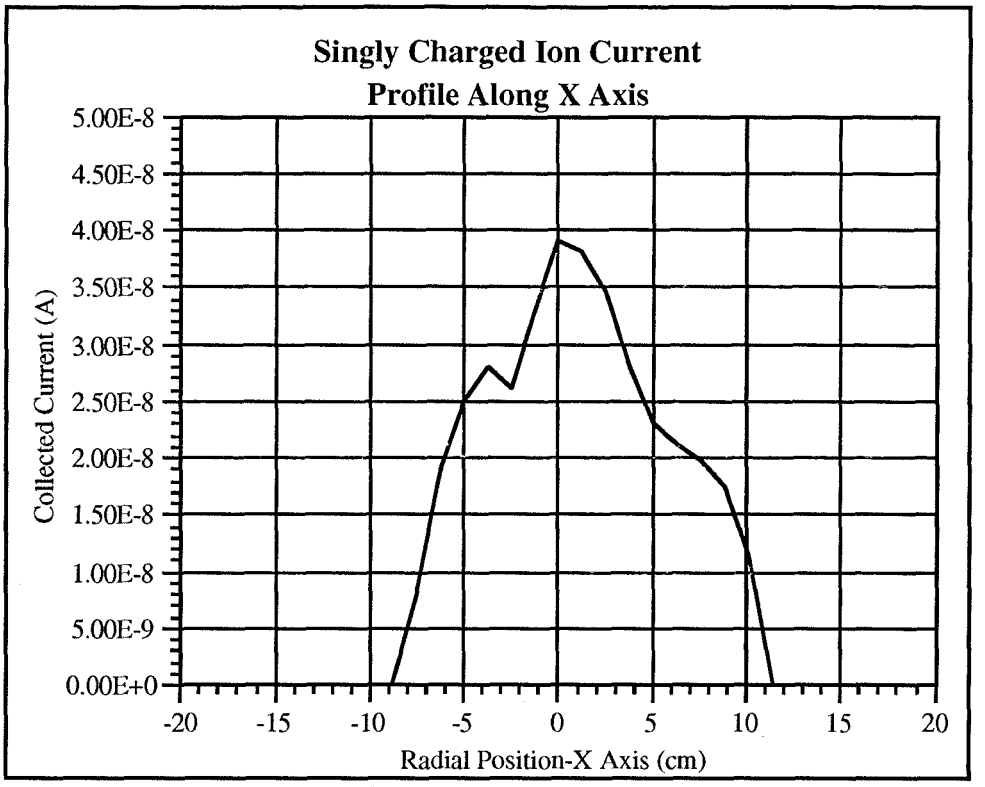

Horizontal Singly Charged Ion Current Profile
Figure 7.2-11

A second possible explanation pertains to the design, construction and motion of the $\bar{E}x\bar{B}$ probe. The collimator slits are aligned with the Y axis and slight misalignments between the slits and differences in slit widths are believed to exist. Ramping of the bias applied to the deflector plates increases the force applied to the ions entering the separator section of the $\bar{E}x\bar{B}$ probe and thus changing the angle of deflection. Ions will be entering the collimator at different angles with respect to the electric field depending upon the location of the $\bar{E}x\bar{B}$ probe. Even though the deflection angle will roughly be the same regardless of where the $\bar{E}x\bar{B}$ probe is located, the misalignment and differences in widths of the slits combined with the angle at which ions will be entering the collimator may cause the filtration of ions to be different. This difference in ion filtration based on probe location may account for the asymmetry observed in figure 7.2-6.

The cause for the current drop registered at X = -2.5 cm is not presently understood and no further data is available to verify repeatability of the result. Review of thruster operational data

during data acquisition at this location did not reveal any thruster operational inconsistencies. However, no similar drop was noted in the vertical I^+ profile as shown in figure 7.2-14 or in the I^{++} profile in figure 7.2-12.

As shown in figure 7.2-12, the doubly charged ion current radial profile is also asymmetric, but more symmetric than the singly charged profile. Unlike the singly charged ion current profile, the 2.45 x 10^{-9} amp peak for doubly charged ions does not lie at X = 0, but at approximately X = +1.25 cm. If the doubly charged profile were assumed symmetric about the peak, the shift along the X axis could possibly be explained by the origin for $\bar{E}x\bar{B}$ radial profiles not being positioned along the discharge chamber centerline.

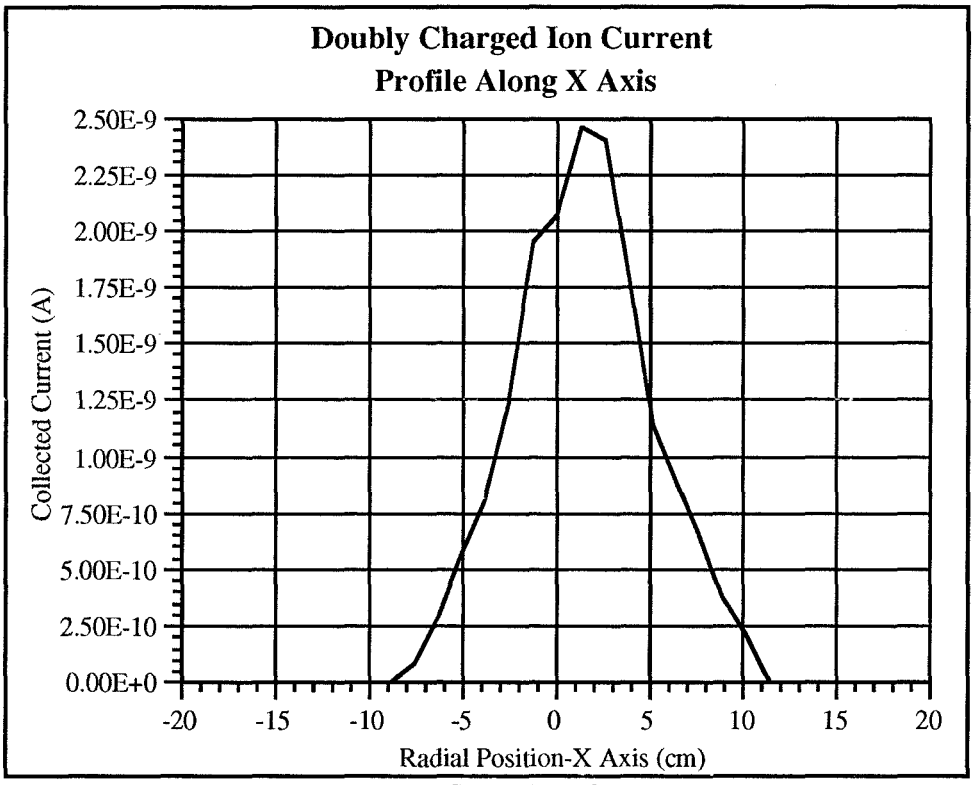

Horizontal Doubly Charged Ion Current Profile
Figure 7.2-12

Figure 7.2-13 displays the charge state number ratio (R_n) as a function of radial position (X). As can be seen in the figure, the profile is not symmetric about the X = 0 position. A prominent

drop in the charge state ratio profile is visible at X = 0 cm with the maximum R_n of 3.5% found at X = +2.5 cm.

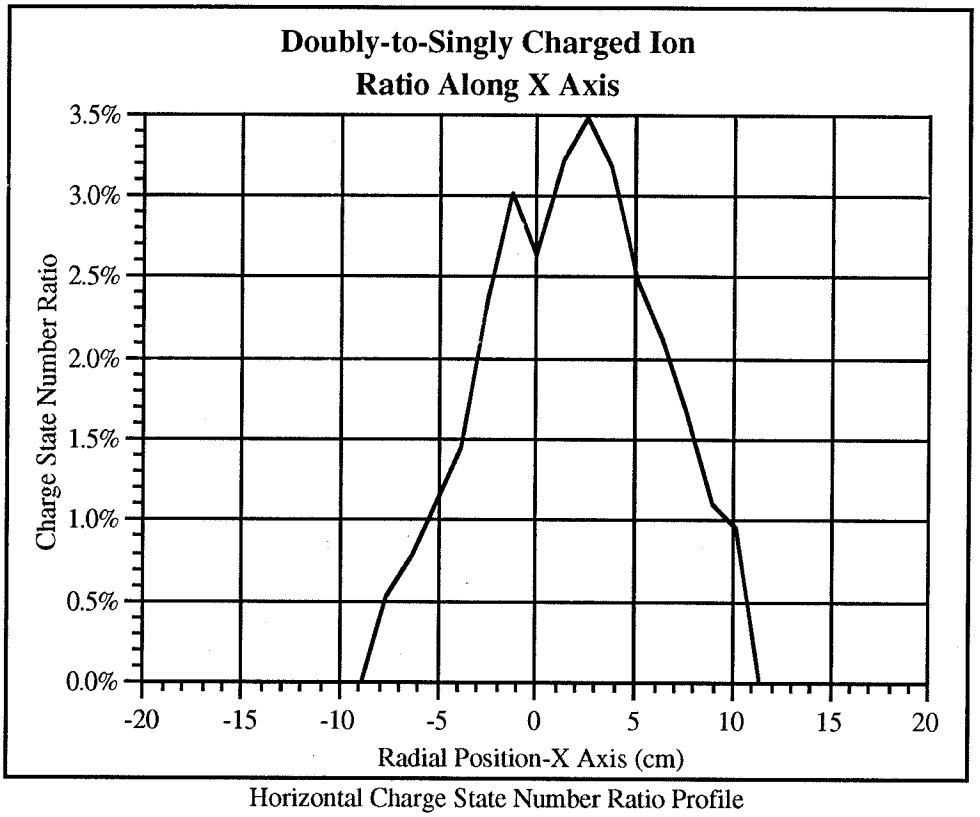

Horizontal Charge State Number Ratio Profile
Figure 7.2-13

7.2.3.2 Charge State Radial Profile Along Y Axis

Figure 7.2-14 displays the singly charged ion current radial distribution obtained from a vertical trace of the $\bar{E}x\bar{B}$ probe passing through the center of segment A. The distribution appears to be symmetric about the Y = 0 axis and has a distribution similar to a gaussian or parabolic profile except near the peak. There it can be seen that the distribution flattens across the peak at three measurement positions. The flat portion of the peak spreads equally in the positive and negative directions demonstrating profile symmetry with a maximum measured current of 4.5 x 10^{-8} A. Additionally, the profile reaches a 0 A level at Y = ±15 cm, further illustrating symmetry of the profile.

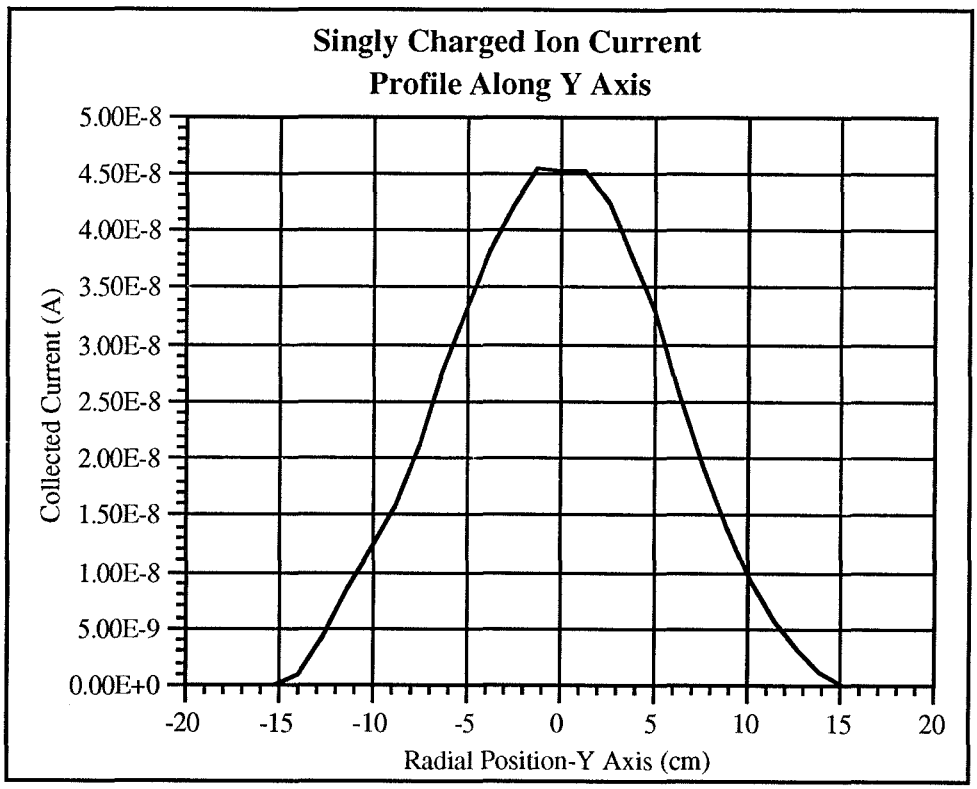

Vertical Singly Charged Ion Current Profile
Figure 7.2-14

The degree of profile symmetry agrees well with the current density plots of segment A. The flatness of the peak also agrees well with the constant current density found toward the center of the contour plots.

In comparison with the X axis I^+ profile, the Y axis I^+ profile is substantially smoother and more symmetric. The X axis profile is also thinner with a lower peak. Differences between X axis and Y axis profile widths are most likely caused by the design of the collimator slits. Alignment of these slits with the Y axis could cause the Y axis profiles to be wider than the X. In reference to figure 7.2-15, the distance from the center of the discharge chamber to the collimator slit is longer when the probe is positioned 10 cm from the centerline along the X axis than when positioned 10 cm along the Y axis. Because of the slit orientation, the probe can view beamlets that are closer to the center of the thruster when moving along the Y axis. Beamlets closer to the center are expected to have greater current and therefore the probe would collect more ions.

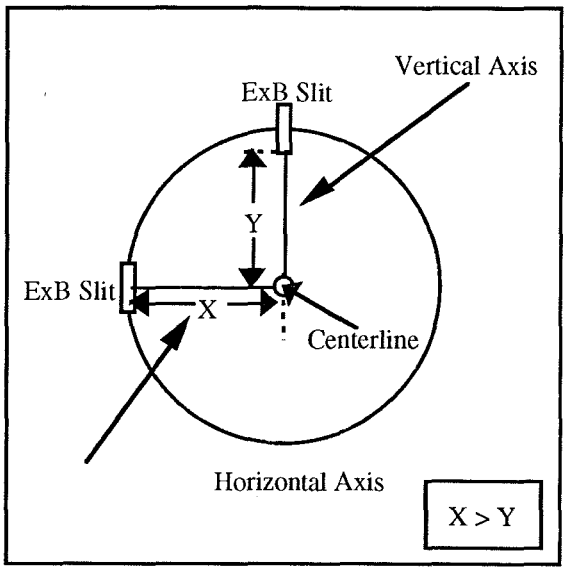

ExB Probe Slit Distance From Centerline
Figure 7.2-15

Although differences in the widths of the profiles can be explained by design of the $\bar{E}x\bar{B}$ probe, difference in peak size cannot. The X axis profile peak was 3.9×10^{-8} A while that for the Y axis was 4.5×10^{-8} A. Thruster operational parameters were reviewed and there does not seem to be a sufficient difference between the two data sets to cause the 13% discrepancy. It is conceivable that the operational parameters for segment A drifted from the recorded values during data collection, but it would be unlikely for this to cause a 13% difference.

The Y axis I^{++} profile shown in figure 7.2-16 is neither as smooth or symmetric as the Y axis I^{+} profile although it is somewhat symmetric about the Y = 0 axis. Symmetry of the profile is not evident at the peak of the profile. A substantial current drop is visible within the peak region at about Y = 0 and the current maximum, which is located at Y = -1.25 cm, has a value of 2.45×10^{-9} A. The profile reaches 0 amps at Y = -14 cm and +15 cm, again showing slight asymmetry in the profile. Difficulty in distinguishing a doubly charged ion current (I^{++}) in the I_c vs. V_d curve at Y = -14 cm could be the cause. Inexact positioning of the $\bar{E}x\bar{B}$ probe could also have been the cause if the probe's path did not pass through the centerline of the discharge chamber.

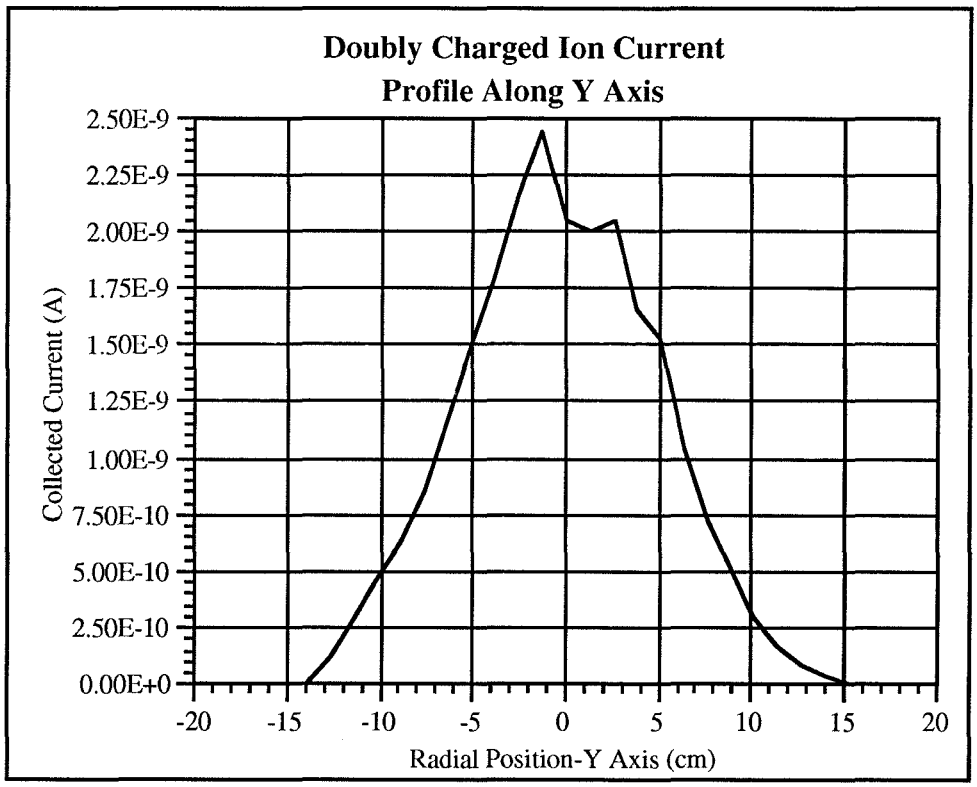

Vertical Doubly Charged Ion Current Profile
Figure 7.2-16

The large decrease in the Y axis I^{++} profile at Y = 0 cm is similar to those identified in the X axis I^{+} profile. Likewise, the basis for this current drop is not known. Width of the Y axis I^{++} profile is also greater than the X axis I^{++} profile. Discussion pertaining to the Y axis I^{+} profile being wider than that of the X axis is also applicable here. Both the Y axis profile and X I^{++} axis profile peaks were 2.45 x 10^{-9} A.

The doubly to singly charged ion ratio radial profile is shown in figure 7.2-17. The profile extends from approximately the Y = -14 cm position to Y = +15 cm with a maximum value of 2.7% at Y = -1.25 cm and the ratio value at Y = 0 is close to 2.25%.

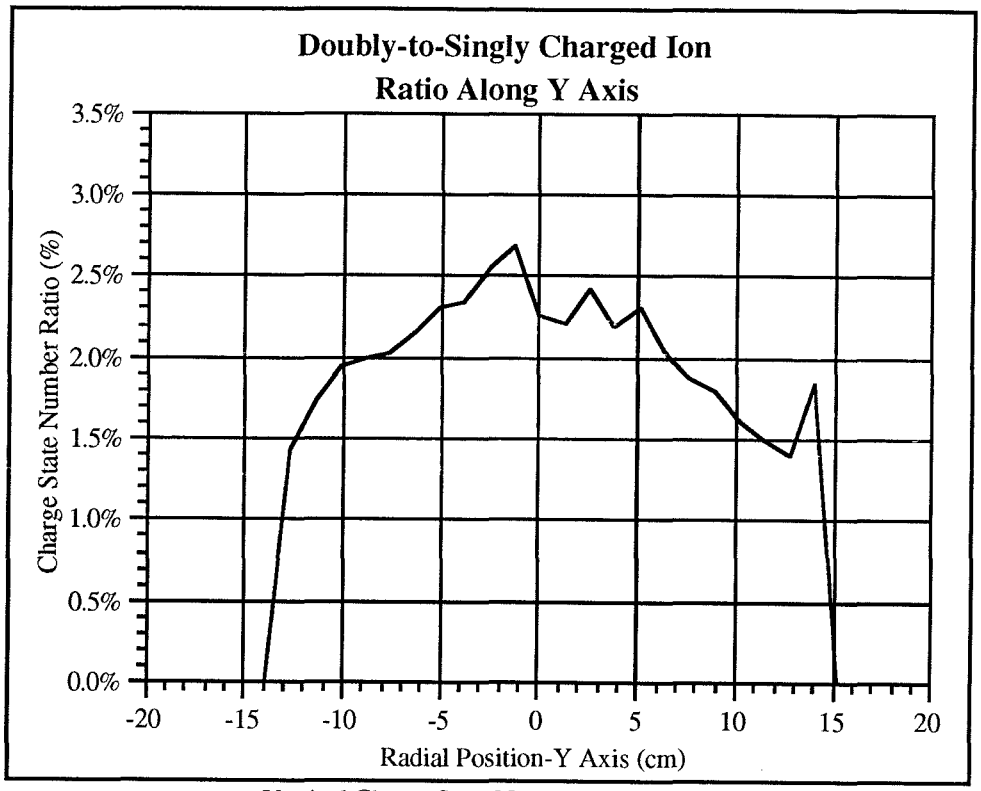

Vertical Charge State Number Ratio Profile
Figure 7.2-17

A possible cause for the ratio profile to produce a R_n of zero at -14 cm and +15 cm lies in the spacing resolution between data points. The discussion above regarding the I^{++} profile reaching zero at these locations will help describe this. Comparison between the X axis R_n profile and the Y axis R_n reveals substantial differences. The first noticeable difference is the relative widths of the profiles. As can be seen in figures 7.2-13 and 7.2-17, the Y axis R_n profile is approximately 50% wider at the base (0 A) and up to 145% wider at R_n = 1.5%. It is suspected that these differences are related to the $\vec{E}x\vec{B}$ probe design. A second difference between the two profiles is the maximum R_n attained by each. The Y axis profile reaches a maximum of 2.7% and the X axis profile has a maximum of about 3.5%, a relative difference of close to 30%.

Chapter 8 Conclusions

8.1 Performance

The charge state thrust correction factor (f_c) is given in figures 7.2-6 through 7.2-10 as a function of metered beam current (I_B) for three propellant flow rates. The values for f_c are based upon the measured charge state number ratio (R_n) along the centerline of the segment A discharge chamber. According to the R_n vs. X plots given in figures 7.2-13 and 7.2-17, the maximum value for R_n is not located along the centerline, and therefore, these f_c values cannot be considered worst case. The worst case values, in reference to the R_n vs. X profiles, are between 17 and 30 percent larger than the centerline values.

The propellant utilization efficiency (η_{pc2}), corrected for doubly charged ion production, is given in figures 7.2-1 through 7.2-5 as a function of the centerline charge state number ratio (R_n) for the same three propellant flow rates used for determination of f_c. The η_{pc2} values given in these figures were also corrected for ingestion of propellant into the discharge chamber due to facility background pressure. Some of the η_{pc2} values given in figures 7.2-2 and 7.2-3 were greater than 1.0. In all but one of these cases, the uncertainty in the measurements was sufficiently large to account for the greater than 1 values. For the single case, shown in figure 7.2-3 at $R_n = 0.14$, in which the uncertainty could not account for the greater than 1 value, the production of triply charged ions is believed to be the cause.

8.2 Spacecraft Interactions

Direct ion impingement was the only interaction effect addressed in this report. So long as spacecraft components are not in the path of primary ions extracted from the thruster accelerator system, the potential for degradation should be minimal. The divergence of the extracted ion beams from segments A, B and C for four different operating conditions of the thruster were evaluated. Beam divergence angles for R = 0.893 cases ranged from 10° to 16° and from 17° to 22° for cases in which R = 0.643. The beam divergence angle was generally greater for segment A than for either segments B or C. These values are presented in figures 7.1-22 through 7.1-24.

Beam divergence appears to primarily be a function of R ratio and ion source and not of beam current or distance from the thruster.

8.3 Lifetime

Ion beam current density asymmetries, downstream beam flatness parameters on the order of 0.25, and peaked charge state number ratio radial profiles are all indications of uneven grid erosion and signify non-ideal grid lifetimes. However, these lifetime limiting characteristics observed here may be out weighed by the increased resistance to erosion of grids made of carbon as opposed to molybdenum.

8.4 Interaction of Multiple Ion Beams

Possible interaction between ion beams was observed through differences in current density contour plots using data collected from the simultaneous operation of multiple ion sources to those generated with superimposed data obtained from individual ion source operation. Some discrepancies were also noted in the integrated beam currents between these two data sets, also indicating possible interaction. Generally the consistency was strong between the current density contour plots generated with real and superimposed data., and the differences observed, which indicated beam interaction, could possibly be explained by slight inconsistencies within the investigation to account for background plasma biases and charge exchange ion effects. Numerically integrated beam currents calculated with real mostly agreed with those calculated with synthesized data within the limits of uncertainty and those that did not could also be explained by background plasma bias and charge exchange effects.

8.5 Repeatability of Construction and Operation

Differences in the beam current density profiles observed for individual operation of each segment demonstrated inconsistencies in construction or fabrication of the ion sources, accelerator systems, or the integration of the system. These differences were observed in both the shape of the individual ion beams as well as the orientation of the beams profiles with respect to

the thruster. Due to some differences between the ion beam profiles measured in an early portion of this study and those presented here signify that the differences in the assembly of the ion optics is the most likely cause.

8.6 Future Work and Recommendations

The beam divergence thrust correction factor (f_d) and the beam flatness parameter (F) measured close to the thruster were not investigated in this effort. Both of these ion beam parameters would be of great value in the overall plume characterization. It is suggested that these be investigated in the future.

In the assessment of interaction between multiple ion beams it may be possible to filter out the charge exchange effects that are believed to have been observed. This could be done by applying a form of equation 6.1-4 to each of the superimposed Faraday probe measurements in order to simulate the same charge exchange environment experienced during the data acquisition from multiple simultaneously operating ion sources. This would facilitate a more appropriate comparison between the two data types.

Large discrepancies exist between X and Y axis charge state number ratio profiles with regard to symmetry and profile shape. This was most likely due to design of the $\bar{E}x\bar{B}$ probe. The applicability of this probe design to investigations of off-axis ion collection should be evaluated. Use of a slits instead of small holes on the collimator and collector may resolve some of these differences. Orientation of the $\vec{E}$ and $\vec{B}$ fields with respect to probe motion should also be investigated.

References

[1] "Ion Propulsion for Spacecraft," NASA Publication, Lewis Research Center, Cleveland, OH, 1977.

[2] Uphoff, C., Reinert, R., French, J.R., "Is It Sep Yet?," Presented at the 30th Space Congress, Cocoa Beach, FL, April 1993.

[3] Yen, C.L., and Sauer, C.G., "Nuclear Electric Propulsion for Future NASA Space Science Missions," IEPC Paper No. 91-035, 22nd International Electric Propulsion Conference, Viareggio, Italy, October 1991.

[4] Sauer, C.G., "Application of Solar Electric Propulsion for Future Planetary Missions," AIAA Paper No. 87-1053, 19th International Electric Propulsion Conference, Colorado Springs, CO, May 1987.

[5] Gilland, J.H., "Synergistic Use of High and Low Thrust Propulsion Systems for Piloted Missions to Mars," AIAA Paper 91-2346, 27th Joint Propulsion Conference, Sacramento, CA, June 1991.

[6] Byers, D.C., Rawlin, V.K., "Critical Elements of Electron-Bombardment Propulsion for Large Space Systems," AIAA Paper No. 76-1039, 12th International Electric Propulsion Conferenece, Key Biscayne, FL, November 1976.

[7] Brophy, J.R., Pless, L.C., Mueller, J., and Anderson, J.R., "Operating Characteristics of a 15-cm dia. Ion Engine for Small Planetary Spacecraft," IEPC Paper No 93-110, 23rd International Electric Propulsion Conference, Seattle, WA, September 1993.

[8] Brophy, J.R., "A Segmented Ion Engine Design for Solar Electric Propulsion Systems," IAF Paper No. 92-0608, 43rd Congress of the International Astronautical Federation, Washington, DC, August 28-September 5, 1992.

[9] Carruth, M.R. Jr., "A Review of Studies on Ion Thruster Beam and Charge Exchange Plasmas," AIAA Paper 82-1944, 16th International Electric Propulsion Conference, New Orleans, LA, November 1982.

[10] Kaufman, Harold R., "Technology of Electron-Bomabardment Ion Thrusters," Advances in Electronics and Electron Physics, Edited by L. Marton, Academic Press, New York, 1974, pg. 265.

[11] Jahn, Robert G.,Physics of Electric Propulsion, McGraw-Hill, New York, 1968.

[12] Cybulski, R.J., et al., "Results from SERT I Ion Rocket Flight Test," NASA TN D-2718, 1965.

[13] Kerslake, W.R., Goldman, R.G., and Nieberding, W.C., "SERT II Mission Thruster Performance and In-Flight Thrust Measurements," Journal of Spacecraft and Rockets, Vol 8, No 3, March 1971, pp 209-213.

[14] S. Shimada, K. Satoh, Y. Gotoh, E. Nishida, T. Noro, H Takegahara, K Nakamaru, H. Nagano, "Ion Thruster Endurance Test Using Development Model Thruster for ETS-VI," IEPC Paper No. 93-169, 23rd International Electric Propulsion Conference, Seattle, WA, September 13-16, 1993.

[15] Shimada, S.et al., "20 mN Class Xenon Ion Thruster for ETS-VI," AIAA Paper No. 87-1029, 19th International Electric Propulsion Conference, Colorado Springs, CO, May 1987.

[16] Shimada, S. et al., "Ion Engine System Development for ETS-VI," IEPC Paper No. 91-145, 22nd International Electric Propulsion Conference, Viareggio, Italy, October 1991.

[17] Sovey, J.S., Rawlin, V.K., "Characterization of In-Flight Performance of Ion Propulsion Systems," AIAA Paper No. 93-2217, 29th Joint Propulsion Conference, Monterey, CA, June 1993.

[18] Wilbur, P.J., Buchholtz, B.W., "Surface Engineering Using Ion Thruster Technology," AIAA Paper No. 94-3235, 30th Joint Propulsion Conference, Indianapolis, IN, June 1994.

[19] Owens, W.L. Jr., "A Noble Gas Ion Propulsion System", AIAA Paper 73-1114, 10th Electric Propulsion Conference, Lake Tahoe, NV, October 1973.

[20] Rawlin, V.K., "Operation of the J-Series Thruster Using Inert Gas", NASA TM-82977, 1982.

[21] Garner, C.E., Brophy, J.R., Aston, G., "The Effects of Gas Mixtures on Ion Engine Erosion and Performance," AIAA Paper No. 87-1080, 19th International Electric Propulsion Conference, Colorado Springs, CO, May 1987.

[22] Byers, D.C., Kerslake, W.R., Grobman, J., NASA TN D-2401, 1964.

[23] Milder, N.L., NASA TN D-2592, 1965.

[24] Leifer, S.D., Rapp, D., Saunders, W.A., "Electrostatic Propulsion Using C_{60} Molecules," Journal of Propulsion and Power, Vol. 8, No. 6, Nov-Dec 1992, pp 1297-1300.

[25] Kerslake, W.R., and Pawlik, E.V., " Additional Studies of Screen and Accelerator Grids for Electron-Bombardment Ion Thrusters," NASA TN D-1411, 1963.

[26] Meserole, J.S., Hedges, D.E., "Comparison of Erosion Rates of Carbon-Carbon and Molybdenum Ion Optics," IEPC Paper No. 93-111, 23rd International Electric Propulsion Conference, Seattle, WA, September 1993.

[27] Hedges, D.E., and Meserole, J.S., "Demonstration and Evaluation of Carbon-Carbon Ion Optics," Journal of Propulsion and Power, Vol. 10, No. 2, March-April 1994, pp. 255-261.

[28] Garner, C.E., and Brophy, J.R., "Fabrication and Testing of Carbon-Carbon Grids for Ion Optics," AIAA Paper No. 92-3149, 28th Joint Propulsion Conference, Nashville, TN, July 1992.

[29] Mueller, J., Brown, D.K., Garner, C.E., Brophy, J.R., "Fabrication of Carbon-Carbon Grids for Ion Optics," IEPC Paper No. 93-112, 23rd International Electric Propulsion Conference, Seattle, WA, Septemeber 1993.

[30] Brophy, J.R., Pless, L.C., Garner, C.E., "Ion Engine Endurance Testing at High Background Pressures," AIAA Paper No. 92-3205, 28th Joint Propulsion Conference, Nashville, TN, July 1992.

[31] Brophy, J.R., "Near Term, 100kW Class ion Engines," AIAA Paper No. 91-3566, Conference on Advanced SEI Technologies, Cleveland, OH, September 1991.

[32] Personal Communication with Charles E. Garner of JPL Advanced Propulsion Group.

[33] Aston, G., "The Ion-Optics of a Two-Grid Electron-Bombardment Thruster," NASA CR-135034, Department of Mechanical Engineering, Colorado State University, May 1976.

[34] Aston, G., Kaufman, H.R., Wilbur, P.J., "Ion Beam Divergence Characteristics of Two-Grid Accelerator Systems," AIAA Journal, Vol. 16, No. 5, May 1978, pp. 516-524.

[35] Aston, G., Kaufman, H.R., "Ion Beam Divergence Characteristics of Three-Grid Accelerator Systems," AIAA Journal, Vol. 17, No. 1, January 1979, pp. 64-70.

[36] Vahrenkamp, R.P., "Measurement of Double Charged Ions in the Beam of a 30-cm Mercury Bombardment Thruster," AIAA Paper 73-1057, 10th Electric Propulsion Conference, Lake Tahoe, NV, October 1973.

[37] Sovey, J.S., "Improved Ion Containment Using a Ring-Cusp Ion Thruster," NASA TM-82990, 1982.

[38] Osher, J.E., Plasma Diagnostic Techniques, Edited by Huddlestone, R.H., Leonard, S.L, Academic Press, New York, 1965, pp. 537-540.

[39] Byers, D., "2.5 kW Advanced Technology Ion Thruster," NASA CR-134687, Hughes Aircraft Company, Malibu, CA,

[40] Personal Communication with Dr. John R. Anderson of JPL Advanced Propulsion Group.

[41] Personal Communication with Charles E. Garner of JPL Advanced Propulsion Group.

[42] Patterson, M.J., Haag, T.W., Williams, G.J., Jr., "Derated Ion Thruster Development Status," AIAA Paper No. 92-3335, 29th Joint Propulsion Conference, Monterey, CA, June 1993.

[43] Patterson, M.J., Haag, T.W., and Hovan, S.A., "Performance of the NASA 30 cm Ion Thruster," IEPC Paper No. 93-108, 23rd International Electric Propulsion Conference, Seattle, WA, Sept. 1993.

[44] Brophy, J.R., Mueller, J., Pless, L.C., Tierney, C.M., Goodfellow, K.D., Anderson, J.R., "Segmented Ion Engine Operation and Performance," AIAA Paper No. 94-2851, 30th Joint Propulsion Conference, Indianapolis, IN, June 1994.

[45] Mueller, J., Brophy, J.R., Brown, K., Garner, C.E., "Performance Characterization of 15-cm Carbon-Carbon Composite Grids," AIAA Paper No. 94-3118, 30th Joint Propulsion Conference, Indianapolis, IN, June 1994.

[46] J. Brophy, C. Garner, "A 5,000 Hour Xenon Hollow Cathod Life Test," AIAA Paper No. 91-2122, 27th Joint Propulsion Conference, Sacramento, CA, June 1991.

[47] Anderson, J.R., Fitzgerald, D., "Experimental Investigations of Fullerene Propellant for Ion Propulsion," IEPC Paper No. 93-033, 23rd International Electric Propulsion Conference, Seattle, WA, September 1993.

[48] Reserved Reference

[49] Smirnov, B.M., and Chibisov, M.I., "Resonance Charge Transfer in Inert Gases," Soviet Physics - Technical Physics, Vol. 10, No. 1, July 1965, pp 88-92.

[50] Randolf, T., Day, M., Kim, V., Kaufman, H., Zhurin, V., Kozubsky, K., "Facility Effects on SPT Thruster Testing," IEPC Paper No. 93-093, 23rd International Electric Propulsion Conference , Seattle, WA, Sept. 1993.

[51] Swokowski, Earl W., Calculus with Analytic Geometry, Third Edition, PWS Publishers, Boston, 1984, pp. 239-245.

[52] M. Tierney, J Brophinteraction [65].gine Plume Characteristics," AIAA Paper No. 94-2740, 30th Joint Propulsion Conference, Indianapolis, IN, June 1994.

[53] Fearn, D.G., Martin, A.R., Smith, P., "Ion Propulsion Development in the U.K.," IAF Paper No. 93-S.5.490, 49th Congress of the International Astronautical Federation, Graz, Austria, October 1993.

[54] Groh, K.H., Kreiling, N., Loeb, H.W., Schmidkunz, Th., "Geam Diagnostics for the Characterization of Ion Thruster Beam Parameters," IEPC Paper No. 91-083, 22nd International Electric Propulsion Conference, Viareggio, Italy, October 1991.

[55] Grafoil® Flexible Graphite, Union Carbide Corporation, Electronics Division.

[56] Igor Pro 2.01, © 1994, WaveMetrics, Inc.

[57] Reserved Reference

[58] Spyglass® Transform 3.01, © 1990-1993 Spyglass.

[59] Personal Communication with K.D. Goodfellow of JPL Advanced Propulsion Group.

[60] Reserved Reference

[61] Loctite™, Loctite Corporation.

[62] Macintosh™, Apple Computer, Inc.

[63] Reserved Reference

[64] Fearn, D.G., "A Mission to Pluto Using Nuclear Electric Propulsion," IEPC Paper No. 93-200, 23rd International Electric Propulsion Conference , Seattle, WA, Sept. 1993.

[65] Fitzgerald, D.J., "Factors in the Design of Spacecraft Utilizing Multiple Electric Thrusters," AIAA Paper No. 75-404, 11th Electric Propulsion Conference, New Orleans, LA, March 1975.

[66] Garner, C.E., et al., "Experimental Evaluation of a Russian Anode Layer Thruster," AIAA Paper No. 94-3010, 30th Joint Propulsion Conference, Indianapolis, IN, June 1994.

[67] Garner, C.E., Polk, J.E., Pless, L.C., Goodfellow, K.D., Brophy, J.R., "Performance Evaluation and Life Testing of the SPT-100," IEPC Paper No. 93-091, 23rd International Electric Propulsion Conference, Seattle, WA, Sept., 1988.

Appendix A

Resistor Sets

Channel	Resistor Set 1 (Ω)	Resistor Set 2 (Ω)	Resistor Set 3 (Ω)	Resistor Set 4 (Ω)
0	4.249	17.140	3.576	8.668
1	4.312	16.899	3.662	8.549
2	4.265	16.708	3.696	8.497
3	4.329	16.983	3.671	8.549
4	4.426	16.630	3.685	8.578
5	4.338	16.749	3.641	8.544
6	4.290	16.696	3.711	8.528
7	4.305	16.775	3.680	8.556
8	4.358	16.725	3.589	8.487
9	4.322	16.643	3.681	8.579
10	4.300	16.665	3.625	8.612
11	4.342	16.778	3.671	8.541
12	4.278	16.670	3.611	8.607
13	4.304	16.800	3.755	8.622
14	4.324	16.711	3.691	8.569
15	4.274	16.653	3.670	8.614
16	4.289	16.848	3.648	8.652
17	4.401	16.791	3.641	8.568
18	4.284	16.730	3.626	8.549
19	4.283	16.633	3.664	8.608
20	4.294	16.779	3.575	8.539
21	4.344	16.996	3.611	8.639
22	4.290	17.101	3.702	8.483
23	4.340	16.691	3.701	8.534

TABLE A-2 Faraday Probe Thruster Operating Conditions

Run #	Seg	I_B (mA)	z (m)	V_S (V)	V_A (V)	V_D (V)	V_{cn} (V)	$\dot{m}_A$ (sccm)	$\dot{m}_B$ (sccm)	$\dot{m}_C$ (sccm)	$\sum \dot{m}_t$ (sccm)	$\dot{m}_n$ (sccm)	$\dot{m}_f$ (sccm)	η_p	R Ratio	Bias (mA)	R Set
15.5	ABC	430	0.356	1250	-150	-100	6.30	6.72	6.42	6.74	19.88	23.92	43.80	0.887	0.893	0.030	1
16.0	ABC	430	0.508	1250	-150	-100	5.97	6.56	6.22	6.44	19.22	22.89	42.11	0.936	0.893	0.030	1
16.1	ABC	430	0.660	1250	-150	-100	5.84	6.47	6.09	6.29	18.55	22.66	41.21	0.950	0.893	0.030	1
16.2	ABC	430	0.813	1250	-150	-100	5.98	6.45	6.09	6.26	18.80	22.50	41.30	0.960	0.893	0.030	1
16.3	ABC	430	0.965	1250	-150	-100	7.77	6.74	6.50	6.92	20.16	23.71	43.87	0.896	0.893	0.030	1
17.4	BC	430	0.660	1250	-150	-100	5.70		6.12	6.39	12.51	15.14	27.65	0.964	0.893	0.025	1
17.5	BC	430	0.813	1250	-150	-100	5.68		6.14	6.36	12.50	15.24	27.74	0.968	0.893	0.025	1
17.6	BC	430	0.965	1250	-150	-100	5.64		6.07	6.31	12.38	15.01	27.39	0.973	0.893	0.025	1
20.0	BC	430	0.356	1250	-150	-100	6.82		6.81	7.12	13.93	16.55	30.48	0.869	0.893	0.025	1
20.1	BC	430	0.508	1250	-150	-100	7.99		6.75	7.07	13.82	16.42	30.24	0.875	0.893	0.025	1
18.1	AC	430	0.356	1250	-150	-100	5.82	6.44		6.31	12.75	15.32	28.07	0.943	0.893	0.025	1
18.2	AC	430	0.508	1250	-150	-100	5.71	6.44		6.26	12.70	15.32	28.02	0.944	0.893	0.025	1
18.3	AC	430	0.660	1250	-150	-100	5.91	6.41		6.26	12.67	15.37	28.04	0.944	0.893	0.025	1
18.4	AC	430	0.813	1250	-150	-100	5.73	6.42		6.24	12.66	15.29	27.95	0.945	0.893	0.025	1
18.6	AC	430	0.965	1250	-150	-100	5.65	6.40		6.21	12.61	15.21	27.82	0.958	0.893	0.025	1
19.0	AB	430	0.356	1250	-150	-100	8.08	7.05	7.34		14.39	16.84	31.23	0.829	0.893	0.025	1
19.1	AB	430	0.508	1250	-150	-100	8.07	7.02	7.21		14.23	16.60	30.83	0.847	0.893	0.025	1
19.2	AB	430	0.660	1250	-150	-100	N/A	6.98	7.11		14.09	***16.53***	***30.62***	N/A	0.893	0.025	1
19.3	AB	430	0.813	1250	-150	-100	7.90	6.99	7.04		14.03	16.53	30.56	0.854	0.893	0.025	1
19.4	AB	430	0.965	1250	-150	-100	7.70	6.92	6.93		13.85	16.24	30.09	0.867	0.893	0.025	1
21.0	A	430	0.356	1250	-150	-100	4.45	6.76			6.76	8.05	14.81	0.890	0.893	0.020	1
21.1	A	430	0.508	1250	-150	-100	4.45	6.73			6.73	8.08	14.81	0.885	0.893	0.020	1
21.2	A	430	0.660	1250	-150	-100	4.42	6.70			6.70	8.05	14.75	0.886	0.893	0.020	1
21.4	A	430	0.813	1250	-150	-100	4.46	6.69			6.69	8.05	14.74	0.902	0.893	0.020	1
21.5	A	430	0.965	1250	-150	-100	4.50	6.67			6.67	7.98	14.65	0.903	0.893	0.020	1
22.0	B	430	0.508	1250	-150	-100	4.50		6.65		6.65	7.92	14.57	0.939	0.893	0.020	1
22.1	B	430	0.660	1250	-150	-100	4.59		6.60		6.60	8.13	14.73	0.901	0.893	0.020	1
22.2	B	430	0.813	1250	-150	-100	4.81		6.55		6.55	8.10	14.65	0.906	0.893	0.020	1
22.3	B	430	0.965	1250	-150	-100	4.81		6.52		6.52	7.98	14.50	0.915	0.893	0.020	1
22.4	B	430	0.356	1250	-150	-100	4.68		6.45		6.45	8.00	14.45	0.928	0.893	0.020	1

TABLE A-2 Faraday Probe Thruster Operating Conditions

Run #	Seg	I_B (mA)	z (m)	V_S (V)	V_A (V)	V_D (V)	V_{cn} (V)	$\dot{m}_A$ (sccm)	$\dot{m}_B$ (sccm)	$\dot{m}_C$ (sccm)	$\sum \dot{m}_t$ (sccm)	$\dot{m}_n$ (sccm)	$\dot{m}_f$ (sccm)	η_p	R Ratio	Bias (mA)	R Set
23.0	C	430	0.508	1250	-150	-100	4.22			6.49	6.49	7.33	13.82	0.950	0.893	0.020	1
23.1	C	430	0.660	1250	-150	-100	3.02			6.44	6.44	8.23	14.67	0.922	0.893	0.020	1
23.2	C	430	0.813	1250	-150	-100	3.51			6.44	6.44	8.16	14.60	0.931	0.893	0.020	1
23.3	C	430	0.965	1250	-150	-100	3.58			6.44	6.44	8.13	14.57	0.931	0.893	0.020	1
23.4	C	430	0.356	1250	-150	-100	3.50			6.34	6.34	8.13	14.47	0.931	0.893	0.020	1
24.0	ABC	312	0.356	1250	-150	-100	19.16	4.56	4.49	4.40	13.45	16.01	29.46	0.966	0.893	0.025	1
24.1	ABC	312	0.660	1250	-150	-100	23.24	4.57	4.49	4.40	13.46	15.86	29.32	0.975	0.893	0.025	1
24.2	ABC	312	0.965	1250	-150	-100	27.06	4.47	4.41	4.32	13.20	15.57	28.77	0.999	0.893	0.025	1
25.0	AB	312	0.356	1250	-150	-100	5.54	4.51	4.62		9.13	10.63	19.76	0.950	0.893	0.020	1
25.1	AB	312	0.660	1250	-150	-100	5.58	4.52	4.62		9.14	10.71	19.85	0.946	0.893	0.020	1
25.2	AB	312	0.965	1250	-150	-100	5.57	4.49	4.59		9.08	10.58	19.66	0.963	0.893	0.020	1
26.2	AC	312	0.965	1250	-150	-100	5.87	4.43		4.55	8.98	10.63	19.61	0.972	0.893	0.020	1
26.3	AC	312	0.356	1250	-150	-100	5.90	4.34		4.37	8.71	10.42	19.13	0.992	0.893	0.020	1
26.4	AC	312	0.660	1250	-150	-100	5.94	4.30		4.35	8.65	10.32	18.97	1.005	0.893	0.020	1
27.0	BC	312	0.356	1250	-150	-100	5.90		4.28	4.22	8.50	10.32	18.82	1.024	0.893	0.020	1
27.1	BC	312	0.660	1250	-150	-100	5.95		4.23	4.17	8.40	10.32	18.72	1.032	0.893	0.020	1
27.2	BC	312	0.965	1250	-150	-100	6.07		4.23	4.17	8.40	10.24	18.64	1.038	0.893	0.020	1
28.0	C	312	0.356	1250	-150	-100	4.38			4.12	4.12	4.96	9.08	1.064	0.893	0.025	1
28.1	C	312	0.660	1250	-150	-100	N/A			***4.10***	***4.10***	***4.96***	***9.06***	N/A	0.893	0.025	1
28.2	C	312	0.965	1250	-150	-100	4.37			4.09	4.09	4.96	9.05	1.067	0.893	0.025	1
30.0	A	312	0.356	1250	-150	-100	4.20	4.14			4.14	4.60	8.74	1.060	0.893	0.025	1
30.1	A	312	0.660	1250	-150	-100	4.33	4.14			4.14	4.65	8.79	1.050	0.893	0.025	1
30.2	A	312	0.965	1250	-150	-100	N/A	***4.14***			***4.14***	***4.65***	***8.79***	N/A	0.893	0.025	1
31.0	B	312	0.356	1250	-150	-100	N/A		***4.12***		***4.12***	***4.75***	***8.87***	N/A	0.893	0.025	1
31.1	B	312	0.660	1250	-150	-100	N/A		***4.12***		***4.12***	***4.75***	***8.87***	N/A	0.893	0.025	1
31.2	B	312	0.965	1250	-150	-100	N/A		***4.12***		***4.12***	***4.75***	***8.87***	N/A	0.893	0.025	1
32.0	B	500	0.356	1250	-150	-100	N/A		***7.20***		***7.20***	***8.00***	***15.20***	N/A	0.893	0.020	3
32.1	B	500	0.660	1250	-150	-100	N/A		***7.20***		***7.20***	***8.00***	***15.20***	N/A	0.893	0.020	3
32.2	B	500	0.965	1250	-150	-100	N/A		***7.20***		***7.20***	***8.00***	***15.20***	N/A	0.893	0.020	3
34.0	C	500	0.356	1250	-150	-100	58.98			7.29	7.29	8.13	15.42	0.958	0.893	0.020	3

TABLE A-2 Faraday Probe Thruster Operating Conditions

Run #	Seg	I_B (mA)	z (m)	V_S (V)	V_A (V)	V_D (V)	V_{cn} (V)	$\dot{m}_A$ (sccm)	$\dot{m}_B$ (sccm)	$\dot{m}_C$ (sccm)	$\sum \dot{m}_t$ (sccm)	$\dot{m}_n$ (sccm)	$\dot{m}_f$ (sccm)	η_p	R Ratio	Bias (mA)	R Set
34.1	C	500	0.660	1250	-150	-100	58.99			7.24	7.24	8.08	15.32	0.972	0.893	0.020	3
34.2	C	500	0.965	1250	-150	-100	58.99			7.19	7.19	***8.00***	***15.19***	0.978	0.893	0.020	3
36.0	A	500	0.356	1250	-150	-100	5.78	7.13			7.13	7.67	14.80	0.977	0.893	0.020	3
36.1	A	500	0.660	1250	-150	-100	5.72	7.08			7.08	7.59	14.67	0.984	0.893	0.020	3
36.2	A	500	0.965	1250	-150	-100	5.70	7.13			7.13	7.74	14.87	0.978	0.893	0.020	3
35.1	AC	500	0.356	1250	-150	-100	59.64	7.22		7.29	14.51	16.37	30.88	0.965	0.893	0.025	3
35.2	AC	500	0.660	1250	-150	-100	59.65	7.17		7.27	14.44	16.30	30.74	0.970	0.893	0.025	3
38.2	AC	500	0.965	1250	-150	-100	16.52	7.49		7.50	14.99	16.52	30.07	0.950	0.893	0.025	3
33.0	BC	500	0.356	1250	-150	-100	6.93		7.49	7.72	15.21	17.04	32.25	0.923	0.893	0.025	3
33.3	BC	500	0.660	1250	-150	-100	59.57		7.21	7.42	14.63	16.50	31.13	0.951	0.893	0.025	3
33.4	BC	500	0.965	1250	-150	-100	59.59		7.42	7.35	14.77	16.68	31.45	0.949	0.893	0.025	3
49.0	AB	500	0.356	1250	-150	-100	59.52	7.42	7.52		14.94	16.37	31.34	0.919	0.893	0.075	3
37.1	AB	500	0.660	1250	-150	-100	6.73	7.49	7.75		15.24	16.79	32.03	0.916	0.893	0.065	3
37.2	AB	500	0.965	1250	-150	-100	6.68	7.42	7.71		15.13	16.68	31.81	0.921	0.893	0.065	3
48.0	ABC	500	0.356	1250	-150	-100	6.63	8.02	7.39	7.95	23.36	26.21	49.57	0.896	0.893	0.080	3
48.1	ABC	500	0.660	1250	-150	-100	7.32	8.00	7.24	7.95	23.19	25.90	49.09	0.898	0.893	0.080	3
48.3	ABC	500	0.965	1250	-150	-100	8.25	6.59	6.24	7.03	22.96	25.75	45.61	0.914	0.893	0.080	3
41.0	ABC	430	0.356	900	-500	-200	59.37	4.65	4.72	4.72	14.09	16.73	30.82	0.927	0.643	0.050	4
41.1	ABC	430	0.660	900	-500	-200	59.49	4.63	4.67	4.67	13.97	16.66	30.63	0.931	0.643	0.050	4
41.2	ABC	430	0.965	900	-500	-200	59.50	4.60	4.64	4.65	13.89	16.63	30.52	0.934	0.643	0.050	4
45.0	A	430	0.356	900	-500	-200	3.31	4.77			4.77	5.30	10.07	0.919	0.643	0.040	4
45.1	A	430	0.660	900	-500	-200	3.28	4.76			4.76	5.25	10.01	0.912	0.643	0.040	4
45.2	A	430	0.965	900	-500	-200	3.30	4.74			4.74	5.22	9.96	0.920	0.643	0.040	4
46.0	B	430	0.356	900	-500	-200	N/A		4.69		4.69	5.22	9.91	N/A	0.643	0.040	4
46.1	B	430	0.660	900	-500	-200	0.94		4.67		4.67	5.40	10.07	0.923	0.643	0.040	4
46.2	B	430	0.965	900	-500	-200	58.00		4.77		4.77	5.37	10.14	0.931	0.643	0.040	4
47.0	C	430	0.356	900	-500	-200	2.30			4.77	4.77	5.61	10.38	0.913	0.643	0.040	4
47.1	C	430	0.660	900	-500	-200	2.60			4.77	4.77	5.58	10.35	0.914	0.643	0.040	4
47.2	C	430	0.965	900	-500	-200	2.63			4.77	4.77	5.58	10.35	0.910	0.643	0.040	4
42.0	AB	430	0.356	900	-500	-200	5.36	4.79	4.54		9.33	10.78	20.11	0.936	0.643	0.040	4

TABLE A-2 Faraday Probe Thruster Operating Conditions

Run #	Seg	I_B (mA)	z (m)	V_S (V)	V_A (V)	V_D (V)	V_{cn} (V)	$\dot{m}_A$ (sccm)	$\dot{m}_B$ (sccm)	$\dot{m}_C$ (sccm)	$\sum \dot{m}_t$ (sccm)	$\dot{m}_n$ (sccm)	$\dot{m}_f$ (sccm)	η_p	R Ratio	Bias (mA)	R Set
42.1	AB	430	0.660	900	-500	-200	N/A	*4.79*	*4.54*		*9.33*	*10.78*	*20.11*	N/A	0.643	0.040	4
42.2	AB	430	0.965	900	-500	-200	N/A	*4.79*	*4.54*		*9.33*	*10.78*	*20.11*	N/A	0.643	0.040	4
43.0	BC	430	0.356	900	-500	-200	N/A		*4.54*	*5.08*	*9.62*	*11.25*	*20.87*	N/A	0.643	0.040	4
43.1	BC	430	0.660	900	-500	-200	N/A		*4.54*	*5.08*	*9.62*	*11.25*	*20.87*	N/A	0.643	0.040	4
43.2	BC	430	0.965	900	-500	-200	N/A		*4.54*	*5.08*	*9.62*	*11.25*	*20.87*	N/A	0.643	0.040	4
44.0	AC	430	0.356	900	-500	-200	N/A	*5.38*		*5.08*	*10.46*	*12.07*	*22.53*	N/A	0.643	0.040	4
44.1	AC	430	0.660	900	-500	-200	5.54	5.38		5.08	10.46	12.07	22.53	0.832	0.643	0.040	4
44.3	AC	430	0.965	900	-500	-200	5.62	5.38		5.08	10.46	12.07	22.53	0.831	0.643	0.040	4
50.1	B	430	0.356	1250	-150	-100	3.50		?		6.53	7.51	14.04	0.926	0.893	0.050	1
50.2	B	430	0.965	1250	-150	-100	3.63		?		5.84	7.23	13.07	1.030	0.893	0.050	1
51.0	B	430	0.660	1250	-150	-100	0.96		?		8.74	9.98	18.72	0.680	0.893	0.050	1
52.0	A	430	0.356	1250	-150	-100	1.19	?			8.68	9.62	18.30	0.694	0.893	0.050	1
52.1	A	430	0.965	1250	-150	-100	2.52	?			6.44	7.33	13.77	0.926	0.893	0.050	1
52.2	A	430	0.660	1250	-150	-100	2.81	?			6.47	7.36	13.83	0.928	0.893	0.050	1

ExB Probe Thruster Operating Conditions - Centerline Profile

Run #	Nom. I_B (mA)	I_B (mA)	I_{DIS} (A)	V_{DIS} (V)	$\dot{m}_t$ (sccm)	$\dot{m}_n$ (sccm)	V_S (V)	V_A (V)	V_D (V)	V_{cn} (V)	η_p
5.0	430	430	3.512	N/A	6.90	**7.38**	1250	-150	-100	14.3	0.868
5.1	430	429	3.517	25.1	6.90	7.38	1250	-150	-100	15.3	0.868
5.2	430	411	3.248	24.9	6.89	7.38	1250	-150	-100	16.5	0.835
5.3	430	389	3.004	24.7	6.85	7.36	1250	-150	-100	18.4	0.790
5.4	430	365	2.749	24.7	6.84	7.31	1250	-150	-100	12.8	0.744
5.5	430	342	2.500	24.9	6.81	7.31	1250	-150	-100	11.0	0.700
5.6	430	320	2.250	25.3	6.84	7.38	1250	-150	-100	10.3	0.653
5.7	430	304	2.001	25.9	6.82	7.33	1250	-150	-100	9.8	0.623
5.8	430	276	1.752	N/A	6.87	**7.25**	1250	-150	-100	9.3	0.560
5.9	430	443	3.752	26.6	6.70	7.18	1250	-150	-100	18.1	0.922
5.10	430	467	4.000	26.8	6.74	7.15	1250	-150	-100	19.3	0.968
5.11	430	481	4.251	28.3	6.63	7.28	1250	-150	-100	20.8	1.014
5.12	430	481	4.251	28.3	6.63	7.05	1250	-150	-100	20.8	1.014
5.13	430	493	4.500	29.2	6.59	7.02	1250	-150	-100	22.0	1.042
5.14	430	501	4.740	30.2	6.62	7.13	1250	-150	-100	22.7	1.058
6.0	312	269	1.752	27.5	4.82	5.32	1250	-150	-100	2.5	0.779
6.1	312	242	1.497	28.0	4.80	5.22	1250	-150	-100	2.1	0.707
6.2	312	309	2.020	28.8	4.79	5.27	1250	-150	-100	3.0	0.904
6.3	312	331	2.255	29.6	4.79	5.27	1250	-150	-100	3.2	0.968
6.4	312	346	2.505	30.4	4.79	5.27	1250	-150	-100	3.5	1.011
6.5	312	362	2.754	31.5	4.75	5.17	1250	-150	-100	3.6	10.63
6.6	312	372	3.009	32.9	4.75	5.22	1250	-150	-100	3.9	1.096
6.7	312	381	3.253	34.4	4.74	5.22	1250	-150	-100	4.0	1.124
6.8	312	386	3.498	35.3	4.72	5.19	1250	-150	-100	4.0	1.141
6.9	312	388	3.747	36.2	4.68	5.12	1250	-150	-100	4.1	1.153
6.10	312	390	3.987	37.1	4.70	5.19	1250	-150	-100	4.1	1.154
6.12	312	393	4.251	38.8	4.71	5.19	1250	-150	-100	4.2	1.165
6.13	312	393	4.251	38.8	4.71	5.19	1250	-150	-100	4.3	1.165
6.14	312	186	1.248	27.5	4.65	5.09	1250	-150	-100	1.6	0.599

ExB Probe Thruster Operating Conditions - Centerline Profile

Run #	Nom. I_B (mA)	I_B (mA)	I_{DIS} (A)	V_{DIS} (V)	$\dot{m}_t$ (sccm)	$\dot{m}_n$ (sccm)	V_S (V)	V_A (V)	V_D (V)	V_{cn} (V)	η_p
7.0	470	255	1.752	25.3	7.19	7.67	1250	-150	-100	.446	0.493
7.1	470	300	2.001	26.3	7.29	7.80	1250	-150	-100	.519	0.574
7.2	470	339	2.255	26.6	7.29	7.77	1250	-150	-100	.596	0.649
7.3	470	376	2.495	26.9	7.27	7.67	1250	-150	-100	.667	0.722
7.4	470	408	2.754	27.2	7.33	7.87	1250	-150	-100	.712	0.778
7.5	470	433	2.999	27.7	7.31	7.80	1250	-150	-100	.761	0.839
7.6	470	454	3.253	27.9	7.31	7.69	1250	-150	-100	.801	0.866
7.7	470	470	3.493	28.0	7.29	7.69	1250	-150	-100	.835	0.901
7.8	470	487	3.752	28.2	7.32	7.82	1250	-150	-100	.860	0.929
7.9	470	500	4.016	28.6	7.31	7.82	1250	-150	-100	.882	0.957
8.0	470	502	3.747	29.4	7.32	7.95	1250	-150	-100	.865	0.958
8.1	470	485	3.507	29.0	7.31	7.95	1250	-150	-100	.827	0.926
8.2	470	469	3.268	28.7	7.28	7.90	1250	-150	-100	.812	0.899
8.3	470	450	3.004	28.4	7.28	7.92	1250	-150	-100	.777	0.862
8.4	470	425	2.754	28.2	7.25	7.90	1250	-150	-100	.743	0.820
8.5	470	394	2.505	27.8	7.26	7.90	1250	-150	-100	.672	0.758
8.6	470	355	2.250	27.2	7.24	7.82	1250	-150	-100	.615	0.685
8.7	470	308	2.006	26.4	7.24	7.82	1250	-150	-100	.519	0.593
8.8	470	248	1.752	N/A	7.26	7.82	1250	-150	-100	.432	0.476
9.0	312	198	1.497	N/A	4.87	5.48	1250	-150	-100	.481	0.566
9.1	312	247	1.747	N/A	4.82	5.45	1250	-150	-100	.603	0.714
9.2	312	296	2.001	28.0	4.85	5.58	1250	-150	-100	.718	0.853
9.3	312	330	2.250	29.1	4.84	5.48	1250	-150	-100	.803	0.952
9.4	312	355	2.500	30.8	4.82	5.45	1250	-150	-100	.880	1.029
9.5	312	379	2.749	33.6	4.83	5.48	1250	-150	-100	.933	1.094
9.6	312	395	2.994	36.7	4.84	5.53	1250	-150	-100	.976	1.139
9.7	312	409	3.253	40.1	4.84	5.50	1250	-150	-100	1.017	1.180
9.8	312	417	3.498	44.2	4.83	5.45	1250	-150	-100	1.045	1.207
9.9	312	425	3.747	49.1	4.85	5.53	1250	-150	-100	1.063	1.224

ExB Probe Thruster Operating Conditions-Radial Profile

Run #	Nom. I_I (mA)	I_B (mA)	I_{DIS} (A)	V_{DIS} (V)	$\dot{m}_t$ (sccm)	$\dot{m}_t$ (sccm)	V_S (V)	V_A (V)	V_D (V)	V_{cn} (V)	η_p	X (cm)
11.0	430	429	3.507	N/A	6.64	N/A	1250	-150	-100	13.8	.904	-11.43
11.3	430	431	4.075	N/A	6.61	N/A	1250	-150	-100	24.3	.904	-10.16
11.4	430	429	4.031	N/A	6.60	N/A	1250	-150	-100	19.5	.905	-8.89
11.5	430	429	4.036	N/A	6.62	N/A	1250	-150	-100	19.3	.908	-7.62
11.6	430	429	4.080	N/A	6.61	N/A	1250	-150	-100	23.2	.902	-7.62
11.7	430	429	4.065	N/A	6.62	N/A	1250	-150	-100	20.2	.903	-6.35
11.8	430	428	4.080	N/A	6.62	N/A	1250	-150	-100	19.5	.902	-5.08
11.9	430	428	4.089	N/A	6.63	N/A	1250	-150	-100	19.3	.907	-3.81
11.12	430	430	4.075	N/A	6.63	N/A	1250	-150	-100	24.4	.906	-2.54
11.13	430	430	3.317	N/A	6.67	N/A	1250	-150	-100	20.3	.900	-2.54
11.14	430	430	3.292	N/A	6.66	N/A	1250	-150	-100	20.0	.904	-1.27
11.16	430	431	3.287	N/A	.654	N/A	1250	-150	-100	20.2	.902	0
11.18	430	432	3.224	N/A	6.66	N/A	1250	-150	-100	20.2	.905	1.27
11.20	430	431	3.224	N/A	6.66	N/A	1250	-150	-100	20.3	.901	2.54
11.21	430	430	3.209	N/A	6.67	N/A	1250	-150	-100	20.3	.903	3.81
11.22	430	429	3.190	N/A	6.68	N/A	1250	-150	-100	20.3	.900	5.08
11.24	430	432	3.199	N/A	6.64	N/A	1250	-150	-100	20.3	.908	6.35
11.26	430	432	3.180	N/A	6.63	N/A	1250	-150	-100	20.2	.906	7.62
11.27	430	432	3.180	N/A	6.63	N/A	1250	-150	-100	20.2	.907	8.89
11.28	430	431	3.190	N/A	6.65	N/A	1250	-150	-100	20.5	.906	10.16
11.29	430	430	3.185	N/A	6.63	N/A	1250	-150	-100	20.5	.903	11.43
11.30	430	431	3.160	N/A	6.61	N/A	1250	-150	-100	20.2	.905	12.70

ExB Probe Thruster Operating Conditions-Radial Profile

Run #	Nom. I_I (mA)	I_B (mA)	I_{DIS} (A)	V_{DIS} (V)	$\dot{m}_t$ (sccm)	$\dot{m}_t$ (sccm)	V_S (V)	V_A (V)	V_D (V)	V_{cn} (V)	η_p	X (cm)
12.4	430	430	3.434	N/A	6.63	N/A	1250	-150	-100	20.6	.897	0
12.5	430	431	3.400	N/A	6.67	N/A	1250	-150	-100	20.8	.899	1.27
12.8	430	431	3.390	N/A	6.65	N/A	1250	-150	-100	21.0	.901	2.54
12.9	430	430	3.395	N/A	6.64	N/A	1250	-150	-100	20.7	.902	3.81
12.10	430	430	3.380	N/A	6.65	N/A	1250	-150	-100	20.8	.902	5.08
12.11	430	429	3.370	N/A	6.65	N/A	1250	-150	-100	20.9	.903	6.35
12.12	430	430	3.366	N/A	6.62	N/A	1250	-150	-100	20.5	.903	7.62
12.13	430	430	3.385	N/A	6.60	N/A	1250	-150	-100	21.0	.900	8.89
12.14	430	429	3.380	N/A	6.65	N/A	1250	-150	-100	21.2	.899	10.16
12.16	430	430	3.375	N/A	6.67	N/A	1250	-150	-100	21.1	.902	11.43
12.17	430	429	3.361	N/A	6.63	N/A	1250	-150	-100	21.5	.905	12.70
12.18	430	430	3.322	N/A	6.63	N/A	1250	-150	-100	21.4	.905	13.97
12.19	430	433	3.302	N/A	6.64	N/A	1250	-150	-100	21.3	.906	15.24
12.21	430	430	3.336	N/A	6.60	N/A	1250	-150	-100	22.0	.900	-1.27
12.22	430	430	3.273	N/A	6.63	N/A	1250	-150	-100	22.0	.903	-2.54
12.23	430	429	3.243	N/A	6.64	N/A	1250	-150	-100	22.1	.903	-3.81
12.24	430	431	3.243	N/A	6.63	N/A	1250	-150	-100	22.3	.902	-5.08
12.25	430	428	3.204	N/A	6.62	N/A	1250	-150	-100	22.3	.904	-6.35
12.26	430	431	3.214	N/A	6.64	N/A	1250	-150	-100	22.4	.903	-7.62
12.27	430	430	3.209	N/A	6.63	N/A	1250	-150	-100	22.7	.903	-8.89
12.28	430	432	3.219	N/A	6.64	N/A	1250	-150	-100	22.7	.902	-10.16
12.29	430	430	3.170	N/A	6.64	N/A	1250	-150	-100	22.9	.901	-11.43
12.30	430	431	3.160	N/A	6.65	N/A	1250	-150	-100	23.0	.905	-12.70
12.31	430	430	3.160	N/A	6.67	N/A	1250	-150	-100	23.0	.904	-13.97
12.32	430	429	3.165	N/A	6.64	N/A	1250	-150	-100	23.8	.900	-15.24

Superposed Data Construction

Run #	Seg	z (m)	Seg A Run #	Seg B Run #	Seg C Run #	$\sum \dot{m}_t$ (sccm)	$\sum \dot{m}_n$ (sccm)	$\dot{m}_f$ (sccm)	$\overline{\dot{m}}_f$ (sccm)
60.0	ABC	0.356	21.0	22.4	23.4	19.55	24.18	43.73	14.58
60.1	AB	0.356	21.0	22.4		13.21	16.05	29.26	14.63
60.2	BC	0.356		22.4	23.4	12.79	16.13	28.92	14.46
60.3	AC	0.356	21.0		23.4	13.10	16.18	29.28	14.64
61.0	ABC	0.508	21.1	22.0	23.0	19.87	23.33	43.20	14.40
61.1	AB	0.508	21.1	22.0		13.38	16.00	29.38	14.69
61.2	BC	0.508		22.0	23.0	13.14	15.25	28.39	14.19
61.3	AC	0.508	21.1		23.0	13.22	15.41	28.63	14.32
62.0	ABC	0.660	21.2	22.1	23.1	19.74	24.41	44.15	14.72
62.1	AB	0.660	21.2	22.1		13.30	16.18	29.48	14.74
62.2	BC	0.660		22.1	23.1	13.04	16.36	29.40	14.70
62.3	AC	0.660	21.2		23.1	13.14	16.28	29.42	14.71
63.0	ABC	0.813	21.4	22.2	23.2	19.68	24.31	43.99	14.66
63.1	AB	0.813	21.4	22.2		13.24	16.15	29.39	14.70
63.2	BC	0.813		22.2	23.2	12.99	16.26	29.25	14.63
63.3	AC	0.813	21.4		23.2	13.13	16.21	29.34	14.67
64.0	ABC	0.965	21.5	22.3	23.3	19.63	24.09	43.72	14.57
64.1	AB	0.965	21.5	22.3		13.19	15.96	29.15	14.58
64.2	BC	0.965		22.3	23.3	12.96	16.11	29.07	14.54
64.3	AC	0.965	21.5		23.3	13.11	16.11	29.22	14.61
65.0	ABC	0.356	30.0	31.0	28.0	12.38	14.31	26.69	8.90
65.1	AB	0.356	30.0	31.0		8.26	9.35	17.61	8.81
65.2	BC	0.356		31.0	28.0	8.24	9.71	17.95	8.98
65.3	AC	0.356	30.0		28.0	8.26	9.56	17.82	8.91
66.0	ABC	0.660	30.1	31.1	28.1	12.36	14.36	26.72	8.91
66.1	AB	0.660	30.1	31.1		8.26	9.40	17.66	8.83
66.2	BC	0.660		31.1	28.1	8.22	9.71	17.93	8.97
66.3	AC	0.660	30.1		28.1	8.24	9.61	17.85	8.93
67.0	ABC	0.965	30.2	31.2	28.2	12.35	14.36	26.71	8.90
67.1	AB	0.965	30.2	31.2		8.26	9.40	17.66	8.83
67.2	BC	0.965		31.2	28.2	8.21	9.71	17.92	8.98

Superposed Data Construction

Run #	Seg	z (m)	Seg A Run #	Seg B Run #	Seg C Run #	$\sum \dot{m}_t$ (sccm)	$\sum \dot{m}_n$ (sccm)	$\dot{m}_f$ (sccm)	$\overline{\dot{m}}_f$ (sccm)
67.3	AC	0.965	30.2		28.2	8.23	9.61	17.84	8.92
68.0	ABC	0.356	36.0	32.0	34.0	21.62	23.80	45.42	15.14
68.1	AB	0.356	36.0	32.0		14.33	15.67	30.00	15.00
68.2	BC	0.356		32.0	34.0	14.49	16.13	30.62	15.31
68.3	AC	0.356	36.0		34.0	14.42	15.80	30.22	15.11
69.0	ABC	0.660	36.1	32.1	34.1	21.52	23.67	45.19	15.06
69.1	AB	0.660	36.1	32.1		14.28	15.59	29.87	14.94
69.2	BC	0.660		32.1	34.1	14.44	16.08	30.52	15.26
69.3	AC	0.660	36.1		34.1	14.32	15.67	29.99	15.00
70.0	ABC	0.965	36.2	32.2	34.2	21.52	23.74	45.26	15..09
70.1	AB	0.965	36.2	32.2		14.33	15.74	30.07	15.04
70.2	BC	0.965	-	32.2	34.2	14.39	16.00	30.39	15.19
70.3	AC	0.965	36.2		34.2	14.32	15.74	30.06	15.03
71.0	ABC	0.356	45.0	46.0	47.0	14.23	16.13	30.36	10.12
71.1	AB	0.356	45.0	46.0		9.46	10.52	19.98	10.99
71.2	BC	0.356		46.0	47.0	9.46	10.83	20.29	10.15
71.3	AC	0.356	45.0		47.0	9.54	10.91	20.45	10.23
72.0	ABC	0.660	45.1	46.1	47.1	14.20	16.23	30.43	10.14
72.1	AB	0.660	45.1	46.1		9.43	10.65	20.08	10.04
72.2	BC	0.660		46.1	47.1	9.44	10.98	20.42	10.21
72.3	AC	0.660	45.1		47.1	9.53	10.83	20.36	10.18
73.0	ABC	0.965	45.2	46.2	47.2	14.28	16.17	30.45	10.15
73.1	AB	0.965	45.2	46.2		9.51	10.59	20.10	10.05
73.2	BC	0.965		46.2	47.2	9.54	10.95	20.49	10.25
73.3	AC	0.965	45.2		47.2	9.51	10.80	20.31	10.15

Faraday Probe Data Analyses Results

RUN	SEGS	R	z (m)	TYPE	I_B (mA)	P (Pa)	n_b	σ_{ce}	I_z	I_z Integ.	Error	ε operation	σ_B (mA)	ε std	ε voltage	ε resistor	ε hardware	ε probes	ε acquisition	ε measured	dQ/Q	dIb/Ib	ε theoretical	ε total	CHECK
21.0	A	0.893	0.356	MAT	430	1.66E-03	4.001E+17	4.20E-19	405.0	430.341	6.25%	1.00%	14.450	3.36%	0.25%	0.25%	0.35%	2.00%	3.92%	4.08%	4.23%	1.00%	4.35%	5.96%	NO
21.0	A	0.893	0.356	RFND	430	1.66E-03	4.001E+17	4.20E-19	405.0	430.857	6.38%	1.00%	14.450	3.35%	0.25%	0.25%	0.35%	2.00%	3.92%	4.08%	4.23%	1.00%	4.35%	5.96%	NO
21.1	A	0.893	0.508	MAT	430	1.66E-03	4.001E+17	4.20E-19	394.8	412.163	4.39%	1.00%	12.793	3.10%	0.25%	0.25%	0.35%	2.00%	3.71%	3.87%	6.04%	1.00%	6.12%	7.24%	OKAY
21.1	A	0.893	0.508	RFND	430	1.66E-03	4.001E+17	4.20E-19	394.8	412.324	4.43%	1.00%	12.793	3.10%	0.25%	0.25%	0.35%	2.00%	3.71%	3.87%	6.04%	1.00%	6.12%	7.24%	OKAY
21.2	A	0.893	0.660	MAT	430	1.65E-03	3.986E+17	4.20E-19	385.0	398.412	3.48%	1.00%	12.227	3.07%	0.25%	0.25%	0.35%	2.00%	3.68%	3.85%	7.81%	1.00%	7.88%	8.77%	OKAY
21.2	A	0.893	0.660	RFND	430	1.65E-03	3.986E+17	4.20E-19	385.0	398.826	3.59%	1.00%	12.227	3.07%	0.25%	0.25%	0.35%	2.00%	3.68%	3.84%	7.81%	1.00%	7.88%	8.76%	OKAY
21.4	A	0.893	0.813	MAT	430	1.65E-03	3.983E+17	4.20E-19	375.3	400.639	6.75%	1.00%	13.663	3.41%	0.25%	0.25%	0.35%	2.00%	3.97%	4.12%	9.62%	1.00%	9.67%	10.51%	OKAY
21.4	A	0.893	0.813	RFND	430	1.65E-03	3.983E+17	4.20E-19	375.3	401.171	6.89%	1.00%	13.663	3.41%	0.25%	0.25%	0.35%	2.00%	3.97%	4.12%	9.62%	1.00%	9.67%	10.51%	OKAY
21.5	A	0.893	0.965	MAT	430	1.64E-03	3.960E+17	4.20E-19	366.2	384.990	5.12%	1.00%	12.639	3.28%	0.25%	0.25%	0.35%	2.00%	3.86%	4.02%	11.35%	1.00%	11.39%	12.08%	OKAY
21.5	A	0.893	0.965	RFND	430	1.64E-03	3.960E+17	4.20E-19	366.2	385.435	5.24%	1.00%	12.639	3.28%	0.25%	0.25%	0.35%	2.00%	3.86%	4.02%	11.35%	1.00%	11.39%	12.08%	OKAY
22.4	B	0.893	0.356	MAT	430	1.62E-03	3.909E+17	4.20E-19	405.6	431.137	6.30%	1.00%	12.976	3.01%	0.25%	0.25%	0.35%	2.00%	3.63%	3.80%	4.13%	1.00%	4.25%	5.70%	NO
22.4	B	0.893	0.356	RFND	430	1.62E-03	3.909E+17	4.20E-19	405.6	430.422	6.12%	1.00%	12.976	3.01%	0.25%	0.25%	0.35%	2.00%	3.64%	3.80%	4.13%	1.00%	4.25%	5.71%	NO
22.0	B	0.893	0.508	MAT	430	1.63E-03	3.940E+17	4.20E-19	395.3	417.424	5.59%	1.00%	13.260	3.18%	0.25%	0.25%	0.35%	2.00%	3.77%	3.93%	5.94%	1.00%	6.03%	7.20%	OKAY
22.0	B	0.893	0.508	RFND	430	1.63E-03	3.940E+17	4.20E-19	395.3	417.405	5.58%	1.00%	13.260	3.18%	0.25%	0.25%	0.35%	2.00%	3.77%	3.93%	5.94%	1.00%	6.03%	7.20%	OKAY
22.1	B	0.893	0.660	MAT	430	1.65E-03	3.981E+17	4.20E-19	385.1	402.517	4.53%	1.00%	12.233	3.04%	0.25%	0.25%	0.35%	2.00%	3.66%	3.82%	7.80%	1.00%	7.87%	8.75%	OKAY
22.1	B	0.893	0.660	RFND	430	1.65E-03	3.981E+17	4.20E-19	385.1	402.114	4.42%	1.00%	12.233	3.04%	0.25%	0.25%	0.35%	2.00%	3.66%	3.82%	7.80%	1.00%	7.87%	8.75%	OKAY
22.2	B	0.893	0.813	MAT	430	1.64E-03	3.960E+17	4.20E-19	375.6	389.134	3.60%	1.00%	11.647	2.99%	0.25%	0.25%	0.35%	2.00%	3.62%	3.79%	9.56%	1.00%	9.61%	10.33%	OKAY
22.2	B	0.893	0.813	RFND	430	1.64E-03	3.960E+17	4.20E-19	375.6	389.042	3.58%	1.00%	11.647	2.99%	0.25%	0.25%	0.35%	2.00%	3.62%	3.79%	9.56%	1.00%	9.61%	10.33%	OKAY
22.3	B	0.893	0.965	MAT	430	1.62E-03	3.922E+17	4.20E-19	366.8	382.222	4.20%	1.00%	11.517	3.01%	0.25%	0.25%	0.35%	2.00%	3.63%	3.80%	11.24%	1.00%	11.29%	11.91%	OKAY
22.3	B	0.893	0.965	RFND	430	1.62E-03	3.922E+17	4.20E-19	366.8	382.402	4.25%	1.00%	11.517	3.01%	0.25%	0.25%	0.35%	2.00%	3.63%	3.80%	11.24%	1.00%	11.29%	11.91%	OKAY
23.4	C	0.893	0.356	MAT	430	1.62E-03	3.914E+17	4.20E-19	405.6	440.330	8.57%	1.00%	12.365	2.81%	0.25%	0.25%	0.35%	2.00%	3.47%	3.64%	4.14%	1.00%	4.26%	5.60%	**NO**
23.4	C	0.893	0.356	RFND	430	1.62E-03	3.914E+17	4.20E-19	405.6	439.989	8.49%	1.00%	12.365	2.81%	0.25%	0.25%	0.35%	2.00%	3.47%	3.64%	4.14%	1.00%	4.26%	5.60%	**NO**
23.0	C	0.893	0.508	MAT	430	1.55E-03	3.749E+17	4.20E-19	396.9	429.349	8.16%	1.00%	11.909	2.77%	0.25%	0.25%	0.35%	2.00%	3.44%	3.62%	5.66%	1.00%	5.74%	6.79%	NO
23.0	C	0.893	0.508	RFND	430	1.55E-03	3.749E+17	4.20E-19	396.9	429.461	8.19%	1.00%	11.909	2.77%	0.25%	0.25%	0.35%	2.00%	3.44%	3.61%	5.66%	1.00%	5.74%	6.79%	NO
23.1	C	0.893	0.660	MAT	430	1.64E-03	3.965E+17	4.20E-19	385.2	413.160	7.25%	1.00%	10.578	2.56%	0.25%	0.25%	0.35%	2.00%	3.27%	3.45%	7.77%	1.00%	7.84%	8.56%	OKAY
23.1	C	0.893	0.660	RFND	430	1.64E-03	3.965E+17	4.20E-19	385.2	412.824	7.16%	1.00%	10.578	2.56%	0.25%	0.25%	0.35%	2.00%	3.27%	3.46%	7.77%	1.00%	7.84%	8.56%	OKAY
23.2	C	0.893	0.813	MAT	430	1.63E-03	3.948E+17	4.20E-19	375.8	397.392	5.75%	1.00%	10.074	2.54%	0.25%	0.25%	0.35%	2.00%	3.25%	3.44%	9.53%	1.00%	9.58%	10.18%	OKAY
23.2	C	0.893	0.813	RFND	430	1.63E-03	3.948E+17	4.20E-19	375.8	397.818	5.87%	1.00%	10.074	2.53%	0.25%	0.25%	0.35%	2.00%	3.25%	3.43%	9.53%	1.00%	9.58%	10.18%	OKAY
23.3	C	0.893	0.965	MAT	430	1.63E-03	3.940E+17	4.20E-19	366.5	381.533	4.09%	1.00%	10.025	2.63%	0.25%	0.25%	0.35%	2.00%	3.32%	3.50%	11.29%	1.00%	11.34%	11.87%	OKAY

Faraday Probe Data Analyses Results

RUN	SEGS	R	z (m)	TYPE	I_B (mA)	P (Pa)	n_b	σ_{ce}	I_z	I_z Integ.	Error	ε operation	σ_B (mA)	ε std	ε voltage	ε resistor	ε hardware	ε probes	ε acquisition	ε measured	dQ/Q	dIb/Ib	ε theoretical	ε total	CHECK
23.3	C	0.893	0.965	RFND	430	1.63E-03	3.940E+17	4.20E-19	366.5	382.350	4.31%	1.00%	10.025	2.62%	0.25%	0.25%	0.35%	2.00%	3.32%	3.50%	11.29%	1.00%	11.34%	11.86%	OKAY
19.0	AB	0.893	0.356	MAT	860	3.39E-03	8.187E+17	4.20E-19	760.9	825.250	8.46%	1.00%	20.239	2.45%	0.25%	0.25%	0.35%	2.00%	3.18%	3.37%	8.66%	1.00%	8.71%	9.34%	OKAY
60.1	AB	0.893	0.356	SYN	860	1.64E-03	3.955E+17	4.20E-19	810.6	860.417	6.14%	1.00%	19.421	2.26%	0.25%	0.25%	0.35%	2.00%	3.04%	3.24%	4.18%	1.00%	4.30%	5.38%	NO
19.1	AB	0.893	0.508	MAT	860	3.35E-03	8.085E+17	4.20E-19	723.7	801.092	10.69%	1.00%	17.983	2.24%	0.25%	0.25%	0.35%	2.00%	3.03%	3.23%	12.20%	1.00%	12.24%	12.66%	OKAY
61.1	AB	0.893	0.508	SYN	860	1.64E-03	3.971E+17	4.20E-19	790.1	829.766	5.01%	1.00%	18.425	2.22%	0.25%	0.25%	0.35%	2.00%	3.01%	3.21%	5.99%	1.00%	6.07%	6.87%	OKAY
19.2	AB	0.893	0.660	MAT	860	3.33E-03	8.032E+17	4.20E-19	688.3	769.235	11.75%	1.00%	16.524	2.15%	0.25%	0.25%	0.35%	2.00%	2.96%	3.16%	15.74%	1.00%	15.78%	16.09%	OKAY
62.1	AB	0.893	0.660	SYN	860	1.65E-03	3.983E+17	4.20E-19	770.1	800.632	3.97%	1.00%	17.296	2.16%	0.25%	0.25%	0.35%	2.00%	2.97%	3.17%	7.81%	1.00%	7.87%	8.49%	OKAY
19.3	AB	0.893	0.813	MAT	860	3.32E-03	8.017E+17	4.20E-19	654.1	742.781	13.56%	1.00%	15.067	2.03%	0.25%	0.25%	0.35%	2.00%	2.87%	3.08%	19.36%	1.00%	19.38%	19.63%	OKAY
63.1	AB	0.893	0.813	SYN	860	1.64E-03	3.972E+17	4.20E-19	750.9	790.858	5.32%	1.00%	17.953	2.27%	0.25%	0.25%	0.35%	2.00%	3.05%	3.24%	9.59%	1.00%	9.64%	10.17%	OKAY
19.4	AB	0.893	0.965	MAT	860	3.27E-03	7.897E+17	4.20E-19	624.5	715.202	14.53%	1.00%	14.179	1.98%	0.25%	0.25%	0.35%	2.00%	2.84%	3.05%	22.63%	1.00%	22.65%	22.86%	OKAY
64.1	AB	0.893	0.965	SYN	860	1.63E-03	3.941E+17	4.20E-19	733.0	769.455	4.97%	1.00%	17.100	2.22%	0.25%	0.25%	0.35%	2.00%	3.01%	3.21%	11.30%	1.00%	11.34%	11.79%	OKAY
18.1	AC	0.893	0.356	MAT	860	3.06E-03	7.382E+17	4.20E-19	770.1	837.436	8.74%	1.00%	14.986	1.79%	0.25%	0.25%	0.35%	2.00%	2.71%	2.93%	7.80%	1.00%	7.87%	8.40%	NO
60.3	AC	0.893	0.356	SYN	860	1.64E-03	3.958E+17	4.20E-19	810.6	870.142	7.35%	1.00%	19.018	2.19%	0.25%	0.25%	0.35%	2.00%	2.98%	3.19%	4.18%	1.00%	4.30%	5.35%	**NO**
18.2	AC	0.893	0.508	MAT	860	3.05E-03	7.369E+17	4.20E-19	734.9	807.279	9.85%	1.00%	14.403	1.78%	0.25%	0.25%	0.35%	2.00%	2.70%	2.93%	11.12%	1.00%	11.16%	11.54%	OKAY
61.3	AC	0.893	0.508	SYN	860	1.60E-03	3.875E+17	4.20E-19	791.8	841.786	6.32%	1.00%	17.478	2.08%	0.25%	0.25%	0.35%	2.00%	2.90%	3.11%	5.85%	1.00%	5.93%	6.70%	OKAY
18.3	AC	0.893	0.660	MAT	860	3.05E-03	7.374E+17	4.20E-19	701.0	776.402	10.75%	1.00%	13.305	1.71%	0.25%	0.25%	0.35%	2.00%	2.66%	2.88%	14.45%	1.00%	14.49%	14.77%	OKAY
62.3	AC	0.893	0.660	SYN	860	1.65E-03	3.976E+17	4.20E-19	770.3	811.827	5.40%	1.00%	16.168	1.99%	0.25%	0.25%	0.35%	2.00%	2.84%	3.06%	7.79%	1.00%	7.86%	8.43%	OKAY
18.4	AC	0.893	0.813	MAT	860	3.04E-03	7.351E+17	4.20E-19	669.1	750.678	12.19%	1.00%	13.270	1.77%	0.25%	0.25%	0.35%	2.00%	2.69%	2.92%	17.75%	1.00%	17.78%	18.02%	OKAY
63.3	AC	0.893	0.813	SYN	860	1.64E-03	3.965E+17	4.20E-19	751.1	800.047	6.52%	1.00%	16.975	2.12%	0.25%	0.25%	0.35%	2.00%	2.94%	3.14%	9.57%	1.00%	9.63%	10.13%	OKAY
18.6	AC	0.893	0.965	MAT	860	3.03E-03	7.318E+17	4.20E-19	639.3	732.782	14.63%	1.00%	14.082	1.92%	0.25%	0.25%	0.35%	2.00%	2.80%	3.01%	20.97%	1.00%	21.00%	21.21%	OKAY
64.3	AC	0.893	0.965	SYN	860	1.64E-03	3.950E+17	4.20E-19	732.8	769.857	5.06%	1.00%	16.133	2.10%	0.25%	0.25%	0.35%	2.00%	2.92%	3.13%	11.32%	1.00%	11.37%	11.79%	OKAY
20.0	BC	0.893	0.356	MAT	860	3.31E-03	7.996E+17	4.20E-19	763.1	831.719	8.99%	1.00%	10.079	1.21%	0.25%	0.25%	0.35%	2.00%	2.37%	2.62%	8.45%	1.00%	8.51%	8.91%	NO
60.2	BC	0.893	0.356	SYN	860	1.62E-03	3.912E+17	4.20E-19	811.1	870.049	7.26%	1.00%	17.924	2.06%	0.25%	0.25%	0.35%	2.00%	2.89%	3.10%	4.14%	1.00%	4.26%	5.27%	**NO**
20.1	BC	0.893	0.508	MAT	860	3.29E-03	7.935E+17	4.20E-19	726.1	799.650	10.14%	1.00%	10.027	1.25%	0.25%	0.25%	0.35%	2.00%	2.39%	2.64%	11.97%	1.00%	12.01%	12.30%	OKAY
61.2	BC	0.893	0.508	SYN	860	1.59E-03	3.844E+17	4.20E-19	792.3	846.846	6.89%	1.00%	17.823	2.10%	0.25%	0.25%	0.35%	2.00%	2.92%	3.13%	5.80%	1.00%	5.89%	6.67%	NO
17.4	BC	0.893	0.660	MAT	860	3.01E-03	7.275E+17	4.20E-19	702.9	783.365	11.44%	1.00%	13.508	1.72%	0.25%	0.25%	0.35%	2.00%	2.66%	2.89%	14.26%	1.00%	14.29%	14.58%	OKAY
62.2	BC	0.893	0.660	SYN	860	1.64E-03	3.973E+17	4.20E-19	770.3	816.398	5.98%	1.00%	16.172	1.98%	0.25%	0.25%	0.35%	2.00%	2.84%	3.05%	7.79%	1.00%	7.85%	8.42%	OKAY
17.5	BC	0.893	0.813	MAT	860	3.02E-03	7.298E+17	4.20E-19	670.3	763.450	13.89%	1.00%	13.332	1.75%	0.25%	0.25%	0.35%	2.00%	2.68%	2.90%	17.62%	1.00%	17.65%	17.89%	OKAY

Faraday Probe Data Analyses Results

RUN	SEGS	R	z (m)	TYPE	I_B (mA)	P (Pa)	n_b	σ_{ce}	I_z	I_z Integ.	Error	ε operation	σ_B (mA)	ε std	ε voltage	ε resistor	ε hardware	ε probes	ε acquisition	ε measured	dQ/Q	dIb/Ib	ε theoretical	ε total	CHECK
63.2	BC	0.893	0.813	SYN	860	1.64E-03	3.954E+17	4.20E-19	751.4	788.096	4.89%	1.00%	15.399	1.95%	0.25%	0.25%	0.35%	2.00%	2.82%	3.03%	9.55%	1.00%	9.60%	10.07%	OKAY
17.6	BC	0.893	0.965	MAT	860	2.98E-03	7.208E+17	4.20E-19	642.1	729.123	13.55%	1.00%	12.621	1.73%	0.25%	0.25%	0.35%	2.00%	2.67%	2.89%	20.66%	1.00%	20.68%	20.88%	OKAY
64.2	BC	0.893	0.965	SYN	860	1.63E-03	3.931E+17	4.20E-19	733.3	766.776	4.56%	1.00%	15.269	1.99%	0.25%	0.25%	0.35%	2.00%	2.84%	3.06%	11.27%	1.00%	11.31%	11.72%	OKAY
15.5	ABC	0.893	0.356	MAT	1290	4.72E-03	1.139E+18	4.20E-19	1088.0	1240.980	14.06%	1.00%	20.750	1.67%	0.25%	0.25%	0.35%	2.00%	2.63%	2.86%	12.04%	1.00%	12.09%	12.42%	NO
60.0	ABC	0.893	0.356	SYN	1290	1.63E-03	3.942E+17	4.20E-19	1216.2	1300.300	6.92%	1.00%	23.023	1.77%	0.25%	0.25%	0.35%	2.00%	2.69%	2.92%	4.17%	1.00%	4.29%	5.18%	**NO**
16.0	ABC	0.893	0.508	MAT	1290	4.54E-03	1.096E+18	4.20E-19	1021.0	1183.210	15.89%	1.00%	11.003	0.93%	0.25%	0.25%	0.35%	2.00%	2.23%	2.50%	16.54%	1.00%	16.57%	16.75%	OKAY
61.0	ABC	0.893	0.508	SYN	1290	1.61E-03	3.897E+17	4.20E-19	1187.1	1259.200	6.07%	1.00%	21.939	1.74%	0.25%	0.25%	0.35%	2.00%	2.68%	2.90%	5.88%	1.00%	5.96%	6.63%	OKAY
16.1	ABC	0.893	0.660	MAT	1290	4.44E-03	1.073E+18	4.20E-19	958.1	1134.650	18.43%	1.00%	13.051	1.15%	0.25%	0.25%	0.35%	2.00%	2.33%	2.59%	21.04%	1.00%	21.06%	21.22%	OKAY
62.0	ABC	0.893	0.660	SYN	1290	1.65E-03	3.977E+17	4.20E-19	1155.3	1214.430	5.12%	1.00%	20.274	1.67%	0.25%	0.25%	0.35%	2.00%	2.63%	2.86%	7.80%	1.00%	7.86%	8.36%	OKAY
16.2	ABC	0.893	0.813	MAT	1290	4.45E-03	1.075E+18	4.20E-19	893.5	1089.130	21.89%	1.00%	12.231	1.12%	0.25%	0.25%	0.35%	2.00%	2.32%	2.58%	25.97%	1.00%	25.99%	26.11%	OKAY
63.0	ABC	0.893	0.813	SYN	1290	1.64E-03	3.964E+17	4.20E-19	1126.7	1189.500	5.57%	1.00%	20.586	1.73%	0.25%	0.25%	0.35%	2.00%	2.67%	2.89%	9.57%	1.00%	9.62%	10.05%	OKAY
16.3	ABC	0.893	0.965	MAT	1290	4.72E-03	1.141E+18	4.20E-19	812.4	1025.540	26.24%	1.00%	20.551	2.00%	0.25%	0.25%	0.35%	2.00%	2.85%	3.06%	32.70%	1.00%	32.72%	32.86%	OKAY
64.0	ABC	0.893	0.965	SYN	1290	1.63E-03	3.941E+17	4.20E-19	1099.6	1153.040	4.86%	1.00%	19.822	1.72%	0.25%	0.25%	0.35%	2.00%	2.66%	2.89%	11.29%	1.00%	11.34%	11.70%	OKAY
30.0	A	0.893	0.356	MAT	312	1.02E-03	2.454E+17	4.20E-19	300.8	310.110	3.11%	1.00%	11.313	3.65%	0.25%	0.25%	0.35%	2.00%	4.18%	4.32%	2.59%	1.00%	2.78%	5.14%	OKAY
30.0	A	0.893	0.356	RFND	312	1.02E-03	2.454E+17	4.20E-19	300.8	308.244	2.49%	1.00%	11.313	3.67%	0.25%	0.25%	0.35%	2.00%	4.19%	4.34%	2.59%	1.00%	2.78%	5.16%	OKAY
30.1	A	0.893	0.660	MAT	312	1.02E-03	2.466E+17	4.20E-19	291.4	293.218	0.63%	1.00%	10.397	3.55%	0.25%	0.25%	0.35%	2.00%	4.09%	4.24%	4.83%	1.00%	4.94%	6.51%	OKAY
30.1	A	0.893	0.660	RFND	312	1.02E-03	2.466E+17	4.20E-19	291.4	292.242	0.30%	1.00%	10.397	3.56%	0.25%	0.25%	0.35%	2.00%	4.10%	4.25%	4.83%	1.00%	4.94%	6.51%	OKAY
30.2	A	0.893	0.965	MAT	312	1.02E-03	2.466E+17	4.20E-19	282.3	273.382	-3.17%	1.00%	10.150	3.71%	0.25%	0.25%	0.35%	2.00%	4.23%	4.38%	7.07%	1.00%	7.14%	8.37%	OKAY
30.2	A	0.893	0.965	RFND	312	1.02E-03	2.466E+17	4.20E-19	282.3	273.221	-3.22%	1.00%	10.150	3.71%	0.25%	0.25%	0.35%	2.00%	4.23%	4.38%	7.07%	1.00%	7.14%	8.37%	OKAY
31.0	B	0.893	0.356	MAT	312	1.03E-03	2.487E+17	4.20E-19	300.6	305.436	1.60%	1.00%	13.362	4.37%	0.25%	0.25%	0.35%	2.00%	4.82%	4.95%	2.63%	1.00%	2.81%	5.69%	OKAY
31.0	B	0.893	0.356	RFND	312	1.03E-03	2.487E+17	4.20E-19	300.6	303.860	1.08%	1.00%	13.362	4.40%	0.25%	0.25%	0.35%	2.00%	4.84%	4.97%	2.63%	1.00%	2.81%	5.71%	OKAY
31.1	B	0.893	0.660	MAT	312	1.03E-03	2.487E+17	4.20E-19	291.2	282.928	-2.85%	1.00%	10.630	3.76%	0.25%	0.25%	0.35%	2.00%	4.27%	4.41%	4.87%	1.00%	4.98%	6.65%	OKAY
31.1	B	0.893	0.660	RFND	312	1.03E-03	2.487E+17	4.20E-19	291.2	282.402	-3.03%	1.00%	10.630	3.76%	0.25%	0.25%	0.35%	2.00%	4.28%	4.42%	4.87%	1.00%	4.98%	6.66%	OKAY
31.2	B	0.893	0.965	MAT	312	1.03E-03	2.487E+17	4.20E-19	282.1	266.483	-5.53%	1.00%	9.472	3.55%	0.25%	0.25%	0.35%	2.00%	4.09%	4.24%	7.13%	1.00%	7.20%	8.35%	OKAY
31.2	B	0.893	0.965	RFND	312	1.03E-03	2.487E+17	4.20E-19	282.1	265.212	-5.98%	1.00%	9.472	3.57%	0.25%	0.25%	0.35%	2.00%	4.11%	4.26%	7.13%	1.00%	7.20%	8.36%	OKAY
28.0	C	0.893	0.356	MAT	312	1.05E-03	2.540E+17	4.20E-19	300.4	322.813	7.47%	1.00%	28.951	8.97%	0.25%	0.25%	0.35%	2.00%	9.20%	9.26%	2.69%	1.00%	2.87%	9.70%	OKAY
28.0	C	0.893	0.356	RFND	312	1.05E-03	2.540E+17	4.20E-19	300.4	322.592	7.40%	1.00%	28.951	8.97%	0.25%	0.25%	0.35%	2.00%	9.20%	9.27%	2.69%	1.00%	2.87%	9.70%	OKAY

Faraday Probe Data Analyses Results

RUN	SEGS	R	z (m)	TYPE	I_B (mA)	P (Pa)	n_b	σ_{ce}	I_z	I_z Integ.	Error	ε operation	σ_B (mA)	ε std	ε voltage	ε resistor	ε hardware	ε probes	ε acquisition	ε measured	dQ/Q	dIb/Ib	ε theoretical	ε total	CHECK
28.1	C	0.893	0.660	MAT	312	1.05E-03	2.535E+17	4.20E-19	290.8	322.858	11.01%	1.00%	35.760	11.08%	0.25%	0.25%	0.35%	2.00%	11.26%	11.32%	4.97%	1.00%	5.07%	12.40%	OKAY
28.1	C	0.893	0.660	RFND	312	1.05E-03	2.535E+17	4.20E-19	290.8	321.448	10.53%	1.00%	35.760	11.12%	0.25%	0.25%	0.35%	2.00%	11.31%	11.36%	4.97%	1.00%	5.07%	12.44%	OKAY
28.2	C	0.893	0.965	MAT	312	1.05E-03	2.533E+17	4.20E-19	281.6	305.038	8.34%	1.00%	34.779	11.40%	0.25%	0.25%	0.35%	2.00%	11.58%	11.63%	7.26%	1.00%	7.33%	13.75%	OKAY
28.2	C	0.893	0.965	RFND	312	1.05E-03	2.533E+17	4.20E-19	281.6	305.826	8.62%	1.00%	34.779	11.37%	0.25%	0.25%	0.35%	2.00%	11.55%	11.61%	7.26%	1.00%	7.33%	13.73%	OKAY
25.0	AB	0.893	0.356	MAT	624	2.18E-03	5.263E+17	4.20E-19	576.8	613.113	6.30%	1.00%	17.748	2.89%	0.25%	0.25%	0.35%	2.00%	3.54%	3.71%	5.56%	1.00%	5.65%	6.76%	OKAY
65.1	AB	0.893	0.356	SYN	624	1.02E-03	2.470E+17	4.20E-19	601.4	609.691	1.38%	1.00%	17.508	2.87%	0.25%	0.25%	0.35%	2.00%	3.52%	3.69%	2.61%	1.00%	2.80%	4.63%	OKAY
25.1	AB	0.893	0.660	MAT	624	2.19E-03	5.286E+17	4.20E-19	538.9	581.641	7.92%	1.00%	16.389	2.82%	0.25%	0.25%	0.35%	2.00%	3.47%	3.65%	10.36%	1.00%	10.41%	11.03%	OKAY
66.1	AB	0.893	0.660	SYN	624	1.03E-03	2.477E+17	4.20E-19	582.6	574.553	-1.38%	1.00%	14.869	2.59%	0.25%	0.25%	0.35%	2.00%	3.29%	3.47%	4.85%	1.00%	4.96%	6.05%	OKAY
25.2	AB	0.893	0.965	MAT	624	2.17E-03	5.238E+17	4.20E-19	504.7	541.903	7.38%	1.00%	15.147	2.80%	0.25%	0.25%	0.35%	2.00%	3.46%	3.63%	15.01%	1.00%	15.04%	15.48%	OKAY
67.1	AB	0.893	0.965	SYN	624	1.03E-03	2.477E+17	4.20E-19	564.4	538.038	-4.67%	1.00%	13.883	2.58%	0.25%	0.25%	0.35%	2.00%	3.28%	3.47%	7.10%	1.00%	7.17%	7.96%	OKAY
26.3	AC	0.893	0.356	MAT	624	2.11E-03	5.103E+17	4.20E-19	578.2	632.173	9.34%	1.00%	23.082	3.65%	0.25%	0.25%	0.35%	2.00%	4.18%	4.33%	5.39%	1.00%	5.49%	6.99%	NO
65.3	AC	0.893	0.356	SYN	624	1.03E-03	2.497E+17	4.20E-19	601.1	630.759	4.93%	1.00%	31.083	4.93%	0.25%	0.25%	0.35%	2.00%	5.33%	5.45%	2.64%	1.00%	2.82%	6.13%	OKAY
26.4	AC	0.893	0.660	MAT	624	2.10E-03	5.062E+17	4.20E-19	542.3	594.647	9.65%	1.00%	21.641	3.64%	0.25%	0.25%	0.35%	2.00%	4.17%	4.32%	9.92%	1.00%	9.97%	10.87%	OKAY
66.3	AC	0.893	0.660	SYN	624	1.04E-03	2.501E+17	4.20E-19	582.2	615.049	5.64%	1.00%	37.241	6.05%	0.25%	0.25%	0.35%	2.00%	6.39%	6.48%	4.90%	1.00%	5.00%	8.19%	OKAY
26.2	AC	0.893	0.965	MAT	624	2.16E-03	5.225E+17	4.20E-19	504.9	562.969	11.50%	1.00%	22.785	4.05%	0.25%	0.25%	0.35%	2.00%	4.53%	4.66%	14.97%	1.00%	15.01%	15.72%	OKAY
67.3	AC	0.893	0.965	SYN	624	1.03E-03	2.500E+17	4.20E-19	563.9	579.326	2.74%	1.00%	36.230	6.25%	0.25%	0.25%	0.35%	2.00%	6.58%	6.67%	7.16%	1.00%	7.23%	9.84%	OKAY
27.0	BC	0.893	0.356	MAT	624	2.08E-03	5.023E+17	4.20E-19	578.8	622.054	7.46%	1.00%	14.888	2.39%	0.25%	0.25%	0.35%	2.00%	3.14%	3.33%	5.31%	1.00%	5.40%	6.35%	NO
65.2	BC	0.893	0.356	SYN	624	1.04E-03	2.514E+17	4.20E-19	601.0	625.654	4.10%	1.00%	31.886	5.10%	0.25%	0.25%	0.35%	2.00%	5.49%	5.60%	2.66%	1.00%	2.84%	6.28%	OKAY
27.1	BC	0.893	0.660	MAT	624	2.07E-03	4.998E+17	4.20E-19	543.3	588.523	8.33%	1.00%	14.119	2.40%	0.25%	0.25%	0.35%	2.00%	3.14%	3.34%	9.80%	1.00%	9.85%	10.40%	OKAY
66.2	BC	0.893	0.660	SYN	624	1.04E-03	2.511E+17	4.20E-19	582.0	605.745	4.07%	1.00%	37.306	6.16%	0.25%	0.25%	0.35%	2.00%	6.49%	6.58%	4.92%	1.00%	5.02%	8.28%	OKAY
27.2	BC	0.893	0.965	MAT	624	2.06E-03	4.978E+17	4.20E-19	510.0	553.742	8.58%	1.00%	13.017	2.35%	0.25%	0.25%	0.35%	2.00%	3.11%	3.30%	14.27%	1.00%	14.30%	14.68%	OKAY
67.2	BC	0.893	0.965	SYN	624	1.04E-03	2.510E+17	4.20E-19	563.6	569.757	1.08%	1.00%	36.046	6.33%	0.25%	0.25%	0.35%	2.00%	6.64%	6.74%	7.19%	1.00%	7.26%	9.91%	OKAY
24.0	ABC	0.893	0.356	MAT	936	3.20E-03	7.736E+17	4.20E-19	833.8	907.738	8.87%	1.00%	18.850	2.08%	0.25%	0.25%	0.35%	2.00%	2.90%	3.11%	8.18%	1.00%	8.24%	8.81%	NO
65.0	ABC	0.893	0.356	SYN	936	1.03E-03	2.494E+17	4.20E-19	901.7	933.052	3.47%	1.00%	33.833	3.63%	0.25%	0.25%	0.35%	2.00%	4.16%	4.30%	2.64%	1.00%	2.82%	5.15%	OKAY
24.1	ABC	0.893	0.660	MAT	936	3.19E-03	7.700E+17	4.20E-19	756.1	842.543	11.43%	1.00%	16.748	1.99%	0.25%	0.25%	0.35%	2.00%	2.84%	3.05%	15.09%	1.00%	15.13%	15.43%	OKAY
66.0	ABC	0.893	0.660	SYN	936	1.03E-03	2.496E+17	4.20E-19	873.4	897.673	2.78%	1.00%	38.728	4.31%	0.25%	0.25%	0.35%	2.00%	4.77%	4.90%	4.89%	1.00%	4.99%	6.99%	OKAY
24.2	ABC	0.893	0.965	MAT	936	3.13E-03	7.560E+17	4.20E-19	689.0	788.667	14.47%	1.00%	15.277	1.94%	0.25%	0.25%	0.35%	2.00%	2.81%	3.02%	21.67%	1.00%	21.69%	21.90%	OKAY

Faraday Probe Data Analyses Results

RUN	SEGS	R	z (m)	TYPE	I_B (mA)	P (Pa)	n_b	σ_{ce}	I_Z	I_Z Integ.	Error	ε operation	σ_B (mA)	ε std	ε voltage	ε resistor	ε hardware	ε probes	ε acquisition	ε measured	dQ/Q	dIb/Ib	ε theoretical	ε total	CHECK
67.0	ABC	0.893	0.965	SYN	936	1.03E-03	2.495E+17	4.20E-19	846.0	843.560	-0.28%	1.00%	37.448	4.44%	0.25%	0.25%	0.35%	2.00%	4.88%	5.01%	7.15%	1.00%	7.22%	8.79%	OKAY
36.0	A	0.893	0.356	MAT	500	1.66E-03	3.999E+17	4.20E-19	471.0	512.055	8.72%	1.00%	15.248	2.98%	0.25%	0.25%	0.35%	2.00%	3.60%	3.77%	4.23%	1.00%	4.34%	5.75%	**NO**
36.0	A	0.893	0.356	RFND	500	1.65E-03	3.991E+17	4.20E-19	471.0	510.122	8.30%	1.00%	15.248	2.99%	0.25%	0.25%	0.35%	2.00%	3.61%	3.78%	4.22%	1.00%	4.34%	5.75%	**NO**
36.1	A	0.893	0.660	MAT	500	1.64E-03	3.965E+17	4.20E-19	448.0	481.390	7.46%	1.00%	12.605	2.62%	0.25%	0.25%	0.35%	2.00%	3.31%	3.50%	7.77%	1.00%	7.84%	8.58%	OKAY
36.1	A	0.893	0.660	RFND	500	1.64E-03	3.965E+17	4.20E-19	448.0	479.968	7.15%	1.00%	12.605	2.63%	0.25%	0.25%	0.35%	2.00%	3.32%	3.50%	7.77%	1.00%	7.84%	8.58%	OKAY
36.2	A	0.893	0.965	MAT	500	1.66E-03	4.016E+17	4.20E-19	424.9	462.831	8.93%	1.00%	12.255	2.65%	0.25%	0.25%	0.35%	2.00%	3.34%	3.52%	11.51%	1.00%	11.55%	12.08%	OKAY
36.2	A	0.893	0.965	RFND	500	1.66E-03	4.016E+17	4.20E-19	424.9	461.541	8.63%	1.00%	12.255	2.66%	0.25%	0.25%	0.35%	2.00%	3.34%	3.52%	11.51%	1.00%	11.55%	12.08%	OKAY
32.0	B	0.893	0.356	MAT	500	1.70E-03	4.101E+17	4.20E-19	470.3	515.352	9.59%	1.00%	16.866	3.27%	0.25%	0.25%	0.35%	2.00%	3.85%	4.01%	4.34%	1.00%	4.45%	5.99%	**NO**
32.0	B	0.893	0.356	RFND	500	1.70E-03	4.101E+17	4.20E-19	470.3	512.627	9.01%	1.00%	16.866	3.29%	0.25%	0.25%	0.35%	2.00%	3.87%	4.02%	4.34%	1.00%	4.45%	6.00%	**NO**
32.1	B	0.893	0.660	MAT	500	1.70E-03	4.101E+17	4.20E-19	446.3	481.109	7.81%	1.00%	13.871	2.88%	0.25%	0.25%	0.35%	2.00%	3.53%	3.70%	8.04%	1.00%	8.10%	8.90%	OKAY
32.1	B	0.893	0.660	RFND	500	1.70E-03	4.101E+17	4.20E-19	446.3	481.440	7.88%	1.00%	13.871	2.88%	0.25%	0.25%	0.35%	2.00%	3.53%	3.70%	8.04%	1.00%	8.10%	8.90%	OKAY
32.2	B	0.893	0.965	MAT	500	1.70E-03	4.101E+17	4.20E-19	423.4	451.269	6.57%	1.00%	12.938	2.87%	0.25%	0.25%	0.35%	2.00%	3.51%	3.69%	11.75%	1.00%	11.79%	12.36%	OKAY
32.2	B	0.893	0.965	RFND	500	1.70E-03	4.101E+17	4.20E-19	423.4	454.562	7.35%	1.00%	12.938	2.85%	0.25%	0.25%	0.35%	2.00%	3.50%	3.67%	11.75%	1.00%	11.79%	12.35%	OKAY
34.0	C	0.893	0.356	MAT	500	1.72E-03	4.157E+17	4.20E-19	469.9	505.765	7.64%	1.00%	13.614	2.69%	0.25%	0.25%	0.35%	2.00%	3.37%	3.55%	4.39%	1.00%	4.51%	5.74%	NO
34.0	C	0.893	0.356	RFND	500	1.72E-03	4.157E+17	4.20E-19	469.9	504.136	7.29%	1.00%	13.614	2.70%	0.25%	0.25%	0.35%	2.00%	3.38%	3.56%	4.39%	1.00%	4.51%	5.74%	NO
34.1	C	0.893	0.660	MAT	500	1.71E-03	4.131E+17	4.20E-19	445.9	475.443	6.63%	1.00%	10.723	2.26%	0.25%	0.25%	0.35%	2.00%	3.03%	3.23%	8.10%	1.00%	8.16%	8.78%	OKAY
34.1	C	0.893	0.660	RFND	500	1.71E-03	4.131E+17	4.20E-19	445.9	474.777	6.48%	1.00%	10.723	2.26%	0.25%	0.25%	0.35%	2.00%	3.04%	3.24%	8.10%	1.00%	8.16%	8.78%	OKAY
34.2	C	0.893	0.965	MAT	500	1.70E-03	4.098E+17	4.20E-19	423.5	458.249	8.21%	1.00%	10.179	2.22%	0.25%	0.25%	0.35%	2.00%	3.01%	3.21%	11.74%	1.00%	11.79%	12.22%	OKAY
34.2	C	0.893	0.965	RFND	500	1.70E-03	4.098E+17	4.20E-19	423.5	457.614	8.06%	1.00%	10.179	2.22%	0.25%	0.25%	0.35%	2.00%	3.01%	3.21%	11.74%	1.00%	11.79%	12.22%	OKAY
49.0	AB	0.893	0.356	MAT	1000	3.40E-03	8.208E+17	4.20E-19	884.5	986.622	11.54%	1.00%	48.624	4.93%	0.25%	0.25%	0.35%	2.00%	5.33%	5.45%	8.68%	1.00%	8.74%	10.29%	NO
68.1	AB	0.893	0.356	SYN	1000	1.68E-03	4.050E+17	4.20E-19	941.2	1020.790	8.45%	1.00%	22.736	2.23%	0.25%	0.25%	0.35%	2.00%	3.01%	3.21%	4.28%	1.00%	4.40%	5.45%	**NO**
37.1	AB	0.893	0.660	MAT	1000	3.47E-03	8.391E+17	4.20E-19	792.5	909.192	14.73%	1.00%	78.232	8.60%	0.25%	0.25%	0.35%	2.00%	8.84%	8.91%	16.45%	1.00%	16.48%	18.73%	OKAY
69.1	AB	0.893	0.660	SYN	1000	1.67E-03	4.033E+17	4.20E-19	894.2	962.121	7.59%	1.00%	18.743	1.95%	0.25%	0.25%	0.35%	2.00%	2.81%	3.03%	7.91%	1.00%	7.97%	8.52%	OKAY
37.2	AB	0.893	0.965	MAT	1000	3.45E-03	8.335E+17	4.20E-19	713.3	847.877	18.86%	1.00%	77.982	9.20%	0.25%	0.25%	0.35%	2.00%	9.42%	9.48%	23.89%	1.00%	23.91%	25.72%	OKAY
70.1	AB	0.893	0.965	SYN	1000	1.68E-03	4.059E+17	4.20E-19	848.3	915.380	7.90%	1.00%	17.821	1.95%	0.25%	0.25%	0.35%	2.00%	2.81%	3.03%	11.63%	1.00%	11.67%	12.06%	OKAY
35.1	AC	0.893	0.356	MAT	1000	3.35E-03	8.098E+17	4.20E-19	886.0	981.263	10.76%	1.00%	15.321	1.56%	0.25%	0.25%	0.35%	2.00%	2.56%	2.80%	8.56%	1.00%	8.62%	9.06%	NO

Faraday Probe Data Analyses Results

RUN	SEGS	R	z (m)	TYPE	I_B (mA)	P (Pa)	n_b	σ_{ce}	I_z	I_z Integ.	Error	ε operation	σ_B (mA)	ε std	ε voltage	ε resistor	ε hardware	ε probes	ε acquisition	ε measured	dQ/Q	dIb/Ib	ε theoretical	ε total	CHECK
68.3	AC	0.893	0.356	SYN	1000	1.69E-03	4.078E+17	4.20E-19	940.9	1014.830	7.86%	1.00%	20.441	2.01%	0.25%	0.25%	0.35%	2.00%	2.86%	3.07%	4.31%	1.00%	4.43%	5.39%	**NO**
35.2	AC	0.893	0.660	MAT	1000	3.34E-03	8.062E+17	4.20E-19	799.7	910.417	13.84%	1.00%	13.337	1.46%	0.25%	0.25%	0.35%	2.00%	2.50%	2.74%	15.80%	1.00%	15.84%	16.07%	OKAY
69.3	AC	0.893	0.660	SYN	1000	1.68E-03	4.048E+17	4.20E-19	893.8	955.191	6.86%	1.00%	16.548	1.73%	0.25%	0.25%	0.35%	2.00%	2.67%	2.89%	7.94%	1.00%	8.00%	8.51%	OKAY
38.2	AC	0.893	0.965	MAT	1000	3.42E-03	8.259E+17	4.20E-19	715.5	985.913	37.79%	1.00%	92.370	9.37%	0.25%	0.25%	0.35%	2.00%	9.59%	9.65%	23.67%	1.00%	23.69%	25.58%	**NO**
70.3	AC	0.893	0.965	SYN	1000	1.68E-03	4.057E+17	4.20E-19	848.4	919.237	8.35%	1.00%	15.931	1.73%	0.25%	0.25%	0.35%	2.00%	2.67%	2.89%	11.63%	1.00%	11.67%	12.02%	OKAY
33.0	BC	0.893	0.356	MAT	1000	3.50E-03	8.447E+17	4.20E-19	881.3	966.553	9.67%	1.00%	19.466	2.01%	0.25%	0.25%	0.35%	2.00%	2.86%	3.07%	8.93%	1.00%	8.99%	9.50%	NO
68.2	BC	0.893	0.356	SYN	1000	1.71E-03	4.129E+17	4.20E-19	940.1	1016.470	8.12%	1.00%	21.675	2.13%	0.25%	0.25%	0.35%	2.00%	2.94%	3.15%	4.37%	1.00%	4.48%	5.48%	**NO**
33.3	BC	0.893	0.660	MAT	1000	3.38E-03	8.162E+17	4.20E-19	797.5	923.394	15.78%	1.00%	17.373	1.88%	0.25%	0.25%	0.35%	2.00%	2.77%	2.99%	16.00%	1.00%	16.03%	16.31%	OKAY
69.2	BC	0.893	0.660	SYN	1000	1.70E-03	4.116E+17	4.20E-19	892.2	957.074	7.27%	1.00%	17.532	1.83%	0.25%	0.25%	0.35%	2.00%	2.74%	2.95%	8.07%	1.00%	8.13%	8.65%	OKAY
33.4	BC	0.893	0.965	MAT	1000	3.41E-03	8.243E+17	4.20E-19	716.0	850.760	18.83%	1.00%	15.116	1.78%	0.25%	0.25%	0.35%	2.00%	2.70%	2.92%	23.63%	1.00%	23.65%	23.83%	OKAY
70.2	BC	0.893	0.965	SYN	1000	1.70E-03	4.099E+17	4.20E-19	846.9	912.107	7.70%	1.00%	16.462	1.80%	0.25%	0.25%	0.35%	2.00%	2.72%	2.94%	11.75%	1.00%	11.79%	12.15%	OKAY
48.0	ABC	0.893	0.356	MAT	1500	5.33E-03	1.286E+18	4.20E-19	1237.6	1417.590	14.55%	1.00%	79.391	5.60%	0.25%	0.25%	0.35%	2.00%	5.96%	6.06%	13.60%	1.00%	13.64%	14.92%	OKAY
68.0	ABC	0.893	0.356	SYN	1500	1.69E-03	4.085E+17	4.20E-19	1411.1	1526.050	8.14%	1.00%	26.500	1.74%	0.25%	0.25%	0.35%	2.00%	2.67%	2.90%	4.32%	1.00%	4.43%	5.30%	**NO**
48.1	ABC	0.893	0.660	MAT	1500	5.27E-03	1.274E+18	4.20E-19	1053.7	1280.890	21.56%	1.00%	69.860	5.45%	0.25%	0.25%	0.35%	2.00%	5.82%	5.93%	24.97%	1.00%	24.99%	25.69%	OKAY
69.0	ABC	0.893	0.660	SYN	1500	1.68E-03	4.066E+17	4.20E-19	1340.1	1437.190	7.24%	1.00%	21.593	1.50%	0.25%	0.25%	0.35%	2.00%	2.53%	2.76%	7.97%	1.00%	8.03%	8.49%	OKAY
48.2	ABC	0.893	0.965	MAT	1500	5.23E-03	1.264E+18	4.20E-19	898.5	1157.740	28.85%	1.00%	68.310	5.90%	0.25%	0.25%	0.35%	2.00%	6.24%	6.34%	36.24%	1.00%	36.25%	36.80%	OKAY
70.0	ABC	0.893	0.965	SYN	1500	1.69E-03	4.072E+17	4.20E-19	1271.8	1373.360	7.98%	1.00%	20.523	1.49%	0.25%	0.25%	0.35%	2.00%	2.52%	2.76%	11.67%	1.00%	11.71%	12.03%	OKAY
45.0	A	0.643	0.356	MAT	430	1.16E-03	2.793E+17	4.20E-19	412.4	326.137	-20.92%	1.00%	21.760	6.67%	0.25%	0.25%	0.35%	2.00%	6.97%	7.06%	2.95%	1.00%	3.12%	7.72%	NO
45.0	A	0.643	0.356	RFND	430	1.16E-03	2.793E+17	4.20E-19	412.4	323.984	-21.44%	1.00%	21.760	6.72%	0.25%	0.25%	0.35%	2.00%	7.02%	7.11%	2.95%	1.00%	3.12%	7.76%	NO
45.1	A	0.643	0.660	MAT	430	1.15E-03	2.777E+17	4.20E-19	398.1	297.996	-25.15%	1.00%	18.617	6.25%	0.25%	0.25%	0.35%	2.00%	6.57%	6.66%	5.44%	1.00%	5.54%	8.66%	NO
45.1	A	0.643	0.660	RFND	430	1.15E-03	2.777E+17	4.20E-19	398.1	298.601	-25.00%	1.00%	18.617	6.23%	0.25%	0.25%	0.35%	2.00%	6.56%	6.65%	5.44%	1.00%	5.54%	8.65%	NO
45.2	A	0.643	0.965	MAT	430	1.14E-03	2.765E+17	4.20E-19	384.4	273.117	-28.95%	1.00%	17.437	6.38%	0.25%	0.25%	0.35%	2.00%	6.70%	6.79%	7.92%	1.00%	7.99%	10.48%	NO
45.2	A	0.643	0.965	RFND	430	1.14E-03	2.765E+17	4.20E-19	384.4	274.335	-28.64%	1.00%	17.437	6.36%	0.25%	0.25%	0.35%	2.00%	6.67%	6.77%	7.92%	1.00%	7.99%	10.47%	NO
46.0	B	0.643	0.356	MAT	430	1.14E-03	2.752E+17	4.20E-19	412.7	328.862	-20.31%	1.00%	24.089	7.32%	0.25%	0.25%	0.35%	2.00%	7.60%	7.68%	2.91%	1.00%	3.08%	8.28%	NO
46.0	B	0.643	0.356	RFND	430	1.14E-03	2.752E+17	4.20E-19	412.7	326.740	-20.82%	1.00%	24.089	7.37%	0.25%	0.25%	0.35%	2.00%	7.65%	7.73%	2.91%	1.00%	3.08%	8.32%	NO
46.1	B	0.643	0.660	MAT	430	1.16E-03	2.793E+17	4.20E-19	398.0	297.287	-25.30%	1.00%	21.466	7.22%	0.25%	0.25%	0.35%	2.00%	7.50%	7.58%	5.47%	1.00%	5.56%	9.41%	NO
46.1	B	0.643	0.660	RFND	430	1.16E-03	2.793E+17	4.20E-19	398.0	297.766	-25.18%	1.00%	21.466	7.21%	0.25%	0.25%	0.35%	2.00%	7.49%	7.57%	5.47%	1.00%	5.56%	9.40%	NO

Faraday Probe Data Analyses Results

RUN	SEGS	R	z (m)	TYPE	I_B (mA)	P (Pa)	n_b	σ_{ce}	I_z	I_z Integ.	Error	ε operation	σ_B (mA)	ε std	ε voltage	ε resistor	ε hardware	ε probes	ε acquisition	ε measured	dQ/Q	dIb/Ib	ε theoretical	ε total	CHECK
46.2	B	0.643	0.965	MAT	430	1.16E-03	2.811E+17	4.20E-19	383.7	261.716	-31.79%	1.00%	21.001	8.02%	0.25%	0.25%	0.35%	2.00%	8.28%	8.35%	8.05%	1.00%	8.12%	11.65%	NO
46.2	B	0.643	0.965	RFND	430	1.16E-03	2.811E+17	4.20E-19	383.7	263.700	-31.28%	1.00%	21.001	7.96%	0.25%	0.25%	0.35%	2.00%	8.22%	8.29%	8.05%	1.00%	8.12%	11.61%	NO
47.0	C	0.643	0.356	MAT	430	1.19E-03	2.872E+17	4.20E-19	411.9	342.120	-16.95%	1.00%	26.875	7.86%	0.25%	0.25%	0.35%	2.00%	8.11%	8.19%	3.04%	1.00%	3.20%	8.79%	NO
47.0	C	0.643	0.356	RFND	430	1.19E-03	2.872E+17	4.20E-19	411.9	339.824	-17.50%	1.00%	26.875	7.91%	0.25%	0.25%	0.35%	2.00%	8.17%	8.24%	3.04%	1.00%	3.20%	8.84%	NO
47.1	C	0.643	0.660	MAT	430	1.19E-03	2.864E+17	4.20E-19	397.2	304.718	-23.28%	1.00%	23.206	7.62%	0.25%	0.25%	0.35%	2.00%	7.88%	7.96%	5.61%	1.00%	5.70%	9.79%	NO
47.1	C	0.643	0.660	RFND	430	1.19E-03	2.864E+17	4.20E-19	397.2	305.185	-23.16%	1.00%	23.206	7.60%	0.25%	0.25%	0.35%	2.00%	7.87%	7.95%	5.61%	1.00%	5.70%	9.78%	NO
47.2	C	0.643	0.965	MAT	430	1.19E-03	2.864E+17	4.20E-19	382.9	275.022	-28.17%	1.00%	22.368	8.13%	0.25%	0.25%	0.35%	2.00%	8.38%	8.46%	8.21%	1.00%	8.27%	11.83%	NO
47.2	C	0.643	0.965	RFND	430	1.19E-03	2.864E+17	4.20E-19	382.9	275.607	-28.02%	1.00%	22.368	8.12%	0.25%	0.25%	0.35%	2.00%	8.37%	8.44%	8.21%	1.00%	8.27%	11.82%	NO
42.0	AB	0.643	0.356	MAT	860	2.22E-03	5.352E+17	4.20E-19	793.9	606.215	-23.64%	1.00%	29.220	4.82%	0.25%	0.25%	0.35%	2.00%	5.23%	5.35%	5.66%	1.00%	5.75%	7.85%	NO
71.1	AB	0.643	0.356	SYN	860	1.15E-03	2.772E+17	4.20E-19	825.1	646.227	-21.68%	1.00%	32.462	5.02%	0.25%	0.25%	0.35%	2.00%	5.42%	5.53%	2.93%	1.00%	3.10%	6.34%	NO
42.1	AB	0.643	0.660	MAT	860	2.22E-03	5.352E+17	4.20E-19	741.4	597.871	-19.36%	1.00%	27.565	4.61%	0.25%	0.25%	0.35%	2.00%	5.04%	5.16%	10.49%	1.00%	10.54%	11.73%	NO
72.1	AB	0.643	0.660	SYN	860	1.15E-03	2.785E+17	4.20E-19	796.1	713.706	-10.35%	1.00%	28.414	3.98%	0.25%	0.25%	0.35%	2.00%	4.47%	4.61%	5.46%	1.00%	5.55%	7.21%	NO
42.2	AB	0.643	0.965	MAT	860	2.22E-03	5.352E+17	4.20E-19	692.3	522.359	-24.55%	1.00%	27.508	5.27%	0.25%	0.25%	0.35%	2.00%	5.64%	5.75%	15.34%	1.00%	15.37%	16.41%	NO
73.1	AB	0.643	0.965	SYN	860	1.15E-03	2.788E+17	4.20E-19	768.1	540.724	-29.60%	1.00%	27.296	5.05%	0.25%	0.25%	0.35%	2.00%	5.44%	5.56%	7.99%	1.00%	8.05%	9.78%	NO
44.0	AC	0.643	0.356	MAT	860	2.47E-03	5.969E+17	4.20E-19	786.6	616.547	-21.62%	1.00%	33.227	5.39%	0.25%	0.25%	0.35%	2.00%	5.76%	5.87%	6.31%	1.00%	6.39%	8.67%	NO
71.3	AC	0.643	0.356	SYN	860	1.17E-03	2.832E+17	4.20E-19	824.3	663.328	-19.53%	1.00%	34.580	5.21%	0.25%	0.25%	0.35%	2.00%	5.59%	5.71%	2.99%	1.00%	3.16%	6.52%	NO
44.1	AC	0.643	0.660	MAT	860	2.47E-03	5.969E+17	4.20E-19	728.8	559.846	-23.19%	1.00%	25.430	4.54%	0.25%	0.25%	0.35%	2.00%	4.98%	5.10%	11.70%	1.00%	11.74%	12.80%	NO
72.3	AC	0.643	0.660	SYN	860	1.17E-03	2.821E+17	4.20E-19	795.3	604.804	-23.95%	1.00%	29.751	4.92%	0.25%	0.25%	0.35%	2.00%	5.32%	5.44%	5.53%	1.00%	5.62%	7.82%	NO
44.3	AC	0.643	0.965	MAT	860	2.47E-03	5.969E+17	4.20E-19	675.2	534.672	-20.81%	1.00%	32.064	6.00%	0.25%	0.25%	0.35%	2.00%	6.33%	6.43%	17.11%	1.00%	17.14%	18.30%	NO
73.3	AC	0.643	0.965	SYN	860	1.17E-03	2.814E+17	4.20E-19	767.3	553.153	-27.91%	1.00%	28.361	5.13%	0.25%	0.25%	0.35%	2.00%	5.51%	5.63%	8.07%	1.00%	8.13%	9.89%	NO
43.0	BC	0.643	0.356	MAT	860	2.30E-03	5.546E+17	4.20E-19	791.6	620.620	-21.60%	1.00%	34.039	5.48%	0.25%	0.25%	0.35%	2.00%	5.85%	5.95%	5.86%	1.00%	5.95%	8.42%	NO
71.2	BC	0.643	0.356	SYN	860	1.16E-03	2.812E+17	4.20E-19	824.6	666.549	-19.17%	1.00%	36.091	5.41%	0.25%	0.25%	0.35%	2.00%	5.78%	5.89%	2.97%	1.00%	3.14%	6.67%	NO
43.1	BC	0.643	0.660	MAT	860	2.30E-03	5.546E+17	4.20E-19	737.4	565.843	-23.27%	1.00%	28.058	4.96%	0.25%	0.25%	0.35%	2.00%	5.36%	5.47%	10.87%	1.00%	10.92%	12.21%	NO
72.2	BC	0.643	0.660	SYN	860	1.17E-03	2.828E+17	4.20E-19	795.1	604.298	-24.00%	1.00%	31.612	5.23%	0.25%	0.25%	0.35%	2.00%	5.61%	5.72%	5.54%	1.00%	5.63%	8.03%	NO
43.2	BC	0.643	0.965	MAT	860	2.30E-03	5.546E+17	4.20E-19	686.9	518.354	-24.53%	1.00%	28.457	5.49%	0.25%	0.25%	0.35%	2.00%	5.85%	5.96%	15.90%	1.00%	15.93%	17.00%	NO
73.2	BC	0.643	0.965	SYN	860	1.17E-03	2.837E+17	4.20E-19	766.6	542.586	-29.22%	1.00%	30.681	5.65%	0.25%	0.25%	0.35%	2.00%	6.01%	6.11%	8.13%	1.00%	8.19%	10.22%	NO

Faraday Probe Data Analyses Results

RUN	SEGS	R	z (m)	TYPE	I_B (mA)	P (Pa)	n_b	σ_{ce}	I_z	I_z Integ.	Error	ε operation	σ_B (mA)	ε std	ε voltage	ε resistor	ε hardware	ε probes	ε acquisition	ε measured	dQ/Q	dIb/Ib	ε theoretical	ε total	CHECK
41.0	ABC	0.643	0.356	MAT	1290	3.35E-03	8.083E+17	4.20E-19	1143.1	922.053	-19.34%	1.00%	42.394	4.60%	0.25%	0.25%	0.35%	2.00%	5.03%	5.15%	8.55%	1.00%	8.60%	10.03%	NO
71.0	ABC	0.643	0.356	SYN	1290	1.16E-03	2.805E+17	4.20E-19	1237.0	988.053	-20.13%	1.00%	42.143	4.27%	0.25%	0.25%	0.35%	2.00%	4.72%	4.85%	2.97%	1.00%	3.13%	5.78%	NO
41.1	ABC	0.643	0.660	MAT	1290	3.33E-03	8.034E+17	4.20E-19	1032.4	850.681	-17.61%	1.00%	37.774	4.44%	0.25%	0.25%	0.35%	2.00%	4.88%	5.01%	15.75%	1.00%	15.78%	16.56%	NO
72.0	ABC	0.643	0.660	SYN	1290	1.16E-03	2.811E+17	4.20E-19	1193.3	903.487	-24.29%	1.00%	36.686	4.06%	0.25%	0.25%	0.35%	2.00%	4.54%	4.68%	5.51%	1.00%	5.60%	7.30%	NO
41.2	ABC	0.643	0.965	MAT	1290	3.31E-03	8.006E+17	4.20E-19	932.5	769.958	-17.43%	1.00%	37.721	4.90%	0.25%	0.25%	0.35%	2.00%	5.30%	5.42%	22.95%	1.00%	22.97%	23.60%	OKAY
73.0	ABC	0.643	0.965	SYN	1290	1.16E-03	2.813E+17	4.20E-19	1151.0	818.232	-28.91%	1.00%	35.290	4.31%	0.25%	0.25%	0.35%	2.00%	4.77%	4.90%	8.06%	1.00%	8.12%	9.49%	NO
50.1	B	0.893	0.356	MAT	430	1.58E-03	3.805E+17	4.20E-19	406.2	434.000	6.84%	1.00%	28.356	6.53%	0.25%	0.25%	0.35%	2.00%	6.84%	6.93%	4.02%	1.00%	4.15%	8.08%	OKAY
50.1	B	0.893	0.356	RFND	430	1.58E-03	3.805E+17	4.20E-19	406.2	432.380	6.44%	1.00%	28.356	6.56%	0.25%	0.25%	0.35%	2.00%	6.87%	6.96%	4.02%	1.00%	4.15%	8.10%	OKAY
50.2	B	0.893	0.508	MAT	430	1.47E-03	3.558E+17	4.20E-19	398.6	426.000	6.88%	1.00%	27.929	6.56%	0.25%	0.25%	0.35%	2.00%	6.86%	6.95%	5.37%	1.00%	5.46%	8.84%	OKAY
50.2	B	0.893	0.508	RFND	430	1.47E-03	3.558E+17	4.20E-19	398.6	422.650	6.04%	1.00%	27.929	6.61%	0.25%	0.25%	0.35%	2.00%	6.91%	7.00%	5.37%	1.00%	5.46%	8.88%	OKAY
51.0	B	0.893	0.660	MAT	430	2.07E-03	4.998E+17	4.20E-19	374.4	401.000	7.11%	1.00%	25.264	6.30%	0.25%	0.25%	0.35%	2.00%	6.62%	6.71%	9.80%	1.00%	9.85%	11.92%	OKAY
51.0	B	0.893	0.660	RFND	430	2.07E-03	4.998E+17	4.20E-19	374.4	400.420	6.96%	1.00%	25.264	6.31%	0.25%	0.25%	0.35%	2.00%	6.63%	6.72%	9.80%	1.00%	9.85%	11.92%	OKAY
52.0	A	0.893	0.356	MAT	430	2.02E-03	4.891E+17	4.20E-19	399.7	428.000	7.09%	1.00%	25.663	6.00%	0.25%	0.25%	0.35%	2.00%	6.33%	6.43%	5.17%	1.00%	5.27%	8.31%	OKAY
52.0	A	0.893	0.356	RFND	430	2.02E-03	4.891E+17	4.20E-19	399.7	425.790	6.53%	1.00%	25.663	6.03%	0.25%	0.25%	0.35%	2.00%	6.36%	6.46%	5.17%	1.00%	5.27%	8.33%	OKAY
52.1	A	0.893	0.508	MAT	430	1.55E-03	3.736E+17	4.20E-19	397.1	416.000	4.77%	1.00%	22.136	5.32%	0.25%	0.25%	0.35%	2.00%	5.70%	5.80%	5.64%	1.00%	5.72%	8.15%	OKAY
52.1	A	0.893	0.508	RFND	430	1.55E-03	3.736E+17	4.20E-19	397.1	414.060	4.28%	1.00%	22.136	5.35%	0.25%	0.25%	0.35%	2.00%	5.72%	5.83%	5.64%	1.00%	5.72%	8.17%	OKAY
52.2	A	0.893	0.660	MAT	430	1.55E-03	3.751E+17	4.20E-19	387.5	393.000	1.41%	1.00%	18.726	4.76%	0.25%	0.25%	0.35%	2.00%	5.18%	5.30%	7.35%	1.00%	7.42%	9.12%	OKAY
52.2	A	0.893	0.660	RFND	430	1.55E-03	3.751E+17	4.20E-19	387.5	392.190	1.20%	1.00%	18.726	4.77%	0.25%	0.25%	0.35%	2.00%	5.19%	5.31%	7.35%	1.00%	7.42%	9.12%	OKAY

Thruster Centerline Location

Run #	Segment On	z (m)	x (cm)	y (cm)
21.0	A	0.356	43.18	63.50
21.1	A	0.508	43.18	63.50
21.3	A	0.660	43.18	63.50
21.4	A	0.813	41.91	62.23
21.5	A	0.965	41.91	62.23
22.4	B	0.356	66.04	60.96
22.0	B	0.508	66.04	60.96
22.1	B	0.660	66.04	60.96
22.2	B	0.813	67.31	59.69
22.3	B	0.965	67.31	59.69
23.4	C	0.356	64.77	83.82
23.0	C	0.508	64.77	83.82
23.1	C	0.660	63.50	83.82
23.2	C	0.813	63.50	85.09
23.3	C	0.965	63.50	83.82
30.0	A	0.356	43.18	63.50
30.1	A	0.660	43.18	63.50
30.2	A	0.965	41.91	62.23
31.0	B	0.356	66.04	60.96
31.1	B	0.660	66.04	60.96
31.2	B	0.965	66.04	59.69
28.0	C	0.356	63.50	83.82
28.1	C	0.660	63.50	83.82
28.2	C	0.965	63.50	83.82
36.0	A	0.356	43.18	63.50
36.1	A	0.660	43.18	63.50
36.2	A	0.965	41.91	62.23
32.0	B	0.356	66.04	60.96
32.1	B	0.660	66.04	60.96
32.2	B	0.965	66.04	58.42
34.0	C	0.356	64.77	83.82

Thruster Centerline Location

Run #	Segment On	z (m)	x (cm)	y (cm)
34.1	C	0.660	64.77	83.82
34.2	C	0.965	63.50	83.82
45.0	A	0.356	44.45	62.23
45.1	A	0.660	17.25	62.23
45.2	A	0.965	41.91	60.96
46.0	B	0.356	66.04	60.96
46.1	B	0.660	66.04	59.69
46.2	B	0.965	66.04	60.96
47.0	C	0.356	63.50	83.82
47.1	C	0.660	63.50	85.09
47.2	C	0.965	63.50	85.09
52.0	A	0.356	44.45	60.96
52.1	A	0.508	43.18	59.69
52.2	A	0.660	43.18	59.69
50.0	B	0.356	66.04	59.69
50.1	B	0.508	66.04	58.42
51.0	B	0.660	66.04	57.15

Beam Divergence & Flatness Results

Run #	Seg	R	z (m)	I_B (mA)	I_α (mA)	J_α (mA/cm2)	R_α (cm)	dR_α (cm)	α (deg)	$d\alpha$ (deg)	Jmax (mA/cm2)	F	dF
21.0	A	0.893	0.356	430	409.314	0.444	17.123	0.520	15.126	0.015	2.311	0.192	0.015
21.1	A	0.893	0.508	430	391.708	0.300	20.394	0.588	14.242	0.012	1.677	0.179	0.014
21.2	A	0.893	0.660	430	378.885	0.198	24.667	0.706	14.580	0.011	1.208	0.164	0.012
21.4	A	0.893	0.813	430	N/A	N/A	N/A	N/A	N/A	N/A	N/A	N/A	N/A
21.5	A	0.893	0.965	430	N/A	N/A	N/A	N/A	N/A	N/A	N/A	N/A	N/A
22.4	B	0.893	0.356	430	408.901	0.624	14.439	0.408	11.030	0.012	2.730	0.229	0.017
22.0	B	0.893	0.508	430	396.535	0.391	17.960	0.525	11.635	0.011	1.955	0.200	0.015
22.1	B	0.893	0.660	430	382.008	0.296	20.280	0.577	10.959	0.010	1.420	0.208	0.016
22.2	B	0.893	0.813	430	369.590	0.225	22.874	0.644	10.708	0.009	1.039	0.216	0.016
22.3	B	0.893	0.965	430	363.282	0.181	25.287	0.715	10.444	0.009	0.8049	0.225	0.017
23.4	C	0.893	0.965	430	417.990	0.537	15.738	0.426	13.029	0.013	2.441	0.220	0.016
23.0	C	0.893	0.965	430	407.988	0.311	20.426	0.549	14.276	0.012	1.828	0.170	0.012
23.1	C	0.893	0.965	430	392.183	0.233	23.164	0.595	13.351	0.010	1.366	0.170	0.012
23.2	C	0.893	0.965	430	N/A	N/A	N/A	N/A	N/A	N/A	N/A	N/A	N/A
23.3	C	0.893	0.965	430	N/A	N/A	N/A	N/A	N/A	N/A	N/A	N/A	N/A
30.0	A	0.893	0.356	312	292.832	0.366	15.953	0.515	13.358	0.015	1.697	0.216	0.018
30.1	A	0.893	0.660	312	277.630	0.139	25.246	0.798	15.050	0.013	0.7933	0.175	0.014
30.2	A	0.893	0.965	312	N/A	N/A	N/A	N/A	N/A	N/A	N/A	N/A	N/A
31.0	B	0.893	0.356	312	288.667	0.076	34.747	1.286	37.429	0.029	1.794	0.042	0.004
31.1	B	0.893	0.660	312	268.282	0.187	21.342	0.702	11.845	0.012	0.7887	0.238	0.020
31.2	B	0.893	0.965	312	251.951	0.099	28.517	0.904	12.286	0.010	0.3947	0.250	0.020
28.0	C	0.893	0.356	312	306.462	0.355	16.566	1.143	14.287	0.032	1.777	0.200	0.034
28.1	C	0.893	0.660	312	305.376	0.117	28.790	2.435	17.878	0.035	0.8881	0.132	0.027
28.2	C	0.893	0.965	312	290.535	0.068	36.780	3.177	16.879	0.032	0.4752	0.144	0.030
36.0	A	0.893	0.356	500	484.616	0.596	16.089	0.453	13.564	0.014	2.728	0.218	0.016
36.1	A	0.893	0.660	500	455.970	0.268	23.274	0.607	13.441	0.010	1.371	0.195	0.014
36.2	A	0.893	0.965	500	438.464	0.148	30.741	0.807	13.541	0.009	0.7613	0.194	0.014
32.0	B	0.893	0.356	500	486.996	0.612	15.921	0.477	13.308	0.014	2.885	0.212	0.017
32.1	B	0.893	0.660	500	457.368	0.326	21.141	0.582	11.677	0.010	1.404	0.232	0.017
32.2	B	0.893	0.965	500	431.834	0.186	27.208	0.744	11.543	0.009	0.7763	0.239	0.017
34.0	C	0.893	0.356	500	478.929	0.639	15.450	0.409	12.589	0.012	2.324	0.275	0.019

Beam Divergence & Flatness Results

Run #	Seg	R	z (m)	I_B (mA)	I_α (mA)	J_α (mA/cm2)	R_α (cm)	dR_α (cm)	α (deg)	$d\alpha$ (deg)	Jmax (mA/cm2)	F	dF
34.1	C	0.893	0.660	500	451.038	0.276	22.814	0.550	13.063	0.010	1.043	0.264	0.017
34.2	C	0.893	0.965	500	434.733	0.151	30.272	0.724	13.278	0.009	0.5494	0.275	0.018
45.0	A	0.615	0.356	430	307.785	0.236	20.377	1.078	19.886	0.029	1.085	0.217	0.028
45.1	A	0.615	0.660	430	283.671	0.095	30.854	1.528	19.486	0.022	0.3843	0.247	0.030
45.2	A	0.615	0.965	430	N/A	N/A	N/A	N/A	N/A	N/A	N/A	N/A	N/A
46.0	B	0.615	0.356	430	310.403	0.274	18.991	1.092	17.889	0.030	1.218	0.225	0.032
46.1	B	0.615	0.660	430	282.878	0.123	27.108	1.528	16.546	0.023	0.3891	0.315	0.044
46.2	B	0.615	0.965	430	N/A	N/A	N/A	N/A	N/A	N/A	N/A	N/A	N/A
47.0	C	0.615	0.356	430	322.833	0.212	21.995	1.349	22.155	0.035	1.215	0.175	0.026
47.1	C	0.615	0.660	430	N/A	N/A	N/A	N/A	N/A	N/A	N/A	N/A	N/A
47.2	C	0.615	0.965	430	N/A	N/A	N/A	N/A	N/A	N/A	N/A	N/A	N/A
52.0	A	0.893	0.356	430	404.501	0.474	16.487	0.792	14.168	0.022	2.182	0.246	0.032
52.1	A	0.893	0.508	430	393.357	0.371	18.377	0.797	12.085	0.016	1.798	0.216	0.028
52.2	A	0.893	0.660	430	372.581	0.280	20.589	0.813	11.217	0.013	1.312	0.213	0.026
50.1	B	0.893	0.356	430	410.761	0.680	13.868	0.718	10.142	0.021	2.766	0.217	0.026
50.2	B	0.893	0.508	430	401.518	0.437	17.107	0.892	10.709	0.018	2.022	0.206	0.022
51.0	B	0.893	0.660	430	380.399	0.277	20.897	1.046	11.474	0.016	1.300	0.213	0.021

MAT vs. RFND Data Comparison

	MAT Data			RFND Data	
Run #	I_Z	dI_Z/I_Z	I_Z	dI_Z/I_Z	Delta
21.0	430.341	4.08%	430.857	4.08%	+0.12%
21.1	412.163	3.87%	412.324	3.87%	+0.04%
21.2	398.412	3.85%	398.826	3.84%	+0.10%
21.4	400.639	4.12%	401.171	4.12%	+0.13%
21.5	384.990	4.02%	385.425\	4.02%	+0.11%
22.4	431.137	3.80%	430.422	3.80%	-0.17%
22.0	417.424	3.93%	417.405	3.93%	-0.01%
22.1	402.517	3.82%	402.114	3.82%	-0.10%
22.2	389.134	3.79%	389.042	3.79%	-0.02%
22.3	382.222	3.80%	382.402	3.80%	+0.05%
23.4	440.330	3.64%	439.989	3.64%	-0.08%
23.0	429.349	3.62%	429.461	3.61%	+0.03%
23.1	413.160	3.45%	412.824	3.46%	-0.08%
23.2	397.392	3.44%	397.818	3.43%	+0.11%
23.3	381.533	3.50%	382.350	3.50%	+0.21%
30.0	310.110	4.32%	308.244	4.34%	-0.60%
30.1	293.218	4.24%	292.242	4.25%	-0.33%
30.2	273.382	4.38%	273.221	4.38%	-0.06%
31.0	305.436	4.95%	303.860	4.97%	-0.52%
31.1	282.928	4.41%	282.402	4.42%	-0.19%
31.2	266.483	4.24%	265.212	4.26%	-0.48%
28.0	322.813	9.26%	322.592	9.27%	-0.07%
28.1	322.858	11.32%	321.448	11.36%	-0.44%
28.2	305.038	11.63%	305.826	11.61%	+0.26%
36.0	512.055	3.77%	510.122	3.78%	-0.38%
36.1	481.390	3.50%	479.968	3.50%	-0.30%
36.2	462.831	3.52%	461.541	3.52%	-0.28%
32.0	515.352	4.01%	512.627	4.02%	-0.53%

MAT vs. RFND Data Comparison

	MAT Data			RFND Data	
Run #	I_Z	dI_Z/I_Z	I_Z	dI_Z/I_Z	Delta
32.1	481.109	3.70%	481.440	3.70%	+0.07%
32.2	451.269	3.69%	454.562	3.67%	+0.73%
34.0	505.765	3.55%	504.136	3.56%	-0.32%
34.1	475.443	3.23%	474.777	3.24%	-0.14%
34.2	458.249	3.21%	457.614	3.21%	-0.14%
45.0	326.137	7.06%	323.984	7.11%	-0.66%
45.1	297.996	6.66%	298.601	6.65%	+0.20%
45.2	273.117	6.79%	274.335	6.77%	+0.46%
46.0	328.862	7.68%	326.740	7.73%	-0.65%
46.1	297.287	7.58%	297.766	7.57%	+0.16%
46.2	261.716	8.35%	263.700	8.29%	+0.76%
47.0	342.120	8.19%	339.824	8.24%	-0.67%
47.1	304.718	7.96%	305.185	7.95%	+0.15%
47.2	275.022	8.46%	275.607	8.44%	+0.21%
52.0	428.	6.43%	425.790	6.46%	-0.52%
52.1	416.	5.80%	414.060	5.83%	-0.47%
52.2	393.	5.30%	392.190	5.31%	-0.21%
50.1	434	6.93%	432.380	6.96%	-0.37%
50.2	426	6.95%	422.650	7.00%	-0.79%
51.0	401	6.71%	400.420	6.72%	-0.15%

MAT vs. SYN Data Comparison

	MAT Data			SYN Data			Total
Run #	I_Z	dI_Z/I_Z	Run #	I_Z	dI_Z/I_Z	Delta	Uncertainty
19.0	825.250	3.37%	60.1	860.417	3.24%	4.26%	4.68%
19.1	801.092	3.23%	61.1	829.766	3.21%	3.58%	4.55%
19.2	769.235	3.16%	62.1	800.632	3.17%	4.08%	4.48%
19.3	742.781	3.08%	63.1	790.858	3.24%	6.47%	4.47%
19.4	715.202	3.05%	64.1	769.455	3.21%	7.59%	4.43%
18.1	837.436	2.93%	60.3	870.142	3.19%	3.91%	4.33%
18.2	807.279	2.93%	61.3	841.786	3.11%	4.28%	4.27%
18.3	776.402	2.88%	62.3	811.827	3.06%	4.56%	4.20%
18.4	750.678	2.92%	63.3	800.047	3.14%	6.58%	4.28%
18.6	732.782	3.01%	64.3	769.857	3.13%	5.06%	4.34%
20.0	831.719	2.62%	60.2	870.049	3.10%	4.61%	4.05%
20.1	799.650	2.64%	61.2	846.846	3.13%	5.90%	4.10%
17.4	783.365	2.89%	62.2	816.398	3.05%	4.22%	4.20%
17.5	763.450	2.90%	63.2	788.096	3.03%	3.23%	4.19%
17.6	729.123	2.89%	64.2	766.776	3.06%	5.16%	4.21%
15.5	1240.980	2.86%	60.0	1300.300	2.92%	4.78%	4.09%
16.0	1183.210	2.50%	61.0	1259.200	2.90%	6.42%	3.83%
16.1	1134.650	2.59%	62.0	1214.430	2.86%	7.03%	3.86%
16.2	1089.130	2.58%	63.0	1189.500	2.89%	9.18%	3.87%
16.3	1025.540	3.06%	64.0	1153.040	2.89%	12.43%	4.21%
25.0	613.113	3.71%	65.1	609.691	3.69%	-0.56%	5.23%
25.1	581.641	3.65%	66.1	547.553	3.47%	-5.86%	5.03%
25.2	541.903	3.63%	67.1	538.038	3.47%	-0.71%	5.02%
26.3	632.173	4.33%	65.3	630.759	5.45%	-0.22%	6.96%
26.4	594.647	4.32%	66.3	615.049	6.48%	3.43%	7.79%
26.2	562.969	4.66%	67.3	579.326	6.67%	2.91%	8.14%
27.0	622.054	3.33%	65.2	625.654	5.60%	0.58%	6.52%
27.1	588.523	3.34%	66.2	605.745	6.58%	2.93%	7.38%
27.2	553.742	3.30%	67.2	569.757	6.74%	2.89%	7.51%
24.0	907.738	3.11%	65.0	933.052	4.30%	2.79%	5.31%

MAT vs. SYN Data Comparison

	MAT Data			SYN Data			Total
Run #	I_Z	dI_Z/I_Z	Run #	I_Z	dI_Z/I_Z	Delta	Uncertainty
24.1	842.543	3.05%	66.0	897.673	4.90%	6.54%	5.77%
24.2	788.667	3.02%	67.0	843.560	5.01%	6.96%	5.85%
49.0	986.622	5.45%	68.1	1020.790	3.21%	3.46%	6.33%
37.1	909.192	8.91%	69.1	962.121	3.03%	5.82%	9.41%
37.2	847.877	9.48%	70.1	915.380	3.03%	7.96%	9.95%
35.1	981.263	2.80%	68.3	1014.830	3.07%	3.42%	4.16%
35.2	910.417	2.74%	69.3	955.191	2.89%	4.92%	3.98%
38.2	985.913	9.65%	70.3	919.237	2.89%	-6.76%	10.07%
33.0	966.533	3.07%	68.2	1016.470	3.15%	5.17%	4.40%
33.3	923.394	2.99%	69.2	957.074	2.95%	3.65%	4.20%
33.4	850.760	2.92%	70.2	912.107	2.94%	7.21%	4.14%
48.0	1417.590	6.06%	68.0	1526.050	2.90%	7.65%	6.72%
48.1	1280.890	5.93%	69.0	1437.190	2.76%	12.20%	6.54%
48.2	1157.740	6.34%	70.0	1373.360	2.76%	18.62%	6.92%
42.0	606.215	5.35%	71.1	646.227	5.53%	6.60%	7.69%
42.1	597.871	5.16%	72.1	713.706	4.61%	19.38%	6.92%
42.2	522.359	5.75%	73.1	540.724	5.56%	3.52%	8.00%
44.0	616.547	5.87%	71.3	663.328	5.71%	7.59%	8.19%
44.1	559.846	5.10%	72.3	604.804	5.44%	8.03%	7.46%
44.3	534.672	6.43%	73.3	553.153	5.63%	3.46%	8.55%
43.0	620.620	5.95%	71.2	666.549	5.89%	7.40%	8.37%
43.1	565.843	5.47%	72.2	604.298	5.72%	6.80%	7.92%
43.2	518.354	5.96%	73.2	542.586	6.11%	4.68%	8.54%
41.0	922.053	5.15%	71.0	988.053	4.85%	7.16%	7.07%
41.1	850.681	5.01%	72.0	903.487	4.68%	6.21%	6.86%
41.2	769.958	5.42%	73.0	818.232	4.90%	6.27%	7.31%

ExB Probe Data Analyses Results

Run #	I^+ (A)	I^{++} (A)	Rc	dRc	Rn	$\dot{m}_f$ (sccm)	P (N/m2)	n_b (#/m3)	V (m/s)	$\dot{m}_i$ (sccm)	$d\dot{m}_i$ (sccm)	$\dot{M}_T$ (sccm)	β	$d\beta$	η_p	$d\eta_p$	η_{pc1}	$d\eta_{pc1}$	η_{pc2}	$d\eta_{pc2}$	η_{pc3}	$d\eta_{pc3}$	f_d
5.0	1.872E-08	0.0000E+00	0.00000	0.00000	0.00000	14.280	1.60E-03	3.866E+17	2.199E+02	2.179E-01	1.090E-01	7.118	1.00000	0.00000	0.868	0.050	0.868	0.050	0.842	0.043	0.842	0.043	1.00000
5.1	1.588E-08	0.000E+00	0.00000	0.00000	0.00000	14.280	1.60E-03	3.866E+17	2.199E+02	2.179E-01	1.090E-01	7.118	1.00000	0.00000	0.866	0.050	0.866	0.050	0.840	0.043	0.840	0.043	1.00000
5.2	1.206E-08	0.000E+00	0.00000	0.00000	0.00000	14.270	1.60E-03	3.863E+17	2.199E+02	2.178E-01	1.089E-01	7.108	1.00000	0.00000	0.831	0.050	0.831	0.050	0.805	0.041	0.805	0.041	1.00000
5.3	1.214E-08	0.000E+00	0.00000	0.00000	0.00000	14.210	1.59E-03	3.848E+17	2.199E+02	2.169E-01	1.085E-01	7.067	1.00000	0.00000	0.791	0.050	0.791	0.050	0.767	0.039	0.767	0.039	1.00000
5.4	1.339E-08	0.000E+00	0.00000	0.00000	0.00000	14.150	1.59E-03	3.833E+17	2.199E+02	2.160E-01	1.080E-01	7.056	1.00000	0.00000	0.743	0.050	0.743	0.050	0.721	0.037	0.721	0.037	1.00000
5.5	1.397E-08	0.000E+00	0.00000	0.00000	0.00000	14.120	1.58E-03	3.825E+17	2.199E+02	2.156E-01	1.078E-01	7.026	1.00000	0.00000	0.700	0.050	0.700	0.050	0.678	0.034	0.678	0.034	1.00000
5.6	1.392E-08	0.000E+00	0.00000	0.00000	0.00000	14.220	1.59E-03	3.851E+17	2.199E+02	2.170E-01	1.085E-01	7.057	1.00000	0.00000	0.652	0.050	0.652	0.050	0.632	0.032	0.632	0.032	1.00000
5.7	1.383E-08	0.000E+00	0.00000	0.00000	0.00000	14.150	1.59E-03	3.833E+17	2.199E+02	2.160E-01	1.080E-01	7.036	1.00000	0.00000	0.621	0.050	0.621	0.050	0.602	0.031	0.602	0.031	1.00000
5.8	1.305E-08	0.000E+00	0.00000	0.00000	0.00000	14.050	1.58E-03	3.807E+17	2.199E+02	2.146E-01	1.073E-01	7.015	1.00000	0.00000	0.565	0.050	0.565	0.050	0.548	0.028	0.548	0.028	1.00000
5.9	1.252E-08	6.984E-10	0.05580	0.00056	0.02790	13.920	1.56E-03	3.774E+17	2.199E+02	2.127E-01	1.064E-01	6.953	0.97357	0.00025	0.916	0.050	0.891	0.049	0.864	0.044	0.888	0.045	0.98451
5.10	1.285E-08	7.285E-10	0.05671	0.00057	0.02836	13.870	1.56E-03	3.762E+17	2.199E+02	2.120E-01	1.060E-01	6.932	0.97317	0.00025	0.968	0.050	0.942	0.049	0.913	0.046	0.938	0.048	0.98428
5.11	1.065E-08	9.786E-10	0.09188	0.00092	0.04594	13.980	1.57E-03	3.790E+17	2.199E+02	2.136E-01	1.068E-01	6.914	0.95792	0.00038	1.000	0.050	0.958	0.048	0.928	0.047	0.969	0.049	0.97534
5.12	1.124E-08	1.042E-09	0.09271	0.00093	0.04635	13.680	1.54E-03	3.713E+17	2.199E+02	2.093E-01	1.047E-01	6.839	0.95758	0.00039	1.011	0.050	0.968	0.048	0.938	0.048	0.980	0.050	0.97514
5.13	1.184E-08	1.345E-09	0.11362	0.00114	0.05681	13.610	1.53E-03	3.695E+17	2.199E+02	2.083E-01	1.042E-01	6.798	0.94899	0.00046	1.042	0.050	0.989	0.047	0.959	0.049	1.010	0.051	0.97011
5.14	1.225E-08	1.593E-09	0.13005	0.00130	0.06503	13.750	1.54E-03	3.731E+17	2.199E+02	2.103E-01	1.052E-01	6.830	0.94246	0.00051	1.054	0.050	0.994	0.047	0.963	0.049	1.022	0.052	0.96628
6.0	2.483E-08	3.423E-10	0.01378	0.00014	0.00689	10.140	1.16E-03	2.811E+17	2.199E+02	1.584E-01	7.922E-02	4.978	0.99320	0.00007	0.777	0.050	0.772	0.050	0.748	0.038	0.753	0.038	0.99602
6.1	1.928E-08	1.212E-10	0.00629	0.00006	0.00314	10.020	1.15E-03	2.780E+17	2.199E+02	1.567E-01	7.836E-02	4.957	0.99688	0.00003	0.702	0.050	0.700	0.050	0.678	0.035	0.680	0.035	0.99817
6.2	3.024E-08	5.550E-10	0.01835	0.00018	0.00918	10.060	1.16E-03	2.790E+17	2.199E+02	1.573E-01	7.864E-02	4.947	0.99099	0.00009	0.899	0.050	0.891	0.050	0.862	0.044	0.870	0.044	0.99472
6.3	3.344E-08	1.085E-09	0.03244	0.00032	0.01622	10.060	1.16E-03	2.790E+17	2.199E+02	1.573E-01	7.864E-02	4.947	0.98429	0.00015	0.963	0.050	0.947	0.049	0.917	0.047	0.932	0.047	0.99079
6.4	3.548E-08	1.869E-09	0.05267	0.00053	0.02633	10.060	1.16E-03	2.790E+17	2.199E+02	1.573E-01	7.864E-02	4.947	0.97498	0.00024	1.006	0.050	0.981	0.049	0.950	0.048	0.974	0.050	0.98534
6.5	3.652E-08	2.749E-09	0.07527	0.00075	0.03764	9.920	1.14E-03	2.754E+17	2.199E+02	1.553E-01	7.764E-02	4.905	0.96500	0.00032	1.062	0.050	1.024	0.048	0.992	0.051	1.028	0.052	0.97949
6.6	3.650E-08	3.741E-09	0.10248	0.00102	0.05124	9.970	1.15E-03	2.767E+17	2.199E+02	1.560E-01	7.800E-02	4.906	0.95352	0.00042	1.091	0.050	1.040	0.048	1.007	0.051	1.056	0.054	0.97276
6.7	3.624E-08	4.703E-09	0.12980	0.00130	0.06490	9.960	1.14E-03	2.765E+17	2.199E+02	1.558E-01	7.792E-02	4.896	0.94256	0.00050	1.120	0.050	1.055	0.047	1.022	0.052	1.084	0.055	0.96634
6.8	3.610E-08	5.383E-09	0.14910	0.00149	0.07455	9.910	1.14E-03	2.752E+17	2.199E+02	1.551E-01	7.756E-02	4.875	0.93512	0.00056	1.139	0.050	1.065	0.047	1.031	0.053	1.103	0.056	0.96198
6.9	3.650E-08	5.811E-09	0.15922	0.00159	0.07961	9.800	1.13E-03	2.724E+17	2.199E+02	1.535E-01	7.677E-02	4.834	0.93132	0.00059	1.155	0.050	1.076	0.047	1.041	0.053	1.118	0.057	0.95976
6.10	3.634E-08	6.240E-09	0.17168	0.00172	0.08584	9.890	1.14E-03	2.747E+17	2.199E+02	1.548E-01	7.742E-02	4.855	0.92674	0.00062	1.156	0.050	1.071	0.046	1.037	0.053	1.119	0.057	0.95707
6.12.13	3.755E-08	7.068E-09	0.18823	0.00188	0.09412	9.900	1.14E-03	2.749E+17	2.199E+02	1.550E-01	7.749E-02	4.865	0.92079	0.00066	1.162	0.050	1.070	0.046	1.036	0.053	1.125	0.057	0.95358
6.14	1.364E-08	0.000E+00	0.00000	0.00000	0.00000	9.740	1.12E-03	2.709E+17	2.199E+02	1.527E-01	7.634E-02	4.803	1.00000	0.00000	0.557	0.050	0.557	0.050	0.539	0.027	0.539	0.027	1.00000
7.0	2.412E-08	8.506E-11	0.00353	0.00004	0.00176	14.860	1.66E-03	4.014E+17	2.199E+02	2.262E-01	1.131E-01	7.416	0.99824	0.00002	0.494	0.050	0.493	0.050	0.478	0.024	0.479	0.024	0.99897

ExB Probe Data Analyses Results

Run #	I^+ (A)	I^{++} (A)	Rc	dRc	Rn	$\dot{m}_f$ (sccm)	P (N/m2)	n_b (#/m3)	V (m/s)	$\dot{m}_i$ (sccm)	$d\dot{m}_i$ (sccm)	$\dot{M}_T$ (sccm)	β	$d\beta$	η_p	$d\eta_p$	η_{pc1}	$d\eta_{pc1}$	η_{pc2}	$d\eta_{pc2}$	η_{pc3}	$d\eta_{pc3}$	f_d
7.1	3.256E-08	1.823E-10	0.00560	0.00006	0.00280	15.090	1.69E-03	4.073E+17	2.199E+02	2.295E-01	1.148E-01	7.520	0.99722	0.00003	0.573	0.050	0.572	0.050	0.554	0.028	0.556	0.028	0.99837
7.2	4.105E-08	2.737E-10	0.00667	0.00007	0.00333	15.060	1.68E-03	4.065E+17	2.199E+02	2.291E-01	1.146E-01	7.519	0.99669	0.00003	0.648	0.050	0.646	0.050	0.626	0.032	0.628	0.032	0.99806
7.3	4.698E-08	4.024E-10	0.00856	0.00009	0.00428	14.940	1.67E-03	4.034E+17	2.199E+02	2.274E-01	1.137E-01	7.497	0.99575	0.00004	0.720	0.050	0.717	0.050	0.696	0.035	0.699	0.035	0.99751
7.4	5.151E-08	1.046E-09	0.02031	0.00020	0.01015	15.200	1.70E-03	4.101E+17	2.199E+02	2.311E-01	1.156E-01	7.561	0.99005	0.00010	0.775	0.050	0.768	0.050	0.744	0.038	0.752	0.038	0.99417
7.5	5.364E-08	1.712E-09	0.03191	0.00032	0.01595	15.110	1.69E-03	4.078E+17	2.199E+02	2.298E-01	1.149E-01	7.540	0.98454	0.00015	0.825	0.050	0.812	0.049	0.788	0.040	0.800	0.041	0.99094
7.6	5.418E-08	2.324E-09	0.04289	0.00043	0.02144	15.000	1.68E-03	4.050E+17	2.199E+02	2.282E-01	1.141E-01	7.538	0.97944	0.00020	0.865	0.050	0.847	0.049	0.822	0.042	0.839	0.043	0.98795
7.7	5.391E-08	2.673E-09	0.04959	0.00050	0.02479	14.980	1.67E-03	4.044E+17	2.199E+02	2.280E-01	1.140E-01	7.518	0.97638	0.00022	0.898	0.050	0.877	0.049	0.850	0.043	0.871	0.044	0.98616
7.8	5.333E-08	3.259E-09	0.06111	0.00061	0.03056	15.140	1.69E-03	4.085E+17	2.199E+02	2.303E-01	1.151E-01	7.550	0.97120	0.00027	0.927	0.050	0.900	0.049	0.873	0.044	0.899	0.046	0.98313
7.9	5.338E-08	4.130E-09	0.07737	0.00077	0.03869	15.130	1.69E-03	4.083E+17	2.199E+02	2.301E-01	1.151E-01	7.540	0.96409	0.00033	0.953	0.050	0.919	0.048	0.891	0.045	0.924	0.047	0.97896
8.0	1.419E-08	1.260E-09	0.08877	0.00089	0.04439	15.270	1.71E-03	4.118E+17	2.199E+02	2.321E-01	1.161E-01	7.552	0.95923	0.00037	0.955	0.050	0.916	0.048	0.888	0.045	0.926	0.047	0.97611
8.1	1.653E-08	1.156E-09	0.06991	0.00070	0.03495	15.260	1.70E-03	4.116E+17	2.199E+02	2.320E-01	1.160E-01	7.542	0.96733	0.00030	0.924	0.050	0.894	0.048	0.867	0.044	0.896	0.046	0.98086
8.2	1.803E-08	1.030E-09	0.05709	0.00057	0.02854	15.180	1.70E-03	4.095E+17	2.199E+02	2.308E-01	1.154E-01	7.511	0.97300	0.00026	0.897	0.050	0.873	0.049	0.846	0.043	0.870	0.044	0.98418
8.3	1.993E-08	7.958E-10	0.03993	0.00040	0.01997	15.200	1.70E-03	4.101E+17	2.199E+02	2.311E-01	1.156E-01	7.511	0.98080	0.00018	0.861	0.050	0.845	0.049	0.819	0.042	0.835	0.042	0.98875
8.4	2.041E-08	6.124E-10	0.03001	0.00030	0.01500	15.150	1.69E-03	4.088E+17	2.199E+02	2.304E-01	1.152E-01	7.480	0.98543	0.00014	0.817	0.050	0.805	0.049	0.780	0.040	0.791	0.040	0.99146
8.5	2.082E-08	4.496E-10	0.02160	0.00022	0.01080	15.160	1.69E-03	4.090E+17	2.199E+02	2.305E-01	1.153E-01	7.491	0.98943	0.00010	0.756	0.050	0.748	0.049	0.725	0.037	0.733	0.037	0.99381
8.6	2.141E-08	2.753E-10	0.01286	0.00013	0.00643	15.060	1.68E-03	4.065E+17	2.199E+02	2.291E-01	1.146E-01	7.469	0.99365	0.00006	0.683	0.050	0.679	0.050	0.658	0.033	0.662	0.034	0.99628
8.7	2.130E-08	2.062E-10	0.00968	0.00010	0.00484	15.060	1.68E-03	4.065E+17	2.199E+02	2.291E-01	1.146E-01	7.469	0.99521	0.00005	0.593	0.050	0.590	0.050	0.572	0.029	0.574	0.029	0.99719
8.8	2.064E-08	0.000E+00	0.00000	0.00000	0.00000	15.060	1.68E-03	4.065E+17	2.199E+02	2.291E-01	1.146E-01	7.469	1.00000	0.00000	0.473	0.050	0.473	0.050	0.459	0.023	0.459	0.023	1.00000
9.0	1.595E-08	0.000E+00	0.00000	0.00000	0.00000	10.320	1.18E-03	2.856E+17	2.199E+02	1.610E-01	8.051E-02	5.001	1.00000	0.00000	0.570	0.050	0.570	0.050	0.552	0.028	0.552	0.028	1.00000
9.1	1.897E-08	1.088E-10	0.00574	0.00006	0.00287	10.270	1.18E-03	2.844E+17	2.199E+02	1.603E-01	8.015E-02	4.980	0.99715	0.00003	0.714	0.050	0.712	0.050	0.689	0.035	0.691	0.035	0.99833
9.2	2.350E-08	3.022E-10	0.01286	0.00013	0.00643	10.430	1.19E-03	2.884E+17	2.199E+02	1.626E-01	8.130E-02	5.013	0.99365	0.00006	0.850	0.050	0.845	0.050	0.817	0.042	0.823	0.042	0.99628
9.3	2.103E-08	7.699E-10	0.03661	0.00037	0.01831	10.320	1.18E-03	2.856E+17	2.199E+02	1.610E-01	8.051E-02	5.001	0.98234	0.00017	0.950	0.050	0.933	0.049	0.903	0.046	0.919	0.047	0.98965
9.4	1.825E-08	1.181E-09	0.06470	0.00065	0.03235	10.270	1.18E-03	2.844E+17	2.199E+02	1.603E-01	8.015E-02	4.980	0.96962	0.00028	1.026	0.050	0.995	0.048	0.963	0.049	0.993	0.051	0.98220
9.5	1.742E-08	2.027E-09	0.11638	0.00116	0.05819	10.310	1.18E-03	2.854E+17	2.199E+02	1.609E-01	8.044E-02	4.991	0.94788	0.00046	1.093	0.050	1.036	0.047	1.003	0.051	1.058	0.054	0.96946
9.6	1.659E-08	2.813E-09	0.16955	0.00170	0.08477	10.370	1.19E-03	2.869E+17	2.199E+02	1.617E-01	8.087E-02	5.002	0.92752	0.00061	1.137	0.050	1.054	0.046	1.020	0.052	1.100	0.056	0.95752
9.7	1.595E-08	3.465E-09	0.21725	0.00217	0.10862	10.340	1.18E-03	2.862E+17	2.199E+02	1.613E-01	8.065E-02	5.001	0.91076	0.00072	1.177	0.050	1.072	0.046	1.038	0.053	1.139	0.058	0.94771
9.8	1.505E-08	3.826E-09	0.25424	0.00254	0.12712	10.280	1.18E-03	2.846E+17	2.199E+02	1.604E-01	8.022E-02	4.990	0.89865	0.00079	1.203	0.050	1.081	0.045	1.046	0.053	1.164	0.059	0.94061
9.9	1.470E-08	4.089E-09	0.27819	0.00278	0.13909	10.380	1.19E-03	2.872E+17	2.199E+02	1.619E-01	8.094E-02	5.012	0.89118	0.00083	1.221	0.050	1.088	0.045	1.053	0.054	1.181	0.060	0.93623

Appendix B

	z = 0.356 m	z = 0.508 m	z = 0.660 m	z = 0.813 m	z = 0.965 m
Segment A	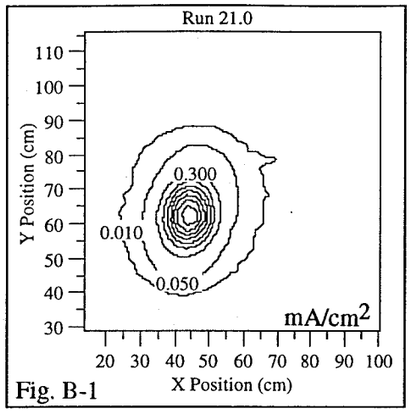 Fig. B-1	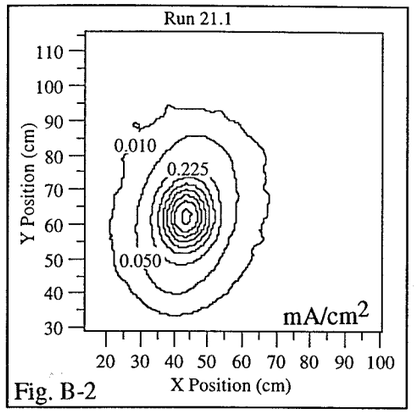 Fig. B-2	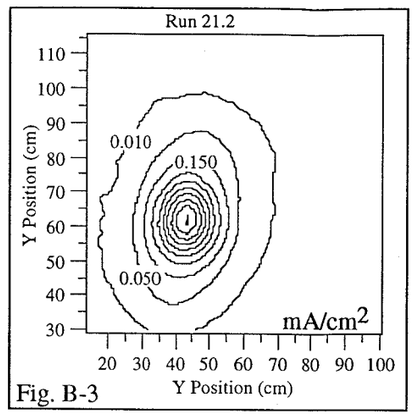 Fig. B-3	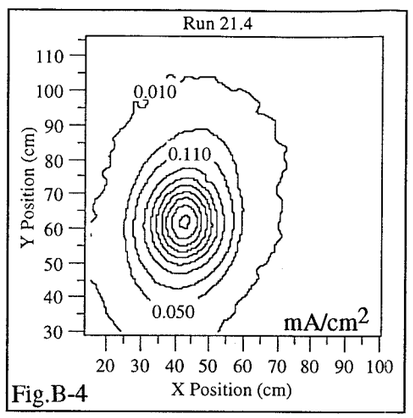 Fig.B-4	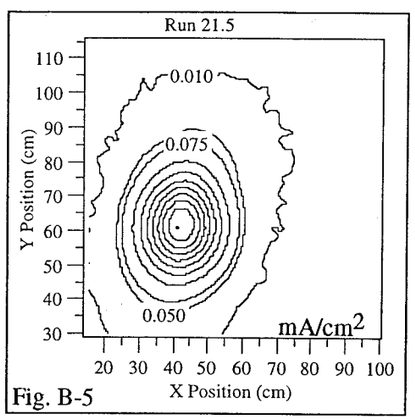 Fig. B-5
Segment B	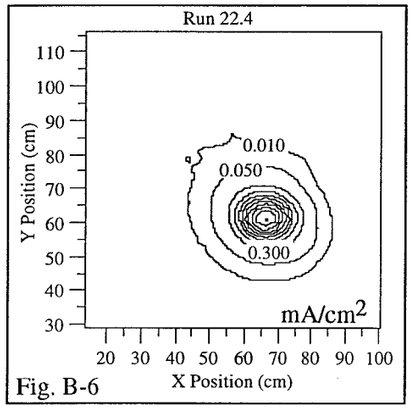 Fig. B-6	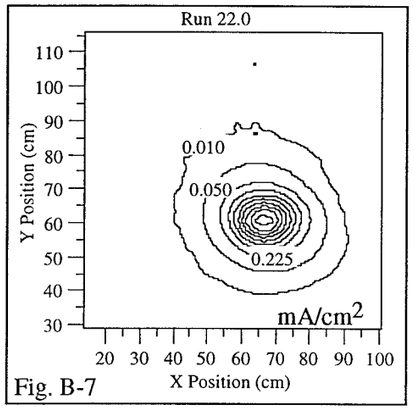 Fig. B-7	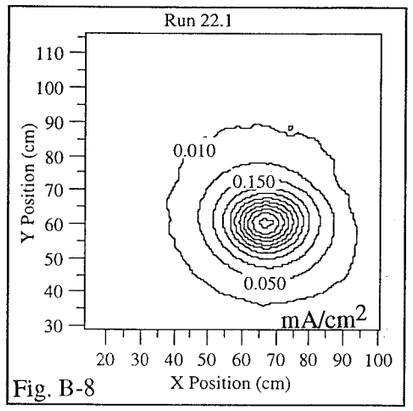 Fig. B-8	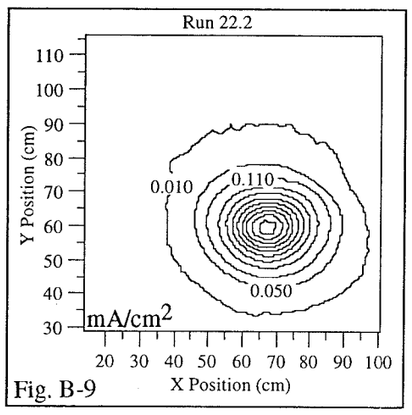 Fig. B-9	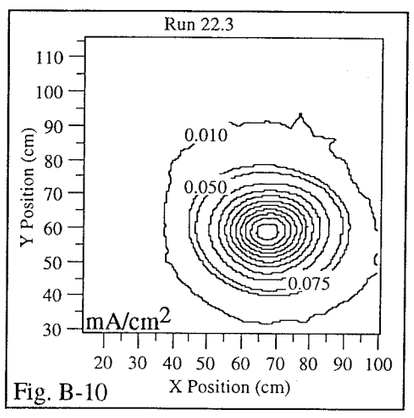 Fig. B-10
Segment C	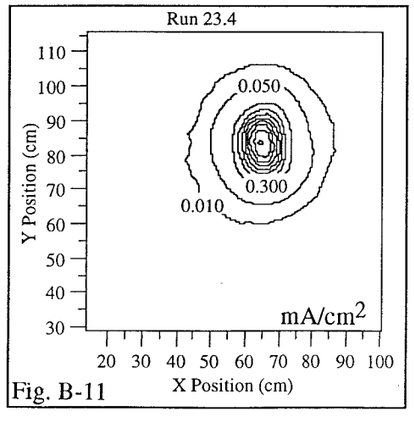 Fig. B-11	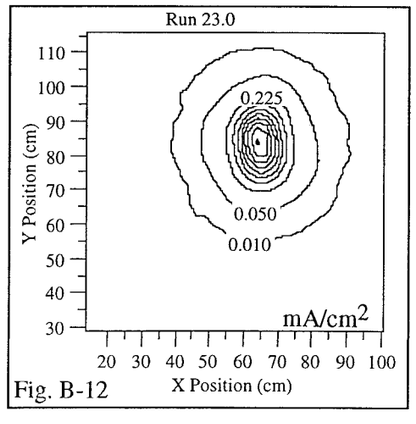 Fig. B-12	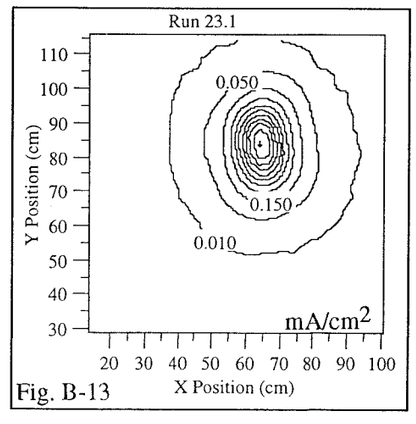 Fig. B-13	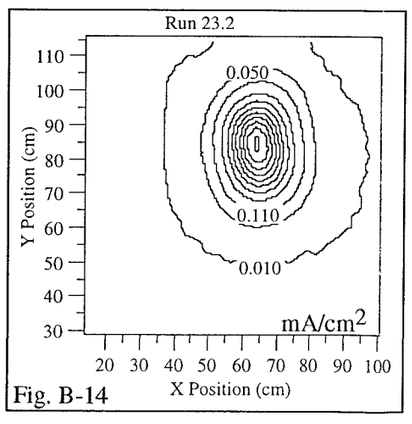 Fig. B-14	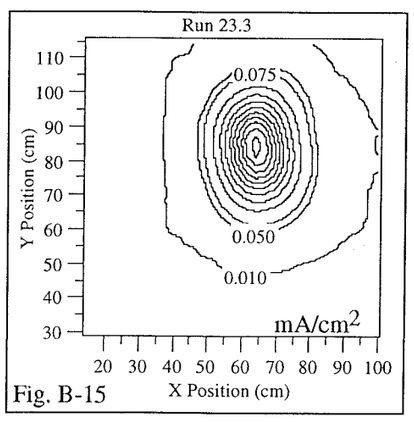 Fig. B-15

Measured Data

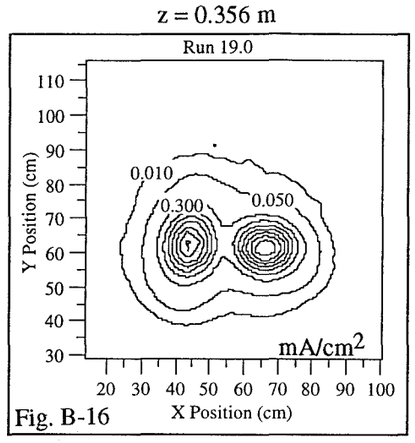

Fig. B-16

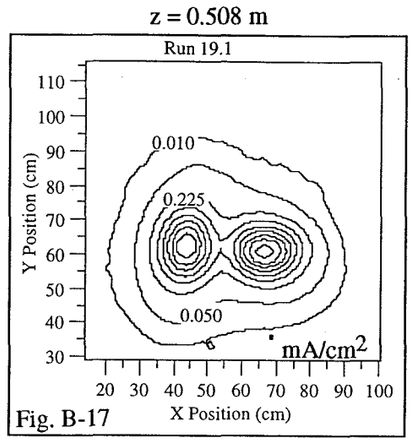

Fig. B-17

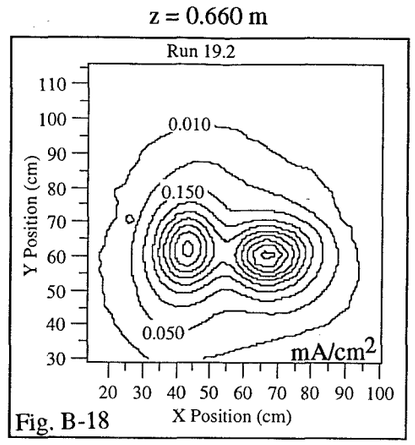

Fig. B-18

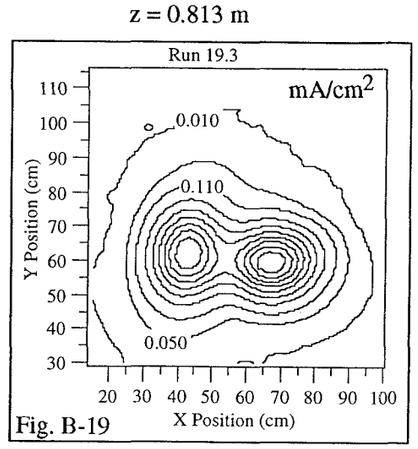

Fig. B-19

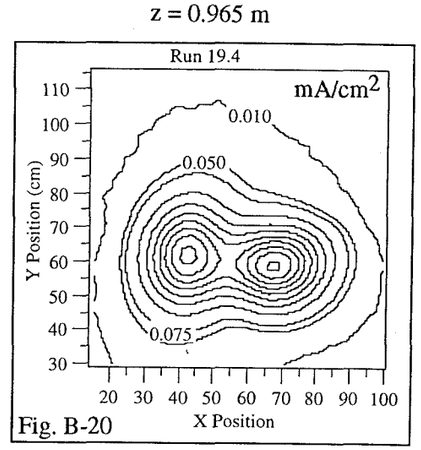

Fig. B-20

Superposition Data

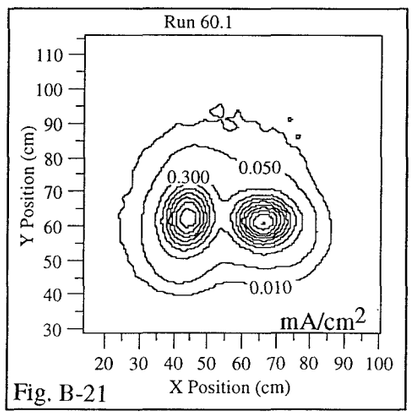

Fig. B-21

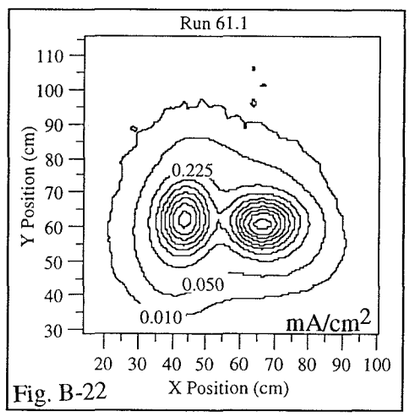

Fig. B-22

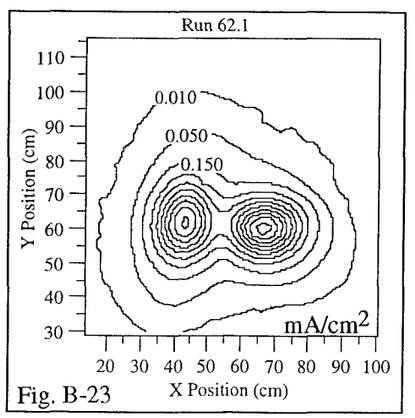

Fig. B-23

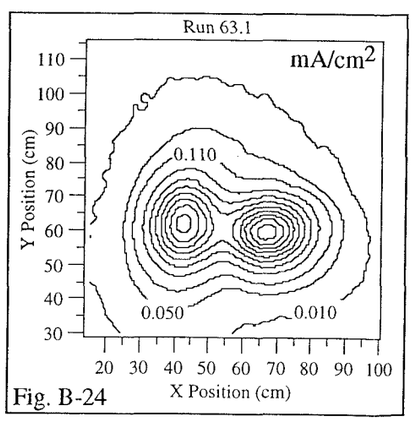

Fig. B-24

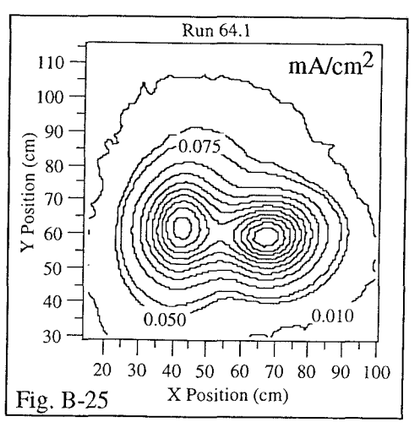

Fig. B-25

Measured Data

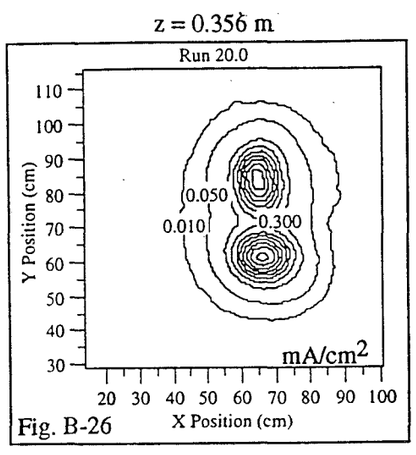

Fig. B-26

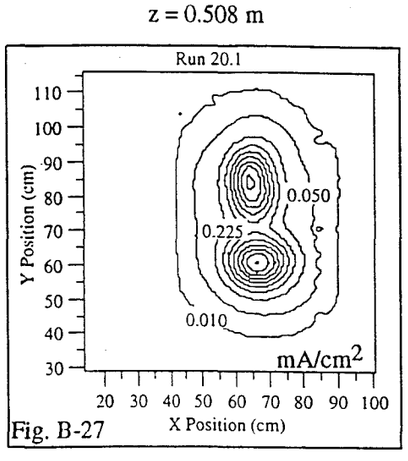

Fig. B-27

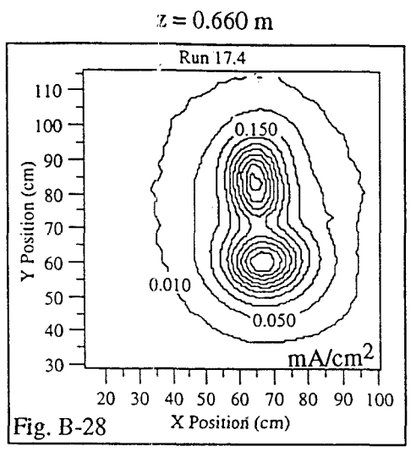

Fig. B-28

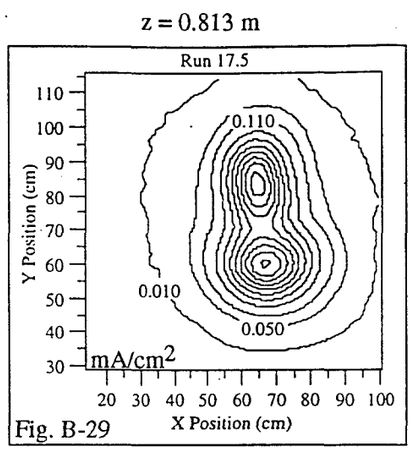

Fig. B-29

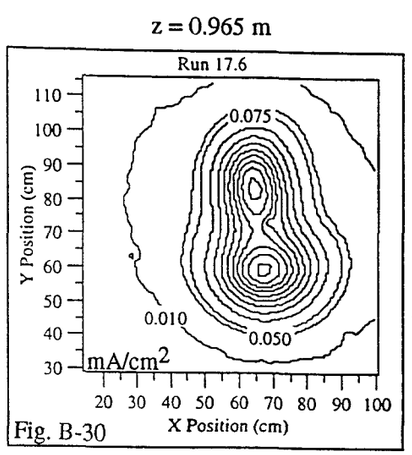

Fig. B-30

Superposition Data

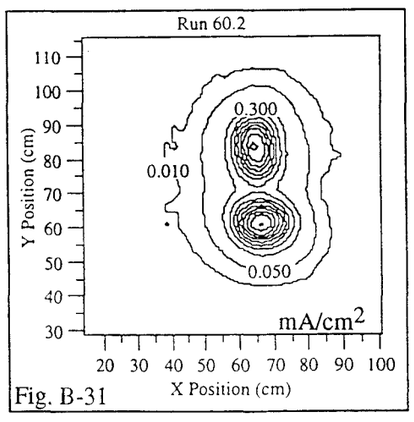

Fig. B-31

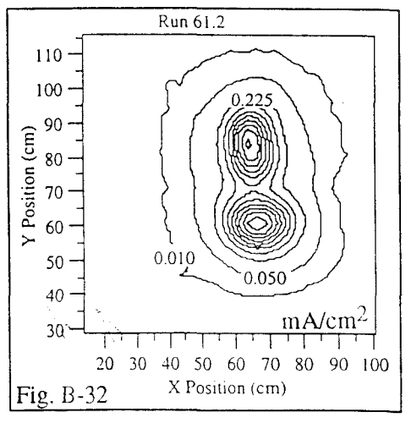

Fig. B-32

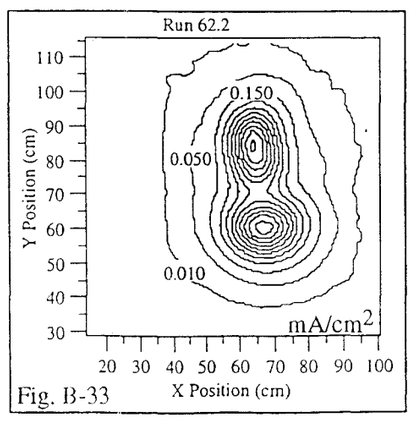

Fig. B-33

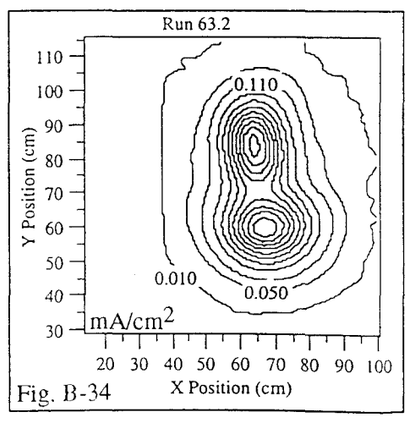

Fig. B-34

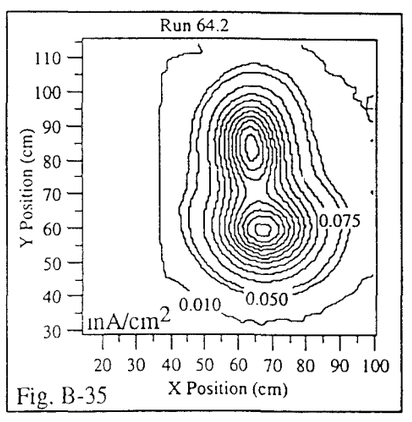

Fig. B-35

Measured Data

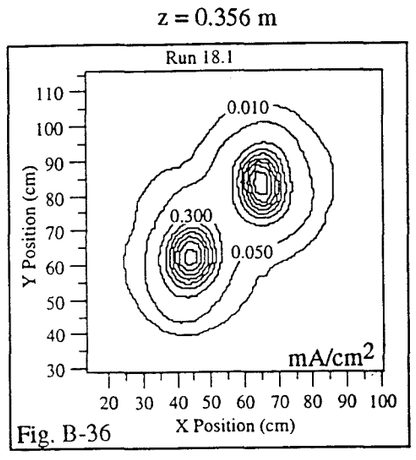

Fig. B-36

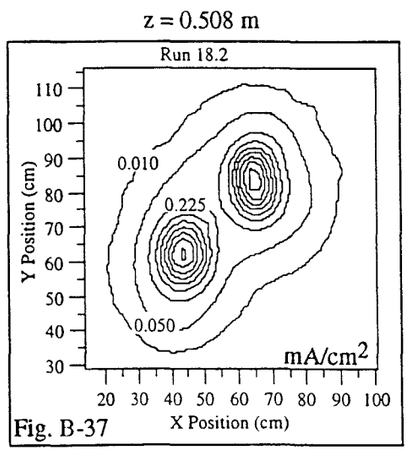

Fig. B-37

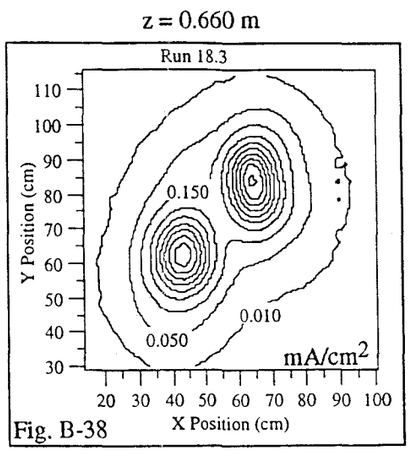

Fig. B-38

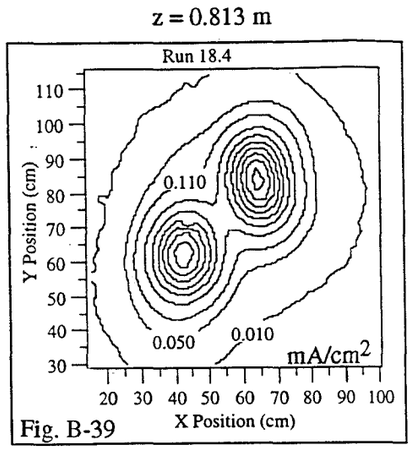

Fig. B-39

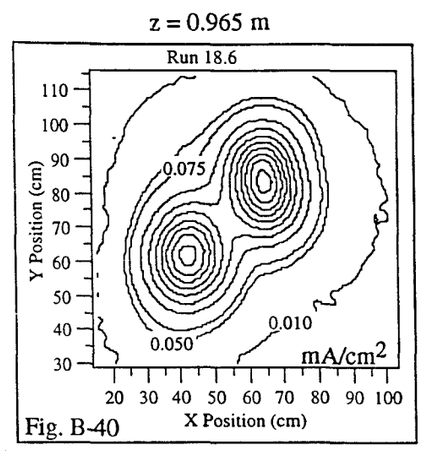

Fig. B-40

Superposition Data

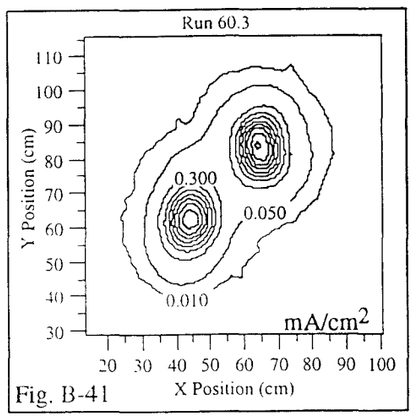

Fig. B-41

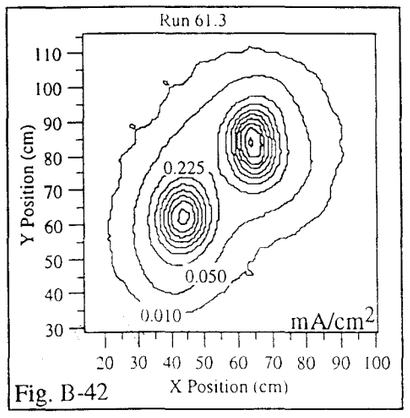

Fig. B-42

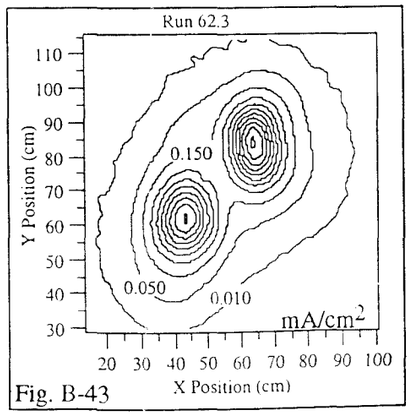

Fig. B-43

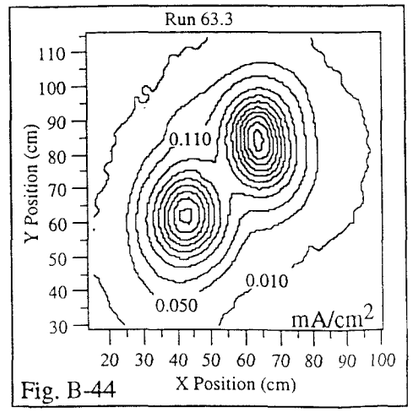

Fig. B-44

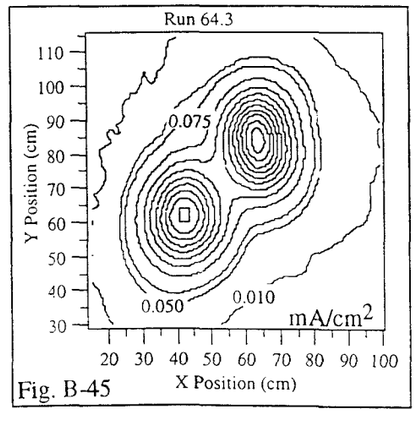

Fig. B-45

Measured Data

z = 0.356 m

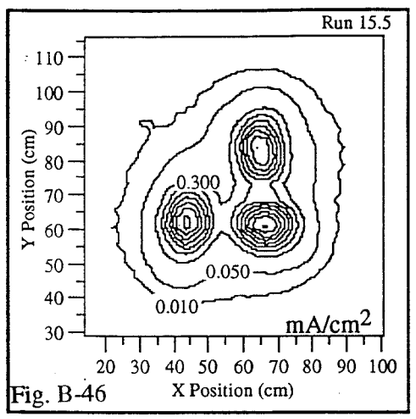

Fig. B-46

z = 0.508 m

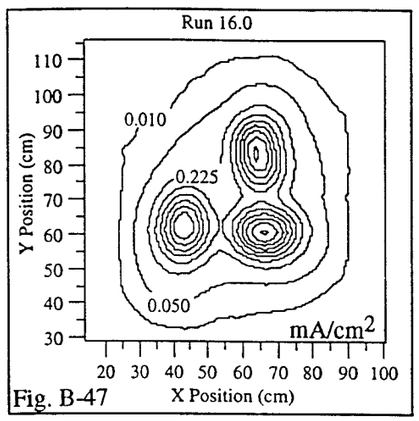

Fig. B-47

z = 0.660 m

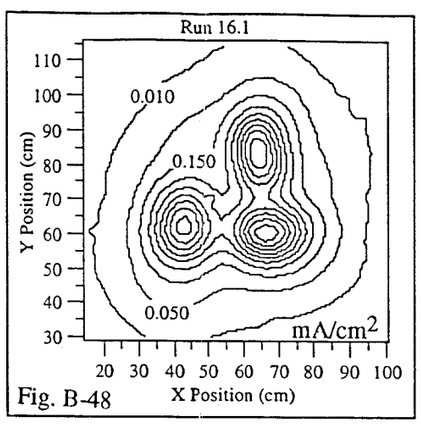

Fig. B-48

z = 0.813 m

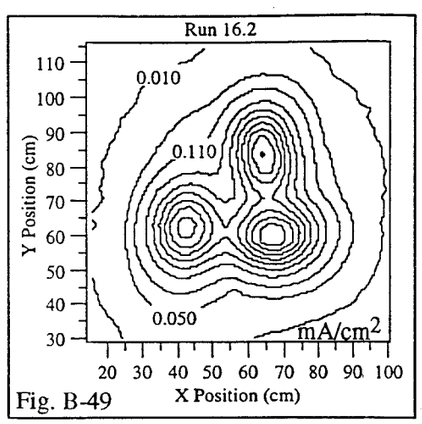

Fig. B-49

z = 0.965 m

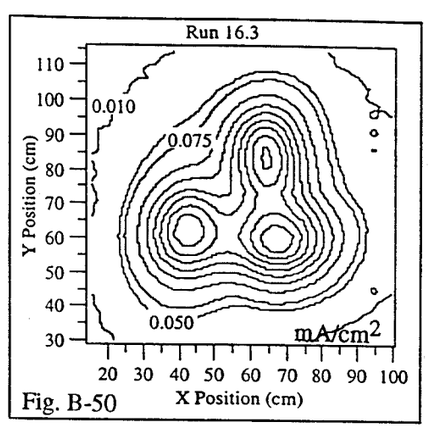

Fig. B-50

Superposition Data

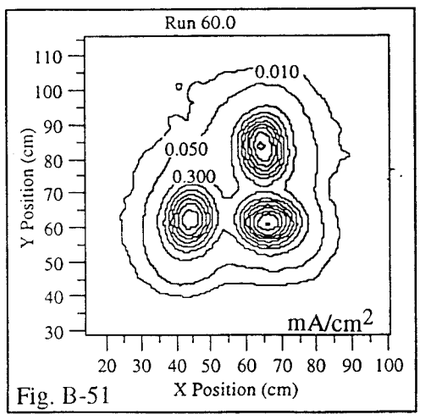

Fig. B-51

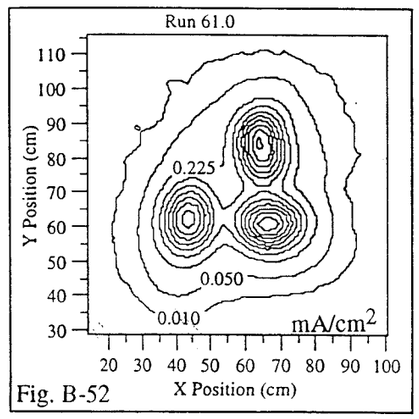

Fig. B-52

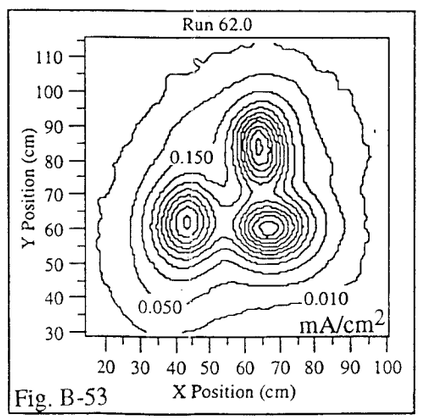

Fig. B-53

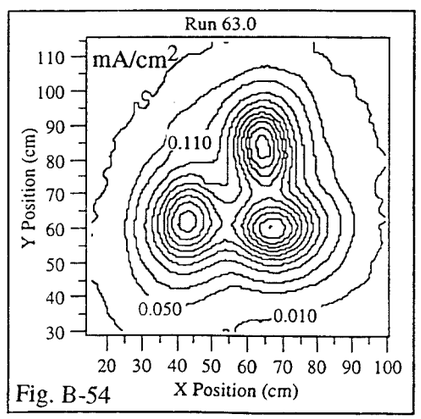

Fig. B-54

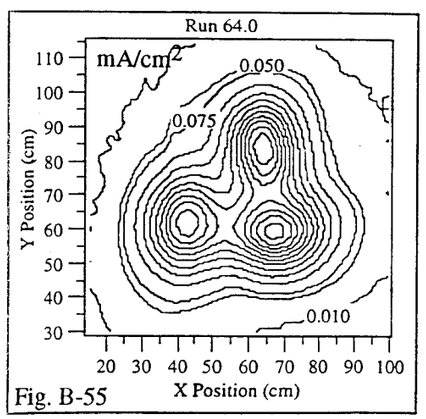

Fig. B-55

	z = 0.356 m	z = 0.660 m	z = 0.965 m
Segment A	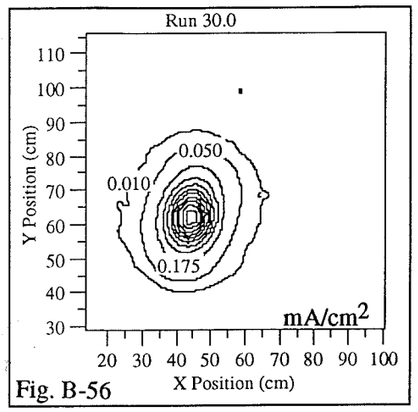 Fig. B-56	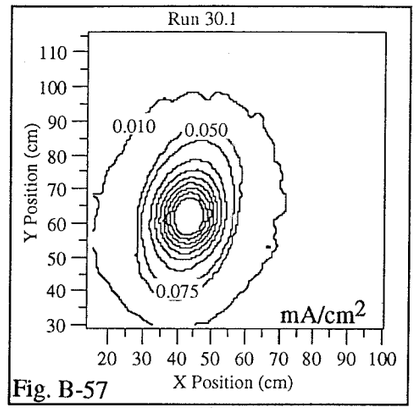 Fig. B-57	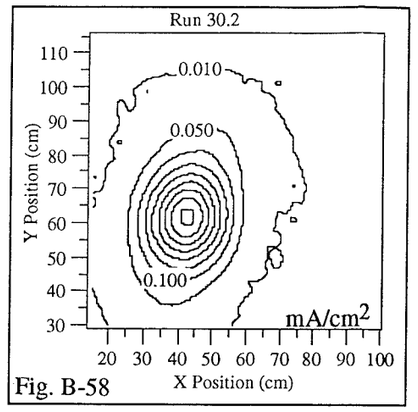 Fig. B-58
Segment B	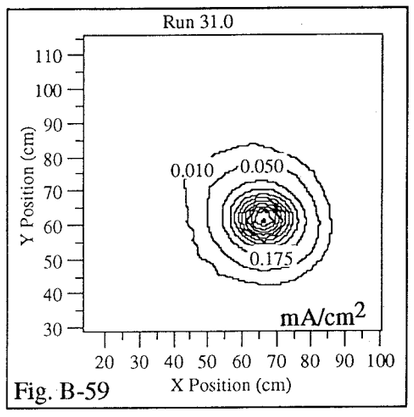 Fig. B-59	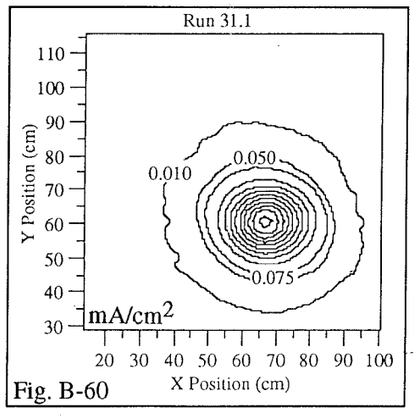 Fig. B-60	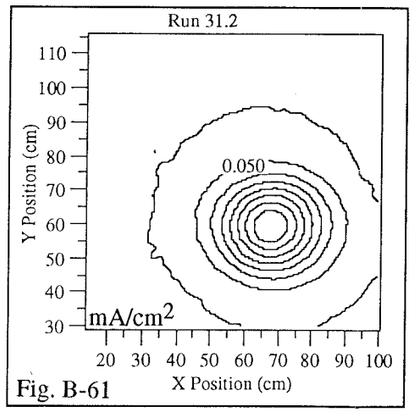 Fig. B-61
Segment C	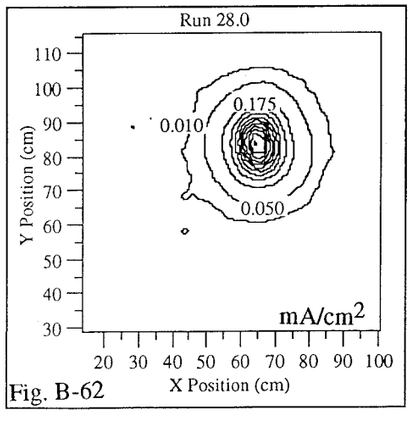 Fig. B-62	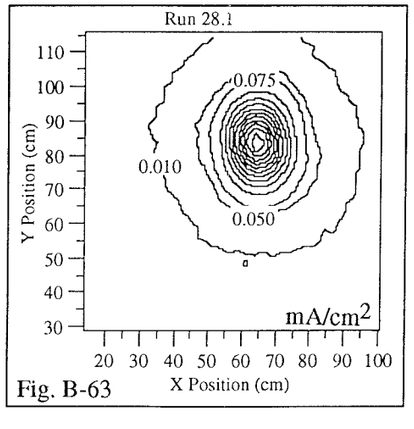 Fig. B-63	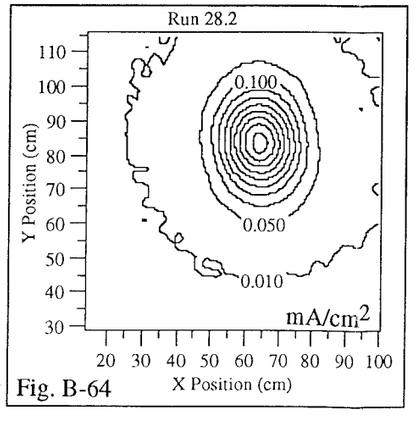 Fig. B-64

Segments AB

Measured Data

Superposition Data

z = 0.356 m

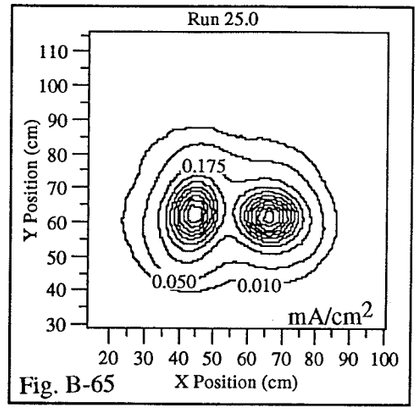

Fig. B-65

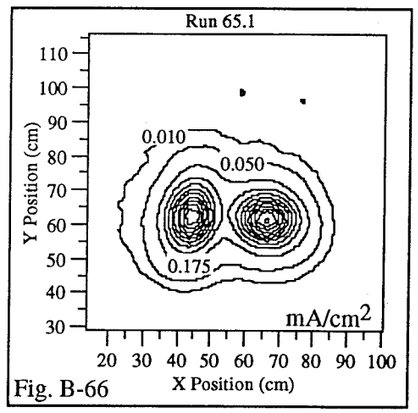

Fig. B-66

z = 0.660 m

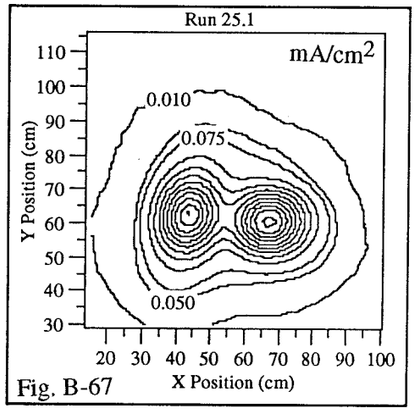

Fig. B-67

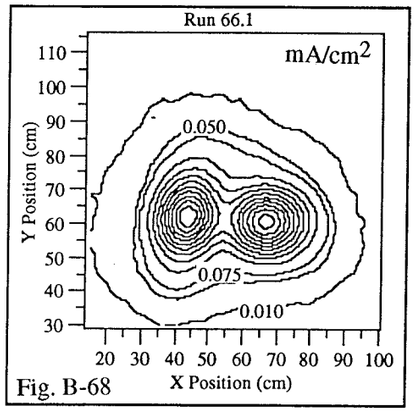

Fig. B-68

z = 0.965 m

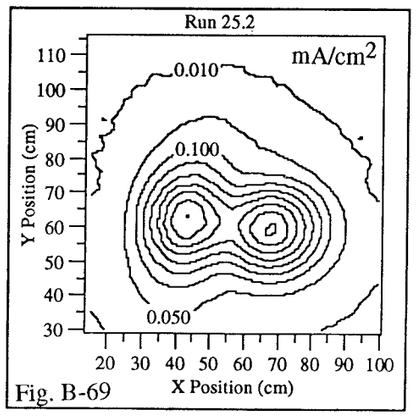

Fig. B-69

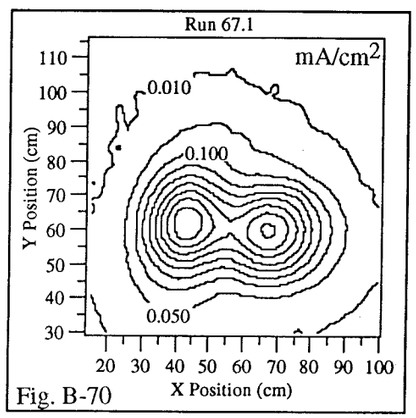

Fig. B-70

Segments BC

Measured Data

Superposition Data

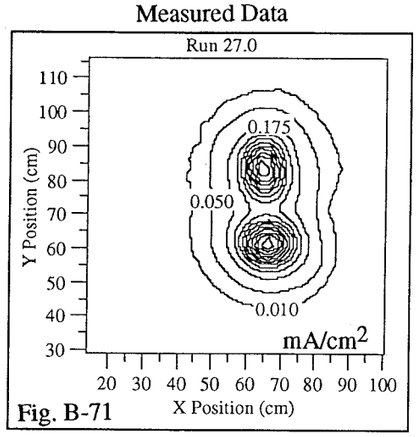

Fig. B-71

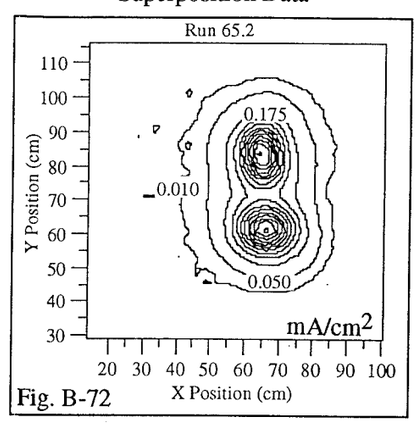

Fig. B-72

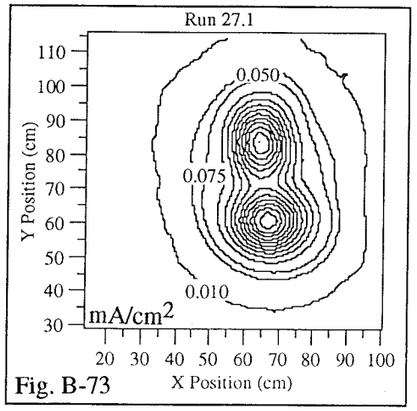

Fig. B-73

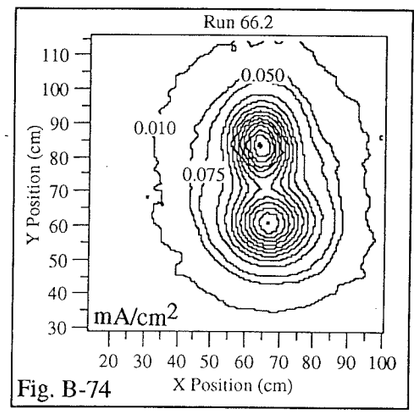

Fig. B-74

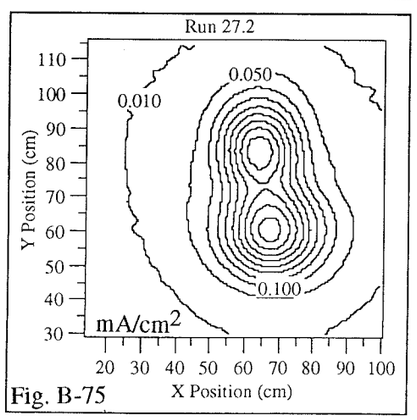

Fig. B-75

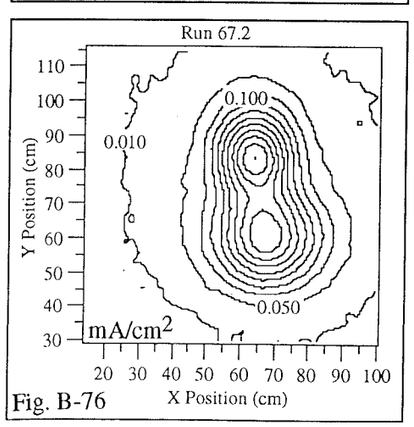

Fig. B-76

Segments AC

Measured Data

Superposition Data

z = 0.356 m

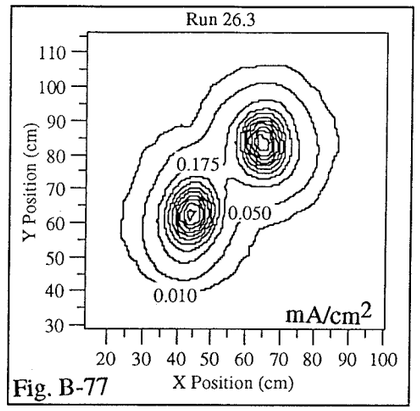

Fig. B-77

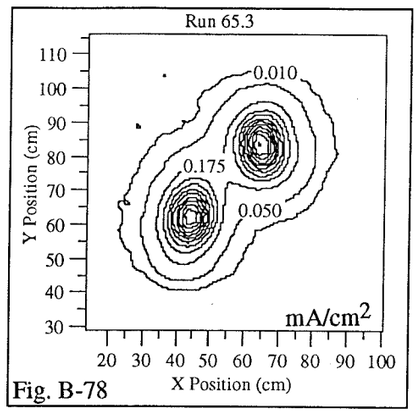

Fig. B-78

z = 0.660 m

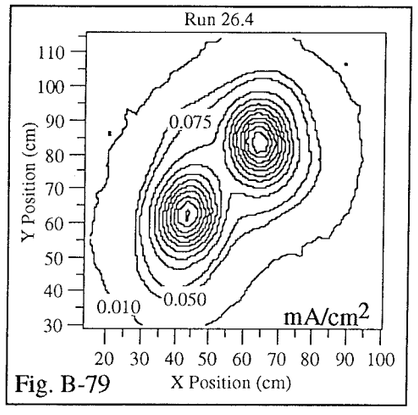

Fig. B-79

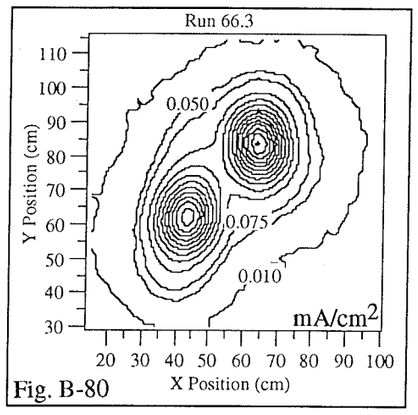

Fig. B-80

z = 0.965 m

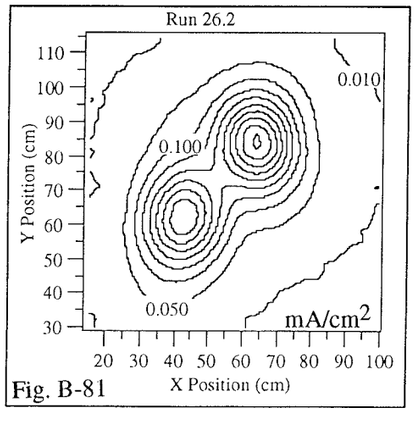

Fig. B-81

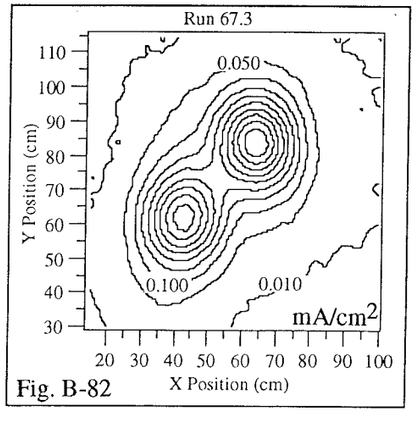

Fig. B-82

Segments ABC

Measured Data

Superposition Data

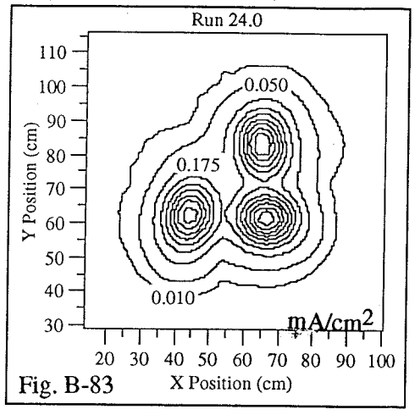

Fig. B-83

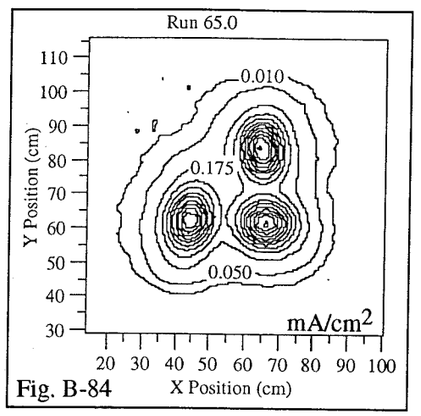

Fig. B-84

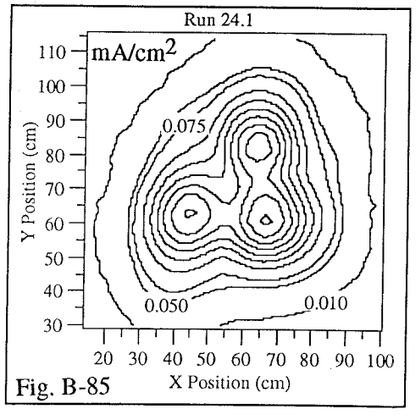

Fig. B-85

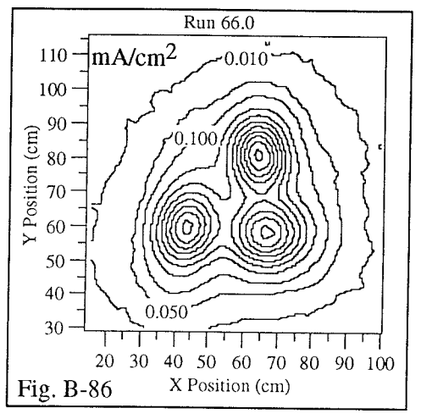

Fig. B-86

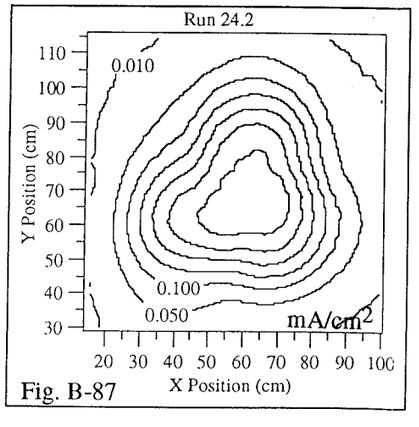

Fig. B-87

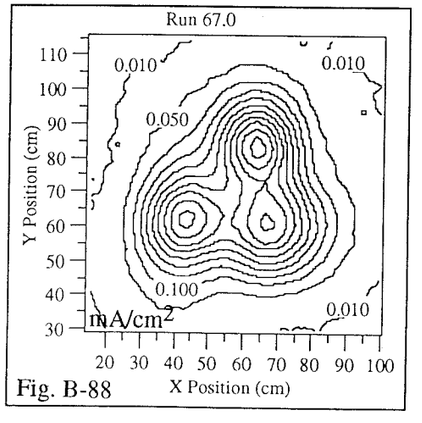

Fig. B-88

	z = 0.356 m	z = 0.660 m	z = 0.965 m
Segment A	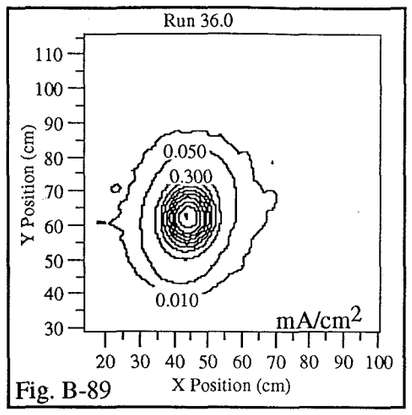 Fig. B-89	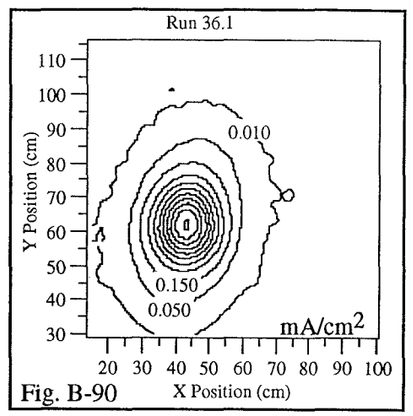 Fig. B-90	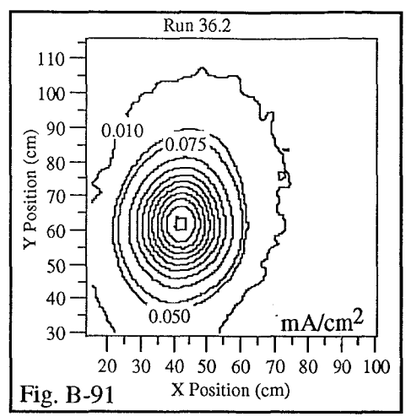 Fig. B-91
Segment B	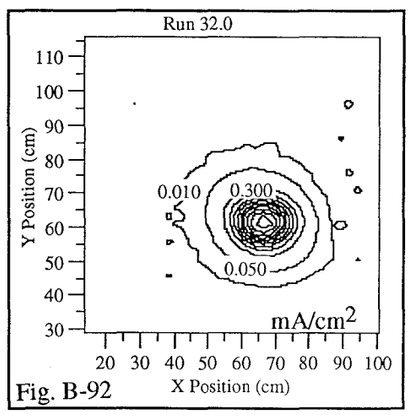 Fig. B-92	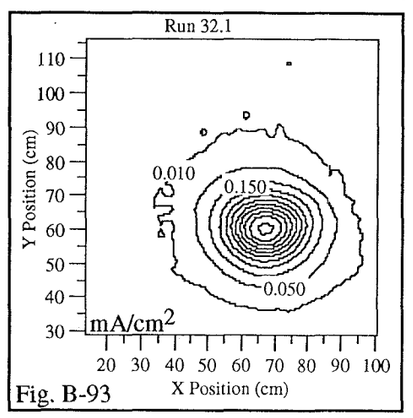 Fig. B-93	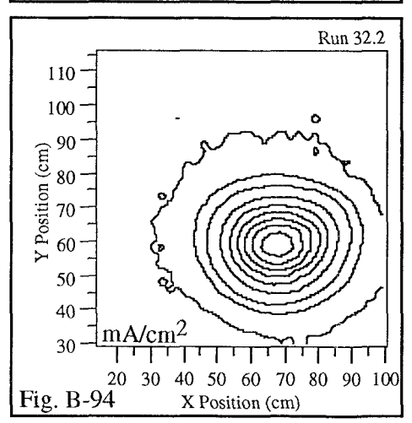 Fig. B-94
Segment C	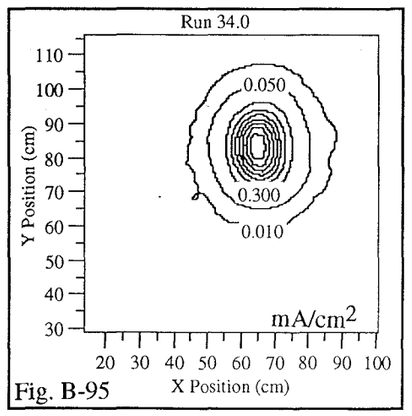 Fig. B-95	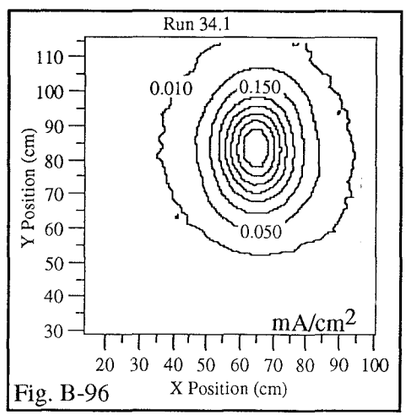 Fig. B-96	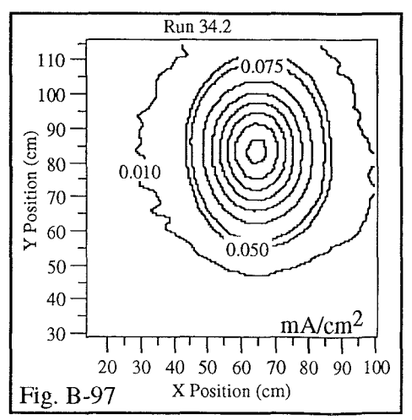 Fig. B-97

Segments AB

Segments BC

Measured Data

Superposition Data

Measured Data

Superposition Data

z = 0.356 m

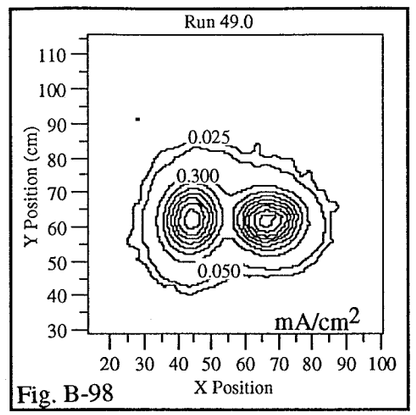

Fig. B-98

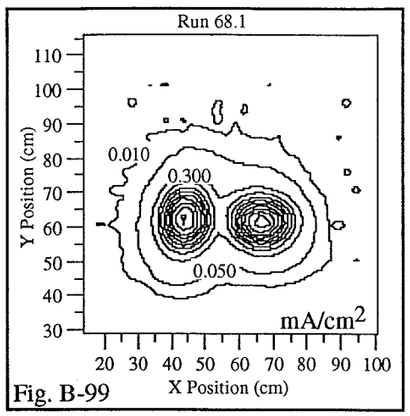

Fig. B-99

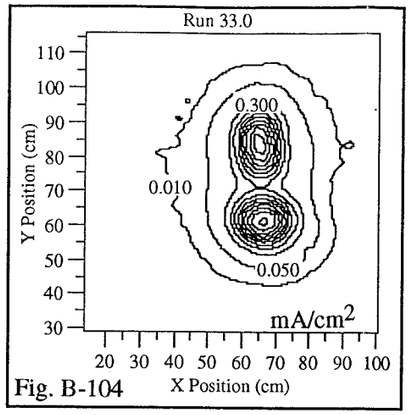

Fig. B-104

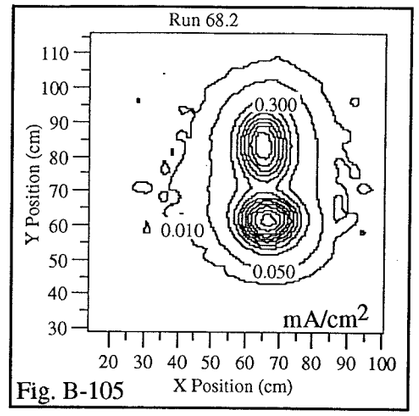

Fig. B-105

z = 0.660 m

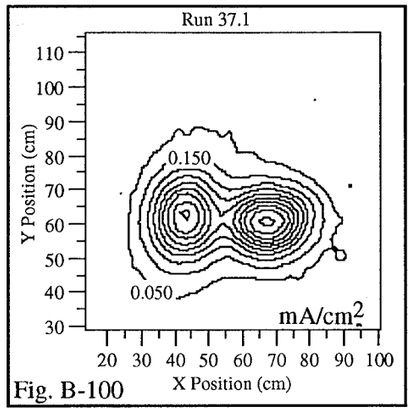

Fig. B-100

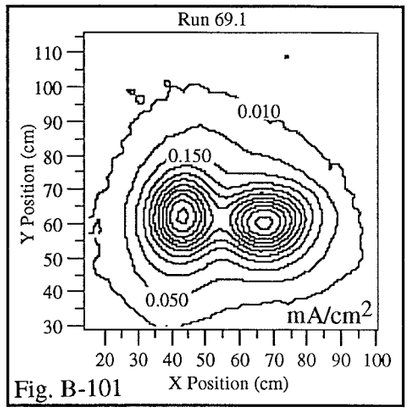

Fig. B-101

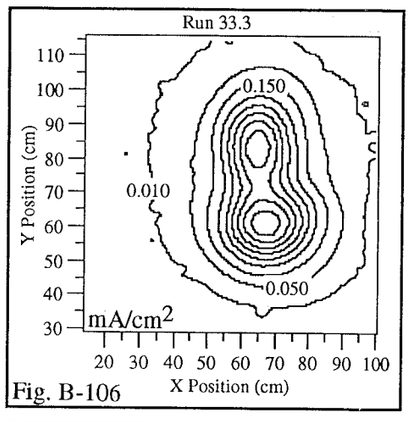

Fig. B-106

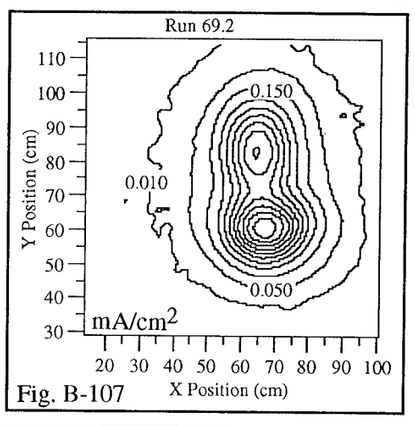

Fig. B-107

z = 0.965 m

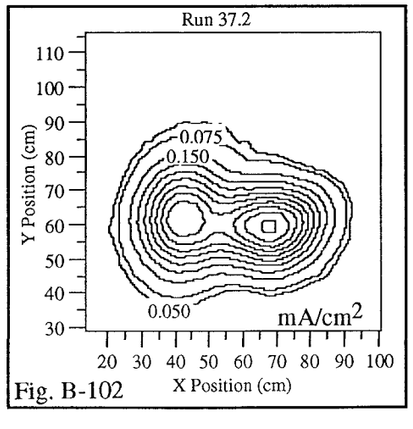

Fig. B-102

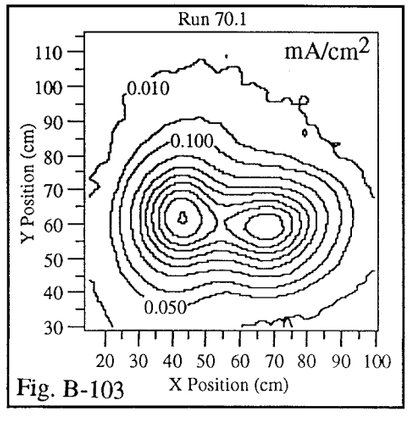

Fig. B-103

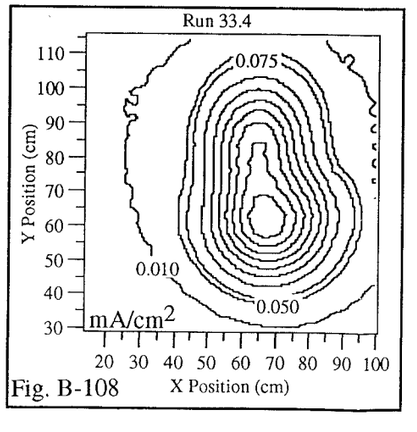

Fig. B-108

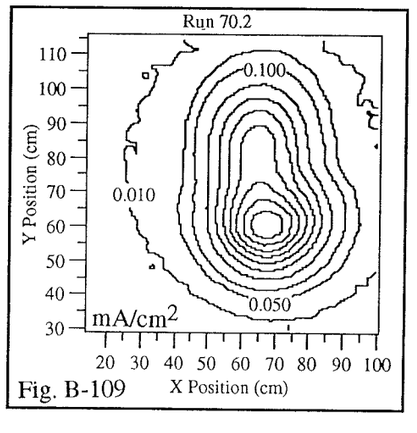

Fig. B-109

Segments AC

Measured Data

Superposition Data

z = 0.356 m

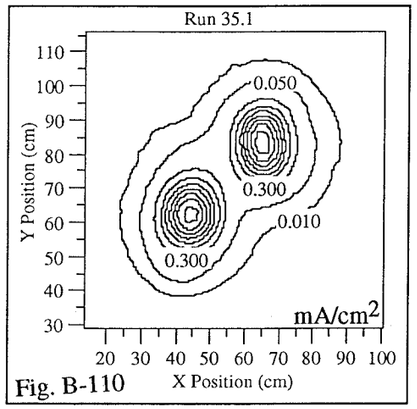

Fig. B-110

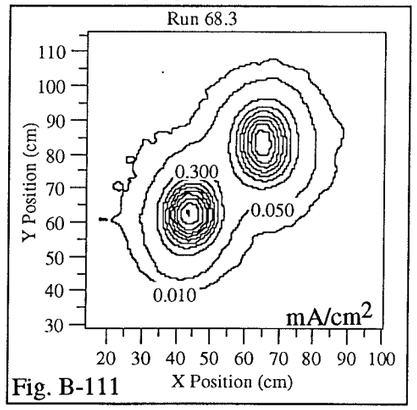

Fig. B-111

z = 0.660 m

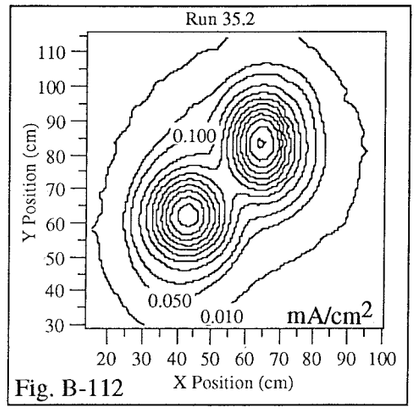

Fig. B-112

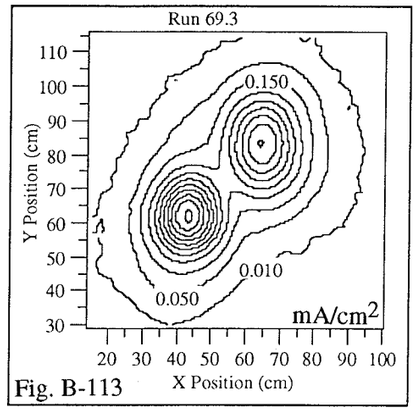

Fig. B-113

z = 0.965 m

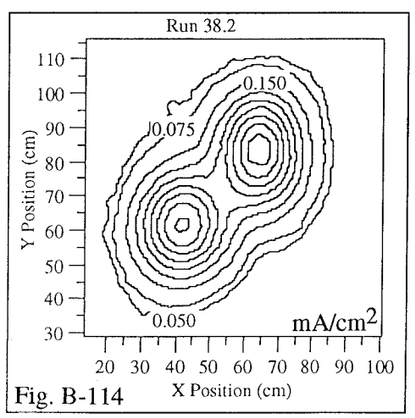

Fig. B-114

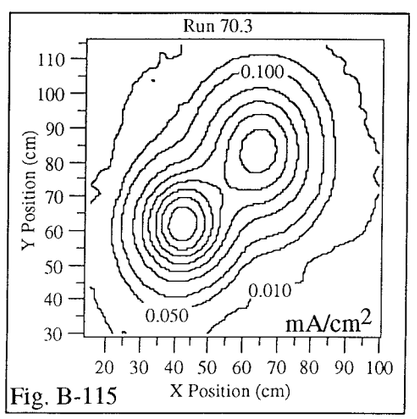

Fig. B-115

Segments ABC

Measured Data

Superposition Data

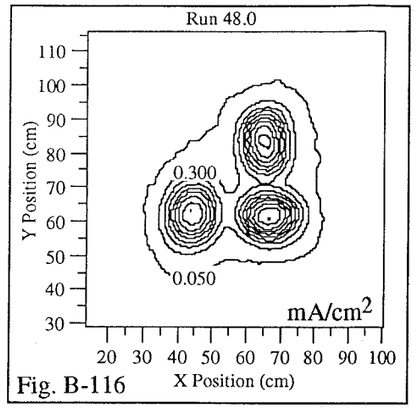

Fig. B-116

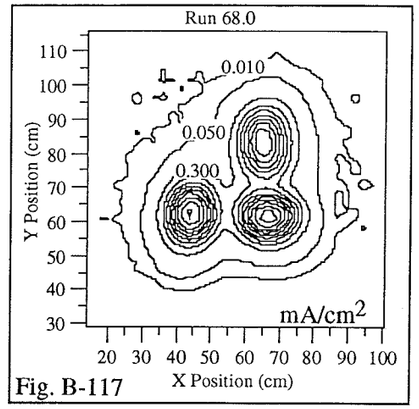

Fig. B-117

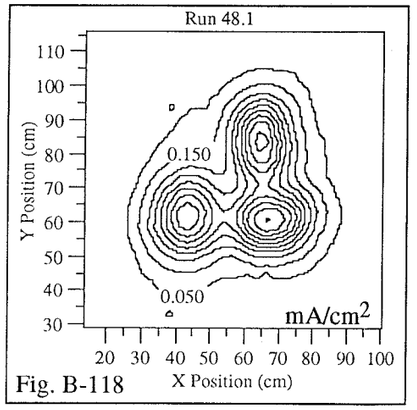

Fig. B-118

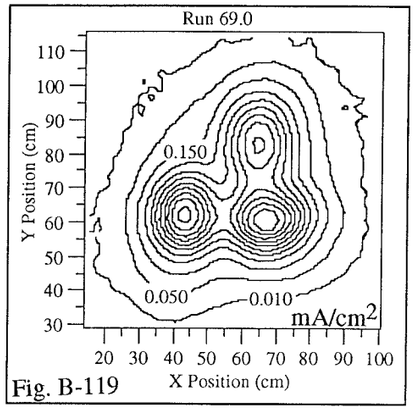

Fig. B-119

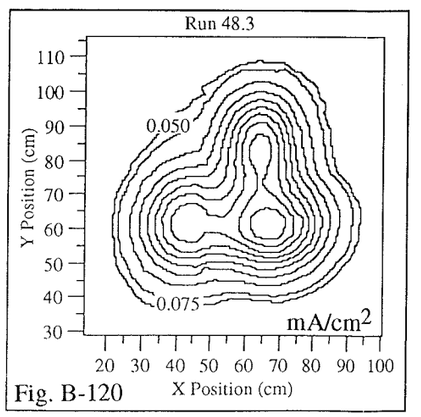

Fig. B-120

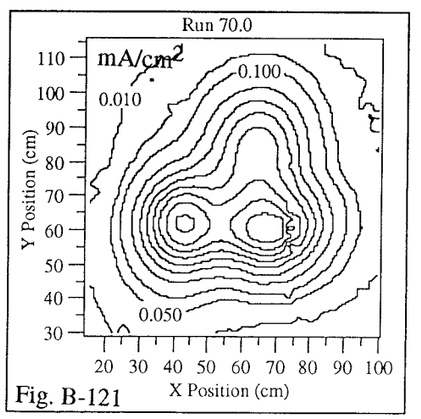

Fig. B-121

	z = 0.356 m	z = 0.660 m	z = 0.965 m
Segment A	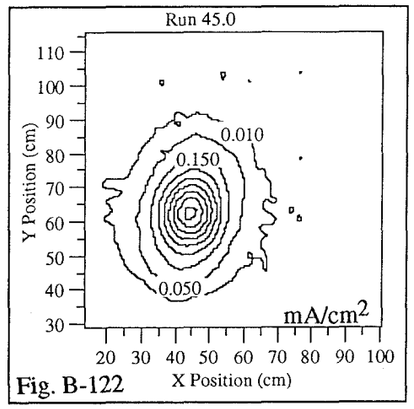 Fig. B-122	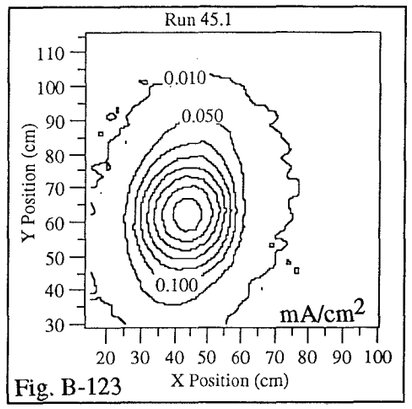 Fig. B-123	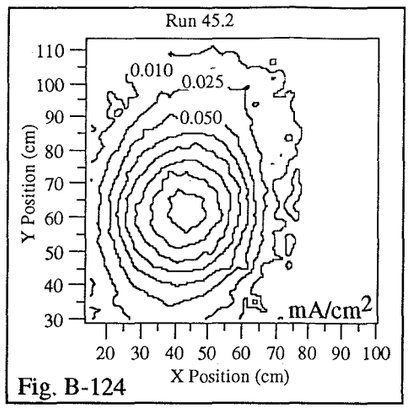 Fig. B-124
Segment B	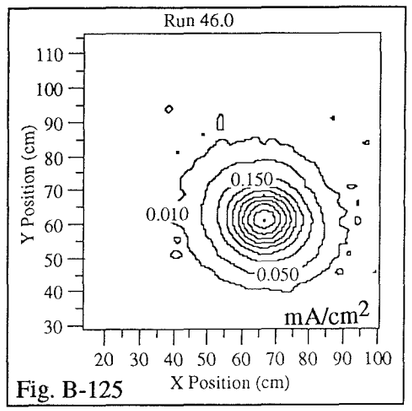 Fig. B-125	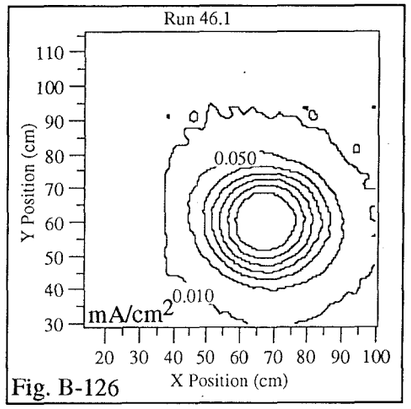 Fig. B-126	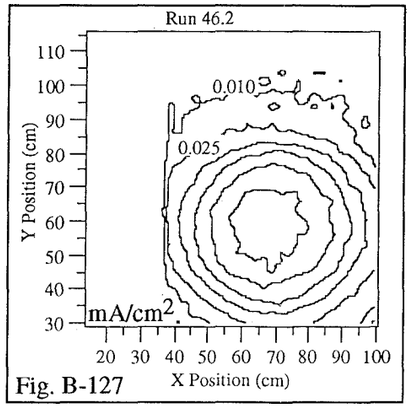 Fig. B-127
Segment C	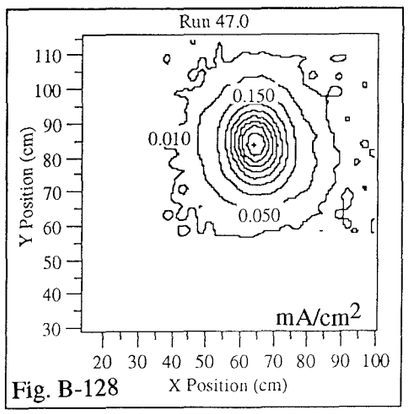 Fig. B-128	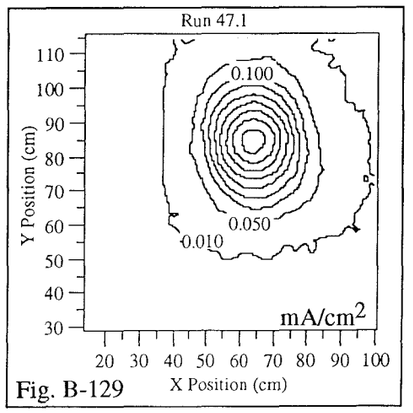 Fig. B-129	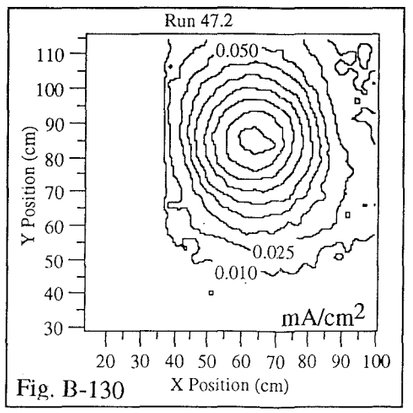 Fig. B-130

Segments AB

Segments BC

Measured Data

Superposition Data

Measured Data

Superposition Data

z = 0.356 m

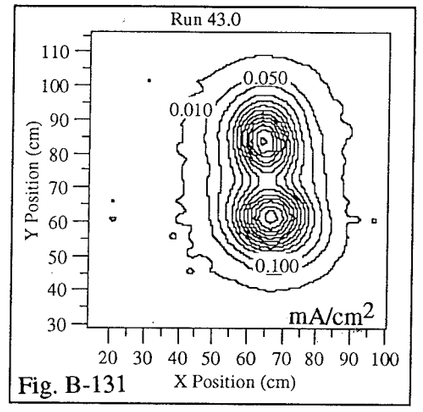

Fig. B-131

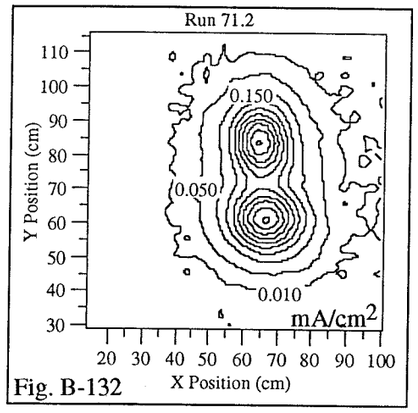

Fig. B-132

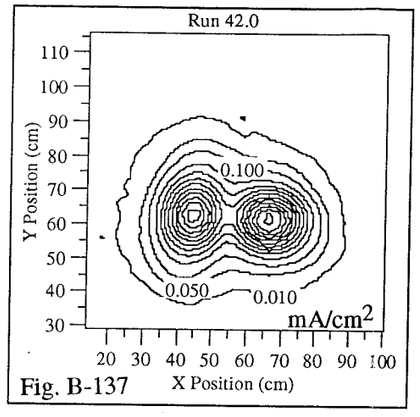

Fig. B-137

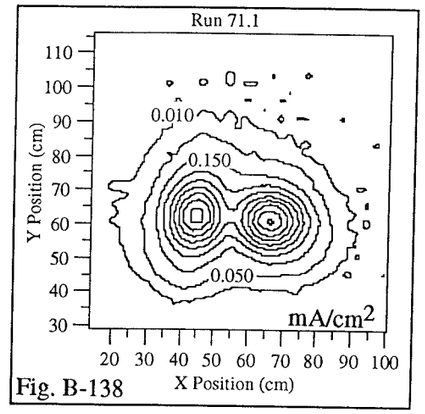

Fig. B-138

z = 0.660 m

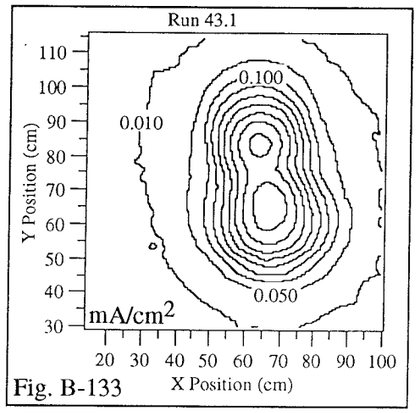

Fig. B-133

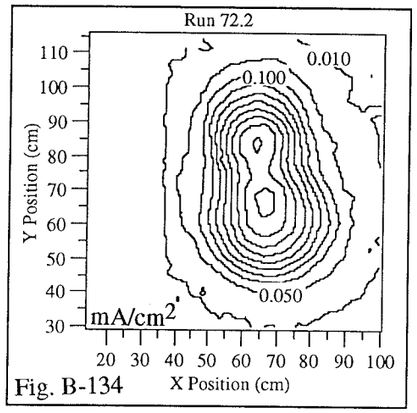

Fig. B-134

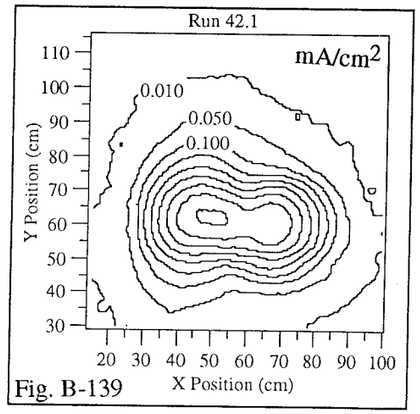

Fig. B-139

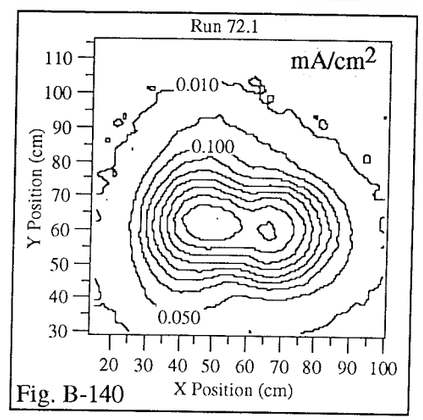

Fig. B-140

z = 0.965 m

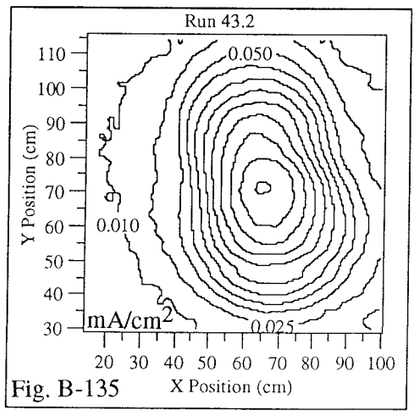

Fig. B-135

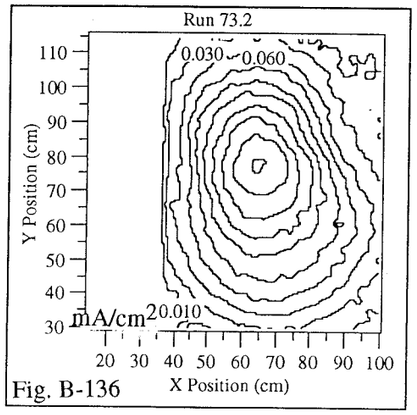

Fig. B-136

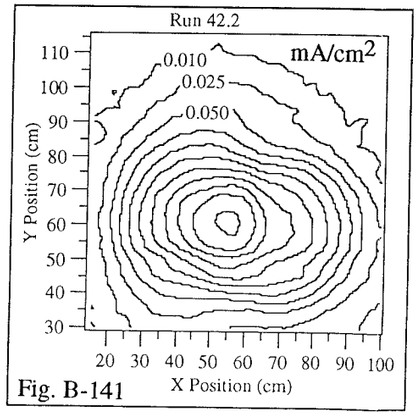

Fig. B-141

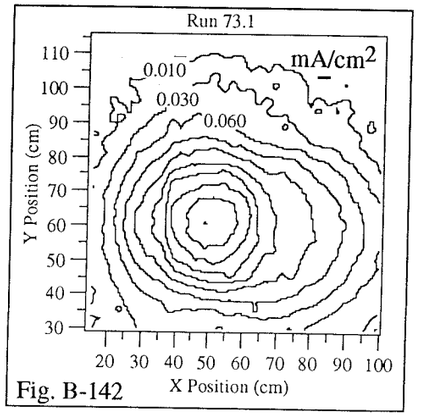

Fig. B-142

Segments AC

Measured Data

Superposition Data

z = 0.356 m

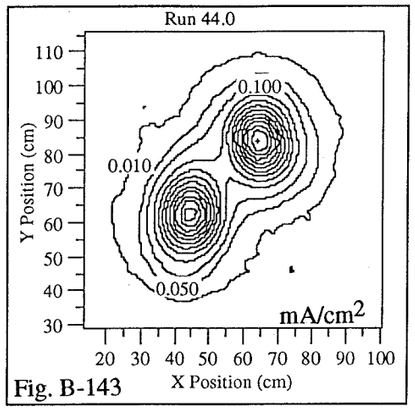

Fig. B-143

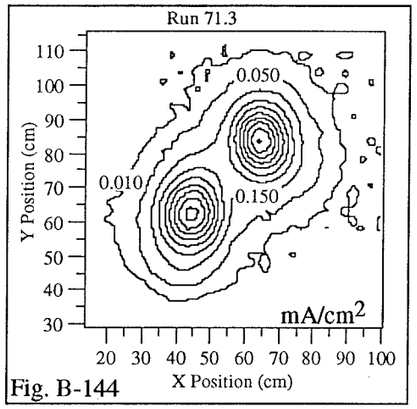

Fig. B-144

z = 0.660 m

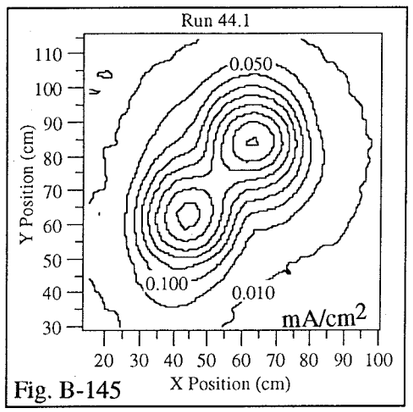

Fig. B-145

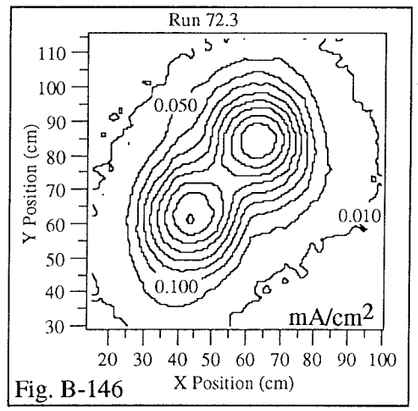

Fig. B-146

z = 0.965 m

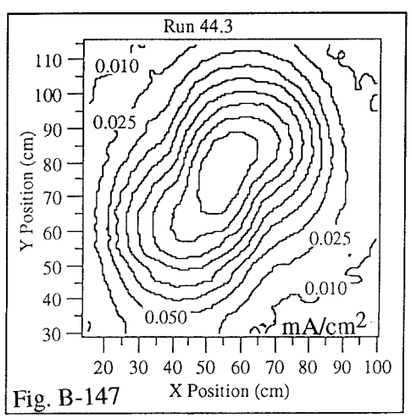

Fig. B-147

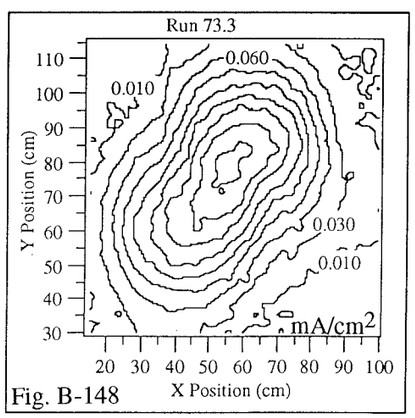

Fig. B-148

Segments ABC

Measured Data

Superposition Data

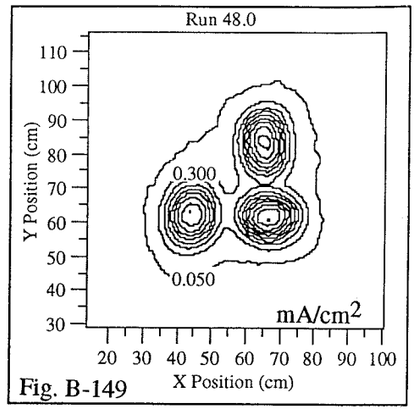

Fig. B-149

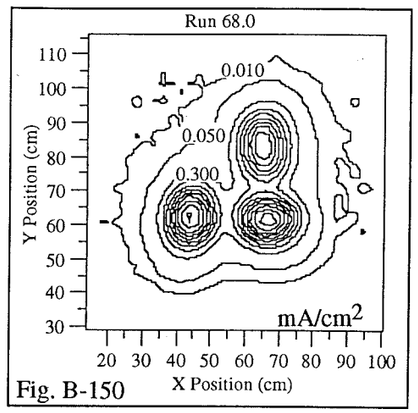

Fig. B-150

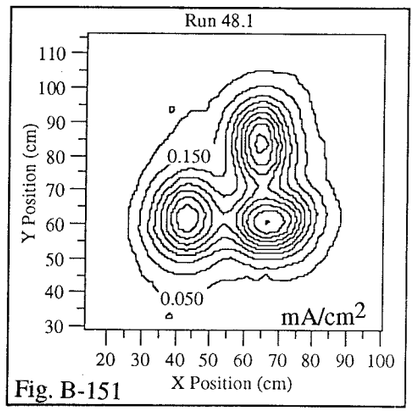

Fig. B-151

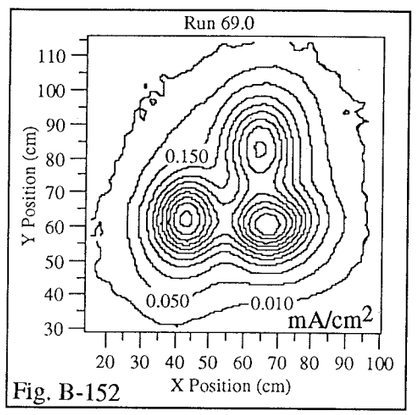

Fig. B-152

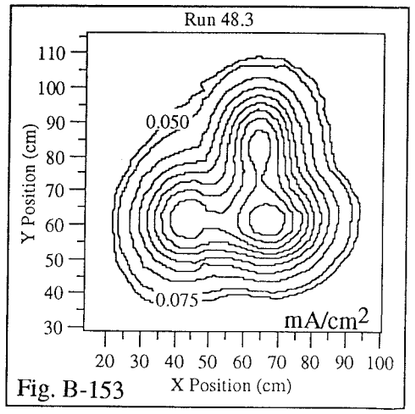

Fig. B-153

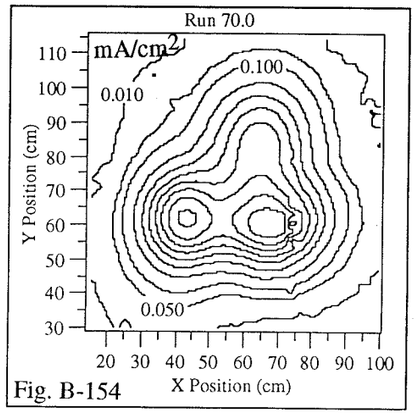

Fig. B-154

Appendix C

2.54 cm Spaced Data

1.27 cm Spaced Data

z = 0.356 m

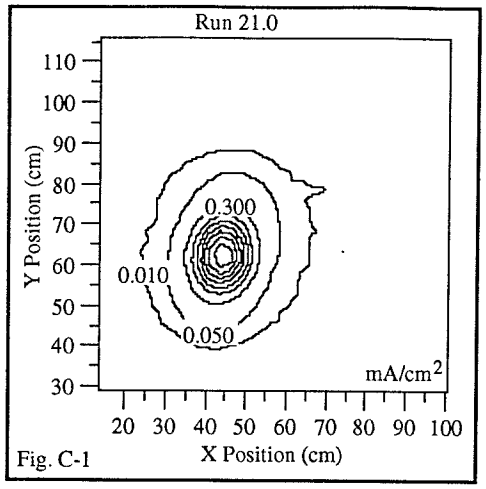

Fig. C-1

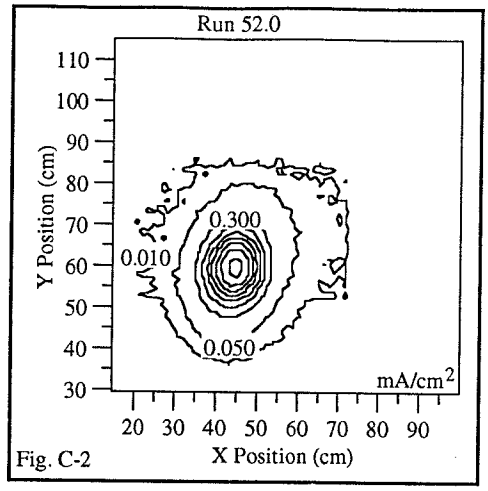

Fig. C-2

z = 0.508 m

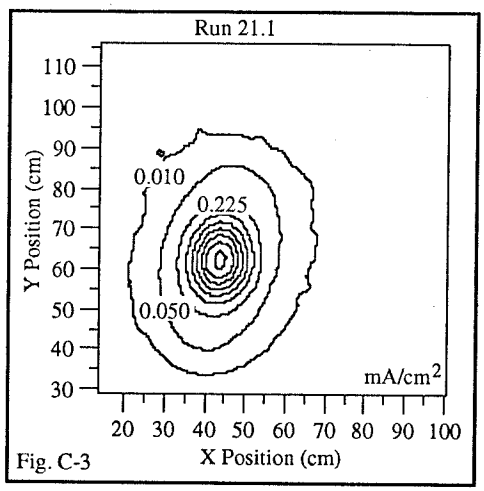

Fig. C-3

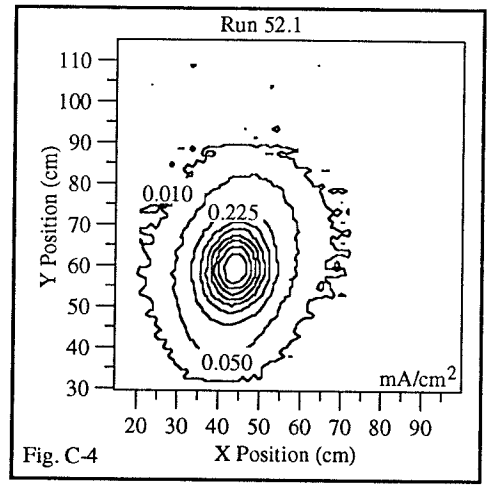

Fig. C-4

z = 0.660 m

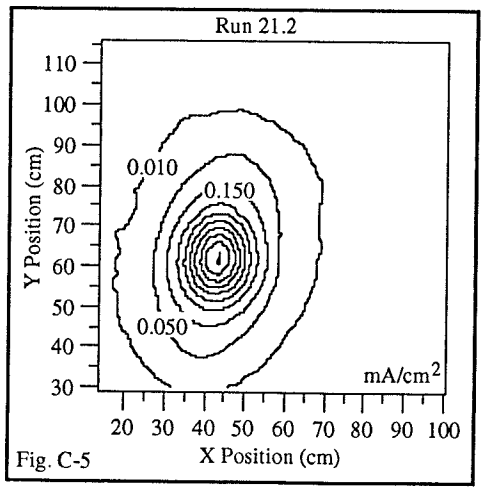

Fig. C-5

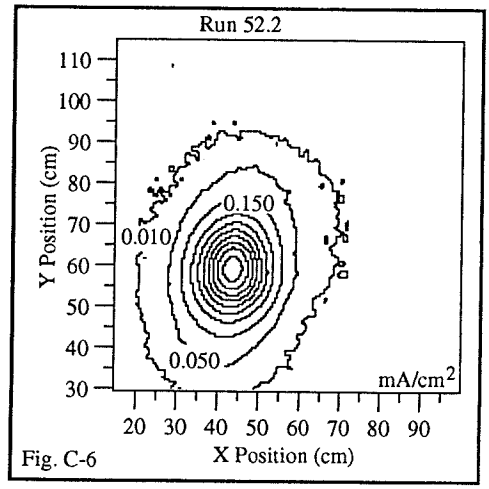

Fig. C-6

2.54 cm Spaced Data

1.27 cm Spaced Data

z = 0.356 m

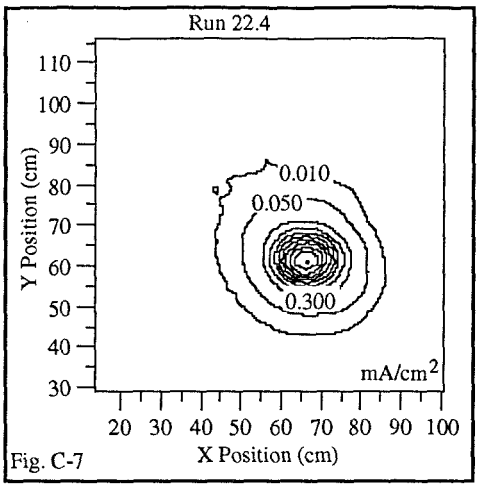

Fig. C-7

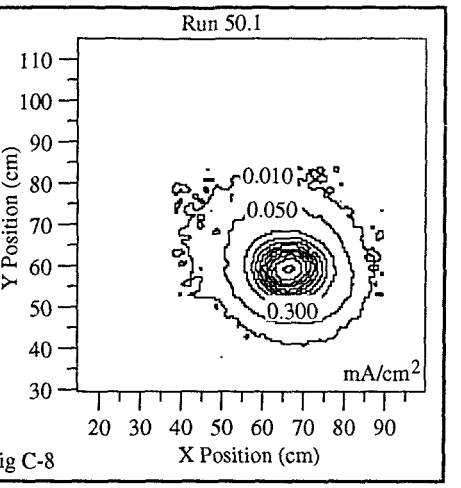

Fig C-8

z = 0.508 m

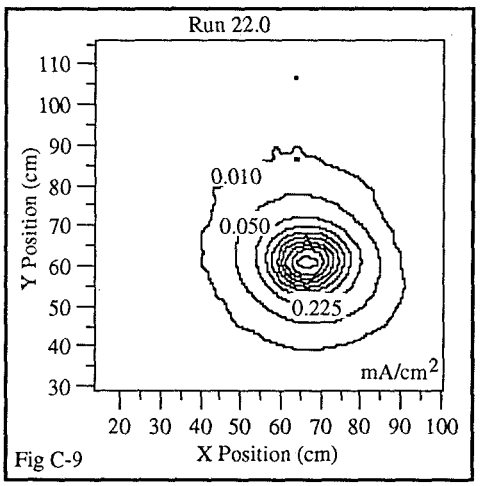

Fig C-9

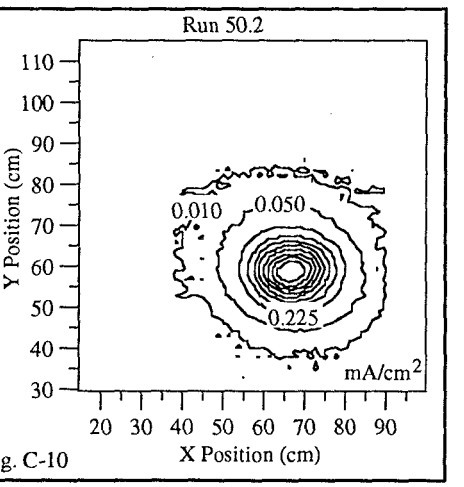

Fig. C-10

z = 0.660 m

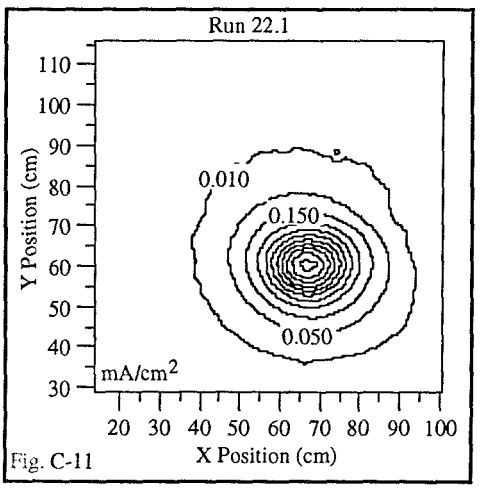

Fig. C-11

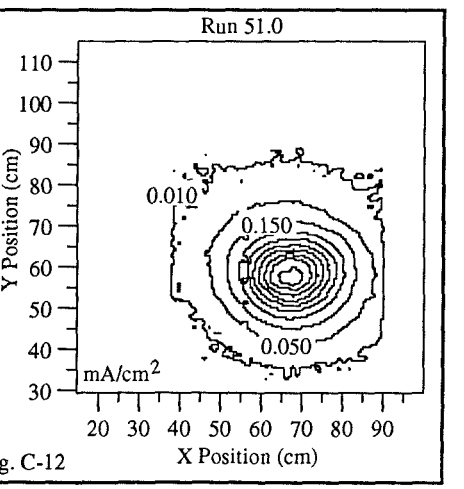

Fig. C-12